

**The Development and Alignment of Engineered
Microvasculature in Fibrin Gel**

A DISSERTATION
SUBMITTED TO THE FACULTY OF
UNIVERSITY OF MINNESOTA
BY

Kristen Thatcher Morin

IN PARTIAL FULFILLMENT OF THE REQUIREMENTS
FOR THE DEGREE OF
DOCTOR OF PHILOSOPHY

Robert T. Tranquillo, Adviser

November 2012

Copyright 2012

Kristen Thatcher Morin

Acknowledgements

In a goal so long in the making as a PhD, it is hardly an individual accomplishment. I want to take this opportunity to thank all those who have provided me with encouragement, technical assistance and money.

Let me begin by thanking my adviser, Bob, for taking a chance on a math/psychology major who wanted to be an engineer. Thank you for teaching me and guiding my thesis research to its successful end.

None of this would be possible without funding from a variety of sources. Many thanks to the Department of Biomedical Engineering for providing teaching assistantships, the Graduate School for a two-year fellowship, the American Heart Association for a pre-doctoral fellowship, and both the University of Minnesota's Institute for Engineering in Medicine and the National Institute of Health for covering the cost of my research.

Great thanks goes out to my lab colleagues, past and present, all of whom lent a critical eye at group meeting or helped me learn a technique. I especially want to thank Pat Schaeffer for her hard work sectioning and staining my samples, and Dr. Lauren Black III, who mentored me early in my career. I also had the privilege of working with many talented undergraduate volunteers. Raj, Paul, Emmelene, Michelle, and Ian, thank you for your hard work and dedication. Paul Carlson deserves special acknowledgement, as he worked with me for 4 years. It was a pleasure to work with you and watch you mature as a researcher. Also, thank you to those colleagues in other labs who lent a hand or just made each day more enjoyable.

I have great gratitude for my family and friends, who were supportive of my decision to pursue a PhD and encouraging throughout the process. Thank you for always asking how my cells were. Special thanks are due to my aunt Cindy, who was (and is) a mentor in the field to me. Thanks for all of your advice over the years.

Thank you to my husband, Eric, for his steadfast love and encouragement. Thank you for being my sounding board, sharing in my excitement when an experiment went well, and cheering me up when my experiments didn't go so well. I couldn't have done it without you.

And, finally, I praise God for blessing me with the ability to accomplish this goal. I pray that my research and achievements have been pleasing to You.

Abstract

The ability to engineer microvasculature would be of great utility for the tissue engineering of highly metabolic tissues such as myocardium. In addition, the alignment of such a network is critical to the success of using it to deliver oxygen to tissue cells because it provides natural inlet and outlet sides for perfusion. In this work, the ability of engineered microvessels to align with their fibrin gel matrix has been examined and a bioreactor has been designed to harness this ability and perfuse the engineered tissue. The results indicate that engineered microvasculature can be aligned via cell-induced gel compaction and that this compaction improves lumen density. Interstitial flow provided an additional increase in lumen density. A mathematical model of fluid flow through engineered microvessels and a variety of image analysis methods were also developed.

Table of Contents

Acknowledgements	i
Abstract	iii
Table of Contents	iv
Chapter 1. Introduction	1
1.1. Anatomy	1
1.1.1. Gross Cardiac Anatomy	1
1.1.2. Anatomy of the Myocardium	2
1.1.3. Coronary Arteries and Veins	2
1.1.4. Coronary Microvasculature.....	4
1.2. Disease	5
1.2.1. Coronary Artery Disease	5
1.2.2. Acute Myocardial Infarction	7
1.2.3. Congestive Heart Failure.....	8
1.3. Current Treatments for Heart Disease	8
1.3.1. Pharmacological	8
1.3.2. Transcatheter	9
1.3.3. Surgical	10
1.3.4. Transplantation.....	10
1.4. Tissue Engineering Strategies	11
1.4.1. Design Criteria.....	11
1.4.2. Scaffolds.....	12
1.4.3. Cell Sources	13
1.4.4. Current Technologies	13
1.5. Engineered Microvasculature.....	14
1.5.1. Design Criteria.....	14
1.5.2. Role of Support Cells.....	15
1.5.3. Scaffolds.....	17
1.5.4. Cell Sources	17
1.5.5. Current Technologies	18
Chapter 2. Alignment of Matrix and Endothelial Sprouts	21
2.1. Introduction	21
2.2. Methods	23

2.2.1. Cell Culture.....	23
2.2.2. Endothelial Cell Spheroid Formation	24
2.2.3. Fibrin Constructs with Magnetic Alignment.....	24
2.2.4. Fibrin Constructs with Cell-Induced Alignment	26
2.2.5. Image Acquisition and Analysis	27
2.2.6. Alignment Mapping.....	28
2.2.7. Histology.....	29
2.2.8. Statistics	29
2.3. Results	30
2.3.1. Increasing fibril alignment via increased magnetic field strength during fibrin gel formation increased EC sprout alignment.	30
2.3.2. Increasing fibril alignment via increased aspect ratio of cell-compacted fibrin gel increased EC sprout alignment.	31
2.3.3. EC sprouts were lengthened by increasing fiber alignment.	31
2.3.4. Sprout orientation influenced nhDF alignment.....	32
2.3.5. Sprouts contained patent lumens and connected when in close proximity.	32
2.4. Discussion.....	33
2.5. Figures	40
Chapter 3. Image Analysis Techniques for the Quantification of Microvascular Network Characteristics.....	47
3.1. Introduction	47
3.2. Methods	50
3.2.1. Cross Section Algorithm Description	50
3.2.2. Whole Mount Algorithm Description	53
3.2.3. Program Validation	56
3.3. Results	56
3.4. Discussion.....	57
3.5. Figures	60
Chapter 4. Alignment of Microvascular Networks formed in Fibrin Gel under Defined Conditions	66
4.1. Introduction	66
4.1.1. Cell Culture.....	70
4.1.2. Isotropic Construct Preparation	70
4.1.3. Aligned Construct Preparation.....	71
4.1.4. Compaction Studies	72

4.1.5. Hybrid Approach.....	72
4.1.6. Fibril Orientation	73
4.1.7. Microvascular Network Evaluation.....	73
4.1.8. Lumen Formation	74
4.1.9. Basement Membrane Deposition	75
4.1.10. Statistics	75
4.2. Results	75
4.2.1. HUVECs and PCs form highly interconnected microvascular networks in fibrin gel under defined conditions.	75
4.2.2. Aligned microvascular networks were formed under defined conditions in slabs of high aspect ratio.	76
4.2.3. Compaction is detrimental to forming networks but not to previously formed networks.	76
4.2.4. EGM-2+ improves compaction of slabs.	78
4.2.5. Hybrid approach yields improved network characteristics over defined medium alone.....	78
4.3. Discussion.....	79
4.4. Figures	86
Chapter 5. A Mathematical Model for Understanding Fluid Flow in Engineered Tissues Containing Microvessels	99
5.1. Introduction	99
5.2. Methods	101
5.2.1. Idealized Model of Fluid Flow in Tissues Containing Engineered Microvessels.....	101
5.2.2. Internal Validation of the Models	105
5.2.3. Comparison Between Models.....	105
5.2.4. Evaluation of Model Predictive Capability.....	107
5.3. Results	108
5.3.1. Model Validation.....	108
5.3.2. Comparison of Model Predictions.....	110
5.3.3. Evaluation of Model Predictive Capability.....	111
5.4. Discussion.....	112
5.5. Tables	119
5.6. Figures	121
Chapter 6. Aligned Microvessels with High Lumen Density via Cell-Induced Fibrin Gel Compaction and Interstitial Flow	131

6.1. Introduction	131
6.2. Methods	137
6.2.1. Cell Culture.....	137
6.2.2. Construct Preparation.....	137
6.2.3. Application of Interstitial Flow to Aligned Constructs	138
6.2.4. Hydraulic Conductivity Measurement	139
6.2.5. Viscosity Measurement	140
6.2.6. Estimation of Shear Stress	140
6.2.7. Histology/Image Analysis	141
6.2.8. Endothelial Barrier Function Assessment.....	143
6.2.9. Fibril Orientation	144
6.2.10. Cross-sectional Area Measurements.....	144
6.2.11. Statistics	145
6.3. Results	145
6.3.1. Cell-induced gel compaction results in aligned fibrils and aligned microvessels and increases lumen density.	145
6.3.2. Low interstitial flow increases microvessel lumen density while maintaining other microvessel properties.	146
6.3.3. High levels of basement membrane were produced by the cells.....	147
6.3.4. Microvessel properties varied along the length of the construct.	147
6.3.5. EphrinB2 expression increases over time in the absence of flow and is reduced in the presence of flow.....	148
6.3.6. Low interstitial flow increased endothelial barrier function.....	148
6.3.7. Cells experienced low levels of shear stress during interstitial flow.	149
6.4. Discussion.....	150
6.5. Figures	157
Chapter 7. Conclusions and Future Directions	170
7.1. Major Contributions	170
7.1.1. Endothelial Capillary Structures Can Be Aligned via Cell-Induced Compaction	170
7.1.2. Development of Semi-Automated Image Analysis Programs to Quantify Microvascular Network Properties.....	171
7.1.3. Highly Interconnected Microvascular Networks in Fibrin Gel can be Formed under Defined Conditions and Aligned via Cell-Induced Gel Compaction	171

7.1.4. Development of an Idealized Mathematical Model of Fluid Flow through Engineered Microvessels	172
7.1.5. Compaction of Fibrin Gel Containing Microvasculature Improves Lumen Density	173
7.1.6. Interstitial Flow at Specific Flow Rates Applied to an Existing Microvascular Network Improves Lumen Density.....	173
7.2. Future Directions.....	174
7.2.1. Hybrid Approaches to Perfuse Engineered Microvasculature	174
7.2.2. Cyclic or Static Strain to Further Improve Lumen Density	175
7.2.3. Tri-culture of ECs, PCs, and Cardiomyocytes	176
References	178
Appendix A. Protocols	192
Appendix B. Image Analysis Codes.....	244
Appendix C. Model Code.....	289

List of Tables

Table 5-1.	119
Table 5-2.	120

List of Figures

Figure 2-1.....	40
Figure 2-2.....	41
Figure 2-3.....	42
Figure 2-4.....	43
Figure 2-5.....	44
Figure 2-6.....	45
Figure 2-7.....	46
Figure 3-1.....	60
Figure 3-2.....	62
Figure 3-3.....	63
Figure 3-4.....	64
Figure 3-5.....	65
Figure 4-1.....	86
Figure 4-2.....	88
Figure 4-3.....	90
Figure 4-4.....	93
Figure 4-5.....	94
Figure 4-6.....	95
Figure 4-7.....	97
Figure 5-1.....	121
Figure 5-2.....	122
Figure 5-3.....	124
Figure 5-4.....	126
Figure 5-5.....	128
Figure 5-6.....	129
Figure 6-1.....	157
Figure 6-2.....	160
Figure 6-3.....	162
Figure 6-4.....	164
Figure 6-5.....	166
Figure 6-6.....	168
Figure 6-7.....	169

Chapter 1. Introduction

1.1. Anatomy

1.1.1. Gross Cardiac Anatomy

The heart is a volume displacement pump with two halves, which drive two circulations: the pulmonary and the systemic.¹ Systemic circulation returns to the heart via the inferior and superior vena cava and enter the right atrium. During atrial systole, the blood is pumped through the tricuspid valve into the right ventricle. From there the contraction of the ventricle pumps the blood through the pulmonary valve into the pulmonary artery. This artery then branches, directing blood to each lung for oxygenation.² The blood returns to the heart via four pulmonary veins, each of which anastomoses with the left atrium.³ From there, the blood traverses the mitral valve and enters the left ventricle (LV), which pumps the blood through the aortic valve into the aorta for systemic delivery. Due to the higher resistance of the systemic circulation than the pulmonary circulation, the LV is thicker than the right ventricle (8-10 mm vs. 2-3 mm).⁴ The atria are box-shaped, whereas the ventricles are conically-shaped, and the left and right halves separated by the atrial and ventricular septa, respectively.² The atria and ventricles are separated by the cardiac skeleton, a region of dense fibrous tissue, which serves to connect the atria and ventricles, strengthen the valve annuli, which all exist within the skeleton, and provide an electrical barrier between the atria and ventricles, facilitating their asynchronous contraction.³ The heart is shaped similarly to an inverted pyramid, with the atria

and great arteries as the base of the pyramid and the ventricles narrowing to become the apex of the pyramid.²

1.1.2. Anatomy of the Myocardium

The ventricular wall can be divided into three layers: the epicardium, which is on the outer surface of the wall and is covered by a layer of epithelial cells, the myocardium, which consists of cardiomyocytes, and the endocardium, which is on the inner surface of the wall and is lined with endothelial cells.³ In the myocardium, the cardiomyocytes are arranged into long interconnected muscle fibers. Each cell is short with several branches, and is connected at its ends to other cardiomyocytes via intercalated discs.³ These discs contain gap junctions which enable the direct passage of ions from one cell to another, facilitating coordinated contraction. The entire ventricle is connected electrically through these junctions.³ The muscle fibers are arranged parallel to one another, although the orientation gradually changes throughout the wall thickness so that the difference in alignment angle between the subepicardium and the subendocardium is 90. This arrangement results in a spiral-like contraction, similar to that of wringing out a rag.⁵

1.1.3. Coronary Arteries and Veins

The myocardium is nourished through the coronary circulation, which stems from the right and left coronary arteries. These two arteries emerge from the aorta at the sinuses of Valsalva, which are located just on the distal side of the aortic valve. The ostia of the coronary arteries are covered by the aortic valve

leaflets when the valve is open, and so flow through the coronary circulation only occurs during ventricular diastole, offset with the remainder of the systemic circulation.³ The course of the large coronary arteries is typically atop the myocardium, following interventricular or atrioventricular sulci. Main coronary branches are also typically found outside rather than within the myocardium.³

The left main coronary artery bisects within 5-10 mm of the aorta into the left anterior descending (LAD) artery and the circumflex artery. The LAD follows the anterior interventricular groove and provides diagonal branches, which supply the right and left ventricles, and septal branches, which supply the ventricular septum. The LAD is variable in length, and can occasionally continue across the apex to the posterior side of the heart.² The circumflex artery follows the atrioventricular sulcus laterally and around to the posterior side of the heart, providing branches that supply the left ventricle and atrium. In addition, in about 40% of hearts, the circumflex artery forms the sinoatrial node artery. In more than 85% of hearts the circumflex artery terminates near the cardiac crux; however, in humans with left arterial dominance, the circumflex artery turns and follows the posterior interventricular groove, becoming the posterior descending artery.⁶ The posterior descending artery supplies the right ventricle, ventricular septum and the atrioventricular node.³

The right coronary artery generates two large branches near the aorta, the conus artery, which supplies the right ventricle, and the atrial branch, which supplies the right atrium. The atrial branch also supplies the sinoatrial node in about 60% of hearts.² From there the right coronary artery follows the

atrioventricular groove in a pattern mirroring the circumflex artery. A variable number of branches supplying the right ventricle and atrium are produced. In most hearts, the right coronary artery turns at the cardiac crux to form the posterior descending artery.³

The coronary veins typically run parallel to the coronary arteries. Approximately 85% of the veins converge into the coronary sinus, which follows the posterior atrioventricular sulcus and enters the right atrium. The remaining 15% of the coronary circulation is divided between 2-4 anterior cardiac veins, which drain the anterior right ventricle, and the myriad Thebesian veins, which drain directly from capillaries and venules within the myocardium into the right atrium.

1.1.4. Coronary Microvasculature

The coronary microvasculature consists of vessels less than 200 μm in diameter and consists of arterioles (10-200 μm), capillaries (<10 μm) and venules (10-200 μm). These vessels are typically arranged in networks parallel to myofibrils, although the distance between an arteriole and venule in the same circuit is 10 fold larger than the average length of a capillary (50 μm), so some non-parallel capillaries exist.⁷ Due to the high metabolic demand of the myocardium, capillaries are extremely dense; on average adult human myocardium contains 2000 capillaries per square millimeter, making the distance between capillaries around 20 μm .^{8,9} At birth, capillary density is closer to 3000/ mm^2 and decreases over the first few years of life to the adult level, suggesting that the coronary microcirculation grows in coordination with the

heart.⁸ In addition, the capillary density varies with depth in the myocardium; the subendocardial muscle has a 10% higher microvascular density than the subepicardial muscle.¹⁰ This increased density counteracts the effects of cardiac contraction on the coronary blood flow. In the subendocardial muscle, microvessels are compressed 10-20% in diameter during systole, which induces retrograde flow in the arterioles. In comparison, microvessel diameter change is negligible in the subepicardial muscle, as is retrograde flow.⁷

At rest, the myocardium extracts 70-80% of the oxygen delivered by the microcirculation (compared to 30-40% for skeletal muscle), so increased demands due to exercise are met primarily by increased blood flow. This requires tight regulation of coronary blood flow, which is accomplished by endocrine and paracrine control of vascular resistance.¹⁰ The majority of vascular resistance is due to the precapillary sphincters of arterioles, which dilate in response to endothelium-produced nitric oxide (NO), among other substances.^{7,10}

1.2. Disease

1.2.1. Coronary Artery Disease

All arteries, including coronaries, consist of three layers. The intima consists of a single layer of endothelial cells on the inner surface of the artery and a thin layer of connective tissue, the basal lamina. The media contains structural (collagen) and elastic (elastin) proteins as well as smooth muscle cells, which maintain the proteins. The final layer is the adventitia, which contains connective tissue.¹¹ Atherosclerosis involves the buildup of fatty plaques within

the intima of an artery and can lead to myocardial ischemia and death. The mechanisms by which these plaques build up are largely unknown; however, the plaques do typically follow a pattern of growth. During the initiation phase, lipids begin to accumulate in the intima and are oxidized, making them recognizable by monocytes. Monocytes then enter the intima and engulf lipids, becoming foam cells.⁶ Extracellular lipids begin to accumulate in the intima during the evolution phase, and coalesce to form the lipid core of the plaque. Smooth muscle cells migrate into the intima and begin to both proliferate and secrete collagens. When a plaque is in the advanced phase, some lipids have crystalized, the core is distinct, and a fibrous cap has been deposited by the smooth muscle cells. At this point, the fate of the plaque is variable. Some remain as is, some calcify, and others become complicated by thrombus.⁶

Thrombi occur in two ways. The first is through denudation of the vessel, which exposes the underlying fibrous cap. A thrombus forms on top of the cap, and is usually small unless a very large area has been denuded. These small thrombi can separate from the plaque, becoming emboli, and serve to occlude smaller distal arteries. The second way is through plaque rupture, in which the stress experienced by the fibrous cap in systole (which can be up to 10 times greater than normal wall stresses) causes the cap to fissure, spilling the lipid contents of the plaque into the arterial lumen. These lipids are highly thrombogenic, and the artery is often completely occluded.⁶

1.2.2. Acute Myocardial Infarction

For unknown reasons, the coronary arteries are highly susceptible to atherosclerosis.⁶ When atherosclerotic lesions cause coronary arteries become critical (more than 50% occluded by diameter), flow disruptions occur, and very small changes in vessel diameter cause large changes in flow rates.¹¹ Vessel narrowing caused by these plaques often induces myocardial ischemia. Occlusions, typically due to thrombi or emboli, result in ischemia and, if reperfusion is not established quickly, infarction of the area distal to the occlusion.¹¹ The size of the affected area (and thus the symptoms of the infarction) varies widely. Small areas in general go unnoticed, but the accumulated damage of many small infarcts can be detrimental. When a large area is affected, immediate treatment is required, with the goal of reperfusion as quickly as possible, thereby rescuing as much myocardium as possible. The time before reperfusion is highly correlated with outcome (longer times leading to poorer outcomes), as cardiomyocytes have a very high demand for oxygen and therefore respond quickly to ischemia. Although the heart is only 0.5% of total body mass, it requires 7% of the body's oxygen.¹² When a cardiomyocyte is exposed to an occlusion of blood flow, it will stop beating after about 60 seconds, and reversible injury occurs after about 20 minutes. By 40 minutes, only 60-70% of the affected area will survive upon reperfusion, and by 3 hours, this percentage has dropped to 10%. After about 6 hours, the entire area is irreversibly damaged.¹³ Therefore, perfusion must be re-established very quickly after infarction to prevent myocardial death.

1.2.3. Congestive Heart Failure

Congestive heart failure (CHF) affects more than 500,000 Americans each year, killing over 50,000 annually, and in the majority of cases, CHF is a sequela to one or more myocardial infarctions.¹⁴ The reduction of function of the infarcted area leads to decreased ejection fraction, triggering compensatory mechanisms.¹⁵ Adrenergic stimulation increases heart rate and contractile force of living myocardium,¹⁴ and increased blood volume in the left ventricle improves contractility via the Frank-Starling mechanism.¹⁵ Over time, these result in cardiomyocyte hypertrophy, which necessitates changes in the cells' electrical biochemical properties.¹⁴ When the infarcted area is small (<20% of the left ventricular circumference), these mechanisms keep cardiac output normal. However, when an infarct is large, or many small infarcts accumulate, the compensatory mechanisms cannot fully offset the damage.¹⁵ Because of this, these initially beneficial modifications progressively become detrimental and ultimately result in CHF.¹⁶

1.3. Current Treatments for Heart Disease

1.3.1. Pharmacological

Many pharmaceuticals are used to treat heart disease patients on the spectrum from atherosclerosis to CHF, but the majority work to improve cardiac output by increasing cardiomyocyte contractility, decreasing heart rate, or decreasing systemic vascular resistance.¹⁴ Inotropes affect intracellular calcium levels, increasing the strength myocyte contraction. Beta blockers are

sympathetic pathway antagonists that reduce heart rate. Combined with improved myocyte contractility, a lower heart rate increases stroke volume, leading to improved overall cardiac output.¹⁴ Vascular resistance can be reduced by vasodilators, such as nitrates, or by agents that reduce blood volume, such as ACE inhibitors and diuretics.¹⁴ Despite the numerous pharmaceuticals that have been developed, none are effective at preventing CHF, and many have extensive side effects.

1.3.2. Transcatheter

Once atherosclerosis is discovered, several transcatheter techniques are often employed to widen diseased vessel in an attempt to prevent MI and CHF. Balloon angioplasty involves the insertion of a balloon over a catheter through a vein to the point of the atherosclerotic lesion. The balloon is then inflated, pushing the vessel wall outward, widening the vessel.¹⁷ Another technique implants a stent, which is crimped over the angioplasty balloon and expands upon the balloon's inflation, providing additional support to keep the vessel open. Now popular are drug-eluting stents, which provide localized delivery of anti-proliferative drug to prevent restenosis, a common problem with angioplasty and standard stents.¹⁷ Although these therapies do provide relief of symptoms, they do little to prevent MI or CHF, because only a small number of vessels are treated. MI is often caused by occlusions in smaller vessels that would not be treated with stents or angioplasty.¹⁷

1.3.3. Surgical

Surgical options for the treatment of heart disease depend on the stage of disease. When atherosclerosis is detected or an MI occurs, coronary artery bypass grafting (CABG) is an option, in which another vessel is used to divert blood around a severe atherosclerotic lesion. Similar to the transcatheter options, CABG treats only major vessels, and so is limited in its ability to prevent future MI or CHF. In addition, only a few vessels can be used for such grafting, leaving some patients without this option.¹⁸ When heart disease is at a more advanced stage, mechanical support of the heart is often used. Typically this is in the form of a ventricular assist device (VAD), although in recent years several total artificial hearts have also been made available. VADs can be either uni- or biventricular, and can have a variety of different pumping mechanisms, including volume displacement, which is similar to the heart, and axial flow, which creates non-pulsatile flow.^{1,19} Although the use of these devices is occasionally associated with cardiac recovery (about 5% of cases), in general patients continue to decline, albeit more slowly, after the initial improvement. In addition, long term use of mechanical support is linked to unfavorable outcomes, and therefore it is most often used as a bridge to heart transplantation.^{1,19}

1.3.4. Transplantation

Cardiac transplantation is the gold standard for the treatment of patients with end-stage CHF.²⁰ The lifespan of a transplanted heart ranges from 10 to 20 years, much longer than mechanical support, and patients tend to improve more after heart transplantation than after the implantation of a mechanical support

device.²¹ However, the major limitation of this technique is the lack of donor hearts; 20-25% of patients on the waiting list die before receiving an organ.^{21,22}

1.4. Tissue Engineering Strategies

1.4.1. Design Criteria

It is evident that the currently available treatments for MI and CHF are insufficient, and new strategies are needed. Tissue engineering, in which the goal is to create living tissue in vitro, provides an opportunity to improve upon available therapies. One such improvement would be to create a “patch” of engineered myocardium, which would then be implanted to replace the function of native myocardium damaged by MI. If implanted soon after MI, this repair would negate the need for compensatory mechanisms, and prevent the progression to heart failure. Clearly this myocardial patch would need to electrically couple with the native myocardium and produce enough contraction force to replace the function of the damaged tissue. This will likely require the production of a large and thick tissue, as the infarcts that eventually cause heart failure tend to be quite large (40% of LV or more) and generally span the entire LV wall thickness (8-10 mm).⁴ The patch would also need match the mechanical properties of myocardium, stiff enough to prevent ventricular dilation, which often occurs after MI, yet flexible enough to reduce its volume upon contraction. In addition to these functional requirements, the ideal patch would be constructed from autologous cells to avoid immunosuppressive drugs. The above design criteria provide a framework from which develop such a myocardial patch

1.4.2. Scaffolds

A variety of scaffolds have been used in the design of engineered myocardium, including synthetic and natural polymers. Synthetic polymers such as polyglycolic acid (PGA) and poly(lactic-co-glycolic acid) (PLGA) are typically biodegradable, and are often modified, coated, or mixed with other polymers to include cell binding domains.²³⁻²⁷ Natural polymers include type I collagen, fibrin, alginate, and Matrigel, a mix of extracellular matrix (ECM) polymers and growth factors derived from tumor cells.²⁸⁻³⁸ In addition to the above approaches, several groups have developed tissues by culturing monolayers of cardiomyocytes and other native heart cells, which produce ECM; however, these are typically quite thin.³⁹⁻⁴¹ As the scaffold provides the bulk of a tissue's mechanical properties, it is critical that the scaffold eventually have the appropriate stiffness for myocardium, to meet the design criterion mentioned above. In general, scaffolds from synthetic polymers are initially too stiff, and those from natural polymers are too soft. Natural polymers have an advantage over synthetic in that they avoid unnatural and possibly toxic (if in high concentrations such as at the tissue site) degradation products. Among natural polymers, fibrin stimulates tissue growth because it is involved in the tissue formation process known as wound healing. Thus, although collagen I may appear to be a more obvious choice because collagen fibrils provide much of the mechanical strength found in native tissues, fibrin gels induce more collagen production by cells than collagen gels, leading to stronger tissues at the end of the culture period.⁴² However, this strength is not only due to the collagen

produce by the cells, but also to the compaction of the gel by the cells, which increases the tissue density. Fibrin, compacted during culture by the entrapped cells, therefore, has been the scaffold of choice used in these studies.

1.4.3. Cell Sources

Cell source is a challenge in myocardial tissue engineering due to the non-proliferative state of adult cardiomyocytes. The majority of work done on engineered myocardium has utilized animal cells, primarily the neonatal rat cardiac population, due to the relative ease of obtaining cells. However, a source of human cardiomyocytes is required, and autologous cells preferred, as noted above. Adult cardiac stem cells have been identified as a possible cell source, but are difficult to isolate. Cardiomyocytes derived from human embryonic stem cells have also been suggested, but they are ethically problematic. Promising cell populations include cardiomyocytes derived from induced pluripotent (iPS) cells or other non-embryonic stem cells, which avoid the problems associated with the above cell types. It remains to be seen if any of these cell types will be appropriate, or if a different cell population will be needed.

1.4.4. Current Technologies

Much progress has been made by numerous groups in the creation of myocardial patches. As noted above, one important design criterion is that the patch generate enough force to be physiologically relevant. Current results for tissues containing rat cardiomyocytes exhibit contraction forces ranging from 0.01-1.3 mN/mm².^{29,32,35,38} This remains quite low in comparison to human

cardiac muscle, which produces a twitch force of 44 mN/mm^2 ,⁴³ although it is unclear whether a contraction force equal to that of native myocardium will be required for the patch to be effective. Recently results of tissues containing human iPS-derived cardiomyocytes were reported; the maximum twitch force achieved was 0.08 mN/mm^2 .³⁷ Alignment of cardiomyocytes, as occurs in native myocardium, has been shown to improve contraction force, via improved gap junction formation, and accounts for the highest forces recorded in engineered myocardium.^{31,38} In addition, the presence of non-cardiomyocytes improves contraction force.³¹

Another important criterion is that the patch be able to electrically integrate with the heart. This has not been demonstrated directly to date, although several groups have shown an improvements in LV function when a patch is implanted in an infarct model.^{30,44} However, it is unclear whether the cells provide additional benefit over just the bare scaffold.⁴⁵

1.5. Engineered Microvasculature

1.5.1. Design Criteria

The high metabolic demands of cardiomyocytes, especially when densely cultured, as would be needed to achieve high contraction forces, eliminates diffusion as a viable means for nutrient delivery to engineered myocardium. One alternative method for delivering nutrients is to engineer a microvascular network within the patch. However, the mere presence of a microvascular network is not enough to provide nutrients; culture medium must flow through the network,

mimicking blood flow in capillaries. Therefore, an engineered microvasculature must be capable of supporting flow and a perfusion circuit must be designed to drive the flow of culture medium through the network. To have directional flow, the network must also have inlet and outlet sides, with aligned vessels in between. In addition, the network must not regress over time, must be permeable to nutrients and waste products, and must be of sufficient capillary density to maintain the cardiomyocytes. Finally, the microvascular network would need to be compatible with the requirements listed above for the heart patch, including aligned and compacted fibrin gel as a scaffold, and the use of autologous cells.

1.5.2. Role of Support Cells

In vivo, capillaries are surrounded by a sparse layer of supporting cells termed pericytes (PCs). PCs are highly mobile and their processes extend to reach many ECs; primary processes extend along the capillary axis while secondary processes extend circumferentially.^{46,47} They are often located within the vascular basement membrane, and are directly connected to ECs via tight junctions.⁴⁶ During development these PCs are recruited to the forming capillaries, and this recruitment signals the end of the microvascular “plasticity window,” in which the microvessels freely grow and regress.^{47,48} ECs recruit PCs by releasing PDGF-B,⁴⁹ and PC recruitment can be blocked by knocking out PDGF or its receptor.^{49,50} The knockout phenotype includes lethality at birth due to microvascular hemorrhage and increased vessel diameter due to unchecked EC proliferation. Interestingly, however, there is no difference in vessel length or branching between knockout and wild type animals.⁵⁰ This suggests that PCs are

responsible for regulating microvascular stability, permeability and diameter, but not microvessel patterning. The mechanism by which PCs have these effects is not fully known, but is thought to involve paracrine signaling from both soluble and insoluble factors. PCs release Ang-1, a vessel stabilizing protein, and in the absence of PCs, Ang-1 can improve microvessel stability, suggesting that the PC-derived Ang-1 is partially responsible for the stabilizing effects.⁵¹ Insoluble factors include type IV collagen and laminin, among other components of the vascular basement membrane. PCs both produce and trigger ECs to produce basement membrane proteins, which are thought to be critical in the maintenance of capillary beds.^{47,52}

In vitro, it has consistently been reported that without the use of support cells microvessels will eventually regress. The support cell types used in the literature vary, including fibroblasts, smooth muscle cells, mesenchymal progenitor cells (MSCs), and PCs.⁵³⁻⁵⁶ The use of these cell types has been met with varying degrees of success, but in general they tend to improve microvessel formation and/or stability. Fibroblasts and MSCs have been shown to behave similarly to PCs in that some of them become recruited to the microvascular niche and promote stability.^{53,54}

Perhaps not unexpectedly, PCs excel at the role of stabilizing engineered microvessels, as shown in numerous publications from the laboratory of George Davis at the University of Missouri. PCs co-entrapped with human umbilical vein ECs (HUVECs) in type I collagen gel recruited to the forming vessels, promoted

the assembly of basement membrane, maintained microvessel diameter within the physiological range, and stabilized the networks for at least several weeks.⁵⁶

1.5.3. Scaffolds

Although a variety of scaffolds have been used for the engineering of microvasculature, the majority of the *in vitro* work has used hydrogels, primarily collagen I or fibrin.^{53,54,56} Both hydrogel types and combinations of them have proved successful; however, fibrin is more advantageous than collagen I due to its natural pro-angiogenic role in wound healing. This, combined with the tissue-formation reasons mentioned above, explains the choice to use fibrin gels as scaffolds in these studies.

1.5.4. Cell Sources

HUVECs are the most widely studied human EC, and are easily isolated and cultured, which explains their popularity. However, HUVECs have limited potential to be autologous for heart disease patients. Other possible EC sources include circulating populations or ECs derived from embryonic stem cells, iPS cells or other stem cells. Aside from embryonic stem cells which evoke ethical issues, all of these are possible autologous sources of ECs. Through collaboration with Robert Hebbel at the University of Minnesota, these studies have used blood outgrowth ECs (BOECs), a type of circulating EC. This cell type is positive for many EC markers and well as negative for the monocyte markers CD14 and CD45. It also has a very high proliferative potential (10^{19} cells in 60 days), making it an ideal candidate for expansion *in vitro*.⁵⁷

1.5.5. Current Technologies

Two basic strategies exist for the engineering of microvasculature. The first is to create channels within the scaffold and line them with ECs.^{58,59} Although this strategy is simple conceptually and results in a network of EC-lined tubes that can be easily connected to a flow circuit, it is difficult to make complex and small (capillary-sized) geometries, and the microvascular patterning must be designed. The other basic strategy involves the self-assembly of ECs into networks. This method is easy technically, and the network morphology is defined by the cells. Within this second method, angiogenic or vasculogenic models can be used. Angiogenic models induce sprouting from existing monolayers of ECs, which are either monolayers on a surface of the scaffold or groups of ECs within the scaffold. Surface monolayers often sprout in response to a VEGF gradient.^{60,61} The mechanism by which sprouts grow from ECs in spheroids or adherent to microcarrier beads is less clear, and may require factors released by support cells.^{62,63} Vasculogenic models begin with ECs dispersed throughout the scaffold, which then spread and connect to form a network; this is the simplest method for forming microvascular networks, and is the method adopted in these studies. Several groups have also explored this method with promising results; three of the most promising are discussed here.

Andrew Putnam's group at the University of Michigan has explored the role of MSCs as support cells. HUVECs and MSCs were entrapped in fibrin gel and cultured in serum- and cytokine-containing medium. HUVECs formed microvascular networks containing lumens and MSCs co-localized with the

microvessels.⁵⁴ After 5 days of culture, the microvessels demonstrated the ability to regulate their permeability.⁶⁴

At the University of California at Irvine, Steve George's group entrapped human endothelial progenitor cells and human lung fibroblasts in fibrin gel, and cultured them in serum- and cytokine-containing medium. Co-localization of the fibroblasts to the forming EC networks was observed, and upon implantation in a nude mouse model, these vessels anastomosed with the host vessels.⁵³ More recent work has shown that interstitial flow in a microfluidic chamber induces EC network formation, and that at least some of the vessels are capable of carrying flow (unpublished work; personal communication).

Finally, George Davis' group at the University of Missouri has demonstrated the formation of highly stable microvascular networks by HUVECs and PCs in collagen I gel under defined conditions. The culture medium contained few cytokines; however three hemopoietic stem cell factors were included in the gel formulation to drive capillary morphogenesis: stem cell factor (SCF), interleukin-3 (IL-3), and stromal derived factor (SDF)-1 α . As noted previously, PCs recruit to the HUVEC tubes and induce basement membrane deposition.⁵⁶

Although the above systems are state-of-the-art, they have several limitations. All of them used small volumes of very porous gel to achieve their results, limiting their use as engineered tissues due to the size and stiffness of the constructs. Clearly a larger initial gel volume and cell-induced gel compaction are required to achieve a functional tissue. Cell-induced gel compaction would

not only strengthen the tissue mechanically, it would also likely increase the capillary density, which is quite low in the above studies. In addition, only one group attempted to perfuse their engineered vessels, and that group did so within a microfluidic system, which is not compatible with the previous requirements of increased size and compaction. More work is certainly required to create a system that would perfuse microvessels in a large compacted tissue. Finally, only one group used potentially autologous ECs, and only one group (a different one) used potentially autologous support cells. The use of autologous cell types, although not entirely required, would improve the heart patch. The work presented here took steps to address these three areas of needed improvement in developing engineered microvasculature for use in a heart patch.

Chapter 2. Alignment of Matrix and Endothelial Sprouts

2.1. Introduction

One of the design criteria for engineered microvasculature is that the microvessels and the matrix be aligned. Alignment of the microvessels not only mimics the native architecture of myocardium,⁶⁵ but also creates natural inlet and outlet sides of the network for directional perfusion. The matrix of such a tissue construct must also be aligned so that the engineered microvasculature is compatible with the myocardial patch, in which alignment has been shown to greatly improve contraction force.³⁸

Studies of cells cultured in 3D environments *in vitro* suggest that cells are able to sense the alignment of nearby extracellular matrix fibers and align with the fibers, a phenomenon known as contact guidance.⁶⁶ For example, when magnetic fields were used to align the fibrils of collagen I gel to different extents, the alignment of entrapped fibroblasts coincided with that of the collagen fibrils.⁶⁷ Similarly, fibroblasts⁶⁸ and cardiomyocytes³⁸ aligned parallel to matrix fibers in fibrin-based tissue-engineered constructs, where the fibril alignment was created from mechanically-constrained cell-induced gel compaction. However, few studies have investigated the contact guidance response of endothelial cells (ECs) or microvessels. ECs elongated in the direction of fiber alignment when plated on aligned collagen I fibers⁶⁹ or aligned electrospun polymer fibers.⁷⁰ Other studies have found that stretching induces the alignment of both fibrin or collagen fibers and EC tubule structures within the gel, although cause and effect were not determined between the fiber and cell alignment.^{71,72} Endothelial

sprouts were also observed to be aligned with local elastin fibers in the rat mesentery, although again cause and effect were not established⁷³. Therefore, detailed study is required to determine whether or not fibril alignment is sufficient to align microvessels.

The entrapment of EC spheroids, or aggregates, in fibrin gels is an attractive method for studying the alignment of microvessels with matrix. EC sprouting from spheroids mimics *in vivo* sprouting angiogenesis, and the fibrin gel can be aligned in several ways to investigate different components of alignment. In addition, when spheroids are entrapped at a relatively low density, they are separated from each other, so alignment phenomena can be observed for a several small isolated systems within a single construct.

Korff and Augustin⁷⁴ first demonstrated that the outer layer of EC spheroids behaved similarly to the endothelium of a vessel with the center of the spheroid as the lumen of the vessel. The surface ECs became quiescent and expressed CD31 at cell-cell contacts, and I-CAM and V-CAM expression was inducible by TNF- α activation. They also showed improved survival of ECs when cultured in suspension as spheroids rather than as single cells. *In vitro* network formation by human umbilical vein EC (HUVEC) spheroids entrapped in collagen I gels has been shown,⁷⁵ and the ability of nearby sprouts to anastomose within fibrin gel has been demonstrated.⁷⁶ In addition, vessel formation was shown *in vivo* using HUVEC spheroids in a Matrigel/fibrin matrix.⁷⁷ The co-entrapment of support cells such as fibroblasts or smooth muscle cells has been shown to aid vessel growth from EC spheroids.⁷⁷

Very limited data is available on the alignment of sprouts from EC spheroids, but Korff et al. showed that EC spheroids entrapped in collagen I gels can exert traction forces and align the collagen fibrils between nearby spheroids.⁷⁶ The sprouts from these spheroids grew towards each other, but cause and effect between sprout growth and collagen fibril alignment and the level of tension in the collagen fibril network was not determined. Interestingly, this local rearrangement of fibrils was not seen when EC spheroids were entrapped in fibrin gel.⁷⁶

In the studies presented below, human blood outgrowth EC (hBOEC) spheroids and neonatal human dermal fibroblasts (nhDFs; both potentially autologous cell types) were co-entrapped in fibrin gel aligned via magnetic force or cell-induced compaction. Because the magnetic forces enabled the fibril alignment to vary independent of other factors, these experiments enabled the determination of causal relationships between fibril and sprout alignment. Sprout length, sprout cellularity, and nhDF alignment were also measured in order to investigate the mechanism of aligned sprouting.

2.2. Methods

2.2.1. Cell Culture

hBOECs were provided by Dr. Robert Hebbel at the University of Minnesota. They were cultured in “hBOEC medium” (EGM-2 (Lonza) with an additional 8% FBS and 1% penicillin-streptomycin) in type I rat tail collagen-coated flasks. Passages 8-12 were used for these experiments.

nhDFs were purchased from Lonza and maintained in 50/50 DMEM/F-12 with 10% FBS, and 1% antibiotic-antimycotic. Passages 8-12 were used for these experiments.

2.2.2. Endothelial Cell Spheroid Formation

hBOEC spheroids were made via the method of Laib et al.⁷⁸ by suspending 500 cells stained with CellTracker Green (Invitrogen) in a 25 μ l drop of “spheroid medium” and placing the drops on a petri dish. Spheroid medium contained 80% hBOEC medium and 20% methylcellulose medium (1.2% w/v methyl cellulose in EBM-2 (Lonza)). The dishes were inverted, and cultured overnight. The spheroids were harvested by covering the bottom of the dish with HBSS, and pipetting the volume into a conical tube. The spheroids had settled to the bottom of the tube within 15 minutes, from where they were removed and entrapped in fibrin gel.

2.2.3. Fibrin Constructs with Magnetic Alignment

Due to the diamagnetic anisotropy of the fibrinogen molecule, fibrin gels can be aligned if they are polymerized in the presence of a strong magnetic field.^{79,80} Teflon rings were attached to rectangular glass coverslips using sterile vacuum grease to create wells 1.5 cm in diameter. Fibrin gels (500 μ l each) were formed within these wells by combining hBOEC spheroids, nhDFs, bovine fibrinogen (Sigma) in 20 mM HEPES-buffered saline, bovine thrombin (Sigma) in saline, and EGM-2 (Lonza) without FBS. Final gel concentrations were 3.3 mg/ml fibrin, 0.08 U/ml thrombin, 68% (v/v) EGM-2 without FBS, 80 spheroids/ml, and

250,000 nhDFs/ml. Gels were allowed to polymerize in the presence of a 9.4 T magnetic field, a 7 T magnetic field, or no magnetic field (isotropic control) for 15 minutes. 1 ml of hBOEC medium was added to each well and was replaced every 2 days. Fibroblasts were included in these constructs because limited sprout growth was observed in constructs without co-entrapped nhDFs.

Because others have found effects of magnetic field exposure on fibroblast and endothelial cell behavior,^{81–85} additional constructs were made with or without spheroids to test the effect of magnetic field exposure on sprout growth and proliferation, and on angiogenic factor production by nhDFs. Isotropic gels were formed as above and half were exposed to a 9.4T magnetic field after gelation for 15 minutes. RNA was harvested from constructs containing only nhDFs using an RNeasy extraction kit (Qiagen) after 1 and 3 days of culture, and quantitative RT-PCR was performed to investigate VEGF-A, bFGF2, and Ang-1 production. The forward (f) and reverse (r) primers used were obtained via Primer-BLAST (NIH) and are as follows: fVEGF-A TTGAATCGGGCCGACGGCTT, rVEGF-1 TTGCCCTGTCGCTTTCGCT, fbFGF2 GCAAGATGCAGGAGAGAGGAAGCC, rbFGF2 TGCCACGTGAGAGCAGAGCA, fAng-1 TGCCTGCTTCCAGCTTGGCT, and rAng-1 TGCCTGAGTCAGCTGCGTGT. Constructs containing only nhDFs were harvested after 3 days of culture for DNA quantification using a modified Hoescht assay, assuming 7 pg of DNA per cell.⁸⁶ Spheroids were imaged at day 3 of culture and sprout lengths and anisotropy indices were quantified as described below.

2.2.4. Fibrin Constructs with Cell-Induced Alignment

Fibrin constructs were made in slab geometries by mixing hBOEC spheroids, nhDFs, bovine fibrinogen (Sigma) in 20 mM HEPES-buffered saline, bovine thrombin (Sigma) in saline, and EGM-2 (Lonza) without FBS. Final gel concentrations were 3.3 mg/ml fibrin, 1.25 U/ml thrombin, 68% (v/v) EGM-2 without FBS, 36 spheroids/ml, and 250,000 nhDFs/ml. Three geometries were used to create slabs with aspect ratios of 1, 2, and 3. The aspect ratio was defined as the ratio of the length of the construct to its width. Rectangular score marks were made on the bottom of a 150 mm petri dish in sizes 1 cm x 2 cm, 1 cm x 3 cm, and 1 cm x 4 cm. A 0.5 cm wide porous polyethylene space was fixed inside the score mark at each end using sterile vacuum grease. Gel-forming solution was mixed for 20 seconds and pipetted into the rectangle between the spacers, giving initial construct sizes of 1 cm x 1 cm (250 μ l gel), 1 cm x 2 cm (500 μ l gel), and 1 cm x 3 cm (750 μ l gel), corresponding to aspect ratios 1, 2 and 3 respectively. Constructs were allowed to polymerize for 5 minutes at room temperature, after which 35 ml of hBOEC medium was added. hBOEC medium was replaced on the day after casting and every 2 days subsequently.

The following day, slabs were lifted from the dish via the spacers and the spacers were reattached to a new dish, with the distance between the spacers remaining constant. This action detached the construct from the dish, allowing the cells to compact and align the fibrin fibrils between the two spacers.

2.2.5. Image Acquisition and Analysis

Constructs were cultured for 7 days, after which spheroids from each condition were imaged using confocal microscopy with a 10x objective. Z-stacks were used when required to ensure that all sprout lengths were included. The length and angle of each sprout was measured in the XY-projections of the spheroids using ImageJ (NIH). Sprouts were predominately linear structures. Therefore, a straight line was drawn over each sprout representing the average length and angle, and the length and angle of this line was recorded (Figure 2-1). The X and Y components of each length were calculated and summed for all sprouts within a given construct. The sums were then used to calculate the average sprout anisotropy index, defined as the ratio of total X length to total Y length (where X is the direction of fibrin fibril alignment). With this definition, a high anisotropy index indicates strong sprout alignment, and an anisotropy index of 1 is perfectly isotropic.

For magnetically-aligned constructs, spheroids were also imaged on day 0. The X and Y diameters were measured and their ratio taken to determine whether any elongation of the spheroid in the direction of alignment had occurred.

For nuclear labeling and nhDF alignment measurements, constructs were fixed in 4% paraformaldehyde, permeabilized with 0.1% Triton-X, and stained with rhodamine phalloidin and Hoescht 33342. Sprouts were then imaged with confocal microscopy using a 10x objective and 3x optical zoom. Nuclei fully

within the boundaries of CellTracker Green staining were considered within the sprout and were manually counted.

F-actin expressing cells that did not contain the CellTracker Green were considered nhDFs. The nhDFs displayed elongated morphology, with nuclei also elongated in the same direction as the f-actin fibers. The angle of nuclear elongation was measured with ImageJ for nhDFs with nuclei at varying distances from the sprout. In the case where the sprout grew at an angle 15-90° from the overall fibril alignment direction, the difference between the angle of each nucleus and that of the sprout and the difference between the angle of that nucleus and that of the overall fibril alignment direction were computed. If the difference between the nucleus and sprout angles was smaller than the difference between the nucleus and overall fibril angles, the nhDF was considered to be more aligned with the sprout than the overall fibril alignment direction. For cases where the sprout grew at an angle less than 15° from the overall fibril alignment direction, the anisotropy index was calculated as above using a standard length for every cell.

2.2.6. Alignment Mapping

The fibril alignment of each construct was measured via polarized light imaging.⁸⁷ Briefly, each sample was placed between two linear polarizers, and images were taken as one of the polarizers rotated. A custom Matlab script was used to calculate the average retardation and alignment direction at each pixel. The retardation normalized to tissue thickness is the tissue birefringence, a measure of fibril alignment strength. Although the quantitative relationship

between fibril alignment distribution and birefringence is unknown, it is monotonic.⁸⁸ For magnetically-aligned samples, the average birefringence of the largest square fitting within the well was reported. For constructs with cell-induced alignment, the average birefringence (across the construct width) in the middle of the slab, where birefringence is the highest, was reported, and only spheroids in areas where the average birefringence (across the construct width) was within 10% of the middle value were analyzed. The Matlab script also generated alignment maps, in which line segments representing the local strength and direction of alignment overlay a grayscale image indicating the retardation of the construct at each pixel. Alignment mapping was performed on days 0 and 7 for magnetically-aligned constructs and only on day 7 for cell-aligned constructs.

2.2.7. Histology

Constructs were fixed in 4% paraformaldehyde and frozen in OCT embedding medium. 9 μm sections were taken both parallel and perpendicular to the direction of alignment using a cryostat. Sections were stained with hematoxylin and eosin.

2.2.8. Statistics

Data were analyzed in Minitab. Comparisons were made using ANOVA with Tukey post-hoc tests, and correlations using linear regression. Both comparisons and correlations were considered significant at $p < 0.05$. At least 30 sprouts were analyzed in each condition, with 4 magnetically-aligned constructs

and 3-4 cell-aligned constructs per condition. PCR data were analyzed by the comparative C(T) method followed by ANOVA.⁸⁹

2.3. Results

2.3.1. Increasing fibril alignment via increased magnetic field strength during fibrin gel formation increased EC sprout alignment.

Alignment mapping of magnetically-aligned and isotropic control constructs formed within wells made from Teflon rings verified that fibrin fibril alignment increased with magnetic field strength (Figure 2-2A-C,G). The alignment was uniform across each construct. The spheroids were round immediately after gel formation regardless of the application of a magnetic field (data not shown). Decreases in fibril alignment occurred between days 0 and 7 for the 9.4 T and 7 T conditions; however, all measurements of the alignment strength of 9.4 T constructs were higher than those of 7 T constructs regardless of day, and likewise between 7 T and isotropic control constructs (data not shown). In all conditions, the constructs were thinner after 7 days of culture than immediately after gelation (data not shown), and thickness varied little across the construct. Representative images of spheroids in each condition after 7 days of culture are shown in Figure 2-2D-F. Sprout anisotropy index positively correlated with increasing birefringence ($R^2 = 0.84$; Figure 2-2H), indicating that the sprouts aligned with the fibrin fibrils.

Alignment mapping of constructs exposed to a 9.4T magnetic field after gelation confirmed that the application of a magnetic field after gelation did not

induce fibril alignment (data not shown). PCR analysis indicated that the 15 min magnetic field exposure itself did not have an effect on the production of VEGF-A, bFGF2, or Ang-1 (Figure 2-3A). The magnetic field exposure also did not have an effect on nhDF proliferation (Figure 2-3B). No difference in sprout length was observed between spheroids exposed to the magnetic field and those not exposed (Figure 2-3C).

2.3.2. Increasing fibril alignment via increased aspect ratio of cell-compacted fibrin gel increased EC sprout alignment.

As shown with alignment mapping, fibrin fibril alignment was increased within slab constructs aligned via cell-induced gel compaction by increasing the construct aspect ratio (Figure 2-4A-C,G). Alignment was stronger in the center of the slab constructs and weaker nearer the porous spacers, and quantification was thus restricted to the central region where alignment was homogeneous. Figure 2-4D-F displays representative images of spheroids in constructs of each aspect ratio. Again the sprouts aligned with the fibrin fibrils, as evidenced by the positive correlation of sprout anisotropy index with construct birefringence ($R^2 = 0.75$; Figure 2-4H).

2.3.3. EC sprouts were lengthened by increasing fiber alignment.

Longer sprouts were observed when the sprouts and fibrin fibrils were more aligned, regardless of the method used to align the fibrils. Sprout length was positively correlated with sprout anisotropy index for both magnetically-aligned constructs ($R^2 = 0.71$) and cell-aligned constructs ($R^2 = 0.51$; Figure 2-5).

A positive correlation also existed between sprout length and construct birefringence for both magnetically-aligned ($R^2 = 0.62$) and cell-aligned constructs ($R^2 = 0.62$; data not shown). In addition, the number of cells per sprout increased with sprout length ($R^2 = 0.38$), but the average length per cell (i.e. sprout length divided by number of cells; a measure of cell elongation) did not.

2.3.4. Sprout orientation influenced nhDF alignment.

nhDF orientation near sprouts in magnetically-aligned constructs was observed via rhodamine phalloidin and Hoescht staining (Figure 2-6A-B). Within 10 μm of sprouts that grew in directions 15-90° from the overall fibril alignment direction, approximately 50% of nhDFs were oriented more closely with the sprout than with the overall fibril alignment direction. This percentage is greater than that of nhDFs located at distances 10-50 μm and 50-100 μm of a sprout (Figure 2-6D). Near sprouts that grew in directions less than 15° from the overall fibril alignment direction, a trend was observed that the anisotropy index of the nhDFs within 10 μm of the sprout was higher than that of nhDFs at distances 10-50 μm and 50-100 μm from the sprout, and that of nhDFs in regions with no sprouts (Figure 2-6F).

2.3.5. Sprouts contained patent lumens and connected when in close proximity.

Sprouts from spheroids in close proximity were able to connect (Figure 2-7A,B). It is unclear whether the lumens connected as well so as to form an anastomosis. H&E staining and vWF immunostaining of histological sections of these tissues revealed the presence of lumens within the spheroids (lumen

diameter was 50 ± 5.5 (s.d.) μm) and sprouts (lumen diameter was 8.5 ± 0.64 (s.d.) μm ; Figure 2-7C,D).

2.4. Discussion

Previous studies of the alignment of endothelial sprouts with extracellular matrix proteins have shown correlations between fibril alignment and sprout alignment, but cause and effect relationships were not established. The method of using magnetic forces to systematically vary the alignment strength of fibrin fibrils leads to the conclusion that fibril alignment is sufficient to induce sprout alignment.

The reduction in thickness of the magnetically-aligned constructs over the culture period indicates that cell-mediated tension present within the constructs caused compaction in the Z direction. However, construct thickness near the edge of the gel was not different from that in the middle of the construct, indicating that the construct was not adherent to the Teflon wall. This observation reduces the possibility of the formation of an anisotropic tension field, which further justifies the conclusion that fibril alignment is sufficient to cause sprout alignment. In addition, the sprout alignment effect was still seen to the same extent (slope = 0.51 in the plot equivalent to Figure 2-4K) in gels that had been deliberately detached from the Teflon wall. The cells producing the compaction-causing tension and alignment are likely the more numerous nhDFs, although the ECs could contribute as well. However, aside from inducing compaction in the Z-direction, the nhDFs had only a minor effect, if any, on fibril alignment. This is evident from the fact that all measurements of alignment strength, even those

taken on different days, were different between conditions. Differences did exist between days in magnetically-aligned samples, but this may have been due to any number of factors other than nhDFs.

Sprouts from EC spheroids also aligned with fibrin fibrils in the constructs that were aligned via cell-induced fibrin gel compaction. However, this method of fibril alignment has confounding factors that preclude the same conclusion that fiber alignment induces sprout alignment. For example, an anisotropic tension exists, with tension in the alignment direction, due to the anchorage of the gel to the spacers. Also, the matrix and fibroblast densities may vary with aspect ratio because of the different degrees of gel compaction, and associated gradients of fiber density could also affect sprout alignment. Additionally, the physical necking of the gel could play a role in aligning sprouts, as necking will cause the Y component of a sprout's length to decrease. However, previous results suggest that the time scale of necking is slow enough for this effect to be neglected.⁹⁰ Rather, the results of this experiment indicate that cell-induced compaction is an effective way to align EC sprouts, a conclusion which is pertinent due to the ease of using this method for tissue engineering purposes. As mentioned previously, cell-induced compaction and alignment of fibrin gel is a critical component to creating engineered myocardium,³⁸ where a functional microvasculature is critical for maintaining viability in a tissue with physiologically-relevant thickness. This work has shown that EC will align compacted fibrin fibrils, suggesting that the inclusion of ECs within a compacting fibrin gel is a feasible method for achieving an aligned microvascular network.

The mechanism by which fibril alignment leads to sprout alignment is unknown, but several mechanisms are possible.^{66,91} 1) an aligned fibril matrix has pores that are elongated in the direction of fibril alignment, so there is a smaller physical barrier to sprout growth in the direction of alignment; 2) sprouts growing along fibrils encounter more adhesion sites, promoting growth in the alignment direction; and 3) the anisotropic stiffness of the matrix promotes growth in the alignment direction by reducing a sprout's ability to contract the fibril network if it is growing in the alignment direction (high stiffness). Clearly these potential mechanisms are not mutually exclusive.

The finding that sprout length increased with alignment suggests that mimicking the native vascular structure may not be the only benefit of aligning endothelial sprouts. Longer microvessels more easily encounter a neighboring microvessel, which would possibly lower the EC density required to achieve a microvascular network. The analysis of isotropic gels either exposed to magnetic fields or not suggests that the increased sprout length was due to the fibril alignment, not to the exposure of the cells to a magnetic field. This result is not unexpected, as many groups have shown that the length of neurite outgrowth is increased when the substrate fibers are aligned.^{79,92-95} The number of cells per sprout was positively correlated with sprout length and the mean length per cell was not, suggesting that either cell proliferation or recruitment of cells to the sprout was responsible for the increased sprout length. The mechanism of this increased sprout length is also unknown, but the above hypotheses may explain this effect as well.^{66,91}

A major difference of interest between the two methods of inducing fibrin fibril alignment is that the cell-aligned constructs aligned gradually, whereas the magnetically-aligned constructs were fully aligned at gelation. This might cause one to hypothesize that because sprouts in magnetically-aligned constructs grew in an aligned environment for the full seven days but sprouts in the cell-aligned constructs initially grew in an isotropic environment, sprouts in magnetically-aligned constructs would have a higher anisotropy index for a given day 7 birefringence level. In support of this idea, it was found that the anisotropy index of rat BOEC sprouts in cell-aligned constructs did increase gradually, mirroring the gradual increase in fibril alignment (Morin and Tranquillo, unpublished data). However, this result was not observed when comparing the relationship between birefringence and anisotropy index for different alignment methods. The linear regression equation was the same for both magnetically-aligned and cell-aligned constructs. The above logic neglects all of the confounding effects occurring in the cell-aligned constructs. Anisotropic tension could easily contribute to sprout alignment, as could gradients of fibril density. Therefore, it appears that the anisotropy index of sprouts in cell-aligned constructs reflects alignment due to both contact guidance and other factors, and the sum of all of these effects is equivalent to that of contact guidance alone when the sprouts are entrapped in a relatively unchanging aligned matrix.

Comparing the relationship between anisotropy index and sprout length for various alignment methods yields another interesting result. The values for both linear regression intercept and slope were higher for magnetically-aligned

constructs than cell-aligned constructs. Here the first result is likely explained by the gradual fibril alignment in cell-aligned constructs. Initially the sprouts grew into an isotropic matrix, in which they did not have the cue for longer growth, but as the fibrils aligned, the sprouts were able to grow longer. This contact guidance response led to longer sprouts overall in more aligned constructs, but they are shorter for a given level of sprout alignment due to the gradual fiber alignment. The difference in slope indicates that other factors besides contact guidance played a role in sprout length. Perhaps the increase in fiber or fibroblast density inhibited sprout growth in the cell-aligned constructs.

Numerous studies have detailed the ability of fibroblasts to align with extracellular matrix fibers.^{67,96} However, the presence of hBOEC sprouts introduced an additional factor into the contact guidance response of the nhDFs. Instances where sprouts were not aligned with the overall fibril alignment direction were particularly interesting because there were potentially two conflicting contact guidance signals. Analysis of these cases demonstrated that the fraction of nhDFs aligned more closely with the sprout than the overall fibril alignment direction was higher for nhDFs within 10 μm of the sprout than those outside of 10 μm . These data suggest that the sprout did produce an alignment cue, but its range was limited. Evidence for this alignment cue from sprouts was also apparent when sprouts grew within 15° of the overall fibril alignment direction. Analysis of the nhDF anisotropy index indicated that nhDFs within 10 μm of a sprout tended to be more aligned than those outside of 10 μm , including those in regions where no sprouts were present. Whereas conflicting alignment

cues existed when sprouts were not parallel to the overall fibril alignment direction, the two alignment cues in this case induced stronger nhDF alignment. Since entrapped nhDF were required to obtain sprouts, the interesting question of whether the contact guidance response of the nhDF to the aligned fibrils amplified the contact guidance response of the sprouts could not be directly answered by comparing the outcomes of magnetically-aligned gels with and without entrapped nhDF.

The fact that nhDFs are necessary to induce sprouting in this system raises the question of whether the mechanical or chemical signals provided by the nhDFs (or both) are required. These two effects are difficult to separate, as they are highly interconnected. For example, using an actin inhibitor would inhibit gel contraction (and consequent alignment) that occurs mainly due to the nhDFs, but this would also likely inhibit sprout growth and affect angiogenic factor production. Use of a tissue cell type with a different angiogenic factor production profile in lieu of nhDFs (e.g. pericytes) would likely result in a different gel compaction rate as well. The only technique available to separate the mechanical and chemical effects of nhDFs is siRNA or a similar technology to block the expression of specific angiogenic molecules. Because a large number of angiogenic factors would need to be blocked individually and in combination to draw conclusions, future studies will be needed to determine the answer to this interesting question.

The results presented herein that sprouts from EC spheroids align in response to fibril alignment and the evidence for connections between sprouts

and lumens within sprouts indicate that contact guidance may be an effective way to generate aligned microvascular networks within engineered tissues. Such networks are vital to the culture of thick or highly metabolic engineered tissues as they provide inlet and outlet sides for network perfusion. Further research is necessary into the exact parameters required to form an aligned microvascular network *in vitro*.

2.5. Figures

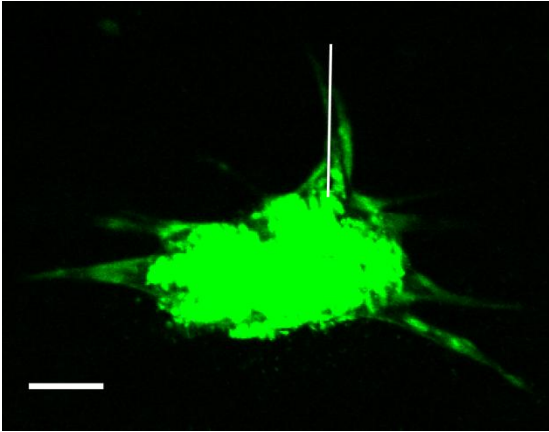


Figure 2-1.

Length and angle measurement for a curved sprout. A line was drawn over the sprout estimating the length and angle of the sprout in ImageJ.

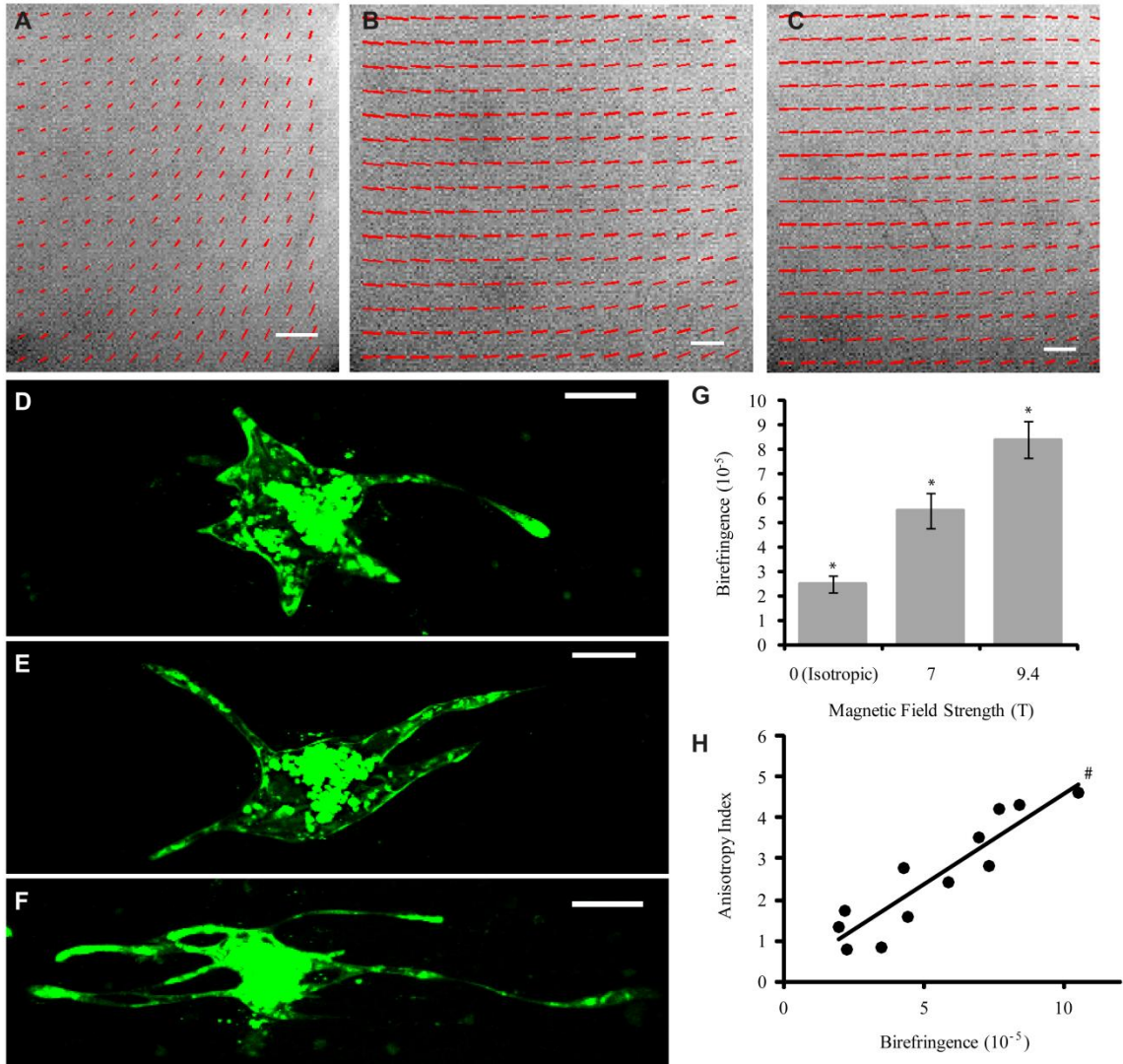


Figure 2-2.

(A-C) Alignment maps of magnetically-aligned constructs. The lines represent the local direction and strength of alignment. Scalebars = 1 mm. (D-E)

Representative spheroids from magnetically-aligned gels. Scalebars = 100 μ m.

(A,D) Isotropic, (B,E) 7T, (C,F) 9.4T. (G) Birefringence of magnetically-aligned gels (mean +/- s.e.m.). * $p < 0.05$ in comparison to both other groups. (H)

Correlation between mean construct birefringence and mean sprout anisotropy index ($R^2 = 0.84$; slope = 0.45). # $p < 0.05$ for linear regression.

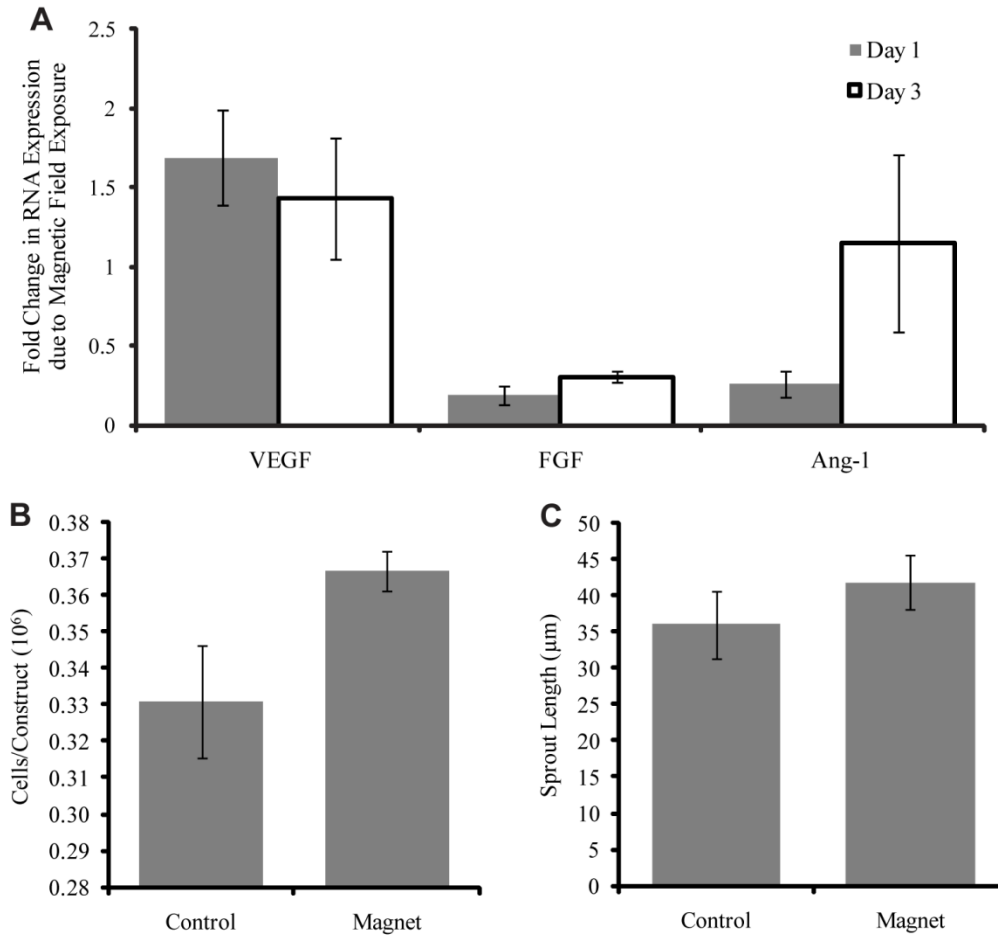


Figure 2-3.

Effects of magnetic field exposure. Constructs containing nhDFs only or nhDFs and hBOEC spheroids were either exposed to a magnetic field for 15 minutes after gelation or not. (A) Fold change in abundance of RNA transcripts for VEGF-A, bFGF2, and Ang-1 due to magnetic field exposure in nhDF-only constructs after 1 and 3 days of culture (mean +/- s.e.m.). (B) Cell numbers at day 3 of culture in nhDF-only constructs (mean +/- s.e.m.). (C) Sprout length at day 3 of culture (mean +/- s.e.m.).

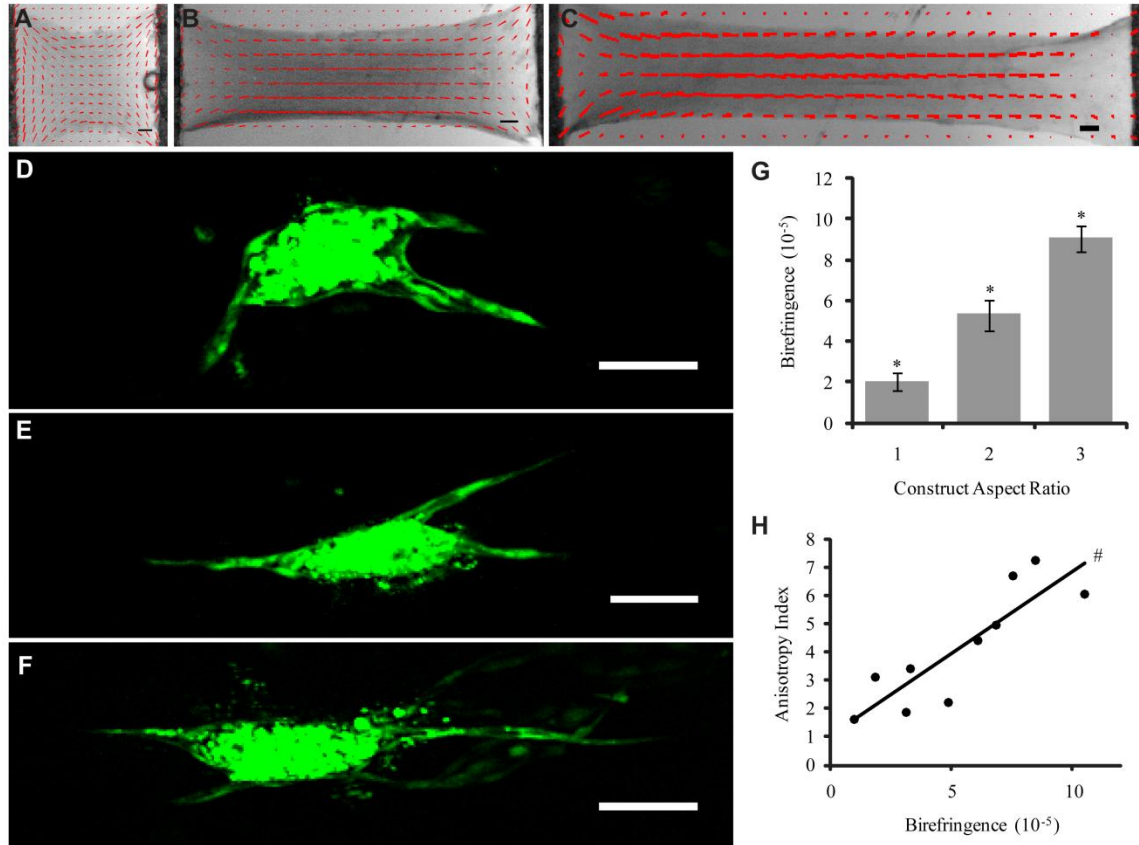


Figure 2-4.

(A-C) Alignment maps of cell-aligned constructs. The lines represent the local direction and strength of alignment. Scalebars = 1 mm. (D-F) Representative spheroids from cell-aligned gels. Scalebars = 100 μ m. Aspect ratios are (A,D) 1, (B,E) 2, and (C,F) 3. (G) Birefringence of cell-aligned gels (mean \pm s.e.m.). * p < 0.05 in comparison to both other groups. (H) Correlation between mean construct birefringence and mean sprout anisotropy index ($R^2 = 0.75$; slope = 0.58). # p < 0.05 for linear regression.

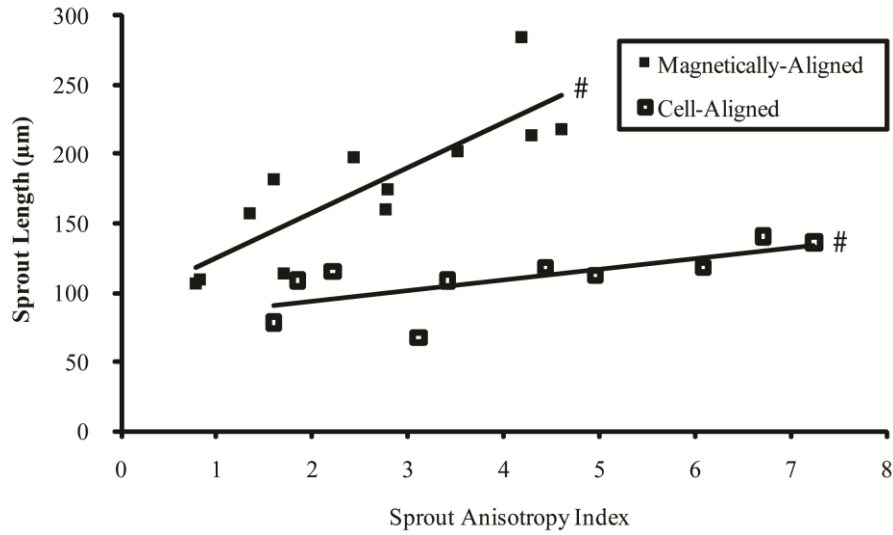


Figure 2-5.

Correlation between mean sprout anisotropy index and mean sprout length for magnetically-aligned ($R^2 = 0.71$; slope = 33) and cell-aligned constructs ($R^2 = 0.51$; slope = 7.9). # $p < 0.05$ for linear regression.

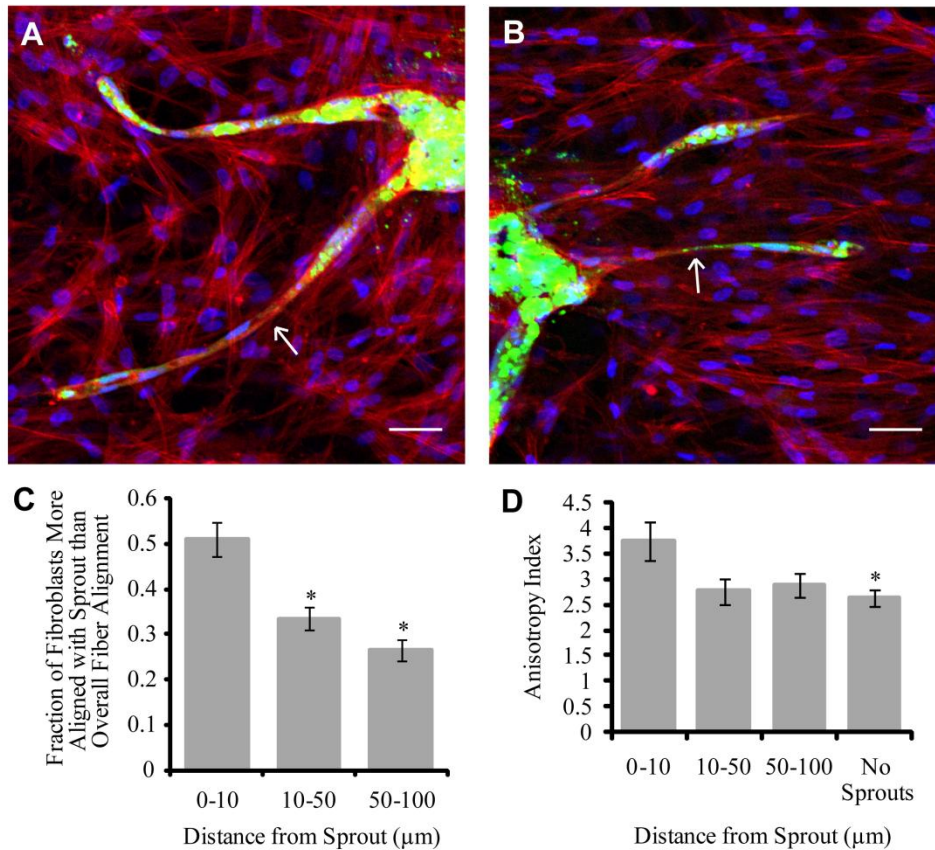


Figure 2-6.

(A-B) Rhodamine-phalloidin stain of magnetically-aligned constructs. Red = f-actin, Green = hBOEC, Blue = nuclei. Angles of sprouts indicated with arrows are (A) 35.34° and (B) 3.48°. Scalebars = 50 μm. (C) Fractions of nhDFs more strongly aligned with the sprout than the overall fibril alignment direction for nhDFs at varying distances from the sprout. Includes only sprouts at angles of 15-90° from the overall fibril alignment direction. *p < 0.05 in comparison to 0-10. (D) Anisotropy index for nhDFs at varying distances from the sprout. This plot only includes data from nhDFs near sprouts at an angle of less than 15° from the overall fibril alignment direction. *p < 0.05 in comparison to 0-10.

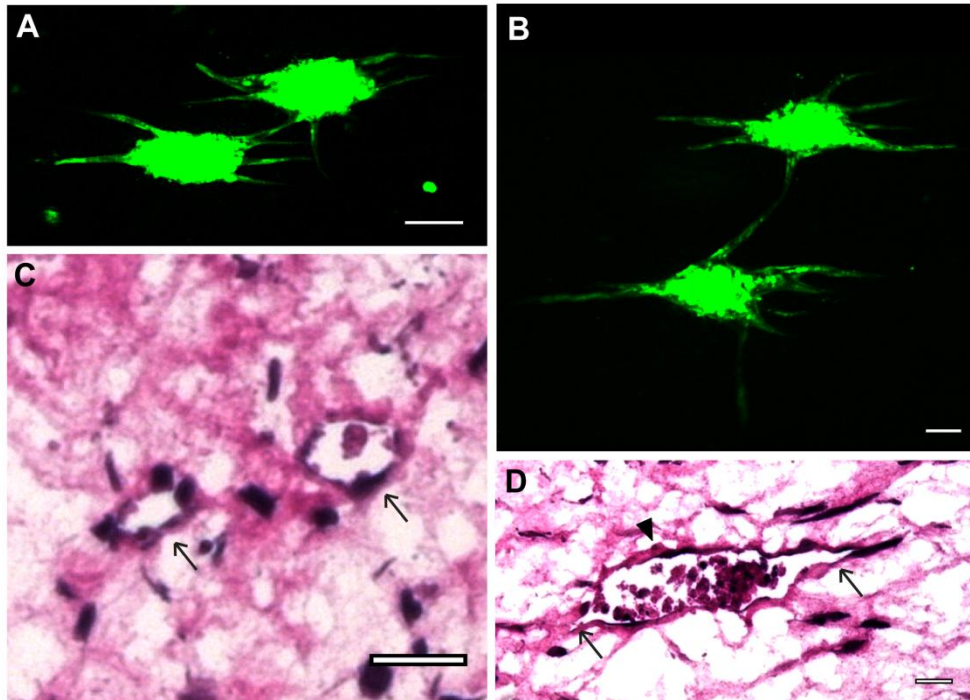


Figure 2-7.

(A-B) Connections of sprouts in cell-aligned gels. Scalebars = 100 μm (C-D) H&E stain of cell-aligned gel sections taken (C) parallel and (D) perpendicular to the alignment direction. In (C-D), arrowheads indicate spheroids and arrows indicate sprouts. Scalebars = 20 μm .

Chapter 3. Image Analysis Techniques for the Quantification of Microvascular Network Characteristics

3.1. Introduction

Before additional work was done on developing engineered microvascular networks, image analysis methods were developed in order to have an objective means of quantifying microvascular network characteristics and comparing between experimental conditions. Although these methods were developed for analyzing the constructs discussed in later chapters, the methods would likely be widely applicable.

The quantification of microvascular network characteristics is of interest to a wide variety of researchers. Changes in the microvasculature have been implicated in a variety of disease processes, from neurological disorders to cancer.^{97,98} In addition, the development of microvascular networks *in vitro* has been pursued by many for either tissue engineering purposes or as a model for the study of endothelial cell (EC) biology. In all of these areas the quantification of microvessel characteristics is of critical importance in order to statistically differentiate between different treatments or experimental conditions.

One of the most commonly used metric is capillary density, which actually comprises several different metrics. One is quantified from tissue cross sections and reported as capillaries/mm².⁹⁹⁻¹⁰¹ A second, also reported as capillaries/mm², is quantified via nailfold capillaroscopy, in which a finger is viewed under light microscopy and the skin capillaries counted.^{102,103} Although these quantification methods are reported with the same units, they are quite

different and should not be compared directly. Both methods typically rely heavily on manual counting, which is tedious and can introduce bias.

Another parameter commonly quantified is the network length per image area.^{53,54} This parameter is typically used when the entire microvascular network can be viewed such as in a whole mount tissue preparation or a dorsal window chamber. However, this method also relies on manual measurement of the lengths of the capillaries, which is time consuming. A high degree of subjectivity is also introduced, as the image often contains capillaries that are varying distances from the focal plane, and the observer must determine which capillaries should be included in the measurement.

The introduction of subjectivity into measurements is extremely important in the analysis of engineered microvascular networks, as the observer must first define what qualifies as a capillary. In cross section, not all EC structures contain lumens, and some structures contain multiple lumens either because it was sectioned near a bifurcation point or because the several small lumens have not yet matured into a single lumen. In whole mount preparations, the microvessels often have abnormal morphology that must be measured accurately or endothelial cell debris that must be eliminated from measurements. These conditions increase the variability in both inter- and intra-observer measurements.

Some work has been done to automate the detection and counting of capillaries. Both Ranefall et al. and Kim et al. reported methods for automated capillary counting in immunostained sections imaged under light

microscopy.^{104,105} Although these methods were shown to be relatively accurate, they counted capillaries by counting positive EC staining rather than the lumens themselves. This poses a problem for use with engineered microvasculature, in which a positively stained object may correspond to zero or several lumens. Additionally, characteristics such as lumen size or shape, which are also of importance in microvascular networks both *in vitro* and *in vivo*, could not be quantified. The alignment of capillaries was also not quantified, which would be present in longitudinal sections of anisotropic native or engineered tissues such as muscle. Finally, the use of immunohistochemistry rather than immunofluorescence limits the possibility of identifying additional cell types, such as mural cells, in the same section, because it would be difficult to separate the different colors from the light microscopy image. Without identifying both cell types in the same section, it would be impossible to accurately quantify parameters such as the recruitment level of the mural cells, which is an important indicator of microvessel maturity.

Much more work has examined automated methods for quantifying microvessel length. Methods have been developed for analyzing both brightfield and fluorescent images, both *in vitro* and *in vivo* networks, and both single images and z-stacks for 3D reconstruction.^{71,106–112} Each method has its advantages and disadvantages; some require the input of a binary image, which is at times non-trivial to obtain,¹¹⁰ some require perfusion of the network for imaging,^{106,109} which cannot always be done for engineered microvasculature, and some require extensive serial sections to create a 3D image of the

network.¹⁰⁷ None of these methods, however, address the quantification of mural cell recruitment or network anisotropy, which are important parameters to assess both *in vitro* and *in vivo*, as they provide information about the maturity and alignment of the network, respectively.

The methods outlined here for analysis of cross sections and whole mount preparations of engineered microvasculature address the limitations noted above. The cross section program detects lumens within fluorescent images based on dark areas surrounded by EC staining, and once they are identified, they can be counted and measured as desired. The whole mount program quantifies microvessel length as well as bifurcation points. Both programs also share two major improvements over others: the inclusion of methods to measure mural cell recruitment to the network and network anisotropy. These inclusions provide additional quantitative information regarding microvascular maturity and alignment, which are useful in many types of microvascular studies.

3.2. Methods

3.2.1. Cross Section Algorithm Description

An image analysis program for use with cross sections of engineered tissues containing microvascular networks was developed in Matlab v. 2012b (The Mathworks). The algorithm first thresholded the CD31+ image using several threshold values, which were automatically generated using the `graythresh` function. The resulting binary images were then dilated slightly to improve connectivity of CD31+ regions. The most dilated image was then presented to

the user for input. A custom function was developed that enabled the user to click two points on the image, after which the values of the pixels in a straight line between the points were changed to 1. The user was able to connect CD31+ regions using this function and thereby enclose lumens that would have otherwise gone undetected (Figure 3-1 a-c). This method of user input maximized accuracy in lumen detection while minimizing the user impact on the size and shape of the detected lumens. A while loop enabled the user to make as many edits to the thresholded image as necessary.

After the user input was complete, all of the binary images generated thus far (including images that were dilated, not dilated and incorporating user input) were assessed for lumens, which were defined as a region of zeros completely surrounded by ones. The imfill function was used to fill in such regions, and subtracting the original binary image resulted in a lumen image, one of which was created for each binary image. The union of all of the lumen images was taken as the first lumen image. Due to the thresholding and dilation, the first lumen image contained much noise, and therefore further processing to remove non-lumens was necessary.

The hallmark of a lumen is a bright ring of CD31+ staining surrounding a dark region. Therefore, the ratio of staining intensity between each region in the first lumen image and its immediate surroundings was used to detect true lumens. Individually, each potential lumen was dilated by two pixels, and the lumen was subtracted to leave the region adjacent to the lumen (Figure 3-1d-f). The intensity of the adjacent region in the original image was then compared to

the intensity of the lumen in the original image. Those lumens with intensity ratios below a given threshold were deleted from the lumen image, forming the second lumen image. The threshold value can be modified for each image set to minimize user input, although the variation in optimal thresholds is small in general. This step is the most computationally expensive, but is critical to minimize user input.

Once the second lumen image was finalized, it was presented to the user for input. A custom function enabled the user to draw a polygon and delete all lumens within that polygon. Non-lumens present in the second lumen image often result from CD31+ structures located near each other; these regions may become completely surrounded by CD31+ staining when the binary image is dilated (Figure 3-1g-i). A while loop enabled the user to remove as many lumens as necessary; after this step was complete, the lumen image was final (Figure 3-1j-k). The lumen density was expressed as the number of lumens per area.

At this point the function `regionprops` was used to calculate properties of the lumens such as their size (area) and length (major axis length). The original thresholded images were also used to calculate the total level of CD31 staining. Additional processing using the `imfill` command filled in the original binary images to produce information about the number of endothelial structures present in the image. This filled image was also used to calculate an anisotropy index for the image, which describes the alignment of the structures. The length of each structure was divided into components parallel and perpendicular to the alignment direction, which was defined as the average angle of all structures.

The anisotropy index was then defined as the ratio of the sum of structure lengths in the direction parallel to alignment to the sum of structure lengths in the direction perpendicular to alignment (Figure 3-1l). The length and angle of each structure was calculated using regionprops (major axis length and orientation).

The program was also able to detect the recruitment of support cells labeled with a different fluorophore. The support cell image was thresholded and small objects (noise) removed using bwareaopen. The intersection of the support cell image and the CD31 image was taken, and support cells that contained an area of overlap with the CD31 image were considered recruited (Figure 3-2). The support cell recruitment level was expressed as the fraction of total support cells that were recruited. The total number of support cells per area was also recorded.

Finally, the total cell number per area was also recorded from nuclear staining. The image was thresholded and noise removed as above, and the total number of nuclei was counted.

3.2.2. Whole Mount Algorithm Description

A second program was developed in Matlab for the analysis of images of whole mount CD31 stains of engineered microvasculature in collaboration with Paul Carlson, an undergraduate chemical engineer. Although lumens are difficult to detect in whole mount staining, other important network characteristics such as total vessel length and interconnectivity are much more easily evaluated from these images than images of cross sections.

Prior to thresholding the CD31 image, the grayscale image was dilated and eroded. This manipulation blurred the staining within the EC structures but maintained a relatively strong difference between the structures and the background. The blurring made the level of staining within the structure more even, enabling easier identification via thresholding. The function `graythresh` was used to automatically detect a threshold level, and a binary image was created using a threshold level obtained by multiplying that determined by `graythresh` by 0.9. Using a threshold level slightly lower than that determined by `graythresh` produced a binary image in which the identified endothelial structures had a similar interconnectivity to the original image (Figure 3-3a-b). Any rounded cells were removed using `bwareaopen`, which removes objects smaller than a certain size. The total number of objects (structures) was then counted.

Next the function `bwmorph` (“thin, Inf” command) was used to skeletonize the image (Figure 3-3c). Although quite accurate, the skeletonization process created small segments that were not part of the original EC geometry, often due to variations in microvessel diameter. To obtain accurate information about the network characteristics, it was necessary to remove these artifacts. A custom function was used to find network bifurcation points using a look up table (LUT), which specified that a pixel was a bifurcation point if 3 or more of the 8 pixels immediately surrounding it also had a value of 1. These bifurcation points were then removed from the skeletonized image, and `bwareaopen` was used to delete small segments, which were the artifacts of the skeletonization process. The remaining segments were considered true segments of the EC network, and their

properties were quantified (Figure 3-3d). The number of segments was counted, and their areas (equaling their lengths; from regionprops) were both averaged and summed to obtain the average segment length and the total vessel length, respectively. All of these parameters were normalized to the area of the image. The orientation of each segment was also quantified using region props and used in conjunction with each segment's length to calculate an anisotropy index, indicating the strength of alignment of the segments. Each segment length was divided into components parallel and perpendicular to the direction of alignment (determined to be the average angle of all segments). The anisotropy index was then defined as the ratio of the sum of segment lengths in the direction parallel to alignment to the sum of segment lengths in the direction perpendicular to alignment.

The bifurcation points were then added back into the skeletonized image and the custom LUT function used again to determine true bifurcation points, as points leading to artifact segments, which were not true bifurcation points, were counted originally. The true bifurcation points were counted and normalized to the image area.

Additional parameters of interest were then calculated including the average length per continuous structure (total length/number of structures), the average length per segment (total length/number of segments) and the average diameter (total structure area/total length).

Finally the number of total cells, the number of support cells, and the level of support cell recruitment were quantified using the same algorithm as described above for the cross section program.

3.2.3. Program Validation

Both of the programs were validated via comparison to manual measurements. For the cross section program, lumens were manually counted using ImageJ in 6 cross sections of engineered microvasculature and compared to the lumen counts generated by the program. For the whole mount program, the total microvessel length, network anisotropy index, and mural cell recruitment were measured for 9 images in ImageJ and compared to values output by the program. Mural cell recruitment and anisotropy index were not quantified for the cross section program because the analysis methods were very similar. Paired t-tests were used to examine differences between manual and automatic counts; p values less than 0.05 were considered significant.

3.3. Results

For the cross section program, no difference was observed between manual and semi-automated lumen density measurements (Figure 3-5a). The percent errors between the counts for individual images were at or under 10%, and the variability in lumen counts appeared to be similar between manual and automated measurements.

For the whole mount program, there were no differences in the measured total network length, mural cell recruitment fraction, and network anisotropy index

between manual measurement and automated quantification (Figure 3-5b-d). The percent errors between measurements of individual images were slightly larger than that of the cross section comparison, but still relatively small. All errors were under 25%, and most were under 10%. The variability was similar across both quantification methods for all measurements.

3.4. Discussion

Despite the previous development of automated image analysis programs for both cross section and whole mount preparations, the majority of recent publications quantifying microvascular networks relied upon manual measurements.^{53,54,61,62,99-103,113} This may be due to the complex nature of image processing algorithms, although some have created graphical user interfaces that obviate the need for understanding the algorithms. Another reason may be that existing programs may not be robust enough to quantify another user's images or a parameter of interest to particular user may not be quantified by the existing program. The Image Processing Toolbox of Matlab, used to create the programs described here, provides a balance in terms of complexity: the built-in functions reduce the level of knowledge of image processing techniques required to use the programs, yet enables users to modify the programs to fit their needs. Once the program was optimized for a user's images and quantification needs, the time required to analyze images would be reduced dramatically, and the objectivity of the analysis would improve dramatically.

Both programs developed here were designed to measure multiple microvascular network characteristics. Previous automated image analysis

programs have measured some of these characteristics, but two are completely novel. The first is the measurement of the level of mural cell recruitment. Higher levels of recruitment are indicative of microvascular maturity, and the measured value could be compared to native levels of recruitment in the tissue of interest. The second is the measurement of microvascular anisotropy. Native capillary networks of cardiac and skeletal muscle are highly aligned with the muscle fibers, and the degree of alignment of the experimental networks could be compared to that of native muscle capillaries. Additionally, alignment of engineered microvascular networks may be necessary to facilitate perfusion *in vitro*.

A high level of agreement was observed between manual and automated measurements of lumen density (cross section program) and total vessel length, mural cell recruitment and network anisotropy (whole mount program). These data suggest that the programs produce highly accurate results. Some subjectivity is introduced into the cross section program via user input; however this input is minimized in terms of both impact on the resulting measurements and the time required for input. For example, in the first user input step, the user connects areas of positive CD31 staining by clicking on the two endpoints of a line between the two areas to be connected. This not only creates a more accurate shape of the lumen as compared to tracing the entire lumen manually, but also drastically reduces the time required to add the lumen. Future work should certainly attempt to fully automate the cross section program to remove all observer subjectivity and further reduce the time of analysis.

These programs were optimized for use with engineered microvascular networks, and no modifications were necessary to use the programs to analyze different image sets. However, it is unclear how many adjustments would be required to use the programs to quantify images of other engineered microvascular networks (e.g. those formed from a different cell type or within a different scaffold) or native networks. Additional work would be necessary to adapt these programs to accurately measure the characteristics of all engineered or native capillary networks.

3.5. Figures

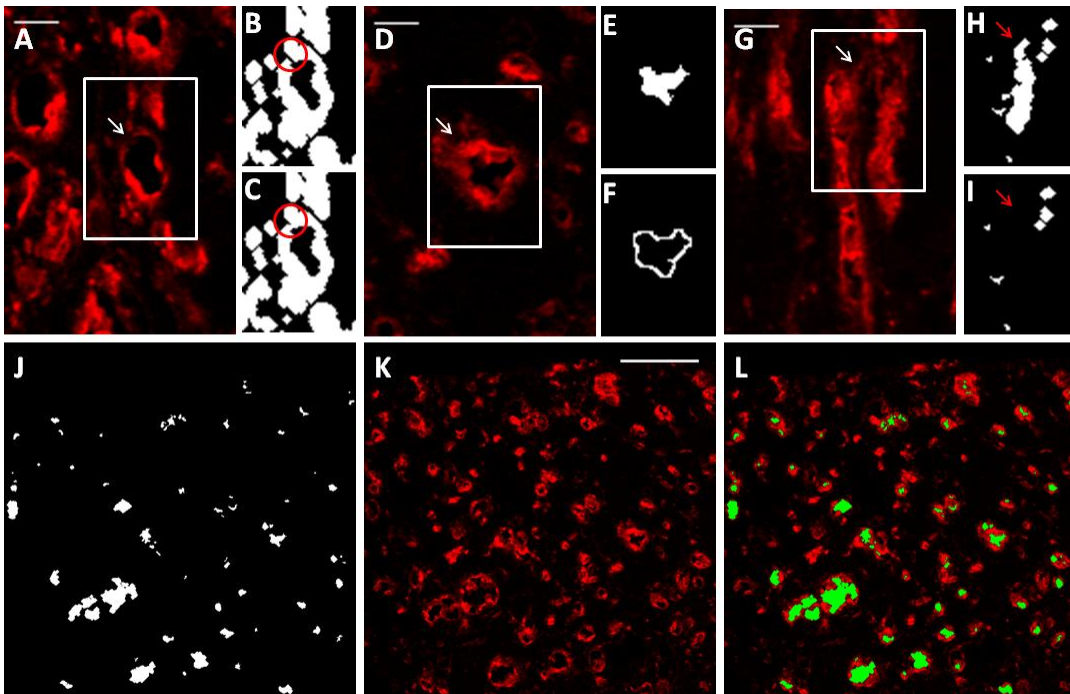


Figure 3-1.

Semi-automated lumen detection in cross sections. (A-C) User input was required in this program for accuracy due to occasional areas of dim CD31 staining. The region outlined in white in (A) is enlarged in (B) and (C). Although the lumen indicated by the arrow is obvious to the eye based on CD31 staining (red; A), the program did not initially recognize the lumen due to a small area of dim staining, which left a gap in the binary image (B; circled). The program enabled the user to correct this error by connecting the ring of CD31 staining with a 1 pixel wide line (C; circled). Scalebar = 20 μm . (D-F) To eliminate some non-lumens that were detected as lumens, the program compared intensity levels (obtained from the original image; D) between the lumen region (E) and the

region immediately surrounding the lumen (F). The region outlined in white in (D) is enlarged in (E) and (F). Lumen regions that had similar intensity values to their surrounding regions were determined to be non-lumens and eliminated. Scalebar = 20 μm . (G-I) User input was again required after lumens were detected to remove any non-lumens. The region outlined in white in (G) is enlarged in (H) and (I). The area between lumens in the original image (G; arrow) was detected by the program as a lumen (H; arrow) due to the close proximity of the surrounding CD31+ structures. The user was able to delete this non-lumen prior to quantification (I; arrow), improving program accuracy. Scalebar = 20 μm . (J-L) The lumen image (J) resulting from these manipulations corresponded well to the original image (K). The lumen image are overlaid the original image for clarity (L). Scalebar = 100 μm .

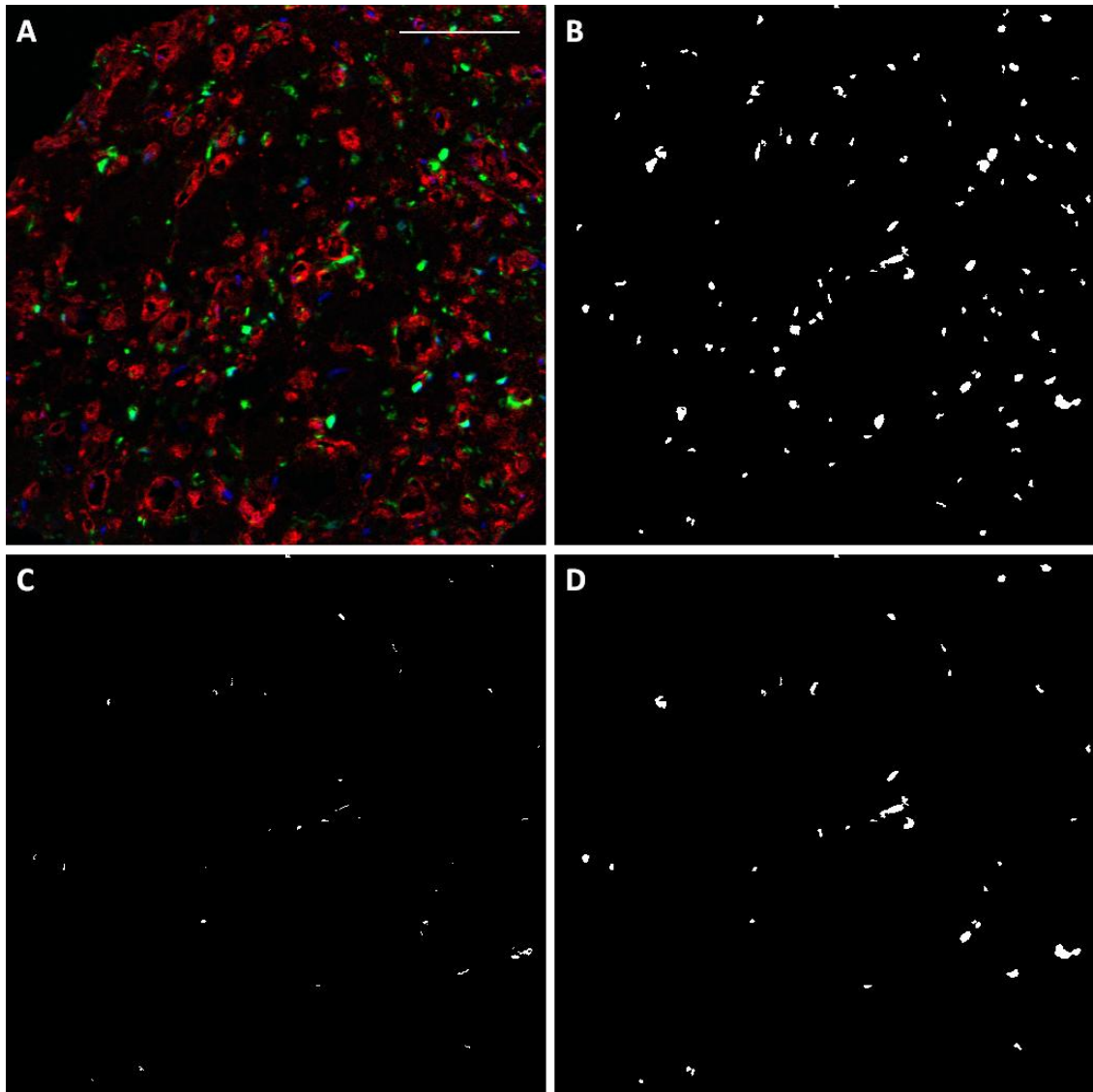


Figure 3-2.

Evaluation of support cell recruitment in cross sections. (A) The original image, in which CD31 staining is red, support cells are green and nuclei are blue. Scalebar = 100 μm . (B) The support cell image (green) was thresholded and noise removed. (C) The intersection between the support cell image and the CD31 image, which defined recruitment. (D) Those PCs that coincided with ECs were considered recruited.

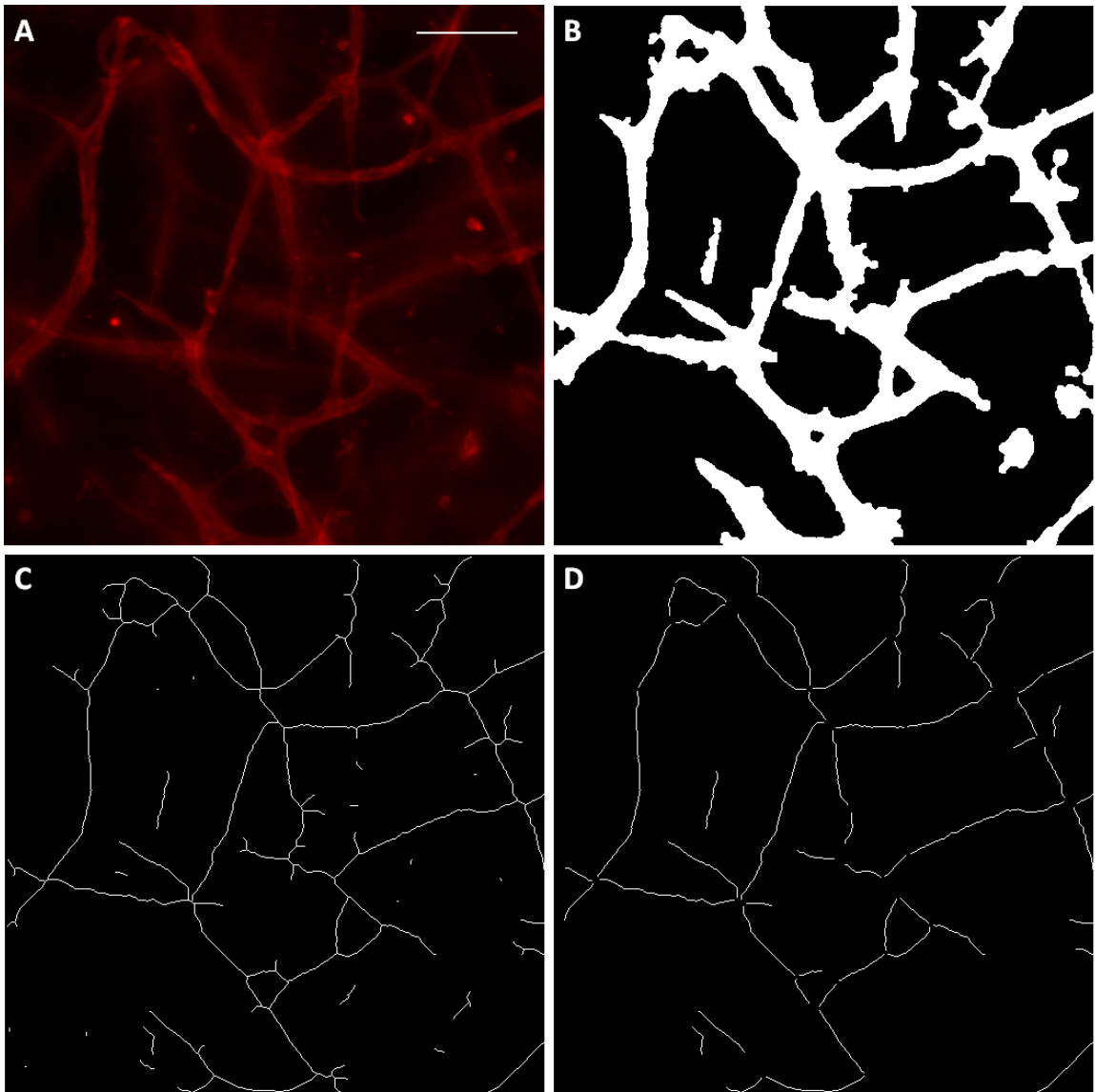


Figure 3-3.

Quantification of network morphology in whole mount images. (A) The original CD31 image. Scalebar = 100 μm . (B) The binary image produced by thresholding and removal of rounded cells. (C) The binary image after skeletonization. Many small segments are present as artifacts of the skeletonization process. (D) The binary image after bifurcation points and the small artifacts were removed. These segments correspond well to the original image.

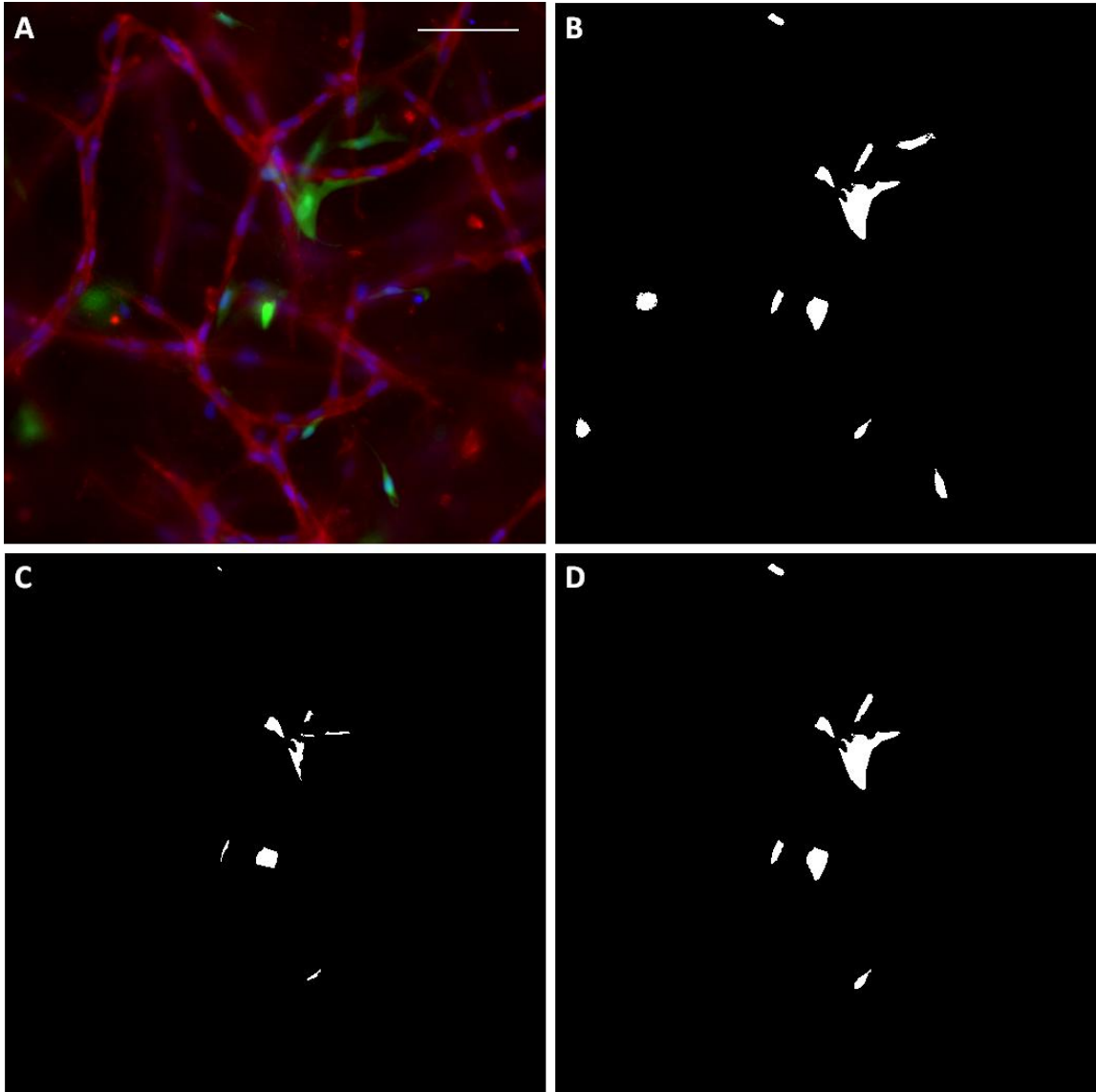


Figure 3-4.

Support cell recruitment quantification in whole mount images. (A) The original image, in which the red indicates CD31 staining, the green indicates support cells, and the blue indicates nuclei. (B) The binary image of support cells. (C) The intersection of the red and green staining, which indicates regions of adjacent ECs and PCs. (D) Those PCs identified in the intersection image were considered recruited.

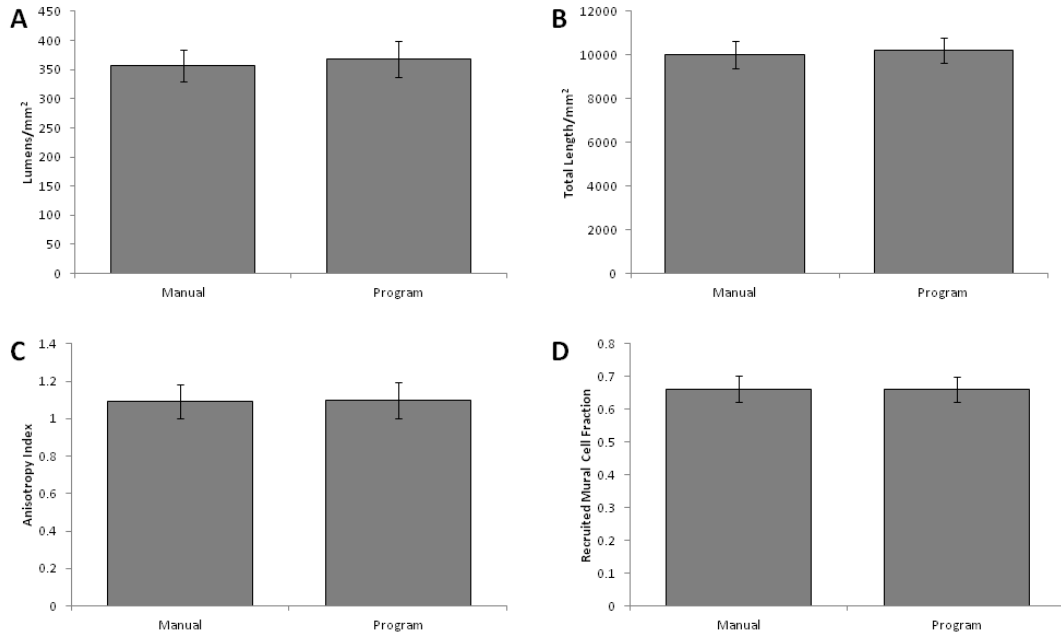


Figure 3-5.

Comparison of manual and automated quantitation methods. Lumen density was measured to evaluate the cross section program (A), and total vessel length was measured to evaluate the whole mount program (B). Network anisotropy (C) and mural cell recruitment (D) were quantified from the whole mount program as an indication of the accuracy of both programs, as the methodology is very similar between the two programs. All automated measurements demonstrated good agreement with their respective manual measurements.

Chapter 4. Alignment of Microvascular Networks formed in Fibrin Gel under Defined Conditions

4.1. Introduction

The need for engineered microvasculature to overcome oxygen diffusion limitations in the growth of engineered tissues *in vitro* has been well established.¹¹⁴ In addition, engineered microvasculature would be of use for studying endothelial behavior in a more controlled environment than animal models. Examples include mechanisms of neovascularization, effects of anti-angiogenesis drugs in cancer research, and endothelial inflammatory responses, among many other topics. Therefore, many researchers are investigating methods for producing engineered microvasculature *in vitro*. Several groups have demonstrated the ability of endothelial cells (ECs) to form monolayers on the inner surfaces of pre-formed tubes within a 3-dimensional scaffold, respond to shear stresses from fluid flow through the tubes,¹¹⁵ and recruit mural cells.⁵⁹ Although these models are useful for studying small numbers of vessels, it would be difficult to create networks of tubes similar to native capillary networks in size, geometry and density, which will be necessary for the delivery of oxygen to engineered tissues. Other investigators have studied the ability of ECs to sprout into 3-dimensional scaffolds from monolayers on the scaffold surface,^{61,116–119} monolayers on embedded microspheres,^{62,120,121} or aggregates of ECs.^{63,76} Though these models of angiogenesis are useful, it has yet to be demonstrated that they can produce large fully interconnected microvascular networks *in vitro*. The method most promising for achieving this goal is the vasculogenic self-

assembly of ECs distributed throughout a scaffold into microvascular networks. This technique, which has been widely studied, has been historically limited by the tendency of ECs to form isolated capillary-like structures, but not assemble fully into a network.^{122,123} However, more recent studies have been much more successful in creating highly interconnected networks,^{54,56,124} including a set of studies from our laboratory in which human umbilical vein ECs (HUVECs) and pericytes (PCs) formed extensive networks in type I collagen gels under defined medium conditions.^{56,61,125}

Many support cell types have been utilized in the self-assembly approach to microvascular network formation, including fibroblasts,¹²⁴ mesenchymal stem cells (MSCs),⁵⁴ and PCs.⁵⁶ Although all of these cell types have been shown to improve EC network formation, PCs are a natural choice due to their association with native capillaries. *In vivo*, PCs are recruited to newly formed capillaries via PDGF-BB and HB-EGF^{49,125} and are essential to the maintenance of capillaries, so much so that the recruitment of PCs is indicative of the end of the plasticity window of neovessels, in which the microvessels are grown and pruned as necessary to maintain the appropriate level of tissue oxygenation.⁴⁸ When recruited to capillaries, PCs promote the production of basement membrane⁴⁷ (which is produced by both ECs and PCs⁵²) and produce the vessel-stabilizing protein angiopoietin-1 (Ang-1),⁵¹ both of which likely contribute to the PCs' stabilizing effect. Additionally, the presence of PCs aids in the maintenance of a quiescent EC phenotype and prevents the dilation of capillaries beyond their physiologic diameters of 5-10 μm .^{50,126} The advantages of using PCs rather than

fibroblasts or MSCs for applications in EC biology or drug delivery are clear, as the network more closely mimic the *in vivo* environment. In addition, PCs can be isolated from dermis,¹²⁷ making them a potentially autologous cell source, which is of critical importance for the development of engineered tissues with microvasculature.

The majority of research on self-assembled EC networks has involved the use of serum. Although culture medium containing serum is typically advantageous in terms of cost, it introduces many uncontrolled variables into tissue growth systems. This makes it difficult to elucidate biological mechanisms, and introduces additional experimental variability. In the worst scenario, a successful model of EC assembly using one serum lot yields much worse results using other lots due to the presence of unknown factors in the original lot. For these reasons, fully defined medium (i.e. containing no serum) is advantageous for engineering microvasculature *in vitro*, whether for EC biology or tissue engineering applications.

Our previously published system of HUVECs and PCs in collagen I gel⁵⁶ meets the above two criteria for the ideal engineered microvasculature, but it misses a third: a scaffold that is conducive to tissue growth. Collagen I gel has limited potential as a scaffold for engineered tissues. Although type I collagen is the major contributor to tissue strength *in vivo*, gels formed from the protein are quite weak and yield only limited production of additional collagen. Fibrin gels, in contrast, are also initially weak, but entrapped cells degrade the fibrin and produce an abundance of extracellular matrix including collagen I,^{42,128} which

ultimately leads to tissues strong enough for implantation into the pulmonary valve system.^{129,130} The results presented here demonstrate the ability of HUVECs and PCs to form fully interconnected microvascular networks in fibrin gel under defined conditions.

In addressing oxygen diffusion limitations in tissue engineering, fluid flow through engineered microvasculature will also be required. To achieve continuous non-stagnant fluid flow, microvessel alignment is also necessary: in an aligned network bifurcations occur at less sharp angles and microvessel loops that receive little flow because they are bypassed by a more streamlined vessel are rare. Aligned microvasculature provides natural inlet and outlet sides for flow as found in tissues such as muscle.⁶⁵ Recent work by our laboratory has indicated that mechanically constrained cell-induced gel compaction is an effective means to align microvessels sprouting from EC aggregates during angiogenesis,⁶³ and that this compaction improves microvessel density to within the physiologic range.¹³¹ The studies reported here harness this mechanism in a vasculogenic system, demonstrating the ability to create a highly interconnected aligned microvascular network via cell-induced gel compaction following microvessel self-assembly, which represents a critical step toward the creation of vascularized engineered tissues.

Studies were first undertaken to assess the effects of medium composition and PCs on the growth of HUVEC networks in fibrin gel. Studies then examined the effects of fibrin gel geometry and compaction on the HUVEC network alignment in defined medium. Finally, a hybrid approach of sequential use of

defined and serum-containing media was examined as a means to further improve network alignment.

Methods

4.1.1. Cell Culture

Human umbilical vein ECs (HUVECs) were purchased from Lonza and grown in “HUVEC medium,” which consisted of M199 with 20% FBS, 400 µg/ml endothelial cell growth supplement (ECGS), 100 µg/ml heparin salt (Sigma), 1% antibiotic/antimycotic (Gibco), and 10 µg/ml gentamicin (Gibco). HUVECs were used at passages 3-5. Approximately 16 hours prior to casting, the HUVECs were primed⁶¹ using M199 with 40 ng/ml FGFb, 40 ng/ml VEGF, 4 µl/ml reduced serum supplement (RSII), 1% antibiotic/antimycotic, and 10 µg/ml gentamicin. The ECGF and RSII were obtained from George Davis.

GFP-labeled human brain pericytes were obtained from George Davis. PCs were cultured in DMEM low glucose with 10% FBS, 1% penicillin/streptomycin (Gibco), and 10 µg/ml gentamicin (Gibco). Passages 6-8 were used in these studies.

4.1.2. Isotropic Construct Preparation

Fibrin gels containing HUVECs and PCs were cast in the wells of 96 well half-area plates with a final volume of 18 µL. Final cell concentrations were 3 million/ml HUVECs and 0.6 million/ml PCs. The fibrin formulation included 7.5 mg/ml plasminogen-depleted fibrinogen (EMD Chemicals), 75 µg/ml fibronectin (Sigma), 150 ng/ml of each of stem cell factor, interleukin 3, FLT3 ligand, stromal

derived factor, and basic fibroblast growth factor (FGFb; all R&D Systems), and 2.75 U/ml thrombin (Sigma). Gels were covered with 100 μ l “defined medium,” which consisted of M199 with 4 μ l/ml RSII, 40 ng/ml FGFb, 50 μ g/ml ascorbic acid, 2 KIU/ml aprotinin, 1% antibiotic/antimycotic, and 10 μ g/ml gentamicin. Constructs were harvested after 3 days of culture.

4.1.3. Aligned Construct Preparation

The same fibrin formulation and cell densities were used to cast constructs with aligned matrix in slab geometries. A rectangle measuring 1.75 cm x 0.5 cm was scored into the well of a 12 well plate. Two porous polyethylene spacers measuring 0.5 cm x 0.5 cm x 0.2 cm were fixed via sterile vacuum grease inside either end of the scored rectangle, leaving a rectangle measuring 0.75 cm x 0.5 cm between them. The gel-cell mixture (50 μ l) was pipetted into the region between the spacers, and the mixture seeped into the pores of the spacers. The dimensions were such that the slab had an aspect ratio (length/width) of 1.5. All aspect ratios reported herein refer to the initial slab dimensions. Two constructs were cultured in each well of a 12 well plate. Additional slabs with higher aspect ratios were also made in a similar manner by adjusting the length of the slab. Aspect ratios of 3 (1.5 cm x 0.5 cm) and 4.5 (2.25 cm x 0.5 cm) were utilized, and these slabs were cultured in 6 well plates with 1 slab per well. After 1-3 days of culture in defined medium, the constructs were detached from the plate via the spacers and reattached to a new plate. This step eliminated the adhesion between the gel and the plate, enabling cellular traction forces to compact and align the matrix fibers. Compacted tissues were

harvested at day 6, while control constructs were harvested at day 3, prior to detachment.

4.1.4. Compaction Studies

Several medium formulations were tested to determine whether or not a defined medium could induce substantial gel compaction of slabs of aspect ratio 1.5. Slabs containing HUVECs and PCs were cultured as described above with 3 days of defined medium followed by 3 days of the test medium. On day 6 of culture, macroscopic images were taken of the slabs, and the width across the middle of each slab was measured using ImageJ (NIH). A reduction in slab width was indicative of gel compaction. Test media included defined medium with 10 ng/ml TGF- β 1, defined medium with supplements from the EGM-2 bullet-kit (Lonza; includes VEGF, bFGF-2, EGF, IGF-1, heparin, hydrocortisone, ascorbate, and GA-1000), and EGM-2 with 2%, 5%, or 10% total FBS.

4.1.5. Hybrid Approach

Slabs of aspect ratio 1.5 containing HUVECs and PCs were cast with the same concentrations and fibrin formulation as above. All constructs were cultured for 3 days in defined medium. On day 3 of culture, some constructs were harvested, and others were cultured for an additional 3 days in either defined medium or “EGM-2+,” which consisted of EGM-2 (Lonza) with an additional 8% FBS and 1% penicillin/streptomycin.

4.1.6. Fibril Orientation

Alignment of matrix fibrils in slabs was verified with polarimetry, as previously described.⁸⁷ Briefly, the slabs were placed between 2 polarizers, and images taken as one of the polarizers rotated. A custom Matlab script measured light intensity at each polarizer angle, and output both an average retardation value (proportional to fibril alignment) and an alignment map, in which lines overlaying the slab image represented the local strength and direction of fibril alignment. The retardation was measured in the middle third of each slab, where alignment is strongest. Normalization to construct thickness yielded birefringence, a measure of fibril alignment.

4.1.7. Microvascular Network Evaluation

Constructs created in 96 well plates (4 per condition) were fixed in 4% paraformaldehyde and stained whole with an antibody against CD31 (Dako). Hoechst 33342 dye was used to label nuclei. Constructs were imaged using a Zeiss inverted epi-fluorescence microscope.

Images were automatically thresholded and analyzed using a custom Matlab code, which yielded network parameters including total network length and network alignment. For the purposes of this analysis, a “segment” was defined as a microvessel between two bifurcation points, and a “structure” was defined as a continuous set of microvessels and could be made up of multiple segments. Alignment was assessed by skeletonizing the network and measuring the length and angle of each segment. An anisotropy index (AI) was defined for each image such that

$$AI = \frac{\sum L_x}{\sum L_y},$$

where L_x is the component of segment length in the direction parallel to alignment, and L_y is the component of segment length in the direction perpendicular to alignment. The direction of alignment was defined as the average angle of all segments. The area fraction of the image stained positively for CD31 (“CD31 fraction”) was taken as an indication of HUVEC density. PC density and recruitment levels were also evaluated in Matlab. A PC (identified by GFP-labeling) was considered recruited if any part of it was immediately adjacent to a CD31-positive microvessel. Total cell density measurements were based off of nuclear counts.

Due to the increased density (caused by compaction) and thickness of the slabs relative to the 96 well plate constructs, whole construct imaging was impossible. Instead, thick (40-60 μm) longitudinal sections were cut, stained for CD31 and imaged and analyzed as above.

4.1.8. Lumen Formation

Constructs were frozen in OCT embedding medium and cross-sections (9 μm) were stained for CD31. A second Matlab code detected lumens via a semi-automated process previously described. Briefly, images were thresholded and potential lumens were detected as dark regions completely surrounded by white (CD31 staining). User input was allowed to either remove non-lumens that were detected (e.g. the space between nearby CD3+ structures), or connect CD31+ regions to enable the program to detect a lumen it previously missed (e.g. a

structure containing a small area of dim staining visible to the eye but below the threshold). A variety of network properties, including lumen density, average lumen area, cell density, and pericyte recruitment were assessed.

4.1.9. Basement Membrane Deposition

Basement membrane deposition was evaluated via immunofluorescent staining of cross-sections using antibodies against collagen IV and laminin (Abcam). Average pixel intensities for exposure-matched images were calculated via Matlab to compare between experimental conditions. Four sections from different areas of the constructs were imaged per condition.

4.1.10. Statistics

Data were analyzed in Minitab using either Student's t-tests (if only two conditions were evaluated) or one-way ANOVAs with Tukey post-hoc tests (if more than two conditions were evaluated). Comparisons to control conditions were performed using Dunnett post-hoc tests. *P* values of less than 0.05 were considered significant.

4.2. Results

4.2.1. HUVECs and PCs form highly interconnected microvascular networks in fibrin gel under defined conditions.

A small volume gel format (18 μ l in 96 well half-area plates) was used to optimize conditions for HUVEC microvascular network formation using defined medium or EGM-2+ with or without co-culture with PCs. Representative images

of whole mount CD31 stains and quantification of the network characteristics are shown in Figure 4-1. HUVECs co-cultured with PCs in defined medium formed the best network in terms of total length and average connected structure length (a measure of network interconnectivity). Additionally, culture in defined medium produced a greater level of PC recruitment to microvessels than culture in EGM-2+.

4.2.2. Aligned microvascular networks were formed under defined conditions in slabs of high aspect ratio.

The cell-induced gel compaction of fibrin gel slabs containing HUVEC networks was investigated under defined conditions using slabs of varying aspect ratio that were detached at day 3 of culture (i.e. gel compaction began on day 3). Macroscopic images of a slab with an initial aspect ratio of 4.5 and its alignment map are shown in Figure 4-2a-b. Representative images of the HUVEC networks are shown in Figure 4-2c-d. Slabs with an aspect ratio of 4.5 compacted much more (Figure 4-2e) and had more aligned matrix (Figure 4-2f) and microvessels (Figure 4-2g) than slabs of aspect ratio 1.5. No differences between aspect ratios were observed in total network length, average continuous structure length, or PC recruitment (Figure 4-2h-j).

4.2.3. Compaction is detrimental to forming networks but not to previously formed networks.

Slabs of aspect ratio 4.5 were cultured in defined medium and detached from the culture plate (enabling compaction to begin) at days 1, 2 or 3. Images of

the resulting HUVEC networks are shown in Figure 4-3a-d. All of the detached slabs compacted more and were more aligned in terms of both matrix and microvessels (Figure 4-3e-g) than the day 3 control slabs that were never detached. Additionally the microvessels of the slabs detached at day 1 were more aligned than any other condition. No differences in total network length or PC recruitment were observed between any of the conditions, but the average structure length (a measure of network connectivity) was reduced in constructs detached at days 1 or 2 in comparison to the control. Constructs detached at day 2 also had lower average structure length than those detached at day 3. The average structure length of constructs detached at day 3 was not different from that of controls (Figure 4-3h-j).

Slabs of aspect ratio 4.5 detached at day 3 were further analyzed for lumen formation and basement membrane deposition. They were compared to 96 well plate controls (created at the same time and cultured for 3 days) for which the culture conditions were optimized. Representative images of CD31 and collagen IV staining are shown in Figure 4-4a-d. Analysis of CD31-stained images revealed that the lumen density, average lumen area and the cell density (including both HUVECs and PCs) were increased in the aligned slabs over the control, although no statistically significant differences were observed in either CD31+ area fraction or PC density (Figure 4-4e-i). No differences were observed in total staining intensity for either laminin or collagen IV staining, but a laminin staining per cell was decreased in the slabs (Figure 4-4j-m).

4.2.4. EGM-2+ improves compaction of slabs.

Additional medium formulations were tested to determine whether or not they could improve the limited compaction and alignment observed in slabs of aspect ratio 1.5. Slabs were cultured in defined medium for 3 days followed by the test medium for 3 days. The addition of TGF- β 1 or growth factors provided by the EGM-2 bulletkit did not improve compaction, but serum-containing EGM-2+ did improve compaction, regardless of the serum concentration (Figure 4-5).

4.2.5. Hybrid approach yields improved network characteristics over defined medium alone.

Due to the relatively low compaction and lumen densities observed using defined medium, a hybrid approach was investigated in which slabs (aspect ratio 1.5) were cultured in defined medium for 3 days followed by EGM-2+ for an additional 3 days. Constructs were detached on day 3. Representative images of the HUVEC networks are shown in Fig. 6a-c. Macroscopic images and alignment maps of day 6 constructs cultured in defined medium or EGM-2+ are shown in Figure 4-6d-g. In comparison to constructs cultured in defined medium for 3 or 6 days, hybrid constructs compacted more and had higher matrix and microvessel alignment (Figure 4-6h-j). In addition, the total network length and average structure length were the same between the day 6 hybrid constructs and the day 3 control, but reduced for the constructs cultured for 6 days in defined medium; PC recruitment was the same for all conditions (Figure 4-6k-m).

Additional network characteristics were quantified from CD31-stained cross sections. Representative images are shown in Figure 4-7a-c. Lumen

density was improved in hybrid constructs over the day 3 control (Figure 4-7d), and mean lumen area was increased in day 6 defined medium constructs over the day 3 control (Figure 4-7e). The total cell density (based on nuclear counts) was increased in hybrid constructs over all other conditions (Figure 4-7f). The area fraction of CD31 staining (which corresponds roughly to EC density) was also increased in hybrid constructs over day 6 defined medium constructs (Figure 4-7g). No differences were observed in PC density (Figure 4-7h). Basement membrane deposition was also examined using laminin and collagen IV stained cross sections. Representative images of collagen IV staining are shown in Figure 4-7i-k; laminin staining was similar and is not shown. A higher total intensity of laminin staining per area was observed in hybrid constructs as compared to day 6 defined medium constructs (Figure 4-7l), but this difference did not exist when the staining intensity was normalized to total cell density (Figure 4-7m). Total collagen IV staining per area was increased in hybrid constructs over both other conditions (Figure 4-7n), but collagen IV per cell was decreased in hybrid constructs in comparison to day 6 defined medium constructs.

4.3. Discussion

The achievement of a highly interconnected microvascular network in fibrin gel under defined conditions is of utility for both EC biologists and tissue engineers. For EC biologists, this fibrin system complements our previously developed type I collagen system⁵⁶ and enables the study of EC interactions with two different biopolymers of physiological relevance. For tissue engineers, the

fibrin gel system is much more advantageous than the collagen gel system because fibrin stimulates the production of extracellular matrix proteins that strengthen the tissue more so than collagen.^{42,128} It is interesting to note that in the fibrin gel system both the defined medium and the PCs were required to achieve a highly interconnected network; in the collagen gel system PCs were not required for the initial network formation. The presence of PCs improved the total network length in both media, but to a lesser degree in serum-containing EGM-2+. One possible explanation is that the serum provided some of the same factors as the PCs, accounting for the difference between medium types in the absence of PCs, and that in the presence of PCs, either the proximity of PCs to the ECs or the additional factors they provided improved the network formation. Additionally, the recruitment of the PCs to the EC microvessels was higher in defined medium. This is likely the result of an increase in local gradients of chemokines (e.g. PDGF-B) due to the relative lack of chemokines present in defined medium in comparison to EGM-2+.

Previous work has shown that the alignment of both matrix and sprouts from EC spheroids in an angiogenic system increases with slab aspect ratio,⁶³ and that appears to be true in this vasculogenic system as well. However, slabs of aspect ratio 3 in the previous report had birefringence values of over 8×10^{-5} , whereas here slabs of higher aspect ratio (4.5) had birefringence values of only 1×10^{-5} . This is likely due to the relatively low level of gel compaction, which drives alignment, obtained in defined medium.

The compaction that did occur in defined medium had a deleterious effect on microvascular network formation. Constructs that were detached on days 1 or 2, prior to the completion of network formation, formed some microvessels, but they were not as interconnected as the day 3 controls. Only day 6 constructs that were detached on day 3, after network formation had occurred, were identical to the day 3 controls in every network characteristic that was assessed. The fact that the total network length was the same across conditions suggests that any increased matrix density caused by compaction or reduction in local matrix tension caused by detachment from the plate had a minimal effect on microvessel growth. However, one possible explanation for the reduced network connectivity observed with premature detachment is that the increased matrix alignment of constructs caused by compaction during network formation prescribed a similar growth direction for all of the microvessels, reducing the probability that microvessels would connect to nearby microvessels. Another effect observed in constructs detached on varying days is that the network alignment was highest in the constructs detached on day 1. This is likely explained by the additional day(s) of compaction-induced alignment experienced by these constructs; constructs detached on day 3 cultured out to day 8 (an equivalent compaction time) would likely show a similar level of alignment. Another factor may be that the microvessels of constructs detached at days 1 or 2 are forming as alignment is developing, enabling a greater role for contact guidance as compared to the constructs detached at day 3 that largely contain

formed microvessels that must reorient with the compacting network of ECM fibers.

Despite the relatively low levels of compaction observed in defined medium, it is clear that the compaction that occurs in slabs of aspect ratio 4.5 detached at day 3 is sufficient to achieve alignment of the microvascular network, as was the goal. Because this fibrin gel system was optimized for the 96 well plate constructs, comparison of the whole mount network characteristics between the aligned slabs and the 96 well plate constructs is of interest. Although the data (presented in Figure 4-1 and Figure 4-2) cannot be statistically compared because they resulted from separate experiments, the differences can give a general idea of how the microvessels compare. The data suggest that the slabs may have a lower total network length per area and a lower length per structure. It is unclear whether these differences are the result of actual network differences, experiment-to-experiment network variation, or differences in sample preparation for imaging (whole mounts, which were 400-500 μm thick, vs. 60 μm thick sections). It is certainly possible that connections between structures were missed in the slabs due to the relatively thin samples that were imaged.

In contrast, the network characteristics obtained from sections (presented in Fig. 4) can be directly compared as the samples were from the same experiment, and they demonstrate improvement in the microvascular characteristics in the slabs over the 96 well plate constructs. The cause of this improvement cannot be determined due to the many differences between the conditions, including the sample geometry, the day of harvest, and the level of

compaction, which has been previously shown to increase lumen density.¹³¹ Additionally, the deposition of basement membrane was assessed in the two construct types. Although there was no difference between conditions in total deposition of either laminin or collagen IV, a reduction in laminin staining per cell was observed in slabs. No difference was observed between conditions in collagen IV staining per cell. This suggests that the production of basement membrane by each cell was decreased in the slabs. This is particularly interesting due to the fact that the slabs were cultured for 3 days longer than the 96 well plate constructs.

Additional experiments were completed to determine whether or not additional factors could be added to the defined medium to induce more gel compaction. Higher levels of compaction would be desirable to increase the alignment and mechanical strength of engineered tissues. EGM-2+ was used as a positive control because it caused a high level of compaction in preliminary experiments. Despite the fact that TGF- β 1 is known to increase cell contractility,¹³²⁻¹³⁴ the addition of TGF- β 1 to defined medium did not increase compaction. Similarly, the addition of EGM-2 bulletkit components (except serum) to the defined medium in the same concentrations used in EGM-2+ did not increase compaction. Varying the amount of serum in EGM-2+ also did not affect compaction. It is unclear which component or combination of components of EGM-2+ induce high levels of compaction, and a more high throughput method than is currently available would be required to answer this question.

Because serum-containing medium was required to achieve high compaction levels, a hybrid approach was attempted in which slabs of aspect ratio 1.5 were cultured in defined medium for 3 days followed by EGM-2+ for 3 days. This would enable microvascular networks to form prior to compaction induction by EGM-2+. This method succeeded in producing highly aligned microvascular networks; not only was the alignment of both matrix and networks stronger in these hybrid constructs than that of constructs cultured entirely in defined medium (birefringence/anisotropy index data presented in Figure 4-6), but it also appeared to be stronger than that of defined medium constructs of aspect ratio 4.5 cultured in defined medium (data presented in Figure 4-2). The fact that the network properties did not vary between the hybrid and day 3 control constructs suggests that the addition of EGM-2+ after network formation did not have a detrimental effect.

Not only did the addition of EGM-2+ have no detrimental effects, it had a beneficial effect on lumen density, bringing the density to within the physiologic range for dermis.^{135,136} EGM-2+ also increased the overall cell density in comparison to the other conditions. This cell density is attributable to increased proliferation of the HUVECs as differences in PC density between conditions were not statistically significant. The density of basement membrane (both laminin and collagen IV) was increased in hybrid constructs; however this difference disappeared (laminin) or reversed (collagen IV) when the staining intensity was normalized to cell number, suggesting that the cellular production of these proteins was the same or lower in the EGM-2+. The high level of basement

membrane proteins were deposited by day 3 likely is part of the reason that these microvascular networks were relatively stable under compaction and the change of medium type.

These results have demonstrated two methods for forming highly interconnected aligned microvascular networks within fibrin gel. The method involving only defined medium results in constructs with relatively low levels of compaction, but would be useful to EC biologists requiring full control over the culture conditions. The hybrid approach, although it relinquishes some control over the culture conditions, yields constructs with relatively high levels of compaction, which is of interest to tissue engineers. Therefore, the HUVEC and PC fibrin gel system developed here has the potential for widespread use.

4.4. Figures

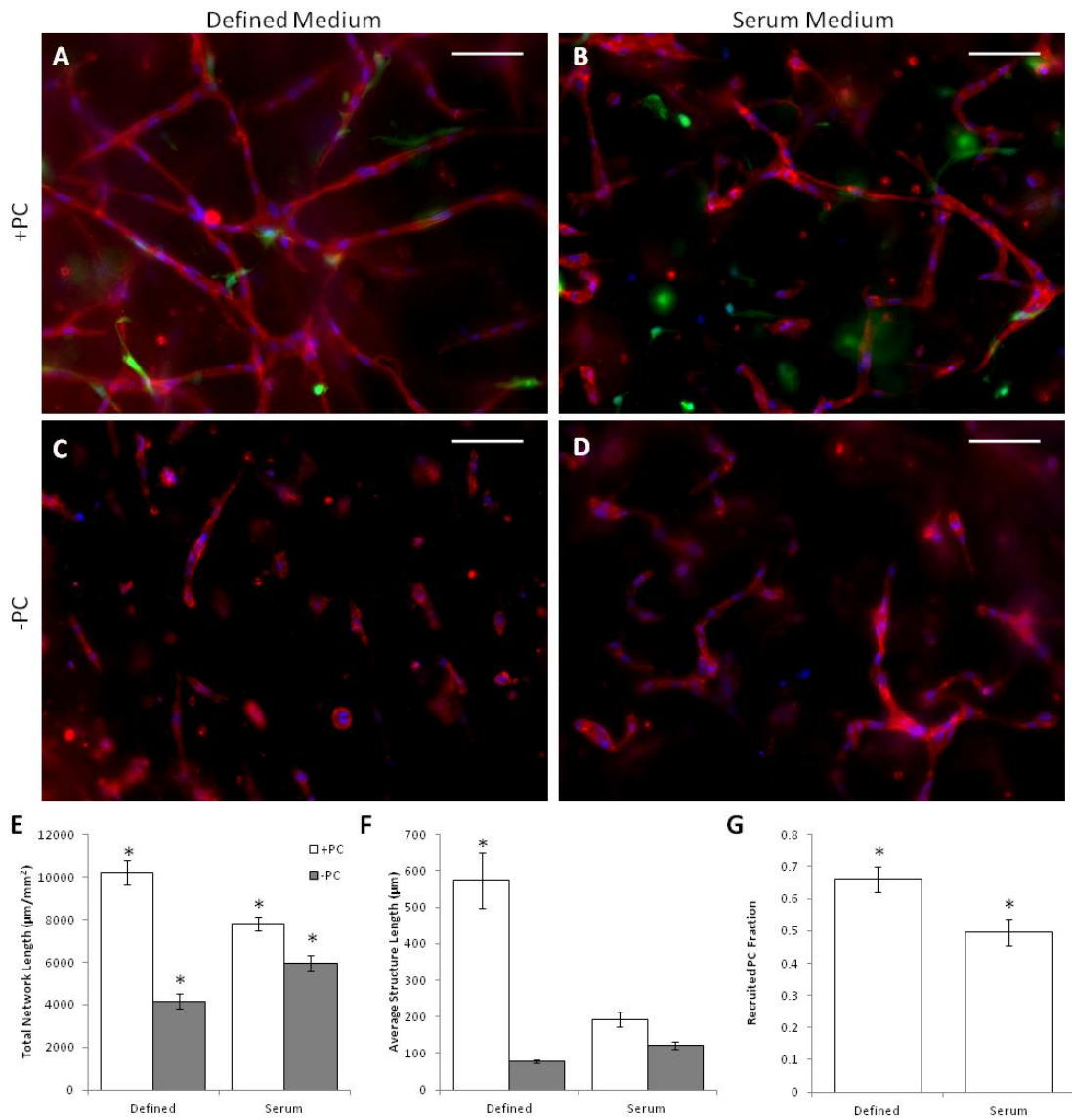


Figure 4-1.

(A-D) Representative images of whole mount CD31 stains of HUVECs (red) with (A-B) or without (C-D) PCs (green) in defined medium (A,C) or EGM-2+ (B,D) after 3 days of culture. Nuclei are stained blue. Scalebars = 100 μm . (E-G) Quantitation of vessel network properties. HUVECs grown with PCs in defined medium demonstrated improved total vessel length (E), average length per

continuous structure (F), and PC recruitment (G) over all other conditions. * $p < 0.05$ in comparison to all other conditions.

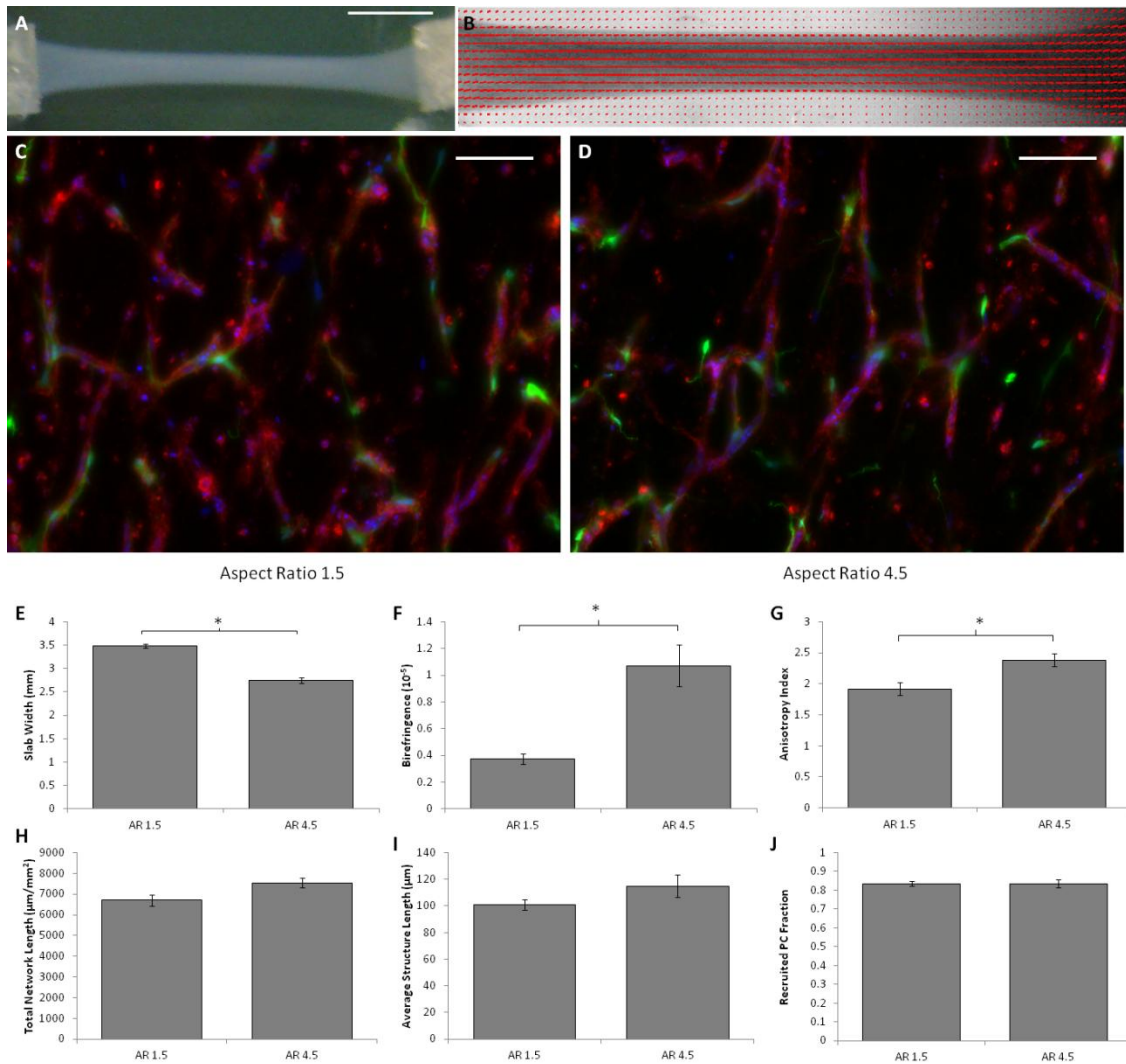


Figure 4-2.

(A) Macroscopic image of a slab with an aspect ratio of 4.5 after compaction in defined medium. Scalebar = 5 mm. (B) Alignment map of the compacted slab shown in (A). The red segments indicate the local strength and direction of fibril alignment. (C-D) Representative images of CD31-stained (red) thick longitudinal sections of slabs with aspect ratios of 1.5 (C) and 4.5 (D). The long axes of the slabs are vertical. PCs are green and nuclei are blue. Scalebars = 100 μm. (E-G) Construct compaction (width at the middle of the slab; E), Matrix alignment

(birefringence; F), and microvessel alignment (anisotropy index; G) show that the slabs with higher aspect ratio that compacted more were also more aligned. (H-J) No differences were observed between slabs of different aspect ratio for a number of microvessel characteristics, including total vessel length per area (H), the average length per continuous structure (I), and the recruited PC fraction (J). $*p < 0.05$.

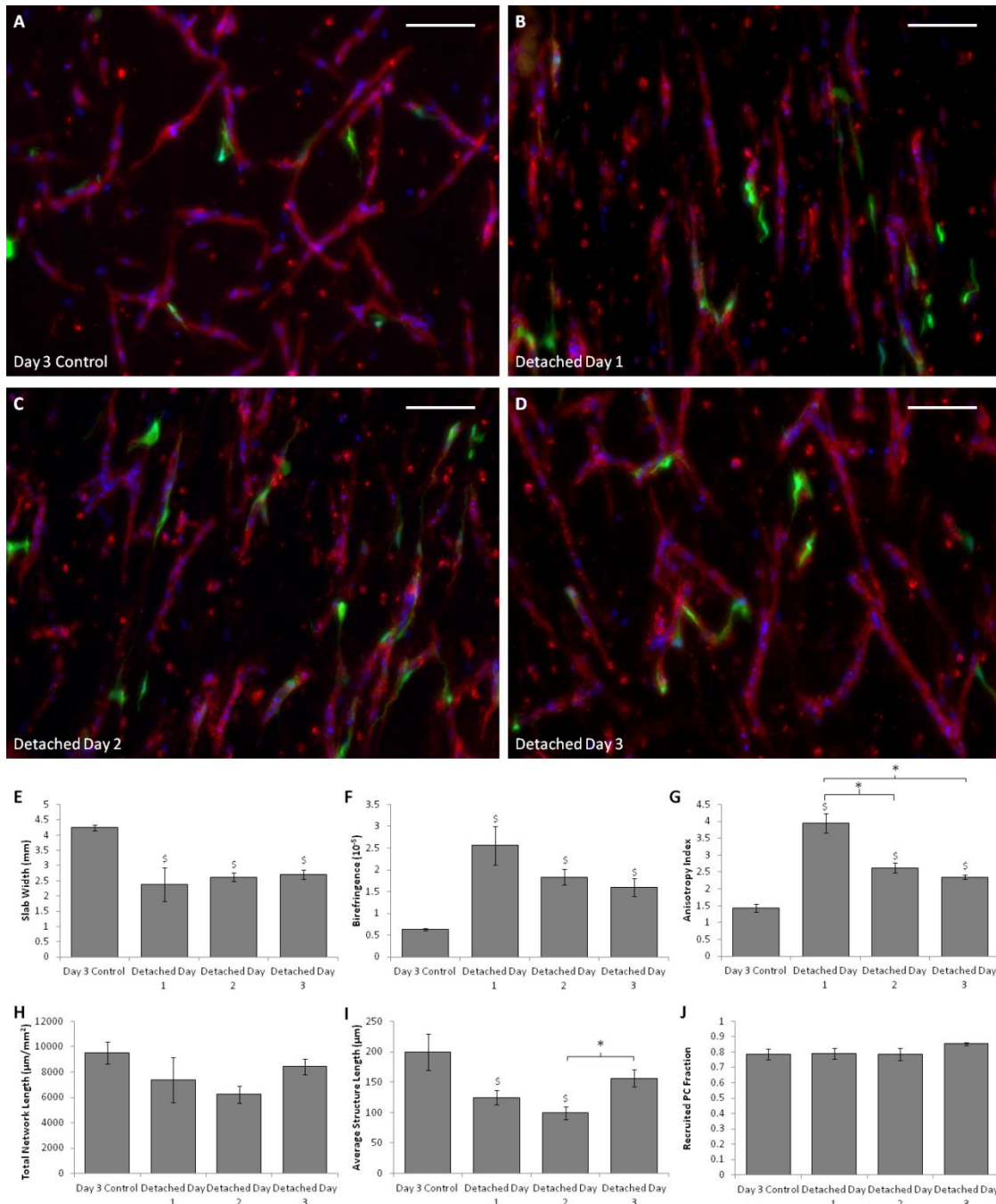


Figure 4-3.

(A-D) Representative images CD31 stains (red) of thick longitudinal sections of slabs cultured in defined medium that were never detached and harvested at day 3 (A), or that were detached at day 1 (B), day 2 (C) or day 3 (D) and harvested at

day 6. The long axes of the slabs are vertical. PCs are green and nuclei are blue. Scalebars = 100 μm . (E-G) Measures of construct compaction (width at the middle of the slab; E), matrix alignment (birefringence; F), and microvessel alignment (anisotropy index; G) indicated that all of the detached slabs compacted and that both the matrix and the microvessels became aligned. (H-J) Measures of microvessel properties, including total microvessel length per area (H), average length per continuous structure (I), and PC recruitment (J), suggested that the aligned microvascular networks present in the slabs detached on day 3 were equivalent to those of the day 3 control slabs. $*p < 0.05$. $\$p < 0.05$ in comparison to the control.

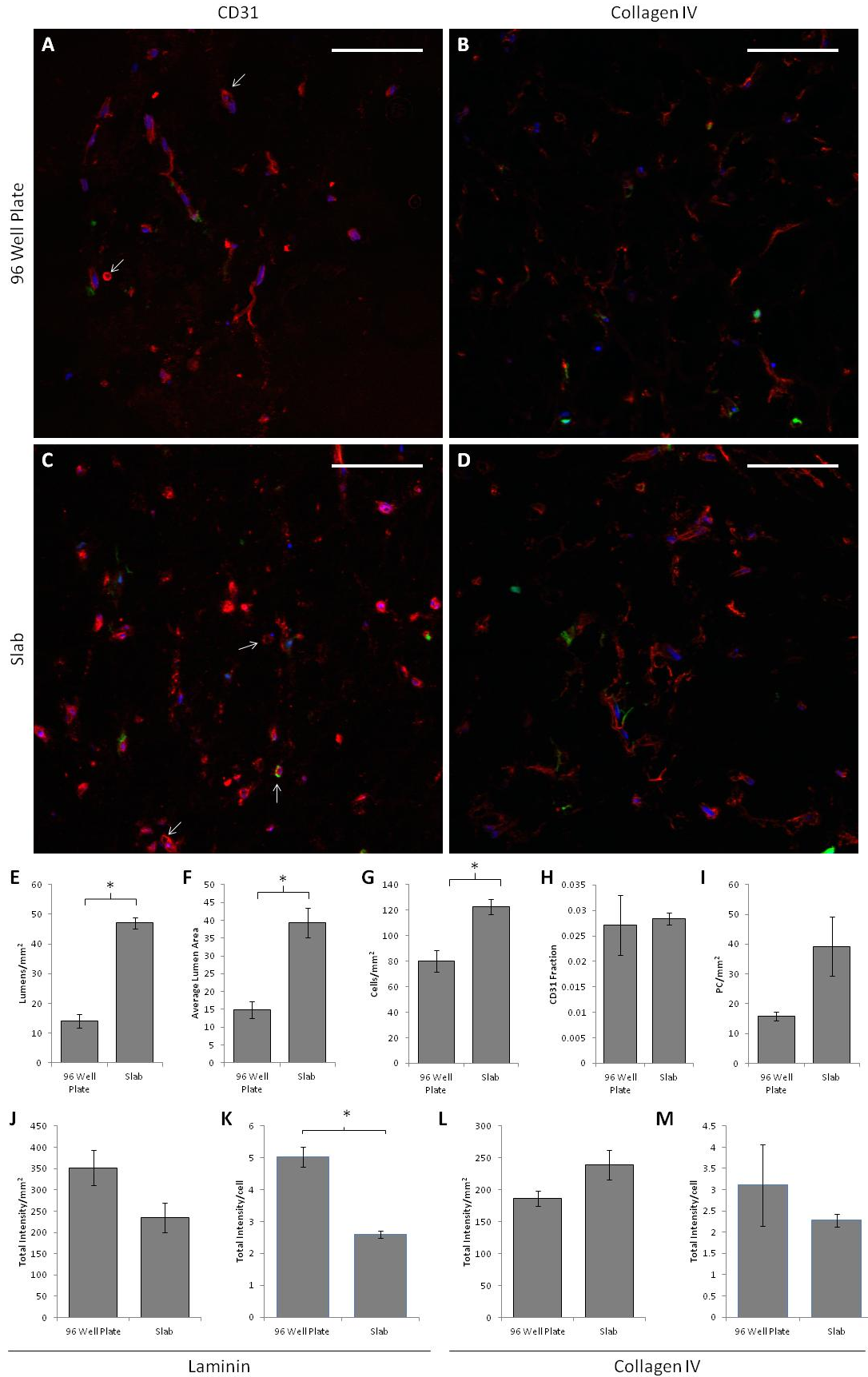


Figure 4-4.

(A-D) Representative images of cross sections of constructs created in 96 well plates (A-B) or in the slab geometry (C-D) and cultured in defined medium stained for either CD31 (A,C) or collagen IV (B,D) in red. PCs are green and nuclei are blue. Arrows indicate the location of lumens. Scalebars = 100 μ m. (E-H) Quantification of microvessel properties from CD31-stained images, including lumen density (E), average lumen area (F), the total cell density (G), the area fraction of CD31 staining (indicative of EC density; H), and the PC density (I). The slabs contain more and larger lumens as well as a higher total cell density, although no differences were observed among conditions for either CD31 fraction or PC density. (J-M) Basement membrane deposition. No differences were observed in total staining intensity of sections stained for laminin (J) or collagen IV (L). However, laminin staining intensity normalized to cell density was reduced in the slab geometry (K). No difference was observed in collagen IV staining per cell. * $p < 0.05$.

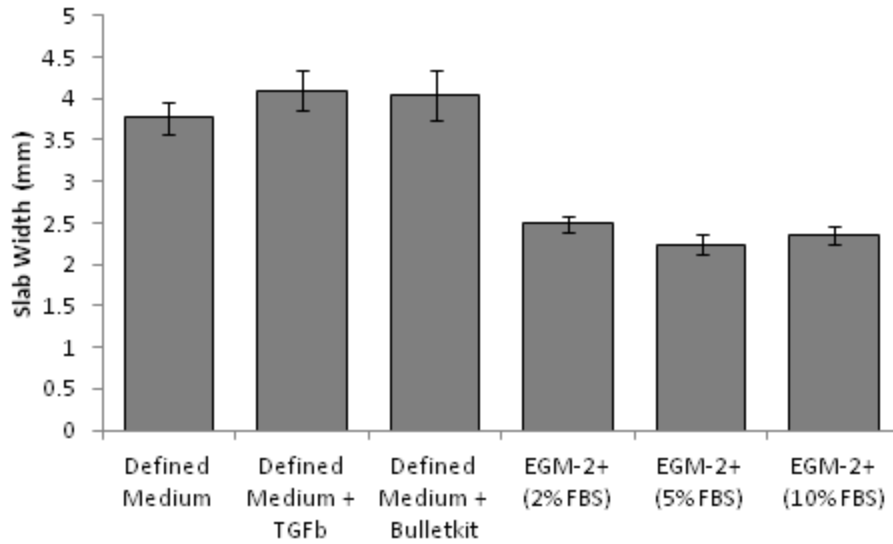


Figure 4-5.

Assessment of media were tested in an attempt to increase compaction in defined medium or reduce compaction speed in EGM-2+. The construct compaction results (width at the middle of the slab) suggest that all defined media caused similar compaction rates and all serum-containing media caused faster compaction rates, which were similar to each other. * $p < 0.05$ compared to all defined media. \$ $p < 0.05$ compared to all serum-containing media.

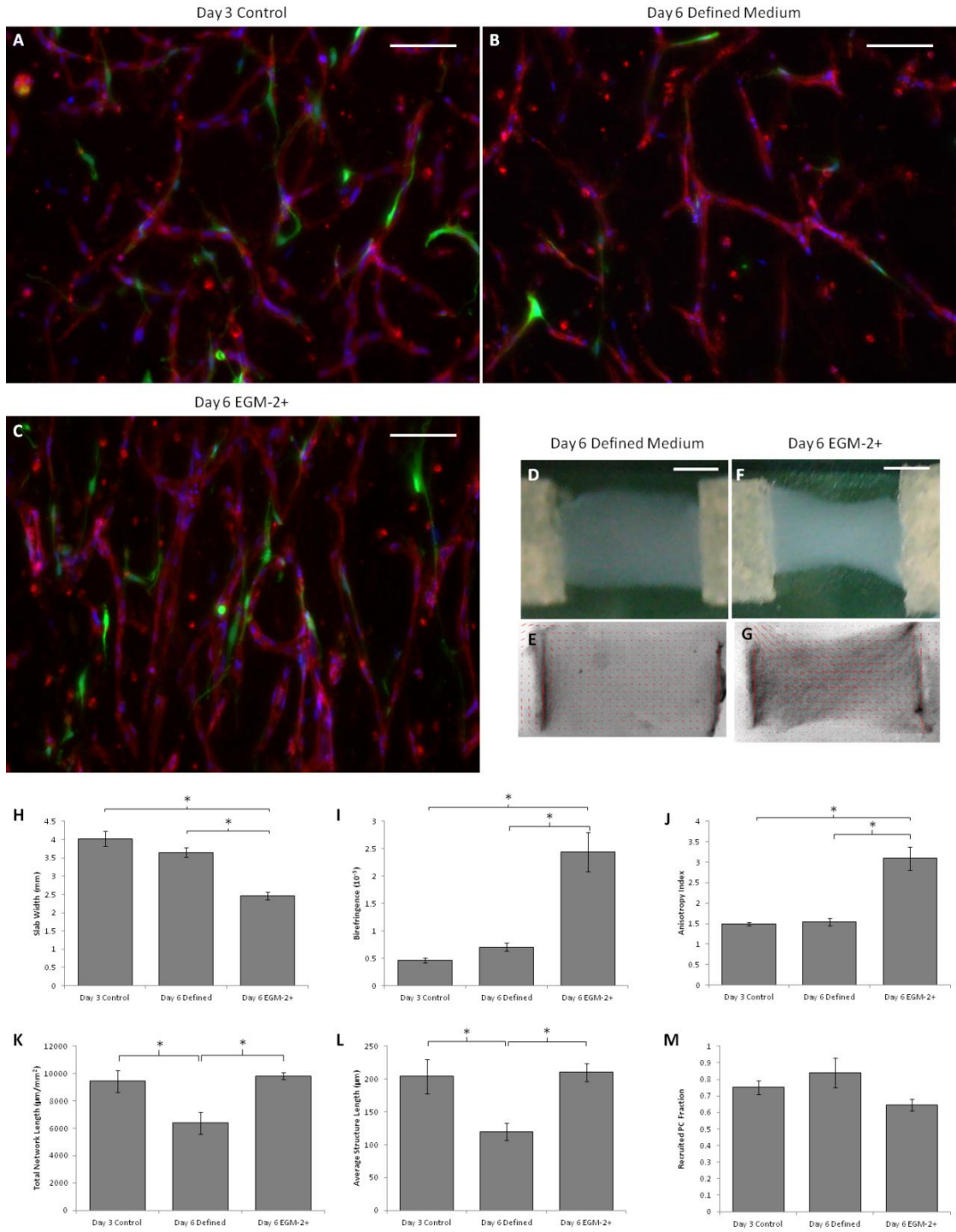


Figure 4-6.

Analysis of the hybrid approach based on whole mount microvessel properties.

(A-C) Representative images of thick longitudinal sections of constructs using the

hybrid approach, in which some constructs were harvested at day 3 (A) and others were cultured for an additional 3 days in either defined medium (B) or EGM-2+ (C). HUVECs were stained for CD31 (red), PCs were GFP-labeled (green) and nuclei were stained blue. The long axes of the slabs are vertical. Scalebars = 100 μ m. (D-G) Macroscopic images (D,F) and alignment maps (E,G) of slabs cultured in defined medium (D-E) or EGM-2+ (F-G). The red segments in the alignment maps indicate the local strength and direction of fibril alignment. (H-J) Alignment and compaction parameters indicated that the constructs cultured in EGM-2+ had higher matrix alignment (birefringence; H), compacted more (smallest width at the middle of the slab; I), and had higher microvessel alignment (anisotropy index; J) than slabs cultured in defined medium. (K-M) Microvascular network characteristics, including total microvessel length per area (K) and average length per continuous structure (L) were similar between slabs cultured in EGM-2+ and the control slabs, but reduced in slabs cultured in defined medium. PC recruitment (M) was similar across all conditions. * $p < 0.05$.

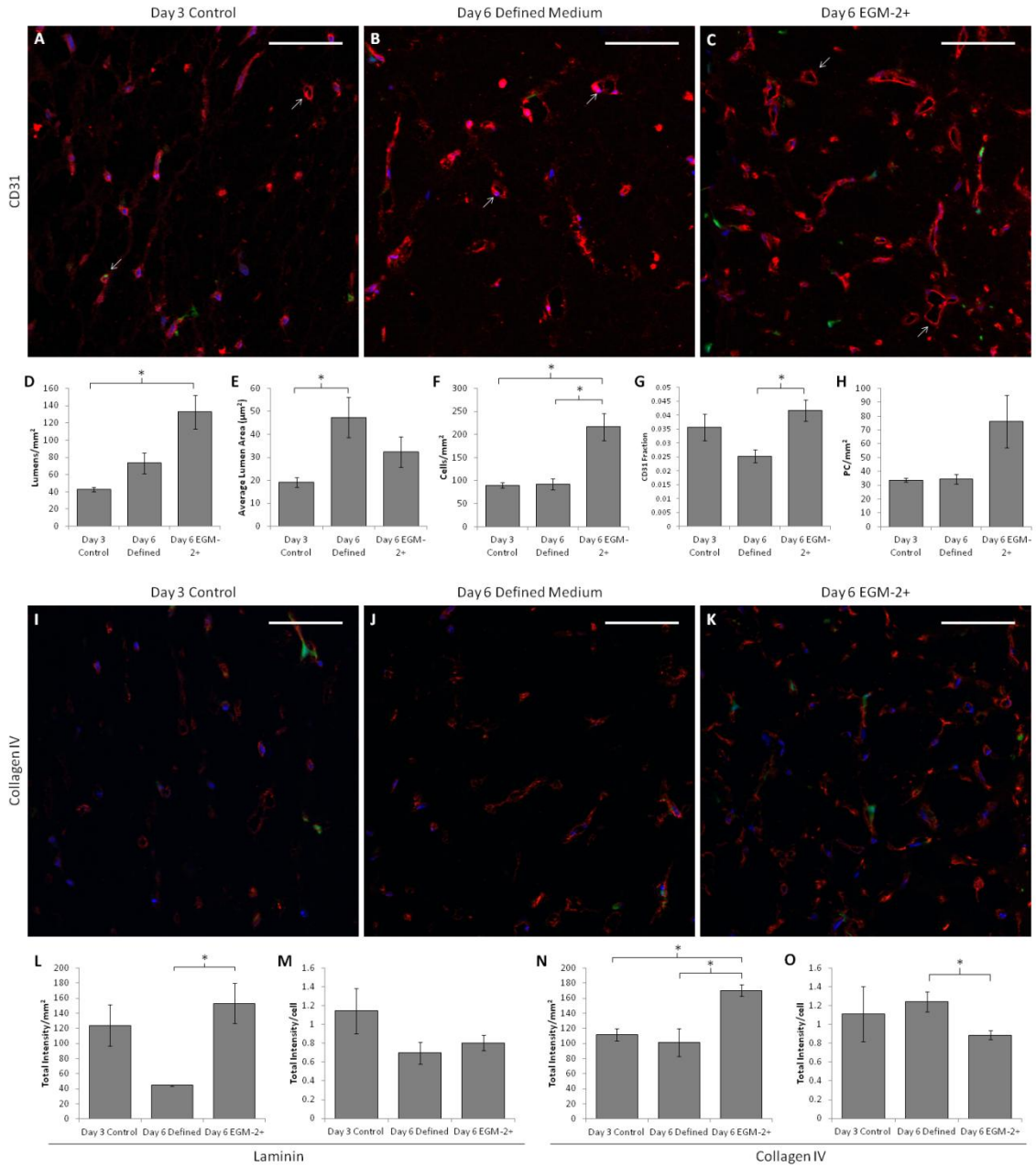


Figure 4-7.

Analysis of the hybrid approach based on cell densities and basement membrane deposition. CD31, laminin and collagen IV staining of construct cross sections was performed. (A-C) Representative CD31 staining (red) of constructs cultured in defined medium for 3 days (A), 6 days (B) or defined medium for 3

days followed by EGM-2+ for 3 days(C). PCs are green and nuclei are blue. Arrows indicate examples of lumens that were characterized. Scalebars = 100 μm . (D-H) Quantification of sections. The lumen density was improved in hybrid constructs over the control (D), and the average lumen area was larger in day 6 defined medium constructs (E). The cell density (F) was highest in the hybrid constructs. The area fraction of CD31 staining (indicative of EC density; G) was increased in hybrid constructs over day 6 defined medium constructs, but the PC density (H) was constant across conditions. (I-K) Representative collagen IV staining of control (I), defined medium (J), and hybrid (K) constructs. Laminin staining was similar, and is not shown. (L-O) Quantification of basement membrane staining. More total laminin staining was present per area in hybrid constructs than day 6 defined medium constructs (L); however no difference was observed in staining intensity per cell (M). A similar trend was observed for collagen IV staining, except that the staining intensity per cell was decreased in hybrid constructs (N-O).

Chapter 5. A Mathematical Model for Understanding Fluid Flow in Engineered Tissues Containing Microvessels

5.1. Introduction

The engineering of microvascular networks *in vitro* is of interest to basic scientists and tissue engineers alike. Much can be learned about endothelial cell (EC) biology from *in vitro* microvascular networks, which are more accessible and controllable than *in vivo* networks. In addition, engineered microvasculature is required to deliver nutrients to engineered tissue with high nutrient demand, such as myocardium. *In vitro* fluid flow through such an engineered microvascular network is an essential component of nutrient delivery, mimicking *in vivo* delivery.

Although a wide variety of mathematical models have been developed to understand fluid flow and nutrient exchange through native capillary networks,^{137–141} no models have been developed for vasculogenic engineered networks. Engineered microvasculature is often quite dissimilar to native microvasculature. Capillary-like structures (microvessels) are often isolated from other cellular structures, and lumens often do not extend the entire length of the structure.^{54,122,123,142} Branches may occur, but they are not necessarily at physiologically relevant angles. In addition, it appears that at times the ends of microvessels are open, enabling fluid from the interstitium to enter the lumen, and at other times are closed, creating luminal space isolated from the interstitial fluid.

Theoretically, if the ends of microvessels were open, interstitial flow would drive fluid through their lumens because the lumens would provide less resistance to flow than the extracellular matrix (ECM). A model describing fluid flow through such an engineered microvasculature could be useful for determining parameters such as the density of structures that receive flow or the frequency of bifurcations within the microvessels, both of which may be difficult to directly measure. In addition, such a model could be extended to determine oxygen concentrations throughout the sample (an understanding of which could be critical to improving the engineered tissues) or the local shear stresses to which microvessels are exposed (which likely play a role in lumen formation when applied to the abluminal surface and are known to affect EC phenotypes and disease processes when applied to the luminal surface¹⁴³).

Research in groundwater flow has led to the development of mathematical models for flow through fractured porous media, in which a porous medium, such as rock, contains fractures with a much higher permeability than the porous medium.¹⁴⁴ One can see the analogy between fractured rock and ECM containing perfusable microvessels. However, some differences apply, making the groundwater flow models ill-suited for describing tissues with engineered microvessels. For example, fractures are assumed to be planar, rather than linear as they would be for microvessels. It is also assumed that fluid can enter from any side of the fractures, whereas in engineered microvessels, fluid should primarily enter through their ends. In addition, the models of fractured porous

media are relatively complex and have an associated large computational demand, which may not be necessary for the study of engineered microvessels.

Therefore, we developed an idealized 2-dimensional flow model and corresponding finite difference approximation (FDA) model to describe pressure and fluid flow through the ECM and engineered capillary-like structures. The FDA model, coded in Matlab (Mathworks), includes tubes (linear “fractures”) that require fluid to enter from the surrounding ECM (“rock”) at only their ends, with a computational time that required only seconds. The model was internally validated and compared to a more accurate (but much more computationally intensive) 3-dimensional finite element approximation (FEA) model created in COMSOL Multiphysics. Example data based on our experience with engineered microvessels was used to demonstrate the potential uses of the model.

5.2. Methods

5.2.1. Idealized Model of Fluid Flow in Tissues Containing Engineered Microvessels

A simple 2-dimensional FDA model was developed in which the ECM was represented by a homogenous porous medium, and microvessels were represented by straight tubes, some with a single bifurcation, of infinitesimal radius between two nodes of the porous medium. Fluid flow in the ECM was governed by Darcy’s Law,

$$\mathbf{v} = -\mathbf{K}_p \nabla P, \quad (1)$$

where \mathbf{v} is fluid velocity, \mathbf{K}_p is the hydraulic conductivity of the ECM, and P is the pressure. The hydraulic conductivity, which is a property of the ECM and the

fluid, was related to the hydraulic permeability, which is a property only of the ECM, as follows:

$$k_p = K_p \mu \quad (2)$$

where k_p is the hydraulic permeability of the ECM and μ is the fluid viscosity.

Fluid flow within tubes followed the Hagen-Poiseuille Equation for steady laminar flow of a Newtonian fluid in a smooth cylindrical tube,

$$Q = \frac{\pi r^4 \Delta P}{8 \mu L}, \quad (3)$$

where Q is the volumetric flow rate, r is the radius of the tube, P is pressure, and L is the length of the tube. Fluid entering or exiting a tube was considered to be a point sink or source, respectively, of mass and linear momentum, which was handled by adding an additional term to the balance equations based on the length, radius (a finite radius for each tube was used to calculate resistance to flow), and orientation of the tube. The following are balance equations for the example of a node (i) at which a tube begins:

$$\text{Mass} \quad \nabla \cdot \mathbf{v} = -\frac{Q_t}{\Delta x^3}, \quad (4)$$

$$x \text{ Momentum} \quad v_{xi} + K_{px} \frac{\partial P}{\partial x} - v_t \cos \theta = 0, \quad (5)$$

$$y \text{ Momentum} \quad v_{yi} + K_{py} \frac{\partial P}{\partial y} - v_t \sin \theta = 0, \quad (6)$$

in which Q_t is the volumetric flow rate through the microvessel, Δx is the distance between nodes, v_{xi} and v_{yi} are the x - and y -components of velocity at node i , respectively, K_{px} and K_{py} are the ECM hydraulic conductivities in the x and y directions, respectively, v_t is the velocity through the tube, and θ is the angle of the tube relative to the x direction. As the equations indicate, at node i the

velocity through the tube and the ECM velocity are assumed to be independent in terms of magnitude and direction. For tubes containing one bifurcation, each portion of the tube was assigned a radius, and flow through each portion was determined by the pressure difference between the bifurcation point and the end open to the ECM. The pressure at the bifurcation point was determined by enforcing mass conservation through the tube. Mass and linear momentum balances were evaluated at each node, except at boundaries, using first order forward (or backward at some boundaries) finite difference approximations (Figure 5-1). (Centered finite differences were initially used but resulted in spatially periodic solutions due to the tube inflows and outflows that occurred at single nodes.) Boundary conditions applied were no flux through the sides of the tissue, fixed and uniform pressure at the tissue outlet, and fixed, uniform and unidirectional flow at the tissue inlet. The system of linear equations was solved for velocity and pressure fields in Matlab (v. R2012b).

Microvessel density was specified as a total number of tubes, and tube location and dimensions could be specified directly or generated randomly based on an average and standard deviation of each tube parameter (length, radius, and angle). Specified tubes were used in model validation, and randomly generated tubes, based on parameters measured from engineered microvessels, were used to produce model results. The results from 6 randomly generated tube configurations were averaged to produce each data point. Parameters used for each case are listed in Table 5-1.

Exact Model of Fluid Flow in Constructs Containing Engineered Microvessels

A 3-dimensional finite element model was created in COMSOL Multiphysics (v. 4.2a) using the Free and Porous Medium module in order to compare and validate results from the FDA Model. Microvessels were again modeled as tubes within a porous ECM. Flow within the ECM was governed by the Brinkman Equations:

$$\frac{\rho}{\varepsilon_p} \left((\mathbf{v} \cdot \nabla) \frac{\mathbf{v}}{\varepsilon_p} \right) = \nabla \cdot \left[-P\mathbf{I} + \frac{\mu}{\varepsilon_p} (\nabla \mathbf{v} + (\nabla \mathbf{v})^T) - \frac{2\mu}{3\varepsilon_p} (\nabla \mathbf{v})\mathbf{I} \right] - \left(\frac{\mu}{k} + \beta_f |\mathbf{v}| + Q \right) \mathbf{v} + \mathbf{F}, \quad (7)$$

$$\rho \nabla \cdot \mathbf{v} = Q, \quad (8)$$

where ρ is fluid density, ε_p is ECM porosity, \mathbf{v} is velocity, P is pressure, μ is dynamic viscosity, k is permeability, β is effective viscosity, Q is volumetric flow rate, and \mathbf{F} is force.

Flow within the tubes was governed by the Navier-Stokes Equations:

$$\rho((\mathbf{v} \cdot \nabla)\mathbf{v}) = \nabla \cdot [-P\mathbf{I} + \mu(\nabla \mathbf{v} + (\nabla \mathbf{v})^T)] + \mathbf{F}, \quad (9)$$

$$\rho \nabla \cdot \mathbf{v} = 0, \quad (10)$$

in which the symbols represent the same variables as in the Brinkman Equations. At the interface between a tube end and the ECM, the normal stresses were equated:

$$[\mu(\nabla \mathbf{v} + (\nabla \mathbf{v})^T)\mathbf{n} - P\mathbf{I}]_{tube} = \left[\frac{\mu}{\varepsilon_p} (\nabla \mathbf{v} + (\nabla \mathbf{v})^T) - P\mathbf{I} \right]_{ECM}, \quad (11)$$

where again the symbols represent the same variables. The boundary conditions for the FEA model were the same as those for the FDA model except that no slip boundary conditions were enforced at the sides of the ECM and all tube edges.

Only prescribed geometries (not randomized) were used in this model, as that enabled direct comparison of the two models. Water was used as the fluid

for the comparison. Once the geometry was defined, a tetrahedral mesh (with a 1 μm element size) was applied, and the equations were solved for the pressure and velocity fields. Standard parameters for the FEA model are given in Table 5-2.

5.2.2. Internal Validation of the Models

Each model was validated internally by varying parameters one at a time and verifying that the results made intuitive sense. A single tube was used for simplicity. While one parameter value was varied, all of the others were held constant at their standard values. Each parameter was examined at 5-7 values in a range that included its standard value. Parameters that were varied in both models included inlet velocity, ECM permeability, fluid viscosity, microvessel radius, and microvessel angle relative to the x direction. In the FDA model, the ECM anisotropy was also varied by decreasing the ECM permeability in the y direction while holding the permeability in the x direction constant. This was not varied in the FEA model because a permeability tensor (which describes ECM anisotropy) was not supported in COMSOL's Free and Porous Medium module.

5.2.3. Comparison Between Models

Comparisons of the results of the FDA model to those of the FEA model were used to further validate the FDA model. First, the results of parameter value variations (described above) were compared between the models. Direct comparison was possible because the geometry assessed was identical between models and because the results were assessed for the same parameter values.

A second comparison was completed, in which the radius of the microvessel in a single tube geometry was varied over a much wider range than in the internal validation studies. The models were expected to agree in the limit as the tube radius approached zero. The only difference in the model geometries used was that the tube wall thickness could not be reduced below 1 μm in the FEA model (the FDA model assumes negligible wall thickness). The error between the models was studied for a variety of parameter values, including the percentage of total flow going through the tube, the fluid velocity within the tube, the pressure drop across the tube, the bulk velocity at the tissue inlet and outlet, and the fluid pressure at the tissue inlet. In addition, velocity vector and pressure plots were visually compared. Three tube angles (0° , 10° and 35°) and two tube lengths (100 and 150 μm) were evaluated in this radius comparison. Because the results were insensitive to variations in these parameter values, only the condition using the standard parameter values is presented here.

A final comparison studied the effects of the separation distance between two tubes. The first tube was held at a constant location whereas the second tube was translated in the x direction to achieve varied distances between the outlet of the first tube and the inlet of the second tube. Standard parameter values were used for both tubes, and the outlet of the first tube and the inlet of the second tube were held at the same y value. The error between the models for the same parameter values used above for the single tube geometry was evaluated. Visual comparisons of velocity vector and pressure plots were also made.

5.2.4. Evaluation of Model Predictive Capability

To evaluate the capability of the FDA model in predicting results, two output parameters were assessed over a range of input parameter values. The output parameters in each case were pressure at the tissue inlet and an effective hydraulic permeability for the tissue (i.e. including flow through both the ECM and tubes), which was obtained via Darcy's Law (Eqns. 1-2), with the velocity set to the x velocity at the tissue inlet. Defined this way, the effective permeability is proportional to the inverse of the tissue inlet pressure. These were chosen because they could easily be measured experimentally. The input parameters that were varied included tube density, percentage of bifurcations, ECM anisotropy, tube anisotropy index, and tube length. Tube density was calculated assuming the model represented the projection of a 3-dimensional tissue with a square cross-section. The number of tubes crossing each column (y direction) of nodes was counted and averaged for the middle third of the tissue and normalized to the assumed cross-sectional area. The variation in microvessel densities calculated when using the same number of tubes is noted in Table 5-1. The ECM anisotropy was varied by decreasing the permeability in the y direction. The tube anisotropy index, a measure of tube alignment in the direction of flow, was defined as

$$AI = \frac{\sum L_x}{\sum L_y}, \quad (12)$$

in which L_x is the tube length in the x direction, and L_y is the tube length in the y direction. A higher anisotropy index reflects a higher degree of tube alignment.

For each analysis, all parameters were kept constant aside from the varied

parameter. Standard parameter values are listed in Table 5-1. Each data point represents the average of 6 runs in which the tubes were randomly generated based on an average radius, length and angle relative to the x direction.

5.3. Results

5.3.1. Model Validation.

The FDA model was first internally validated using a single microvessel by varying parameter values independently and assessing the results intuitively. The results examined were the velocity through the microvessel and the average pressure at the tissue inlet. Example velocity vector plots and pressure maps using the standard parameter values are shown in Figure 5-2a-b. Results of varying the velocity at the tissue inlet are shown in Figure 5-2c. The linear relationships indicate that both the velocity through the microvessel and the pressure at the tissue inlet increased by the same factor as the velocity at the tissue inlet was varied. As the ECM permeability decreased, the inlet pressure remained constant near zero until a permeability on the order of 10^{-12} cm^2 , at which point it rapidly increased (Figure 5-2d). Fluid velocity through the microvessel increased as ECM permeability decreased until approximately the same permeability value, at which point further decreases in permeability did not increase the velocity. Variations in fluid viscosity had minimal effects on microvessel flow velocity, but high viscosities led to increased pressures at the tissue inlet (Figure 5-2e). Microvessel radius was varied in a small, physiologically-relevant range (Figure 5-2f). Tissue inlet pressure remained constant across radii, but the fluid velocity in the microvessel decreased slightly

with increasing radius. The angle of the microvessel relative to the x -direction had little effect on either the inlet pressure or the microvessel velocity (Figure 5-2g). Little effect was observed on tissue inlet pressure when the ECM anisotropy (k_{px}/k_{py}) was varied by decreasing k_{py} , but with increasing anisotropy the microvessel flow velocity decreased (Figure 5-2h).

The FEA model was then validated by varying the same parameter values (where possible) using the single microvessel. Example plots of velocity and pressure are shown in Figure 5-3a-b and parametric dependences are shown in Figure 5-3c-g. Linear relationships were observed between both tissue inlet pressure and microvessel velocity and velocity at the tissue inlet in a log-log plot (Figure 5-3c), indicating that the model results were changed by the same factor as the inlet velocity. Pressure at the tissue inlet remained low as ECM permeability increased until a permeability of order 10^{-12} cm², after which the pressure dramatically increased. Velocity through the microvessel initially rose with increasing permeability, and then reached a plateau at a permeability near 10^{-12} cm² (Figure 5-3d). Variations in fluid viscosity had no effect on microvessel velocity, but tissue inlet pressure increased substantially when the viscosity was above 0.0089 P (Figure 5-3e). Variations in the microvessel radius did not affect either pressure at the tissue inlet or microvessel velocity (Figure 5-3f). Microvessel angle had no effect on the pressure at the tissue inlet, and only a minor decrease in microvessel velocity was observed with increasing angle (Figure 5-3g).

5.3.2. Comparison of Model Predictions

The results of parameter value variations (internal validation) between models (Figure 5-2 and Figure 5-3) were compared. The parameters that could be varied in both models included the velocity at the tissue inlet, the ECM permeability, the fluid viscosity, the microvessel radius, and the microvessel angle. Of these, the results in terms of both the pressure at the tissue inlet and the velocity through the microvessel were very similar for most parameters. The largest discrepancy was that microvessel velocity decreased much more with increasing microvessel radius in the FDA model than in the FEA model.

The differences between the FDA and FEA model predictions were quantified for several parameters at a variety of microvessel radii. Several single microvessel geometries spanning several microvessel lengths and orientations were considered. The results for these different microvessels were similar, so only the results using standard parameter values are presented here. The parameters investigated were the velocity through the microvessel, the percentage of the total flow traveling through the microvessel, the pressure difference across the microvessel, and the pressure at the tissue inlet. Although the models were expected to agree more closely as the vessel radius approached 0, an error minimum was observed for all output parameters at a radius of approximately 2.5 μm (Figure 5-4a). The differences at smaller radii were likely due to the fact that the wall thickness could not be made smaller than 1 μm in COMSOL due to meshing limitations. Percent errors of the FDA model for various parameters are listed in Table 5-2. The percent error was below 30%

for all parameters studied, and close to 1% for one parameter (as shown), indicating good agreement. Reducing the node spacing of the FDA model or using higher order finite difference approximations had little effect on the errors calculated (data not shown).

A second model involving two microvessels was also used to compare the FDA and FEA models. Both microvessels were defined by the standard parameter values, and the distance between the outlet of the first microvessel and the inlet of the second microvessel was varied. The velocity vector plots from each model (Figure 5-5a-b) demonstrated reasonable agreement. The percent error between the two models was quantified for the velocity through the downstream microvessel and the pressure at the tissue inlet. The percent error decreased with increased distance between the microvessels but was relatively low for all separation distances (Figure 5-5c).

5.3.3. Evaluation of Model Predictive Capability

The pressure at the tissue inlet and the effective permeability of the tissue (i.e. including flow through both the ECM and microvessels) were computed outputs from the FDA model with randomly generated microvessels while individual parameter values were varied. The percentage of bifurcations, microvessel anisotropy index and the microvessel length had little effect on either output parameter (Figure 5-6a-c). If the microvessels nearly spanned the tissue region (e.g. 230 μm in length), the outputs were affected, as expected. As ECM anisotropy increased, the tissue inlet pressure decreased, and the effective hydraulic conductivity increased (Figure 5-6d). A similar trend was observed with

increasing microvessel density (Figure 5-6e). Sample pressure plots for microvessel densities of approximately 25 and 550 microvessels/mm² are provided in Figure 5-6f-g.

5.4. Discussion

Overall, both intra- and inter-model validation suggested that the FDA model is reasonably accurate for experimentally-relevant parameter values. Internal validation of both models suggested that the microvessel flow velocity remained constant to changes in fluid viscosity and microvessel angle, as expected. Microvessel angle also had no effect on the pressure at the tissue inlet, but at high viscosities (beyond physiological), the pressure increased dramatically from near zero. This result is intuitive, as more viscous fluids would require larger pressures to drive the same flow rate. Microvessel flow velocity decreased with increasing ECM anisotropy, which may at first appear counterintuitive; however, examination of the velocity vector plots shows that fluid from a variety of y positions enters the tube. If flow is retarded in the y direction, less fluid would enter the microvessel. Increases in the inlet velocity were observed to cause proportional increases in inlet pressure and microvessel flow velocity, as expected. One of the more interesting internal validation plots is the one in which ECM permeability is varied. As the permeability was decreased, the microvessel flow velocity increased, which is logical because the ratio of resistance to flow between the microvessel and the ECM was decreasing; essentially the effective permeability of the tissue remained constant. However, near a permeability of 10^{-12} cm², the microvessel velocity reached a plateau, and

the tissue inlet pressure, which had previously been low, increased substantially. This result is also logical because a high pressure will be required to drive flow through a tissue with a low permeability. The microvessel flow velocity plateau is somewhat less intuitive because the ratio of resistance to flow between the microvessel and the ECM was still decreasing. However, examination of the velocity vector plots at relatively high permeabilities indicates that the higher velocity through the microvessel required fluid to be diverted from a farther distance from the microvessel inlet. In the plateau region, it is logical that a balance was established between the decreasing ratio of resistance to flow and the increasing pressure required to divert fluid through the microvessel from further distances. The largest difference in the results of internal validation between models occurred in the radius variation. In both models, the inlet pressure remained constant, but in the FDA model the microvessel velocity decreased with increasing radius, whereas in the FEA model the microvessel velocity was nearly constant. Although the lack of agreement is somewhat disconcerting, the maximum difference is less than two-fold, a difference that may be acceptable for the computational speed enhancement and other benefits of the FDA model.

Validations between the models demonstrated that the FDA model was most accurate for a small range of microvessel radii. The minimum error between models occurred at a radius of 2.56 μm , which is within the physiologic range for capillaries (2.5-4 μm radius for human coronary capillaries;¹⁴⁵ the radii of engineered microvessels are generally higher by several microns but the

physiological range is the target). Therefore, a radius of 2.5 μm was used for all subsequent evaluations. At a radius of 2.5 μm , the error for a variety of model outputs was less than 30%, indicating good agreement. Although, theoretically, the error between models should decrease with decreasing radius beyond 2.5 μm , the microvessel wall thickness could not be decreased below 1 μm in the FEA model. Because the FDA model assumes negligible wall thickness, this could be the source of additional error at very small radii. Additionally, the differences in the mesh size (1 μm) of the FEA model and the node spacing (5 μm) of the FDA model may account for some error.

At microvessel radii near 1.5 μm , the FDA model predicted reverse flow through the single microvessel geometry, which was not corroborated by the FEA model. These results were taken to be inaccurate, so radii near 1.5 μm were removed from randomly generated microvessel geometries by using a small range of radii centered on 3 μm . Reverse flow was also occasionally observed in one outlet portion of a bifurcating microvessel regardless of radius. Attempts were made to validate these results with the FEA model, but geometries resulting in reverse flow could not be recreated in COMSOL due to its limitations in prescribing microvessel bifurcation angle. Because these instances were rare and not necessarily counterintuitive, they were included in randomly generated geometries.

The error between models was also compared for a two microvessel geometry. As the separation distance between the microvessels was decreased, the error increased. However, at a separation distance of 5 μm (equivalent to one

node apart in the FDA model), the difference between models was well under two-fold. In addition, the velocity vector plots substantially agreed. These data suggest that the FDA model is relatively accurate even when the microvessels are in close proximity.

The rationale for developing the FDA model was for use in predicting the morphometric properties of microvessels within engineered tissues exposed to flow, which may be difficult to determine experimentally. With this goal in mind, the tissue inlet pressure and effective tissue permeability, which are both outputs of the model and easily measurable experimentally, were observed as microvessel morphometric parameters were varied. Several of these parameters had no effect on the inlet pressure or the effective permeability. These parameters include the percentage of microvessels containing a bifurcation, the microvessel anisotropy index, and the average microvessel length. These results suggest that the neither measured pressure at the tissue inlet nor the effective permeability can be used to predict any of these microvessel properties. It also suggests, however, that these parameter values need not be known in order to accurately predict other morphometric properties.

With increasing ECM anisotropy (k_{px}/k_{py} , varied by changing k_{py}), the tissue inlet pressure increased and the effective permeability decreased. Previous modeling has indicated that even in tissues with high levels of anisotropy, the permeability only varies approximately 3-fold;¹⁴⁶ therefore permeability differences greater than 5-fold were not assessed. The results suggest that the inlet pressure or the effectively permeability could be used to

predict the ECM anisotropy. However, ECM anisotropy is relatively simple to measure by taking permeability measurements in orthogonal directions. Thus, the main conclusion from this plot is that the ECM anisotropy must be known to predict other morphometric properties.

As microvessel density increased, the inlet pressure decreased and the effective permeability increased. This result suggests that either the pressure or the permeability could be used to predict the density of perfusable microvessels. The FDA model assumes all microvessels are perfusable and since they have negligible radius, the model predictions are independent of non-perfusable microvessels. The density of perfusable microvessels, although extremely important in understanding the flow through the tissue, is extremely difficult to measure experimentally, because histologic examination does not make a distinction between microvessels that are perfusable and those that are not. The slope of the curve suggests that the model would be most accurate in predicting perfusable microvessel densities less than 500 lumens/mm². Although myocardial capillary density is near 2000 capillaries/mm²,⁹ many other native capillary beds have lumen densities within this range, including skeletal muscle (200-300 capillaries/mm²).^{147,148} In addition, only recently have engineered tissues contained microvascular structures nearing 500 microvessels/mm².¹³¹ Therefore, the tissue inlet pressure or the effective permeability could be used to predict the microvessel density of perfused microvessels. A number of other parameters were shown to influence the pressure at the tissue inlet, so these must also be known to make an accurate prediction. These parameters include

fluid viscosity, the fluid velocity at the tissue inlet, the ECM permeability, the degree of ECM anisotropy, and the average microvessel radius and its standard deviation, all of which are relatively straightforward to measure experimentally. Microvessel length must also be known if it approaches the dimension of the engineered tissue; equivalently the dimension of the modeled tissue must be much greater than the length of a microvessel. Additionally, although the predicated tissue inlet pressure values are low, the modeled region represents only a small portion of the tissue; for example, the model would predict pressures in the range of 0.75 to 2.55 mmHg for a tissue 15 mm in length.

If pressure at the tissue inlet cannot be measured precisely enough to make predictions, the residence time of a pulsed tracer within the tissue could be used. Theoretically, the tracer would reside in the tissue for a shorter time with a higher density of perfusable microvessels due to the faster velocities observed through the microvessels than in the ECM. However, this would require the extension of this model to include the species balance (convection and diffusion) equations for the tracer, which is beyond the scope of this work. Such an extension would also be useful in examining the oxygen distribution within the tissue, a prediction extremely relevant to tissue engineering.

Despite being less accurate, the FDA model has many advantages over the FEA model. The main advantage is computational speed: the FDA model computed within several seconds, even for geometries with a large number of microvessels, whereas the FEA model took 15 minutes for the single microvessel geometry, and would be prohibitively long when many microvessels were

present. The FEA model also had several software limitations, including the inability to handle permeability tensors for the study of ECM anisotropy, a limited range of bifurcation angles, and meshing limitations when using small dimensions.

Although the FDA model has been verified to be reasonably accurate and theoretically useful, it has limitations. One limitation is the restricted geometries: microvessels can either be straight or have one bifurcation. Additional bifurcations could be included using the same principles to define pressures at bifurcation points, but this would add coding complexity. A more general model would allow for true networks of microvessels by connecting microvessels that were randomly placed near to each other; this would enable the examination of percolation behavior and is more similar to the way microvessel networks form *in vitro*. Additional work is necessary to address these limitations.

5.5. Tables

Tissue, Fluid and Boundary Parameters for FDA Model	
<u>Parameter</u>	<u>Value</u>
Permeability	9.92 e-11 cm ²
Tissue Length (x-direction)	250 μm
Tissue Width (y-direction)	200 μm
Matrix Anisotropy	1
Node Spacing	5 μm
Viscosity	0.89 cP
X-Velocity at Tissue Inlet	1.33 μm/s
Pressure at Tissue Outlet	0
Defined Microvessels (Validation Geometries with 1 or 2 Microvessels)	
<u>Parameter</u>	<u>Value</u>
Microvessel Length	100 μm
Microvessel Radius	2.5 μm
Microvessel Angle	10°
Randomly Generated Microvessels	
<u>Parameter</u>	<u>Value</u>
Microvessel Radius (Standard Deviation)	3 μm (0.125 μm)
Microvessel Length (Standard Deviation)	100 μm (10 μm)
Microvessel Angle (Standard Deviation)	0 (20°)
Lumen Density	275 (+/- 2.5%)
Percentage Bifurcating Microvessels	50%

Table 5-1.

Standard parameter values used for the FDA model.

Single Microvessel FEA Model	
<u>Parameter</u>	<u>Value</u>
Permeability*	9.92 e-11 cm ²
Tissue Length (x-direction)	250 μm
Tissue Width (y-direction)	200 μm
Matrix Anisotropy	1
Tissue Porosity	0.95
Viscosity*	0.89 cP
Fluid Density	1000 kg/m ³
X-Velocity at Tissue Inlet	1.33 μm/s
Pressure at Tissue Outlet	0
Microvessel Length	100 μm
Microvessel Radius	2.5 μm
Microvessel Angle	10°
Microvessel Wall Thickness	1 μm

Table 5-2.

Standard parameter values used for the FEA model.

5.6. Figures

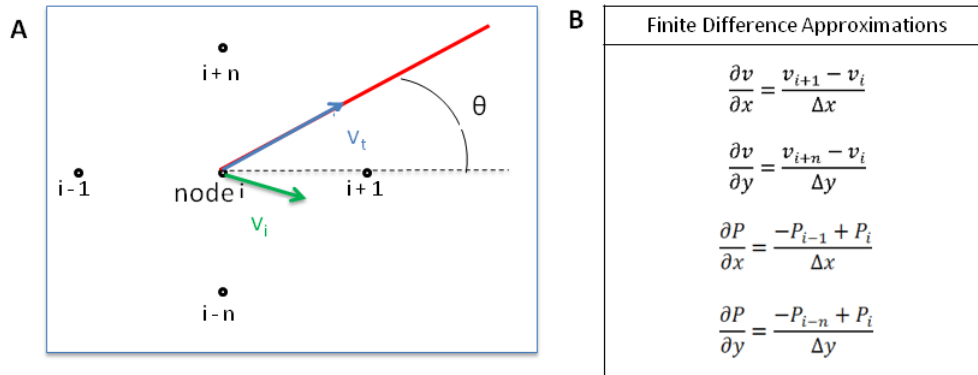


Figure 5-1.

(A) Schematic of a node (i) at which a microvessel begins. The surrounding nodes were labeled $i - 1$ and $i + 1$ in the x direction and $i - n$ and $i + n$ in the y direction, where n is the number of nodes spanning the tissue in the x direction. The microvessel is indicated by the red line, and the blue arrow indicates the fluid velocity in the microvessel (v_t). An ECM velocity (v_i) was also defined at node i , and is indicated by the green arrow. θ represents the angle between the microvessel and the x direction. (B) The finite difference approximations used for the model are listed.

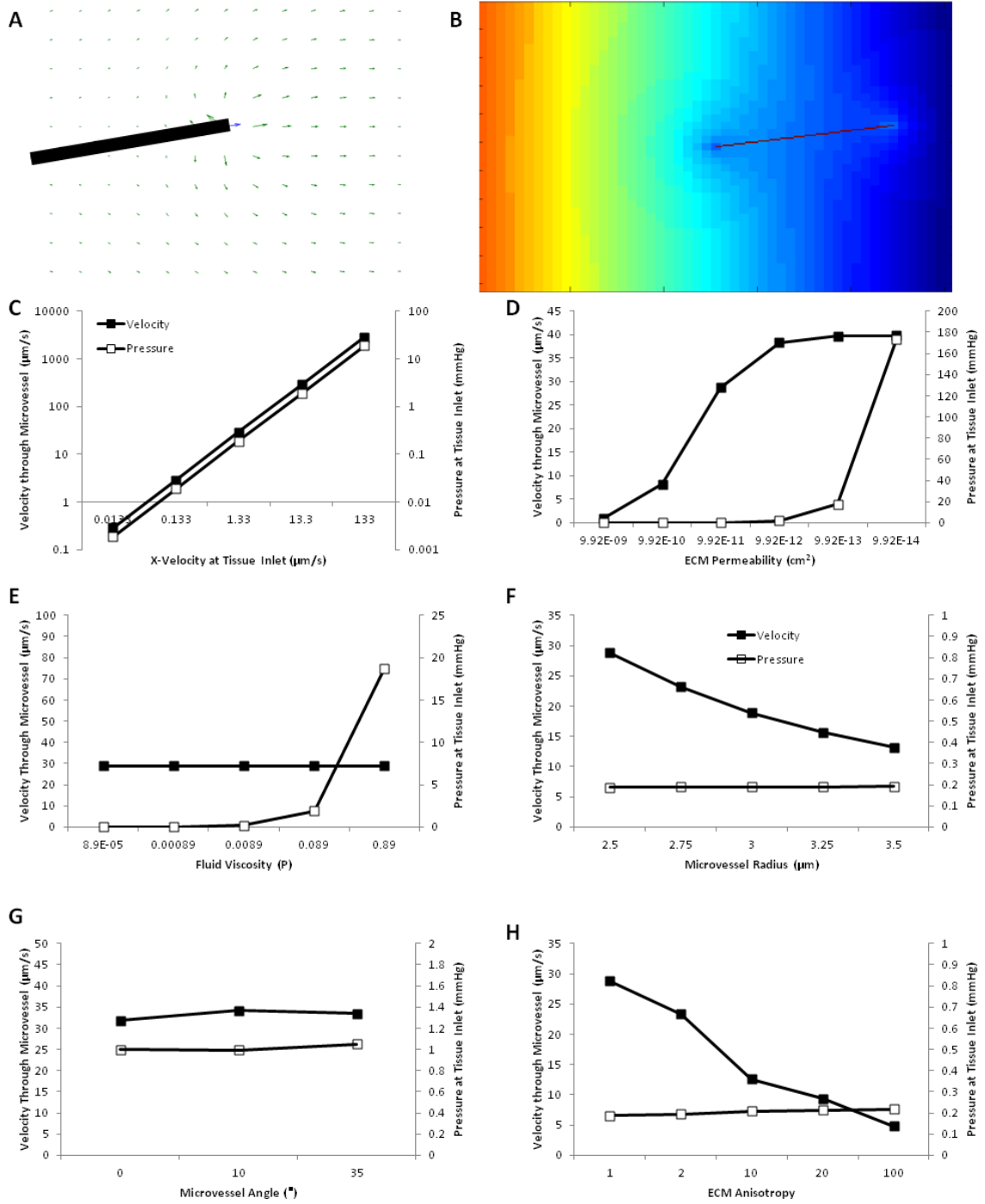


Figure 5-2.

Internal validation of the FDA model using a single microvessel. (A) Velocity vector plot of the outlet of the microvessel (black) under standard conditions. The

green arrows represent ECM velocities, whereas the blue arrow represents the velocity through the microvessel. (B) Pressure map of the entire tissue under standard conditions. The black line represents the microvessel. (C-H) Evaluation of the velocity through the microvessel and the pressure at the tissue inlet as the following input parameters were varied: (C) x velocity at the tissue inlet, (D) ECMmatrix permeability, (E) fluid viscosity, (F) microvessel radius, (G) microvessel angle relative to the x direction, and (H) ECM anisotropy. For each plot, all other input parameters were kept at their standard values.

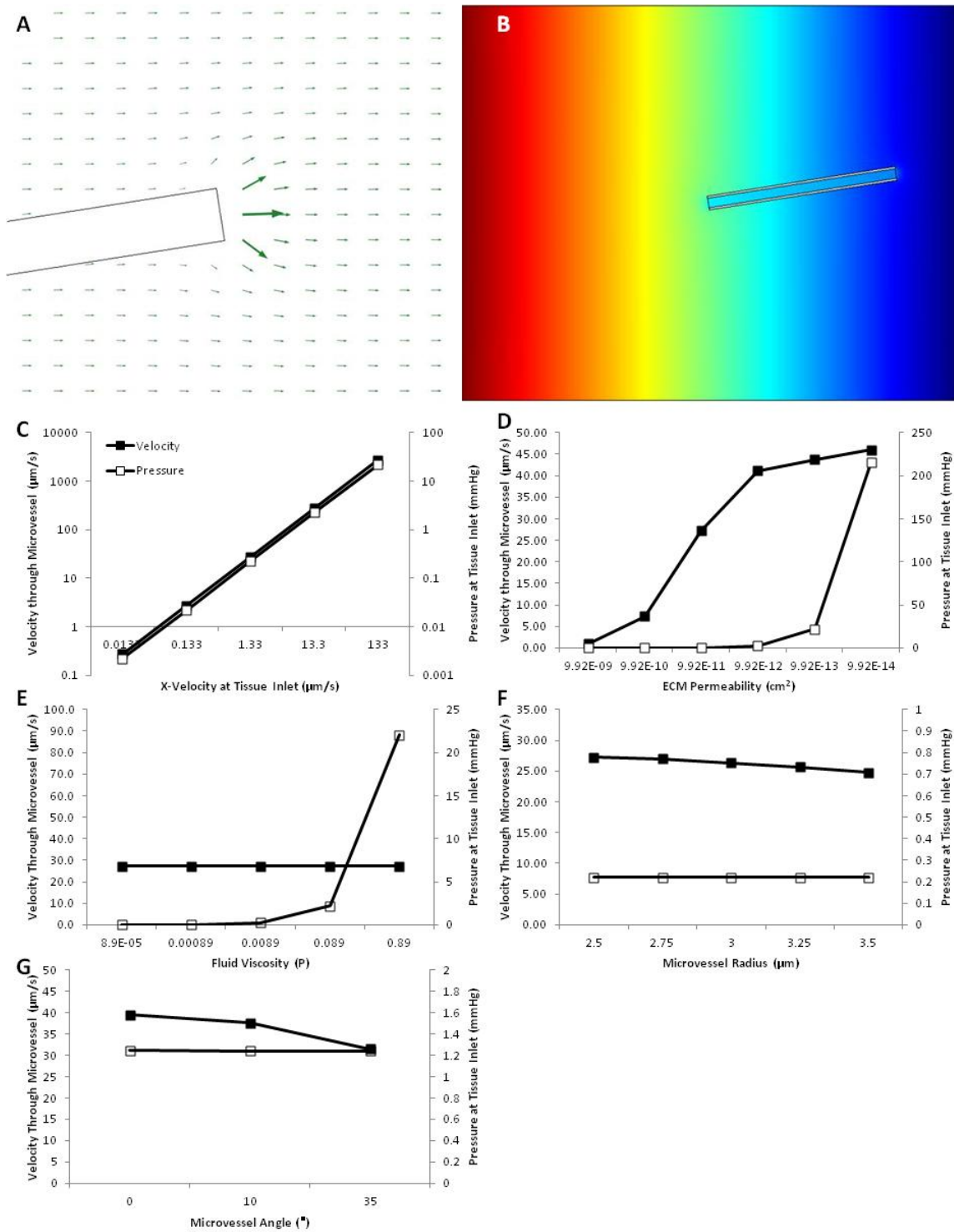
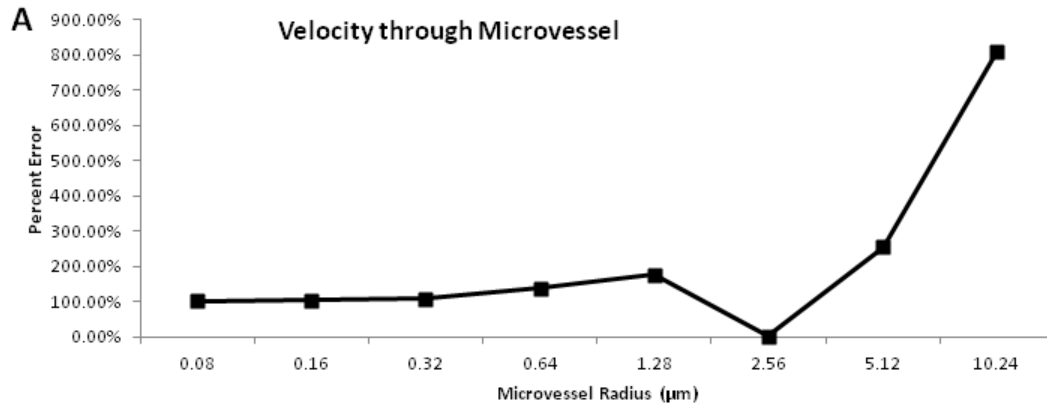


Figure 5-3.

Internal validation of the FEA model using a single microvessel. (A) Velocity vector plot of the region near the microvessel outlet. The arrows indicating the

velocity through the microvessel were removed to more clearly show the ECM velocities. (B) Pressure map of the whole tissue (standard conditions were used). (C-I) Velocity through the microvessel and the pressure at the tissue inlet plotted against the following parameters: (C) x velocity at the tissue inlet, (D) ECM permeability, (E) fluid viscosity, (F) microvessel radius, and (G) microvessel angle relative to the x direction. Within each plot, all other input parameters were held at their standard values.



B

Parameter	Percent Error between FDA and FEA Models (r = 2.56 µm)
Velocity through Microvessel	1.57%
Percentage of Total Flow Traveling through Microvessel	29.73%
Pressure Difference Across Microvessel	19.46%
Pressure at Tissue Inlet	17.50%

Figure 5-4.

Comparison between the FDA and FEA models using a single microvessel. (A) The percent error in the microvessel velocity between the FDA and FEA models for varying microvessel radii. (B) The percent error in a variety of output parameters for a radius of 2.56 µm.

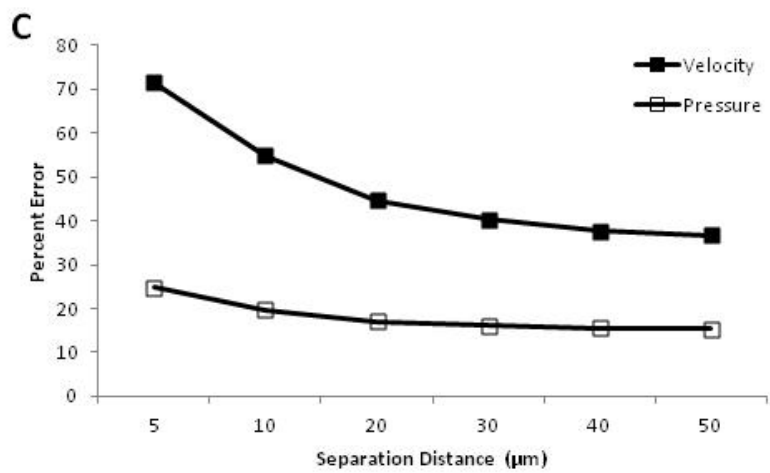
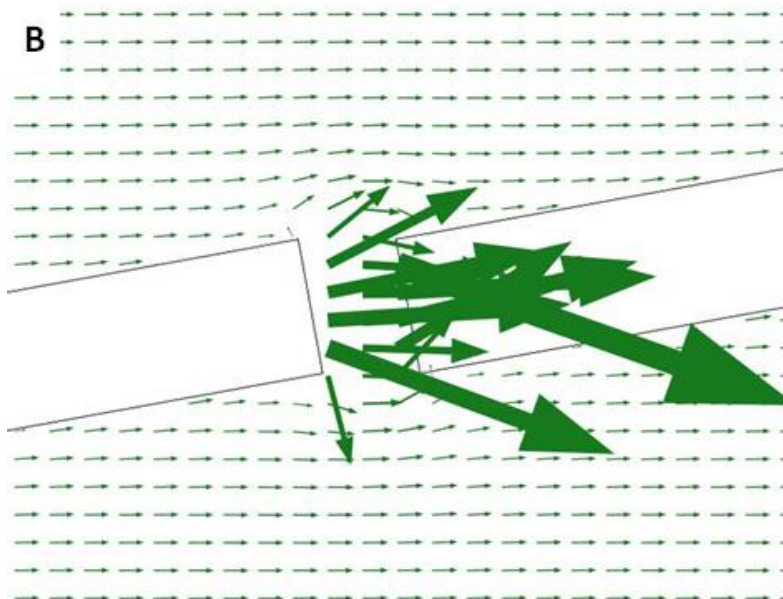
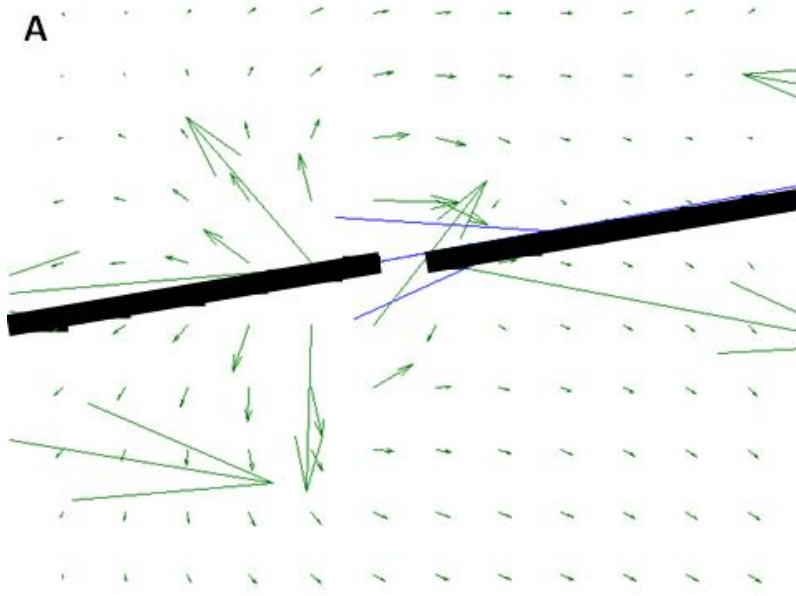


Figure 5-5.

Comparison between the FDA and FEA models using two microvessels. (A) The percent error in the downstream microvessel velocity and pressure at the tissue inlet between the FDA and FEA models for a variety of separation distances between the two microvessels. (B) Velocity vector plot showing the FDA model results for a separation distance of 5 μm . Green arrows represent velocities in the ECM and blue arrows represent velocities through the microvessels. The black lines represent the microvessels. (C) Velocity vector plot results from the FEA model for a separation distance of 5 μm . No velocity vectors for flow within the microvessels are shown so that the ECM velocities can be observed more easily. The white rectangles represent the microvessels.

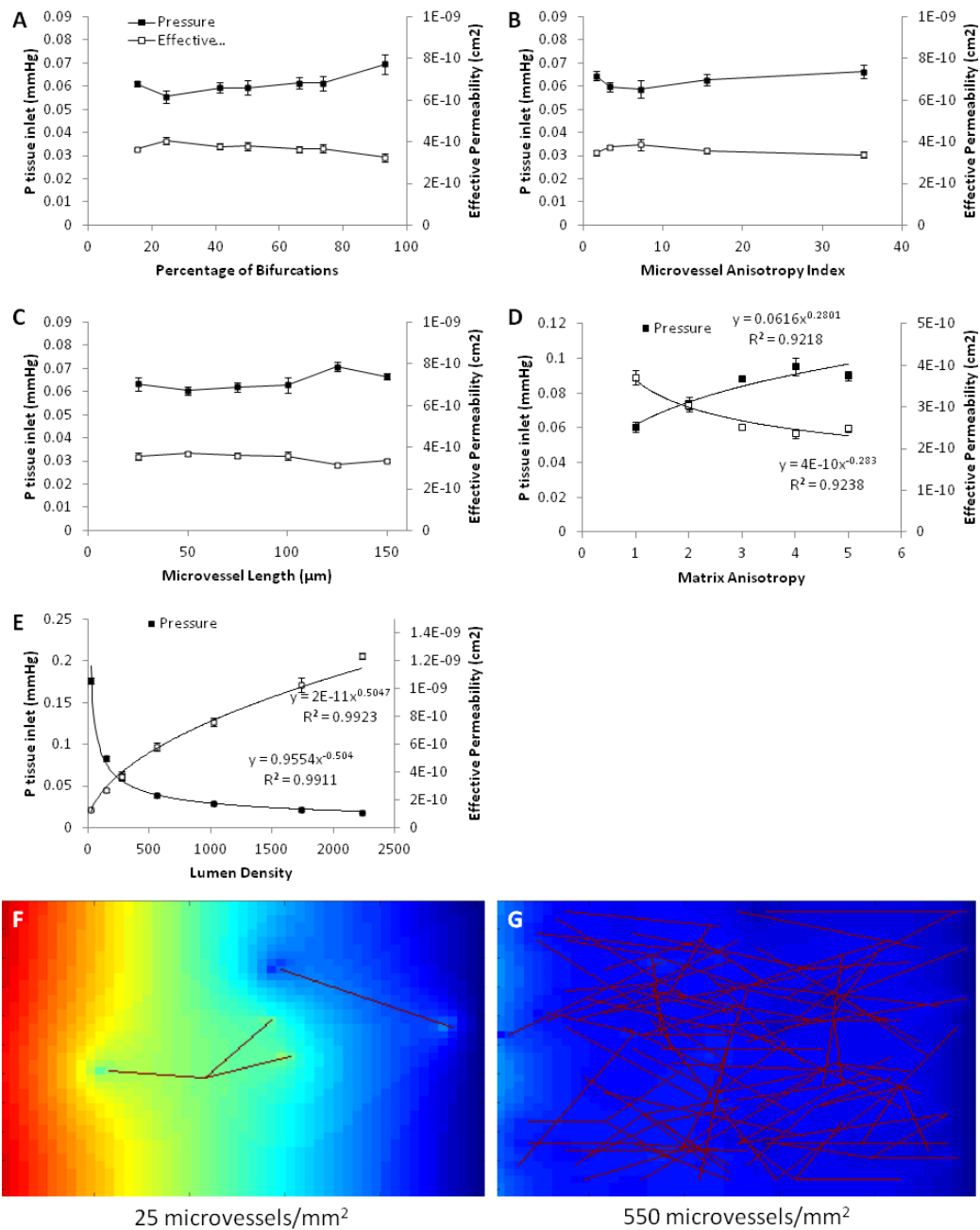


Figure 5-6.

Evaluation of the FDA model predictive capability. Pressure at the tissue inlet and the effective hydraulic permeability are plotted for varying levels of the following parameters: (A) percentage of bifurcations, (B) microvessel anisotropy

index, (C) microvessel length, (D) ECM anisotropy, and (E) lumen density. (D-E) The data were best fit with power equations, which are shown on the plots. (F-G) Example pressure plots for tissues with microvessel densities near 25 (F) or 550 (G) microvessels/mm². The dark lines indicate the location of microvessels. The color scale is the same for both plots.

Chapter 6. Aligned Microvessels with High Lumen Density via Cell-Induced Fibrin Gel Compaction and Interstitial Flow

6.1. Introduction

Co-culture of endothelial cells (ECs) with other support cell types is frequently used in *in vitro* models of angiogenesis and vasculogenesis.^{53,62,120,149–153} These support cells are often fibroblasts, which have been shown to improve angiogenic sprouting⁶² and vessel density¹⁵³ within 3D scaffolds. Although use of these cells has been shown to provide advantages, fibroblasts are not the most logical choice for support cells because they do not associate with vessels *in vivo*. In contrast, pericytes (PCs) are defined by their association with microvasculature.

PCs are mural cells located within the basement membrane of capillaries and in physical contact with multiple ECs.⁴⁶ During physiological angiogenesis or vasculogenesis, PCs are recruited to newly formed microvessels via EC-derived PDGF-BB and HB-EGF^{49,125} and their arrival defines the end of the microvascular “plasticity window,” in which capillaries can undergo growth or regression in response to physiological stimuli such as hyperoxia.⁴⁸ Therefore, PCs are extremely important in stabilizing newly formed capillaries. This stabilizing effect is at least in part due to the production of basement membrane (e.g. collagen IV and laminins) by PCs in contact with ECs.⁴⁷ PC production of the capillary-stabilizing molecule angiopoietin-1 (Ang-1) may also contribute.⁵¹ Studies of PDGF and PDGFR- β knockout mice indicate that the presence of PCs inhibits EC proliferation and maintains capillary diameter. The knockout mice initially had

normal microvasculature formation, developing hemorrhages perinatally, suggesting that PC recruitment is only involved in microvessel stabilization, not formation.^{50,126}

Recent work has shown PCs to induce microvascular network stabilization events in a vasculogenic model involving human umbilical vein ECs (HUVECs) in a type I collagen gel.⁵⁶ PCs were recruited to the forming microvessels and stimulated the production of basement membrane proteins including collagen IV and laminins. PC recruitment and basement membrane production are considered the two indicators of microvessel maturity and stability *in vivo*.¹⁵⁴

The work reported here extends these findings of microvascular maturation induced by PCs to a system involving a type of circulating ECs, blood outgrowth ECs (BOECs), in fibrin gel. This extension is key to moving from using such vasculogenic models for studying EC biology to creating functional microvasculature to deliver oxygen to engineered tissues, as both BOECs and fibrin are more suitable for tissue engineering than HUVECs and collagen I. BOECs are potentially autologous because they are isolated from blood mononuclear cells. They have a high proliferative potential, are positive for myriad EC markers and are negative for monocyte markers.⁵⁷ Likewise, fibrin is a better scaffold for tissue engineering than collagen I because it induces extracellular matrix (ECM) remodeling by entrapped tissue cells,⁴² yielding a stronger tissue, which will be required for the production of engineered tissues for human use.

Most previous work on engineered microvasculature has been in isotropic systems,^{53,54,56} and there is, as yet, no report of an engineered tissue with a microvasculature that is perfusable *in vitro*. However, an aligned network would be advantageous both in terms of mimicking aligned native tissue (e.g. myocardium⁶⁵), and in terms of establishing flow through engineered microvasculature, as alignment creates natural inlet and outlet sides. Recent work has shown that contact guidance in response to aligned matrix fibers is sufficient to align sprouts from BOEC spheroids, and that cell-induced gel compaction resulted in both aligned fibers and sprouts.⁶³ We now extend this work to engineered vasculogenic networks, formed by self-assembly of dispersed BOECs, showing that cell-induced gel compaction also aligns such networks and that the benefits of PC stabilization (i.e. basement membrane deposition and prevention of network regression) are maintained after alignment.

Finally, in many engineered tissues, such as myocardium, a high capillary density will be required to support the highly metabolic cells. Indeed, in native adult myocardium, the average capillary density is 2000 capillaries/mm², and the average intercapillary distance is around 20 μm .^{8,9} To date, no engineered microvascular network has achieved this density. Reported values range from 2-100 lumens/mm² for networks prior to implantation,^{149,152,155,156} although not all reports of engineered microvessels quantified cross-sectional lumen density. Total capillary density increases after implantation, with most studies reporting 200-600 lumens/mm².^{53,124,157} The best capillary density reported was by Shepherd and colleagues, who observed 1400 lumens/mm² after entrapping

microvessel fragments in collagen I gel, culturing them for 7 days and implanting them over myocardial infarcts for 28 days in mice.¹⁵⁶ In the studies reported here we demonstrate vastly increased microvessel density using the same compaction technique used to achieve aligned microvessels, attaining values similar to reported post-implantation values. However, our preliminary studies indicated that even after compaction the microvessels were not dense enough. Therefore, we examined interstitial flow as a method to increase capillary density further.

Interstitial flow occurs physiologically due to pressure differences between the vascular and lymphatic systems and is estimated to occur at flow rates of 0.1-2 $\mu\text{m/s}$.¹⁵⁸ Previous reports have suggested that interstitial flow through engineered tissues containing ECs at superficial velocities of 0.17-15.8 $\mu\text{m/s}$ improves microvessel density or EC sprout length, and evidence indicates that a synergy exists between VEGF stimulation and interstitial flow, leading to improved outcomes.^{118,119,123,159} The shear stresses applied via interstitial flow at these velocities were quite low (on the order of 0.01 $\text{dyne}\cdot\text{cm}^2$), leading the previous investigators to attribute improvements to local morphogen gradients created by flow rather than shear stresses.¹²³ In addition to the improved microvessel density, some alignment of microvessels in the direction of interstitial flow was observed in an initially isotropic construct.¹²³ However, these results were achieved by applying flow throughout the culture period, beginning prior to any sprout or microvessel formation; it is unclear from previous work whether or not interstitial flow can modulate an existing network. Our results demonstrate

that interstitial flow improved lumen density without affecting other network properties in an existing engineered microvascular network.

The permeability of EC monolayers is affected by shear stresses. Acute shear stress (hours) on the order of 1-10 dyne/cm² decreased electrical impedance and increased permeability of EC monolayers.¹⁶⁰⁻¹⁶³ Chronic shear stress (days), however, reduced permeability.¹⁶³ The acute effect appears to be due to transient rearrangement of both tight and adherens junctions,¹⁶⁴ whereas improvement of tight junction functionality explains the chronic effect.^{165,166} However, the majority of studies in this area have observed EC monolayers under laminar flow; it is unclear if the results hold for engineered microvessels exposed to interstitial flow. Additionally, the shear forces applied in this study are 2 orders of magnitude lower than those reported in the literature, which may not be large enough to affect the permeability. The data presented here suggest that chronic low shear stress can decrease the permeability of engineered microvessels.

Shear forces are also known to affect the arterial or venous phenotype of ECs, as indicated by ephrin levels. EphrinB2 and EphB4 have been used to characterize arterial and venous identity both in development^{167,168} and in mature cells.^{169,170} EphrinB2 is a reliable marker of arterial endothelial cells, and may also be expressed on vascular smooth muscle cells, while its receptor EphB4 is used to identify venous endothelial cells.¹⁷¹ In addition to larger diameter vessels, even capillaries may have arterial or venous properties.¹⁷² Ephs and ephrins help regulate angiogenesis through involvement with endothelial cells, pericytes, and

vascular smooth muscle.¹⁷³ For example, activation of EphB4 by ephrinB2 increased endothelial progenitor cell (EPC) recruitment to sites of neovascularization in a hindlimb ischemia model.¹⁷⁴ Additionally, several groups have reported the importance of ephrinB2 for mural cell association with microvessels.¹⁷⁵ With the generation of an engineered microvasculature, the influence of flow on endothelial cell maturation towards an arterial or venous fate is of interest. The influence of shear stress on ephrinB2 expression is dependent on cell type, and has not yet been investigated in BOECs. In the case of stem and progenitor cells, shear stress increases ephrinB2 expression. For example, shear stress increased ephrinB2 protein and mRNA expression in ES cell-derived VEGFR2+ cells while EphB4 mRNA decreased.¹⁷⁶ When EPCs were subjected to shear stress, ephrinB2 mRNA (along with several other arterial endothelial markers) and protein increased, while EphB4 mRNA decreased.¹⁷⁷ In the case of more mature cells, shear stress has the opposite effect. When human endothelial cells (both HUVECs and human coronary artery ECs) were subjected to arterial levels of shear stress, ephrinB2 mRNA was down-regulated. However, venous levels of shear stress did not have an effect.¹⁷⁸ However, again previous work has examined EC monolayers rather than engineered microvessels, so it is unclear if the effects of shear would be the same. The data presented here show that ephrinB2 levels are reduced in response to shear stresses in engineered microvessels.

These studies have examined the effects of cell-induced gel compaction and interstitial flow on the characteristics of engineered microvasculature.

Constructs were formed in a custom chamber that enabled gel compaction followed by interstitial flow. Constructs were exposed to one of two rates of interstitial flow for 3 or 6 days, and compared to both time-matched and baseline controls. A variety of microvascular network properties were examined including lumen density, mural cell recruitment, basement membrane deposition, and arterial/venous phenotype.

6.2. Methods

6.2.1. Cell Culture

Human blood outgrowth endothelial cells (hBOECs) were supplied by Dr. Robert Hebbel at the University of Minnesota. hBOECs were cultured in type I collagen-coated flasks in “hBOEC medium,” which consisted of EGM-2 (Lonza) with an additional 8% FBS and 1% penicillin-streptomycin. Passages 9-10 were used for these experiments.

GFP-labeled human brain pericytes (PCs) were provided by Dr. George Davis at the University of Missouri. They were cultured in gelatin-coated flasks in DMEM with 10% FBS and 1% penicillin-streptomycin. Passages 6-8 were used for these experiments.

6.2.2. Construct Preparation

Constructs were cast in custom 20 x 4.8 mm rectangular ultem wells with rounded corners (Figure 6-1a). At either end of the rectangle, a hole was made, and a glass capillary tube (1 mm outer diameter, 0.58 mm inner diameter) was inserted. The end of each capillary tube inside the well was flared to a diameter

of 2 mm. At casting, hBOECs and PCs were mixed with a solution of fibrinogen in HEPES-buffered saline, M199 and three growth factors: stromal-derived factor 1 α (SDF-1 α), stem cell factor (SCF) and interleukin-3 (IL-3). Thrombin was then added, and the solution was pipetted into the wells. The 400 μ l gel filled the bottom of the well and covered the glass capillary tubes. Final construct concentrations were 2.5 mg/ml fibrin, 1.25 U/ml thrombin, 62% v/v M199, 200 ng/ml SDF-1 α , 200 ng/ml SCF, 200 ng/ml IL-3, 2 million/ml hBOECs, and 0.4 million/ml GFP-labeled PCs. After gelation for 30 minutes at 37°C, the bottom of each well was removed, and the constructs were covered with hBOEC medium, enabling nutrient transport from both sides. This was required because preliminary work showed cell death near the bottom of the well if medium was provided only on the top of the construct. After 5 days of culture, some constructs were harvested, and others were detached from the edges of the well using dental picks. The glass capillary tubes were pushed inward slightly so that the constructs were only adherent to the glass. These glass tubes served to anchor the gel during compaction of the fibrin gel and alignment of the fibrin fibrils (Figure 6-1b-c). Control constructs were harvested at days 5, 8, 11, and 14 (n=3).

6.2.3. Application of Interstitial Flow to Aligned Constructs

On day 8 of culture, aligned constructs were embedded in 5% agarose gel, which had a permeability that was 3 orders of magnitude lower than the constructs. The well top and bottom were added and screwed down tightly to create a fully enclosed chamber. The glass capillary tubes were then connected

to a syringe pump (Harvard Apparatus) and flow of hBOEC medium begun. The presence of the agarose gel prevented fluid from exiting the tissue. Flow rates of 0.015 $\mu\text{l}/\text{min}$ (“low”) and 0.105 $\mu\text{l}/\text{min}$ (“high”) were used, corresponding to superficial velocities of 0.33 $\mu\text{m}/\text{s}$ and 2.33 $\mu\text{m}/\text{s}$, respectively. These flow rates were chosen because they fit within the range of shear stress conditions previously shown to improve lumen formation in engineered microvasculature.^{118,119,123,159} Constructs (from 3 separate castings; n=3), including controls that were not embedded in agarose or exposed to flow, were harvested at days 11 (3 days of flow) and 14 (6 days of flow).

Approximately 24 hours prior to the cessation of flow, gold nanoparticles (GNP; 15 nm diameter; Nanoprobes) were introduced to the inlet flow to evaluate the fluid path through the tissue. A 30 gauge needle was used to inject a concentrated GNP solution into the silastic tubing just proximal to the inlet glass capillary tube. The injection site was covered with sterile vacuum grease to prevent leakage.

6.2.4. Hydraulic Conductivity Measurement

Day 8 constructs (n=3) were embedded in 5% agarose gel, sealed within the chamber, and connected to a flow circuit as described above, except that an in line pressure transducer (Harvard Apparatus) was placed immediately proximal to the construct. Flow was begun and pressure readings were taken every second until steady state was achieved. Steady state pressure and flow rate were compared for 3 flow rates on 3 separate constructs, and the hydraulic conductivity of each construct was calculated from Darcy’s Law

$$-v = K_p \nabla P, \quad (1)$$

where v is velocity, K_p is hydraulic conductivity, and P is pressure. The hydraulic conductivity, K_p , which depends both on tissue properties and fluid viscosity, is related to the hydraulic permeability, k_p , which is a property of the tissue only (including cellular components), by the equation

$$k_p = K_p \mu, \quad (2)$$

where μ is the fluid viscosity.

6.2.5. Viscosity Measurement

The viscosity of hBOEC medium at 37°C was measured using a cone and plate viscometer according to the manufacturer's instructions. Briefly, hBOEC medium was maintained at 37C via a circulating water bath, and the viscosity was measured at three shear rates. Four separate samples of hBOEC medium were tested.

6.2.6. Estimation of Shear Stress

The shear stress experienced by the ECs was estimated using a formula derived by Wang and Tarbell:¹⁷⁹

$$\tau = B \frac{\mu Q}{A \sqrt{k_p}}, \quad (3)$$

where τ is shear stress, μ is fluid viscosity, Q is volumetric flow rate, A is construct cross-sectional area, k_p is the effective hydraulic permeability of the construct, and B is a factor that depends on the volume fraction of the cells. When the volume fraction of cells is negligible, B is essentially 1; however, after compaction the cell volume fraction in the aligned constructs is relatively high, so

in this case the presence of cells could not be ignored. Therefore, the volume fraction of cells was estimated using the initial cell concentration, the reduction in construct volume following compaction, and assuming the cells took up the same volume as spheres of 10 μm diameter. The parameter B was then estimated based on the equation specified by Wang and Tarbell:¹⁷⁹

$$B = \frac{4}{\pi} \frac{(1-0.319285C^2-0.043690C^4)}{\sqrt{(1-C-0.305828C^4)(1+C-0.305828C^4)}}, \quad (4)$$

Where C is the volume fraction of cells.

6.2.7. Histology/Image Analysis

At the day of harvest, constructs were fixed in 4% paraformaldehyde and frozen in OCT tissue embedding medium. Longitudinal sections (4 μm thick) were taken, as well as cross-sections (9 μm thick). Cross-sections were taken from three construct regions (inlet, middle, and outlet; Figure 6-2b) to assess variations in hBOEC microvessel properties along the length of the constructs, which could be caused by flow-induced morphogen gradients. Care was taken to ensure that sections from the inlet and outlet regions were taken from compacted regions rather than the uncompacted regions immediately adjacent to the glass capillary tubes.

Cross-sections were immunostained with an antibody for CD31 (Dako) and imaged at 20x using confocal microscopy (Zeiss). A custom Matlab code (See Chapter 3) detected lumens, defined as dark areas completely surrounded by CD31 positive staining. The program automatically thresholded each image, and allowed for user input to correct any obvious errors. For example, some lumens were surrounded by CD31 staining that was in part dimmer than the rest,

so that the thresholded image contained most of the ECs surrounding the lumen, but not all of it. This was corrected by drawing a line on the thresholded image to connect the CD31 staining. The program then after processing produced a final lumen image, from which a user could delete lumens if necessary. For example, when EC structures were in close proximity, the program occasionally recognized the space between structures as lumens. The program then used the updated lumen image and output various parameters of interest, including microvessel density (number of lumens per square millimeter), average lumen area and structure density (number of CD31+ structures per square millimeter). The analysis code also detected cell density based on Hoechst 33342 staining and determined the level of recruitment of the GFP-labeled pericytes. A PC was considered recruited if any part of it was co-localized with or immediately adjacent to a microvessel. The results of 6 images were averaged for each sample.

Cross-sections were also stained using antibodies for collagen IV, laminin, and ephrinB2 using standard immunofluorescence protocols. EphrinB2 staining and imaging was completed by Jessica Dries-Devlin, a post-doctoral fellow. Sections were imaged on an inverted Zeiss confocal microscope, and 3 images were taken per sample using a 20x objective. Images were analyzed using a custom Matlab script in which the total intensity of fluorescent staining corresponded to a given level of ECM deposition (collagen IV and laminin) or protein expression (ephrinB2). Basement membrane staining data were normalized to the average non-lumen area of each sample, as differences were

seen in total lumen area between conditions. Because both PCs and BOECs expressed ephrinB2, the co-localization of ephrinB2 staining and the GFP-labeling of PCs was used to separate expression levels for each cell type. The BOEC ephrinB2 expression was normalized to the fraction of sections stained positively for CD31. Serial sections were used to obtain the CD31 fraction values; the average CD31 fraction value for each construct was used for normalization.

Longitudinal sections of aligned constructs were stained with the CD31 antibody (Dako) and images were taken using a 20x objective on an inverted Zeiss confocal microscope. The average angle and length of each microvessel was quantified using a custom Matlab code. An anisotropy index for each image (n = 6 per sample) was defined as the ratio of the average x-component of length to the average y-component of length, and was used as a measure of microvessel alignment.

Additional longitudinal sections were stained with HQ Silver (Nanoprobes), which deposited silver particles on the GNP, enlarging them so that they were visible under transmitted light with high magnification. Although only the samples exposed to interstitial flow contained GNP, control samples were also stained as a negative control.

6.2.8. Endothelial Barrier Function Assessment

Endothelial barrier function was assessed using GNP in control constructs at days 8 and 11, as well as low flow constructs at day 11. Constructs (n=3) were embedded in agarose, and a GNP solution pumped into the constructs at a flow rate of 1 $\mu\text{l}/\text{min}$ (22 $\mu\text{m}/\text{s}$) for 30 minutes. Flow of GNP was required due to the

presence of a cell layer on the surface of day 11 control constructs which prevented diffusion of GNP into the constructs from a bath. Although this was not ideal due to the potential effects of acute shear stress, all constructs experienced a large step increase in shear stress, and flow was stopped for 30 minutes in low flow constructs prior to the flow of GNP. Constructs were then fixed, frozen, sectioned longitudinally, and stained with HQ Silver as above. Because the constructs were not at steady state, only lumens at a defined distance from the inlet were analyzed.

6.2.9. Fibril Orientation

Fibrin fibril orientation was determined by polarized light imaging.⁸⁷ Samples were placed between two quarter-wave plates, and images taken through the plates while one plate rotated. The images were processed using a custom Matlab script to determine the average birefringence (a measure of fibril alignment) of each construct. Optical density was also measured from these images by averaging the pixel intensity of the region of interest.

6.2.10. Cross-sectional Area Measurements

The thickness of tissue constructs was measured using a linear variable differential transformer, in which the height of a pin correlated with the voltage output of a multimeter. A second multimeter was connected to a pressure transducer. The construct was placed on the stage and the pin lowered until it touched the construct (as indicated by the pressure transducer output). The voltage (height) of the first multimeter was recorded and compared to that of a baseline measurement of the voltage (height) of the stage. Three measurements

were averaged for each construct. The width of each construct at the locations of the thickness measurements was measured with a caliper.

6.2.11. Statistics

Data from days 11 and 14 were analyzed in Minitab using two-way ANOVA with Tukey post-hoc tests. Comparisons between all control conditions (days 5, 8, 11 and 14) were made using one-way ANOVA with Tukey post-hoc tests. Data from flow conditions was compared to day 8 values using one-way ANOVA with Dunnett post-hoc tests. In comparing data from different construct regions, two-way ANOVA with Tukey post-hoc tests was used for data from days 11 and 14. Data from days 5 and 8 were analyzed separately with one-way ANOVA with Tukey post-hoc tests. In all cases, p values of less than 0.05 were considered significant.

6.3. Results

Figures 2 and 3 detail the effects of compaction and interstitial flow on microvessel characteristics. Representative images of longitudinal and cross sections (from the center of the constructs) stained for CD31 are shown in Figure 6-2c-j and Figure 6-3a-h, respectively.

6.3.1. Cell-induced gel compaction results in aligned fibrils and aligned microvessels and increases lumen density.

Uncompacted constructs demonstrated weak fiber alignment as observed via alignment mapping, whereas strong fiber alignment in the longitudinal direction was observed in compacted constructs (Figure 6-2a-b, k). Longitudinal

sections (Figure 6-2c-e, h, l) showed that the BOEC microvessels were also highly aligned longitudinally in compacted constructs.

Cross-sections (Figure 6-3a-c, f) revealed a decrease in lumen size with compaction. Assuming circular lumens, the mean lumen diameter was 14 μm for uncompact constructs and 7 μm for compacted constructs.

The lumen density of day 8 constructs (after 3 days of compaction) was equivalent to that of day 5 constructs (prior to gel compaction; Figure 6-3j), despite the fact that the density of CD31+ structures was increased (data not shown). After further culture, at days 11 and 14, the lumen density of control constructs was increased over both day 5 and day 8 controls. Using the measured construct cross sectional areas and assuming all of the lumens present in the day 5 constructs would be present in the day 8 constructs, the lumen density of compacted constructs was predicted to be 1285 lumens/ mm^2 .

6.3.2. Low interstitial flow increases microvessel lumen density while maintaining other microvessel properties.

Lumen density, as measured in cross sections from the center of constructs stained for CD31, increased with low interstitial flow over control at both days 11 and 14 (Figure 6-3j). This increase was not seen with high interstitial flow. Lumen density remained constant within conditions between days 11 and 14, and lumen area was the same between compacted constructs (Figure 6-3k).

Some differences in cell number between flow conditions were observed, although no main effects of day or flow existed (Figure 6-3l). Pericyte density was

substantially reduced in both flow conditions (Figure 6-3m), but the fraction of the section stained positively for CD31 (indicative of EC density) did not vary between the conditions yielding compacted constructs, which includes all of the day 8, 11 and 14 conditions. Pericyte recruitment remained constant at 30-35% among all conditions (Figure 6-3n).

Both fibril and microvessel alignment remained constant among all conditions yielding compacted constructs, regardless of flow condition or time point (**Error! Reference source not found.k-l**). Birefringence values were near 5, and AI values were near 5, both indicating high levels of alignment. Among constructs exposed to low flow for 3 days (day 11), lumens extending greater than 200 μm in the plane of the section were frequently observed.

6.3.3. High levels of basement membrane were produced by the cells.

Figure 6-4a-h show representative images of laminin staining of cross-sections from construct centers. The total fluorescent intensity per non-lumen area was quantified from images of both laminin and collagen IV staining (Figure 6-4i-j). For both basement membrane proteins, staining intensity was decreased with interstitial flow (for both flow rates) in comparison to time-matched controls. However, visual inspection of the images suggests that the higher basement membrane levels in the controls are due to increased levels of laminin and collagen IV in the interstitium, rather than within the perivascular region.

6.3.4. Microvessel properties varied along the length of the construct.

Variations in some network properties were observed in cross sections taken from the inlet, middle and outlet regions of the constructs. At day 11, the

lumen density was substantially higher in the middle region than in either the inlet or outlet region for all conditions (Figure 6-5a), but the average lumen area did not depend on position (Figure 6-5b). At day 14, both lumen density and lumen area were increased in the middle region (data not shown). Despite the variation in lumen density across tissue regions, low interstitial flow increased lumen density within each region. In addition, when data from all regions were combined for flow conditions and their time-matched controls, an increase in lumen density was still observed with low interstitial flow. Interestingly, at days 5 and 8, no differences in lumen density (Figure 6-5c) or lumen area (data not shown) were observed between regions. PC recruitment, matrix alignment and tissue optical density did not depend on position at any time for all conditions.

6.3.5. EphrinB2 expression increases over time in the absence of flow and is reduced in the presence of flow.

Images of ephrinB2 expression are shown in Figure 6-6a-b and the ephrinB2 expression of BOECs (obtained by normalizing BOEC ephrinB2 intensity to CD31+ area fraction data shown in Figure 6-3i) is quantified in Figure 6-6c. The data show that ephrinB2 expression in BOECs increased over time in control constructs, and that the application of low interstitial flow reduced BOEC ephrinB2 expression.

6.3.6. Low interstitial flow increased endothelial barrier function.

Fluid flow through the constructs was tracked using GNP added to the perfusate during interstitial flow. GNP were observed throughout the interstitium in longitudinal sections, indicating that fluid was traveling through the constructs

rather than channeling between the constructs and the agarose gel. However, GNP were rarely observed within lumens. This observation prompted an experiment to test the endothelial barrier function after flow exposure. Constructs exposed to low flow for 3 days as well as controls at days 8 and 11 were exposed to a solution containing GNP, and the number of GNP present within lumens at the same distance from the construct inlet (the input location of the GNP solution) was counted. Lumens within both control constructs contained substantially more GNP than those within constructs exposed to low flow, which rarely contained GNP (Figure 6-7).

6.3.7. Cells experienced low levels of shear stress during interstitial flow.

The viscosity of the BOEC medium was measured with a cone and plate viscometer at 37°C, yielding an average viscosity of 0.89 cP. Construct hydraulic conductivity was measured using a syringe pump to control flow rate and an in-line pressure transducer to measure pressure just proximal to the construct. Average hydraulic conductivity was then calculated from Darcy's Law (Eqn. 1) to be $1.83 \times 10^{-5} \text{ cm}^2 \cdot \text{mmHg/s}$. This hydraulic conductivity was converted to a hydraulic permeability via Eqn. 2 for use in Eqn. 3. The final volume of each construct was calculated by measuring the thickness and width of each construct after fixation, and assuming the construct length was 1.5 cm. The average thickness of compacted constructs was 627 μm , and the average width was 1.26 mm, yielding a cross-sectional area of 0.0075 cm^2 , and a volume of 0.0112 cm^3 . These values corresponded to a cross-sectional area after compaction that was 10% of the original.

Due to the relatively high concentration of cells in the compacted constructs, the parameter B of Eqn. 3 was estimated using Eqn. 4. To obtain the volume fraction of cells, each cell was assumed to take up the volume of a sphere 10 μm in diameter. Using the initial cell concentration, 2.4 million/ml, the initial construct volume (400 μl), and the final measured volume of the construct, 0.0112 cm^3 , the cell volume fraction was calculated to be 0.045, and Eqn. 3 yielded a value of 1.274 for the parameter B.

The above parameter values were then substituted into Eqn. 3 along with the volumetric flow rates to estimate shear stresses on the cells. For low flow (0.015 $\mu\text{l}/\text{min}$), shear stress was 0.033 (+/- 0.016) dyne/cm^2 , and for high flow (0.105 $\mu\text{l}/\text{min}$), shear stress was 0.23 (+/- 0.12) dyne/cm^2 .

The COMSOL model of flow around a cylinder embedded in porous medium indicated that the shear stress was 0.012(+/-5.7 x 10⁻⁴) dyne/cm^2 for low flow and 0.056 (+/- 4.1 x 10⁻³) dyne/cm^2 for high flow. These values are 3-fold lower than those estimated above; the true shear stress experienced by the cells is likely between the estimated values.

6.4. Discussion

A major finding of this work is that cell-induced compaction can be used to align microvessels in a vasculogenic model (previous work had shown this to be possible in an angiogenic model⁶³). Strong microvessel alignment not only mimics native microvasculature (e.g. myocardium⁶⁵), but also provides natural inlet and outlet sides of the network for flow. In addition to producing aligned microvessels, construct compaction provided a number of other improvements to

the BOEC microvessels. Compaction caused a reduction in average lumen size, placing the diameter within the typical coronary capillary range of 5-8 μm .¹⁴⁵ In addition, both the CD31+ structure density and the lumen density increased with compaction. Although the CD31+ structure density increased quickly, present at all time points after compaction, lumen density increase was delayed, only present at days 11 and 14. These results suggest that initially compaction caused some lumens to collapse, but once compaction had subsided, the lumens were re-established. It is clear, however, that only approximately a third of the lumens were re-established with compaction alone, based on the predicted lumen density. Previous studies suggested that flow can induce alignment;¹²³ however, increased alignment with flow was not observed here. This may merely indicate that compaction and associated fibrin fibril alignment provided a much stronger alignment effect via contact guidance, and that the additional alignment produced by flow was either present but negligible or was not present due to the fact that the fibrils and cells were highly aligned prior to the onset of flow. The fact that the microvessel anisotropy index was above 1 for isotropic samples is likely due to the fact that the anisotropy index was defined relative to the average angle of microvessels in that image. This was necessary because it was impossible to image all of the sections with the longitudinal axis of the construct at the same angle. Because the microvessel density was low in the isotropic samples, one long microvessel could skew the average angle and therefore the anisotropy index as well.

A second major finding of this work is that interstitial flow can modulate the properties of existing microvessels. Previous work demonstrated the ability of interstitial flow to increase microvessel formation in engineered microvessels when the onset of flow was at the time of casting rather than after initial microvessel formation.^{118,119,123,159} The results presented here indicate that at the flow rate used can substantially affect the results. Low flow (0.015 $\mu\text{l}/\text{min}$; 0.33 $\mu\text{m}/\text{s}$) produced an increase in lumen density over statically cultured controls, whereas high flow (0.105 $\mu\text{l}/\text{min}$; 2.33 $\mu\text{m}/\text{s}$) did not. However, similar to previous reports,¹²³ the effects of shear stress and flow-induced morphogen gradients in producing the improvements could not be distinguished.

The lumen density observed in these constructs (both control and flow conditions) is substantially higher than previously reported for *in vitro* engineered tissues. At day 14, constructs exposed to low flow achieved a lumen density of nearly 650 lumens/ mm^2 in the middle region, more than 6 times higher than any previous report,^{149,152,155,156} and equivalent or greater than most reports of engineered microvessels after implantation.^{53,124,157} It is still shy of the 2000 lumens/ mm^2 of native adult human myocardium,⁹ but is greater than that of adult human skeletal muscle (200-300 lumens/ mm^2)^{147,148} In addition, lumen density has been reported to increase dramatically upon implantation (14-fold or more^{149,156}), suggesting that these constructs would likely reach the goal of 2000 lumens/ mm^2 soon after implantation, presumably with similar strong alignment.

An unexpected result was that lumen density was greater in the middle region of constructs in comparison to the inlet and outlet regions. This was true

for both control and flow conditions at days 11 and 14, indicating that it is not an effect of flow. Additionally, this effect is not present in controls at days 5 or 8, nor is there any difference in birefringence (indicating differential levels of matrix alignment) or optical density (indicating differential levels of matrix density) between construct regions at any time point. However, the means for most inlet and outlet regions at day 11 fall within the 100-200 lumens/mm² range, as do means for all regions at days 5 and 8. This suggests that the increases in lumen density observed both with additional days of compaction in static culture (after day 8) and with low flow occurred substantially in the middle region of the construct.

Lumens greater than 200 μm in length were frequently observed in longitudinal sections of constructs exposed to low flow for 3 days (day 11). However, due to the potential tortuosity of the lumens and the possibility that sections were not taken exactly parallel to the alignment direction, it is unclear exactly how far the lumens extended. Attempts to image constructs under multiphoton confocal microscopy yielded data only to a depth of approximately 200 μm , likely due to the construct density and opacity, providing no further information about lumen length.

The increase in ephrinB2 expression by BOECs over time in control constructs suggests that they were maturing towards an arterial phenotype. Additionally, the fact that shear stress induced a reduction in ephrinB2 expression in BOECs indicates that the BOECs were more similar to a mature EC than and EPC when flow began.

Fluid tracking via GNP indicated that fluid was traveling through the construct interstitium, as expected. The fact that few GNP were found within lumens suggests that fluid was not entering and flowing through lumens, but rather was limited to the interstitium. This suggests that in these constructs the lumen ends are not open to flow, so other mechanisms of achieving microvessel perfusion will need to be explored. Additionally, this result prevented the comparison of the predictions of the mathematical model developed in Chapter 5 to experimental results. Interestingly, however, an increase in EC barrier function was observed after 3 days of low flow exposure. This result extends previous reports of the increased barrier function of EC monolayers exposed to laminar shear flow^{163,165,166} to include ECs cultured as microvessels in 3 dimensions. The shear stress in this study was applied ablumenally, evidently, and at a level not previously studied in monolayers (approximately 100-fold lower than previous reports), suggesting that either the effect of chronic shear stress on EC barrier function is similar over a wide range of shear stresses and application methods, or that tight junction formation occurs differently in microvessels versus monolayers.

The data presented here demonstrate the success of using PCs as a support cell for BOECs in a remodeled fibrin gel. PCs were recruited to the BOEC microvessels, and abundant basement membrane was formed. As noted earlier, mural cell recruitment and basement membrane formation are the hallmarks of microvessel stability *in vivo*, and thus the PC recruitment and

basement membrane formation observed here likely contributed to the stability of the microvessels over a two week period, even in statically cultured constructs.

The exposure of constructs to interstitial flow at either flow rate reduced the number of PCs. Because the PC density was high at day 8, it is clear that this difference is the result of PC loss. The fact that the fraction of recruited PCs remained constant across conditions suggests that PCs were lost equally from recruited and unrecruited positions. The reason for this loss is not clear; however, it may be related to the relatively low levels of culture medium received by the constructs during flow exposure (greater than 100-fold lower than that of control constructs for low flow). The fact that the ECs were not negatively affected under such conditions is remarkable. Regardless of the mechanism, it is not clear that a high density of PCs is required for microvessel stability in this system due to the deposition of basement membrane. In fact, qualitative assessment of laminin and collagen IV staining suggests that flow conditions had lower levels of staining in the interstitium, which may be related to the presence of fewer PCs (both PCs and ECs produce basement membrane proteins⁵²).

The system used in these studies is highly relevant for tissue engineering. The human BOECs are isolated from peripheral blood, and thereby represent a potentially autologous source of ECs. Although the human brain PCs used here are not an autologous source, PCs can be isolated from dermis, which could be autologous.¹²⁷ Fibrin, due to its role in *in vivo* wound healing, is degraded by cells and stimulates them to produce ECM.⁴² Therefore, a fully mature tissue engineered formed from a fibrin gel could in fact be completely cell-produced.¹⁸⁰

If autologous cells are used, extremely low immune reactivity of the engineered tissue is expected. If the small amount of fibrin remaining after culture proved to be immunogenic, autologous fibrinogen (isolated from peripheral blood) could be used to prepare the tissue. Finally, these constructs have the potential to achieve physiological strength by using fibrin gel that can be remodeled into a tissue *in vitro*. The results presented herein make strides towards the production of vascularized tissue comprising aligned microvessels of a size and strength relevant to humans.

6.5. Figures

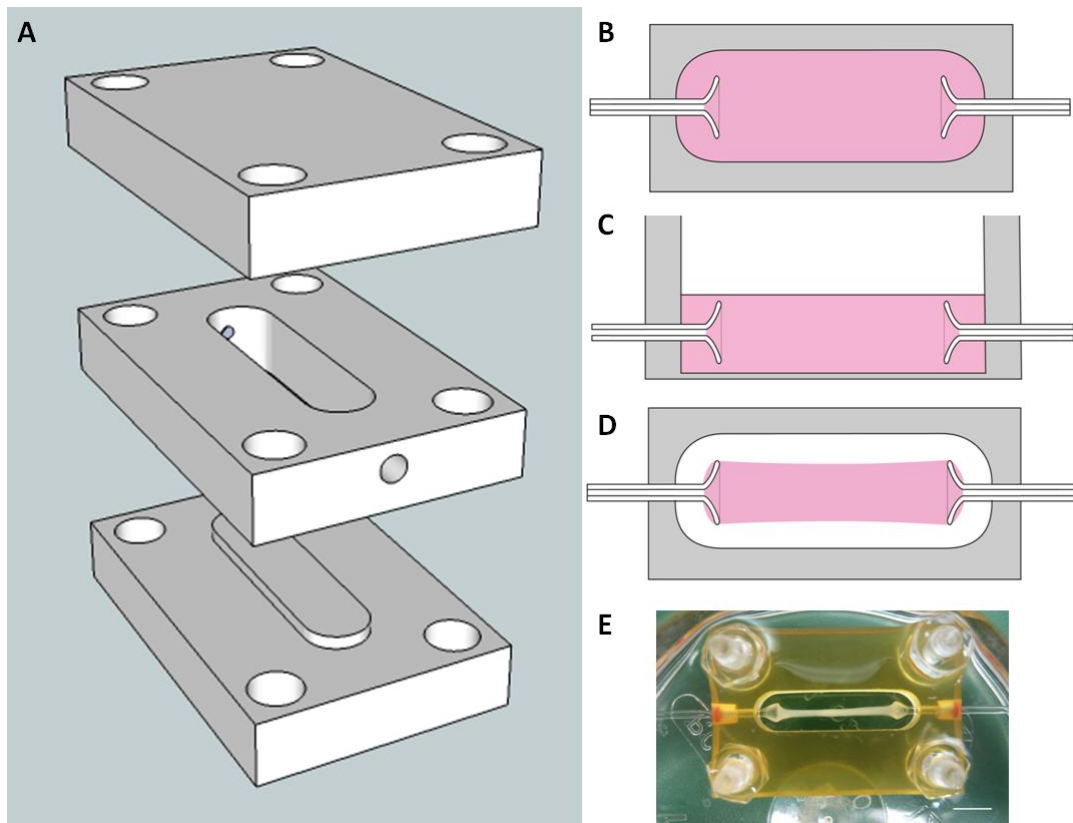
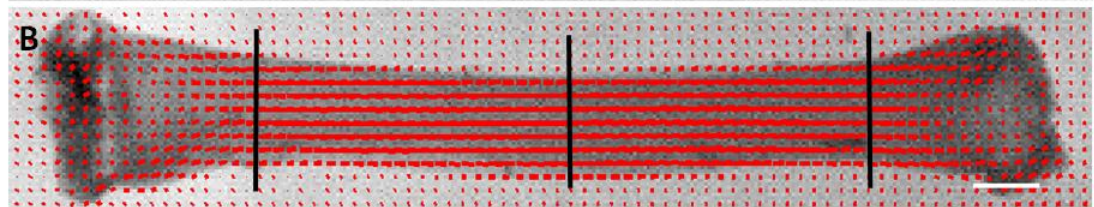
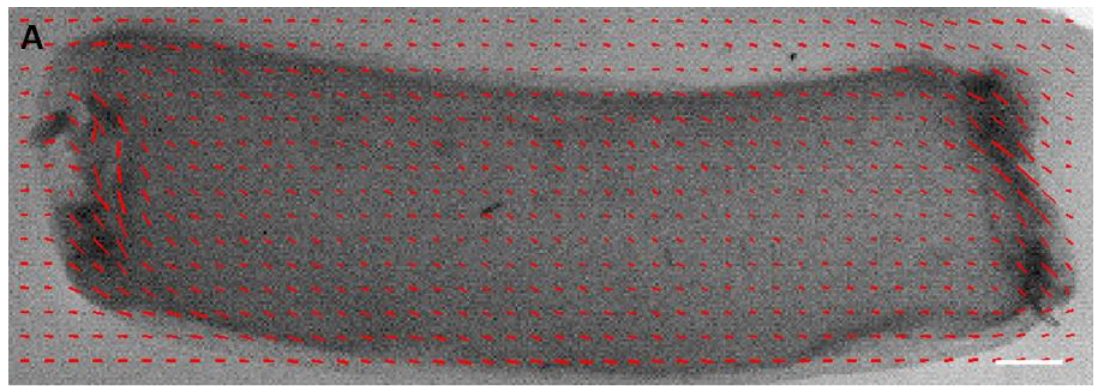


Figure 6-1.

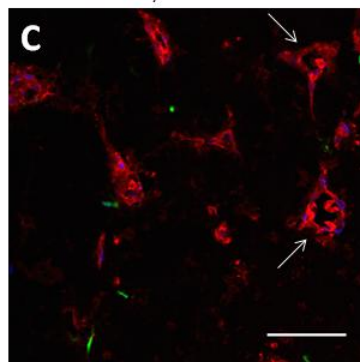
(A-D) Schematics of interstitial flow chamber design. (A) The chamber bottom snapped into the well for casting, at which point the well measured 20 mm (l) x 4.8 mm (w) x 4 mm (h). Flared glass capillary tubes (1 mm outer diameter, 0.58 mm inner diameter) were inserted into the small holes in the sides of the well. The chamber bottom and top were used to enclose the gel during interstitial flow. The pieces were tightened together using a screw at each corner. (B) Top view of a construct at casting. (C) Side view of a construct at casting. The gel (pink) filled the entire well and covered the glass capillary tubes. (D) Top view of a construct after compaction, prior to embedding with agarose gel. The construct

was only adherent to the glass capillary tubes. (E) A compacted construct after 8 days of culture. Scalebar = 5 mm.

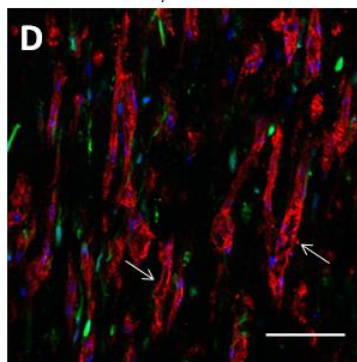


Day 5 Control

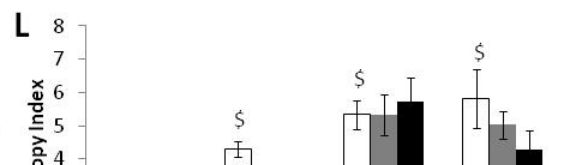
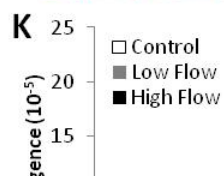
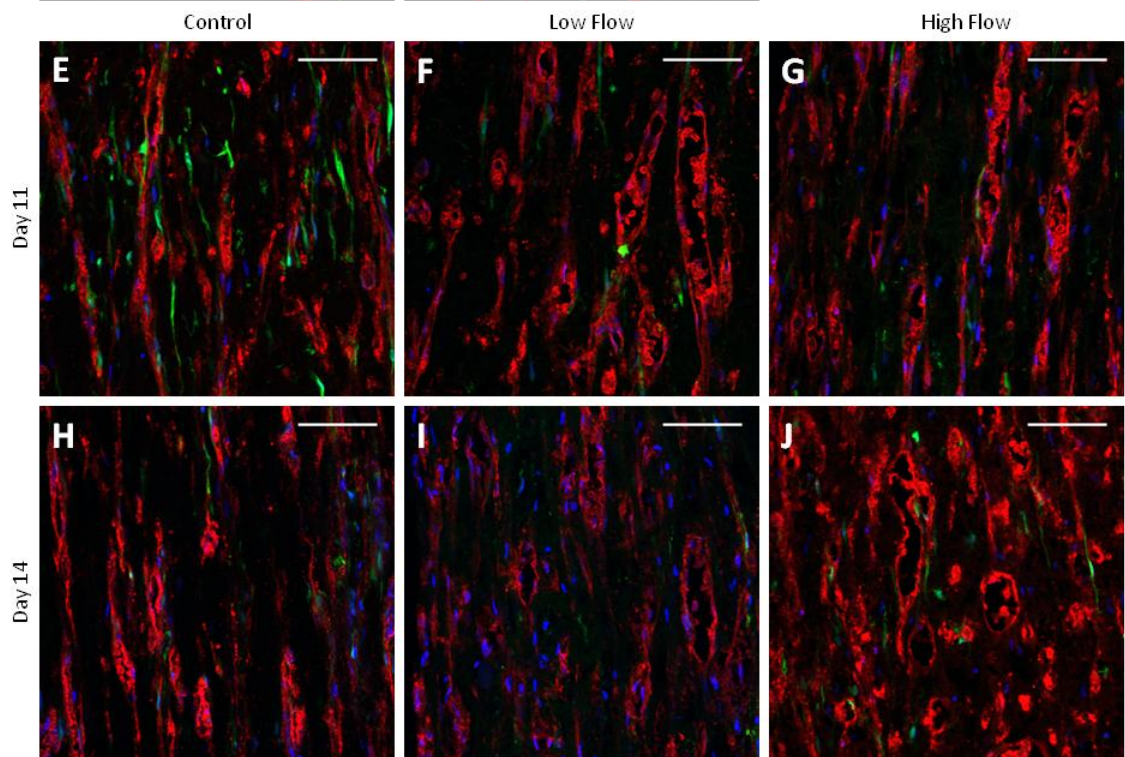
Day 8 Control



Control



Low Flow



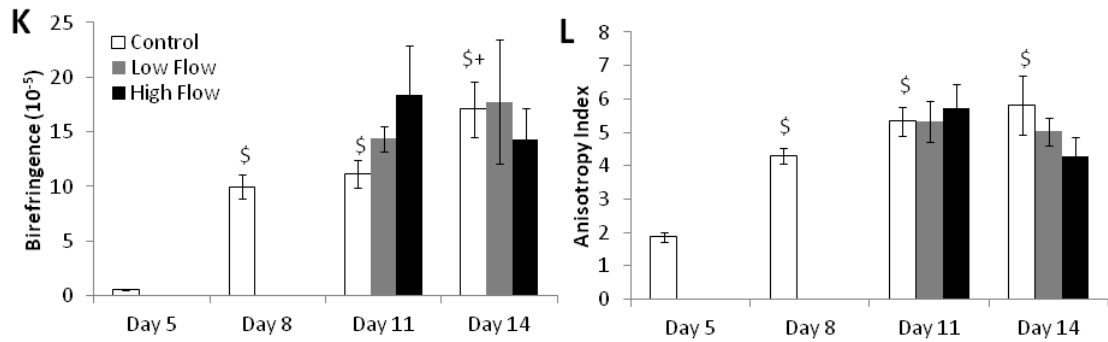
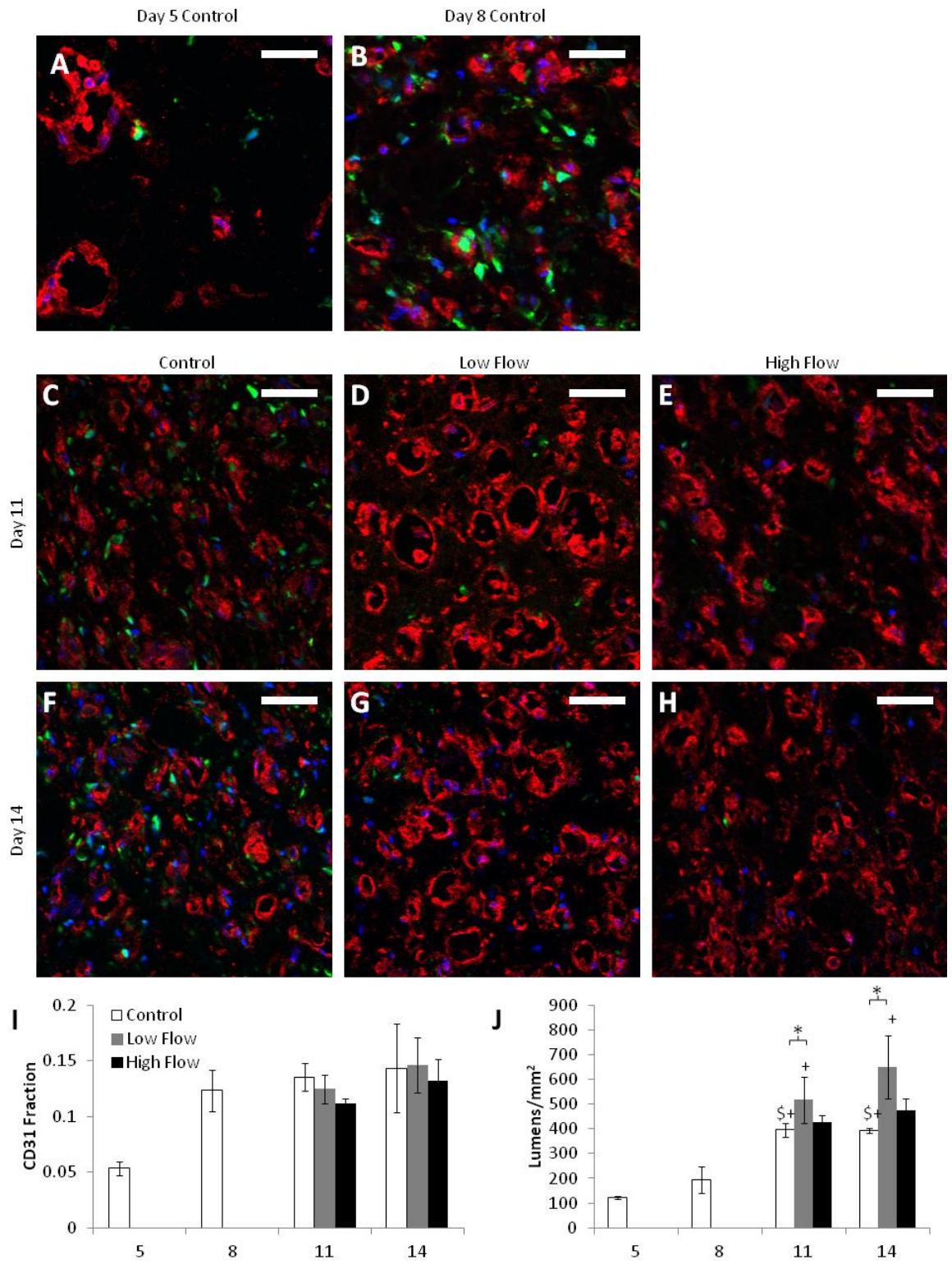


Figure 6-2.

(A-B) Representative alignment maps of uncompacted (day 5; A) and compacted (day 8; B) constructs, in which the red lines indicate the local direction and strength of alignment. Scalebars = 1 mm. The black lines in (B) indicate the approximate locations of inlet, middle and outlet cross sections. (C-J) Representative longitudinal sections stained for CD31 (red) of control and flow constructs. PCs were GFP-labeled (green), and nuclei were stained with Hoechst 33342 (blue). The axial direction is vertical. The arrows in (C-D) indicate some of the microvessels with lumens. Scalebars = 100 μ m. (G) Birefringence (a measure of fibril alignment), quantified from polarimetry, increased with compaction, but did not vary among compacted conditions, suggesting that flow did not have an effect on fibril alignment. (F) Microvessel anisotropy index, a measure of microvessel alignment obtained from images, also increased with compaction but did not vary among compacted conditions. \$ $p < 0.05$ in comparison to day 5 control. + $p < 0.05$ in comparison to day 8 control.



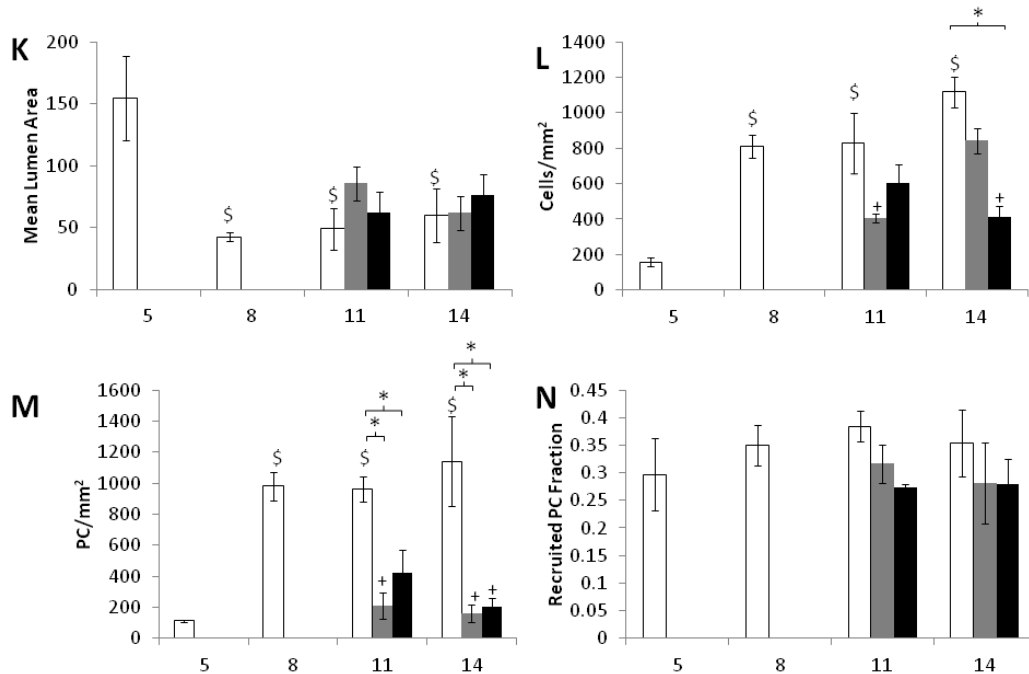


Figure 6-3.

(A-H) Representative cross-sections stained for CD31 (red) from the middle region of constructs from all days and flow conditions studied. PCs were GFP-labeled (green), and nuclei were stained with Hoechst 33342 (blue). Scalebars = 50 μ m. (I-N) Quantification of images. (I) The fraction of the section stained positively for CD31 remained constant across all compacted conditions. (J) The number of lumens per square millimeter was increased by low flow relative to time-matched controls but not by high flow. (K) The mean cross sectional area of lumens decreased with compaction but was independent of day or flow condition. (L) The cell number per square millimeter, based on Hoechst 33342 staining, was somewhat variable between conditions, but no trends emerged. (M) The number of PCs per square millimeter, was reduced with exposure to either flow rate. (N) The fraction of pericytes that were recruited to CD31+ microvessels was

the same across all conditions. * $p < 0.05$. \$ $p < 0.05$ in comparison to day 5 control. + $p < 0.05$ in comparison to day 8 control.

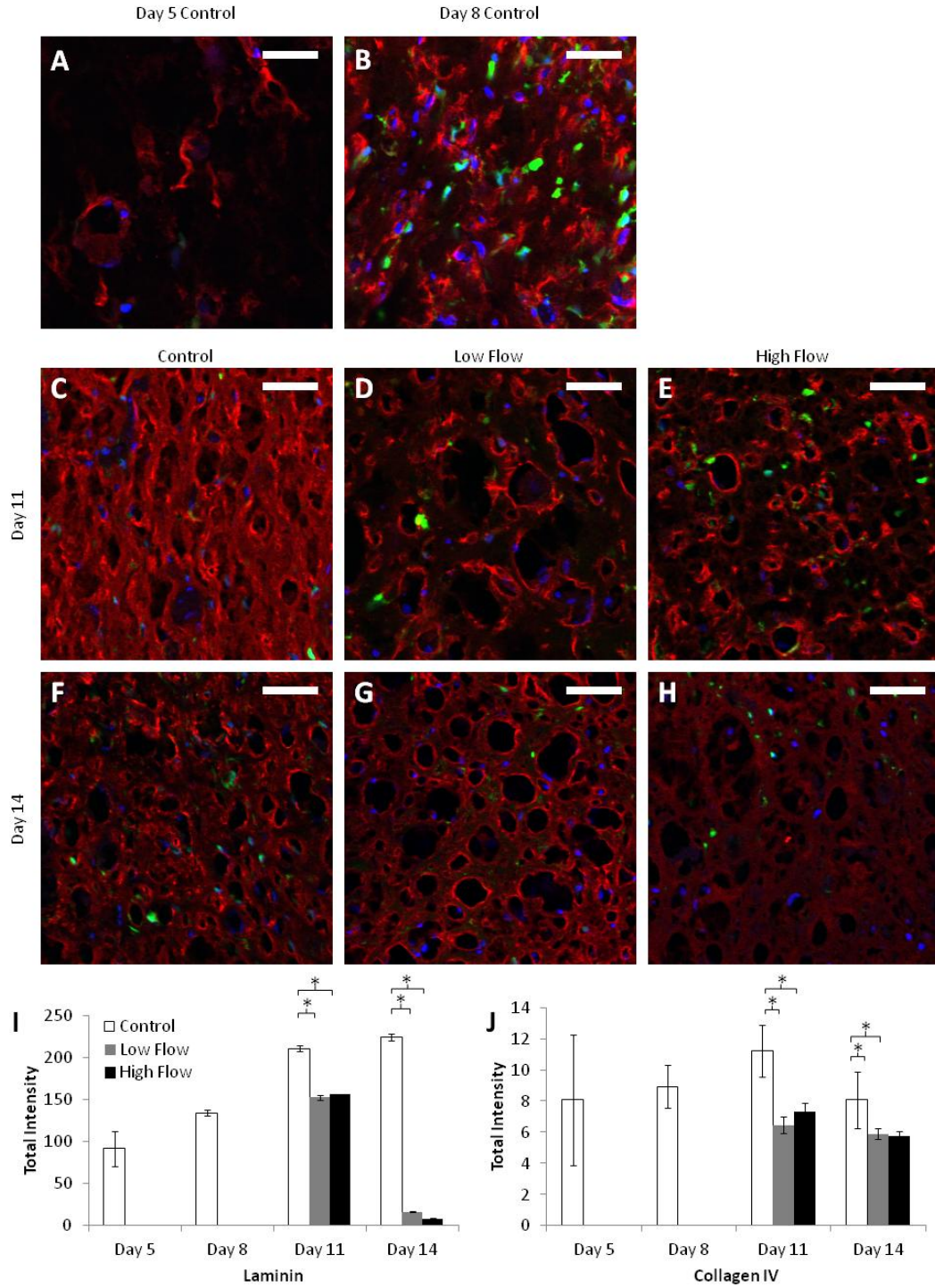


Figure 6-4.

(A-H) Representative cross sections from the middle region of constructs in all day and flow conditions studied, stained for laminin (red). PCs were GFP-labeled

(green), and nuclei were stained with Hoechst 33342 (blue). Scalebars = 50 μm . Collagen IV staining was similar and therefore is not shown. (I-J) Quantification of the total staining intensity per non-lumen area for laminin (I) and collagen IV (J). The increased staining in control constructs appeared to be due to additional protein in the interstitial space rather than the perivascular region. * $p < 0.05$ for main effect.

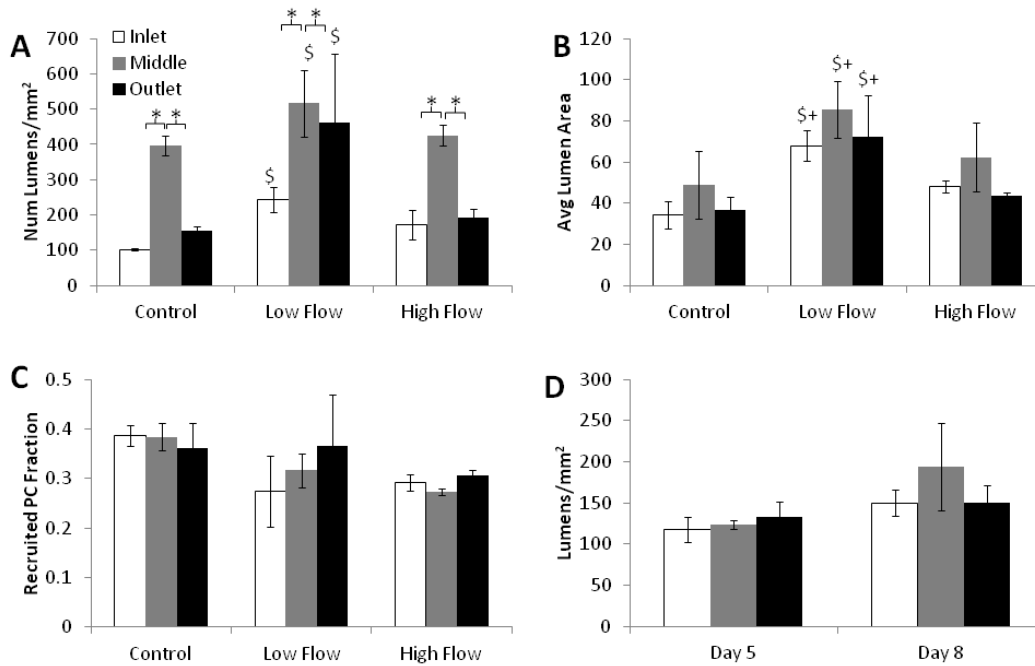


Figure 6-5.

Quantification of CD31 stained cross-sections from various tissue regions. (A) At day 11, lumen density was increased in the middle region over the inlet and outlet regions. However, even when all of the data was combined, the increase in lumen density with low flow remained. (B) Average lumen area at day 11 did not vary by tissue region, but was larger in constructs exposed to low flow. (C) No differences in PC recruitment occurred between regions or flow conditions at day 11. (D) At days 5 and 8, no differences in lumen density occurred across tissue regions. * $p < 0.05$ for main effects. \$ $p < 0.05$ for main effects between control and low flow. + $p < 0.05$ for main effects between low and high flow.

EphrinB2

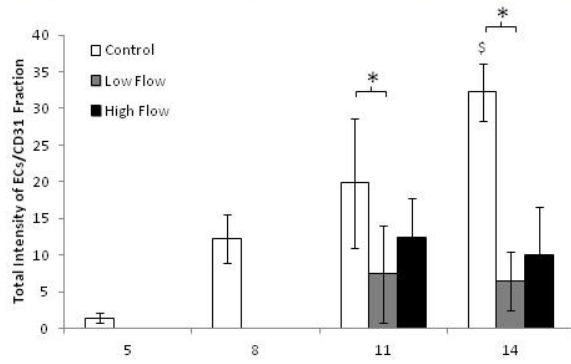
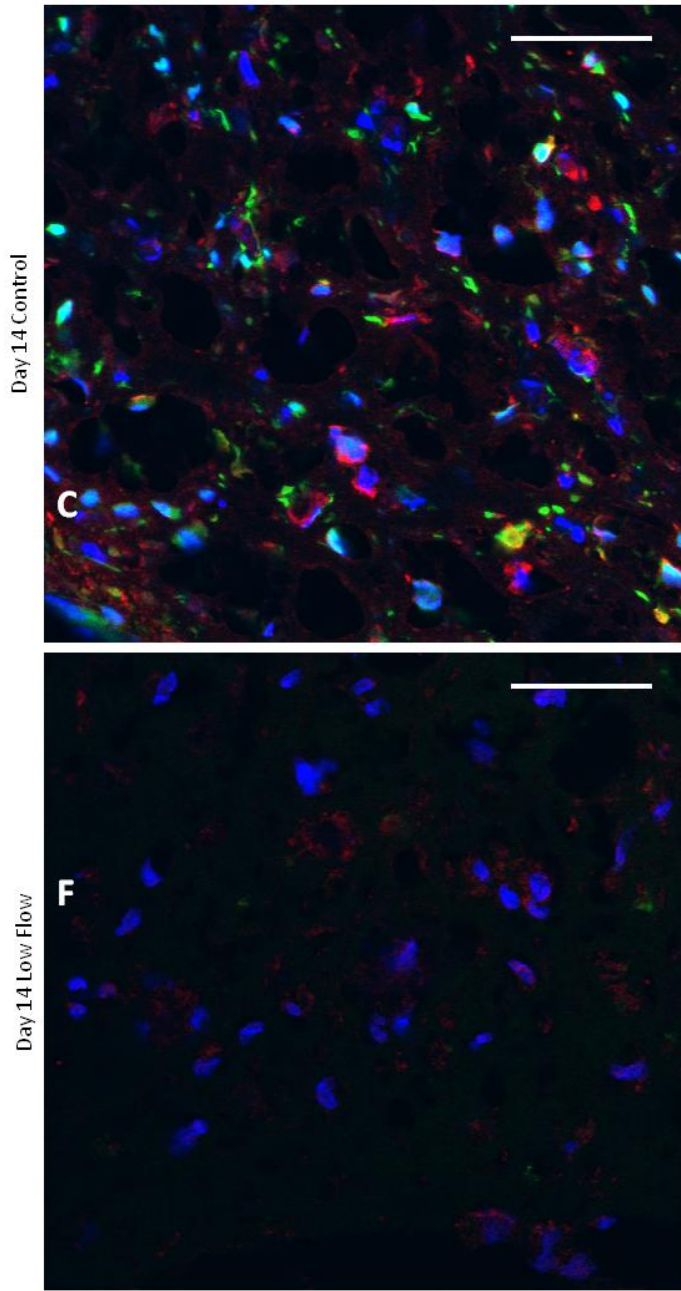


Figure 6-6.

(A-B) Representative images of sections of control (A) and low flow (B) constructs from day 14 stained for ephrinB2 (red). PCs are green and nuclei are blue. Scalebars = 50 μm . (C) Quantification of BOEC ephrin staining, normalized to values of CD31 fraction obtained from staining of nearby sections (data shown in Figure 6-3i).

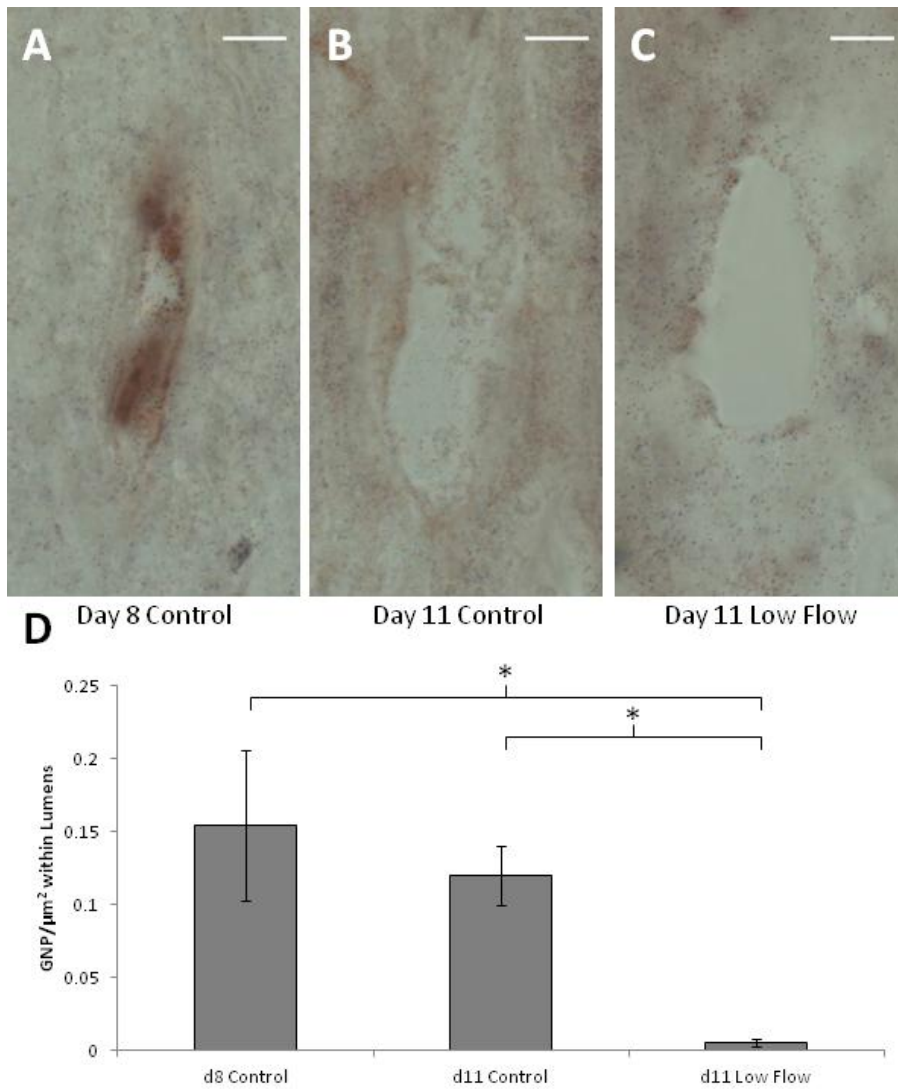


Figure 6-7.

Endothelial barrier function assay. (A-C) Representative images of lumens within control constructs at days 8 (A) and 11 (B) as well as constructs exposed to low flow for 3 days (from day 8 to day 11; C). Scalebar = 10 μm. (D) Quantification of the GNP present with the lumens; low levels of GNP within lumens of constructs exposed to low flow indicated strong EC barrier function.

Chapter 7. Conclusions and Future Directions

7.1. Major Contributions

The work presented in this dissertation has contributed substantially to the field of engineered microvasculature. Five manuscripts have been published or are in preparation, in addition to numerous oral and poster presentations at international and local meetings. The major conclusion and contributions to the literature are summarized here.

7.1.1. Endothelial Capillary Structures Can Be Aligned via Cell-Induced Compaction

One of the largest contributions is that cell-induced compaction of fibrin gel can be utilized to align microvascular structures of multiple types. This topic was addressed in three chapters. Data from magnetically-aligned fibrin in Chapter 2 suggested that fibril alignment alone was sufficient to align sprouts from EC spheroids, and that those sprouts could also be aligned by cell-induced compaction. This basic research provided the foundation for inducing alignment of both HUVEC microvessels (Chapter 4) and BOEC microvessels (Chapter 6). Interestingly, it was determined that serum was a critical to the compaction process and that both cell types (ECs and PCs) were required for compaction.

7.1.2. Development of Semi-Automated Image Analysis Programs to Quantify Microvascular Network Properties

Prior to this work, the quantification of microvessel density and other properties of the microvasculature in our laboratory was limited to manual counting, and many reports in the literature used manual quantification techniques. Chapter 3 describes the development of Matlab scripts to analyze images of tissue sections and whole mount preparations stained for CD31. The programs were mostly automated, but a small amount of user input modifying the lumens detected by the program to more closely match the original image yielded highly accurate results. The programs output a variety of microvessel properties including lumen density, average lumen area, total microvessel length and microvessel alignment. Additionally, if nuclei and support cells were also stained, the programs provided information about cell density and mural cell recruitment. Automated quantification of mural cell recruitment and microvessel alignment are entirely novel in the field. These programs not only save time in quantifying images, but also reduce the subjectivity of the results, which is especially important in analysis of engineered microvasculature in which not all EC structures contain well-formed lumens and EC debris is often present.

7.1.3. Highly Interconnected Microvascular Networks in Fibrin Gel can be Formed under Defined Conditions and Aligned via Cell-Induced Gel Compaction

Cell culture in defined medium (i.e. medium containing no serum) is advantageous because the unknowns of the culture conditions are limited, leading to more reproducible results. Therefore, with the aid of collaborators at

the University of Missouri, the ability of HUVECs to form fully interconnected microvascular networks in fibrin gel was assessed. The results of these studies, described in Chapter 4, demonstrated that highly interconnected networks were only formed in the presence of PCs and defined medium (ie. medium containing no serum); the absence of PCs or presence of serum disrupted the network formation. These results suggest that the PCs provide paracrine factors that direct the HUVECs and that the myriad cytokines present in serum mask these effects. Although cell-induced gel compaction was detrimental to network formation, the mechanism could be harnessed to align networks that had already been formed either in defined medium or serum-containing medium, suggesting that the networks are quite stable after formation.

7.1.4. Development of an Idealized Mathematical Model of Fluid Flow through Engineered Microvessels

Chapter 5 describes the development of a two-dimensional finite difference model of flow through a tissue containing engineered microvessels. The tissue matrix was modeled as a porous medium, and the microvessels were modeled as straight tubes. The inlets and outlets of the microvessels were treated as point sinks and sources, respectively, of fluid mass and momentum in the governing equations. The model assumed that the microvessels were open to flow at their ends, which turned out not to be accurate at this time in the tissues studied in Chapter 6, but other researchers have reported open lumens at the ends of microvessels. The model demonstrates a methodology for determining the percentage of perfused microvessels, a parameter that may be difficult to

determine experimentally. In addition, the model would provide estimates of flow rates through the microvessels and could be coupled with solute diffusion equations to estimate the delivery of nutrients and oxygen throughout the tissue.

7.1.5. Compaction of Fibrin Gel Containing Microvasculature Improves Lumen Density

Cell-induced compaction of fibrin gel was chosen not only for its ability align microvessels, but also because it increases tissue density. In and of itself, increase tissue density is critically important for achieving the necessary mechanical properties in engineered tissues, but we also hypothesized that the lumen density would be improved after compaction because the same number of microvessels would be condensed into a smaller volume. This hypothesis turned out to be correct (as evidenced by the data from Chapter 6), although interestingly, the compaction initially led to lumen collapse. At early time points, the lumen density remained constant despite a reduction in tissue volume and an increase in CD31+ staining density. However, by later time points, the lumens had reformed and the lumen density had improved 3.2-fold over uncompact controls.

7.1.6. Interstitial Flow at Specific Flow Rates Applied to an Existing Microvascular Network Improves Lumen Density

Despite the improvement in lumen density observed with compaction alone, lumen density was still 5-fold lower than that of adult human myocardium. Interstitial flow was examined as a means to further improve lumen density. The

results described in Chapter 6 indicated that interstitial flow improved lumen density, achieving densities 65% higher than statically cultured controls after 6 days of flow. This result was especially interesting because all previous reports of the effects of interstitial flow on microvessel formation had used flow throughout the culture period, whereas here flow was begun after microvessel formation. Therefore, these results suggest that interstitial flow can modulate an existing network. Furthermore, a second (higher) flow rate was used in the same system, and did not improve lumen density over controls. This suggests that ECs are exquisitely sensitive to the rate of interstitial flow.

7.2. Future Directions

Despite the progress made toward the goal of vascularized engineered myocardium, much work remains. The perfusion system was designed to enable gel compaction and perfuse both the interstitium and the microvessels, and while it performed well at the first two, it failed to perfuse microvessels. In addition, although the lumen density under interstitial flow was greatly improved over controls, the final lumen density was still 3-fold lower than that of native human myocardium. Finally, vascularized engineered myocardium requires both microvasculature and cardiomyocytes, so additional work will be necessary to combine the two.

7.2.1. Hybrid Approaches to Perfuse Engineered Microvasculature

The major limiting factor to the perfusion of microvessels in the system described here is that the fluid within the lumens was separated from the fluid

pumped through the system. Although it is exciting that the engineered microvessels exhibited strong barrier function, this prevented fluid from flowing through them. Most likely a hybrid approach in which other methods of engineering microvasculature are combined with EC self-assembly will be necessary to open the lumens to perfusion. For example, one could seed ECs on the surfaces of the gel that are present inside the glass capillary tubes. Given the right conditions, these ECs could sprout into the gel and anastomose with the self-assembling EC network. These sprouts would then form a direct connection between the chamber's inlet flow and the luminal space of the microvascular network. Literature reports suggest sprouting into a gel can occur from a monolayer on the surface of the gel in response to VEGF or interstitial flow.^{61,118,119} Another possibility would be to create channels lined with ECs that extend partway into the gel from both the inlet and outlet sides. Sprouting could occur from these channels,⁵⁹ or self-assembled EC structures could intersect these channels. This would create a situation similar to *in vivo* capillary beds, which are filled and drained by larger vessels. In either case, once the luminal space of the engineered microvasculature is directly connected with the inlet and outlet fluid, perfusion of the vessels should be straightforward.

7.2.2. Cyclic or Static Strain to Further Improve Lumen Density

In order to reach 2000 lumens/mm², the lumen density of adult human myocardium, additional methods instead of or in addition to interstitial flow will be required. One possible method is cyclic or static strain. A number of animal studies have suggested that capillary density is increased in skeletal muscle

when it is permanently stretched (i.e. static strain).^{181–183} Although it is unclear whether these results will translate to an *in vitro* model of microvasculature under static strain, it is worth investigating. In addition, static stretch could easily be combined with interstitial flow in this system for possibly additive or even synergistic effects. Limited data exist on cyclic stretch of engineered microvasculature, but one group found that it disrupted EC cord formation on top of Matrigel.¹⁸⁴ However, many reports suggest that the angiogenic capability of ECs is improved when they are stretched in monolayer.^{185–187} In addition, cyclic stretching of EC monolayers has been shown to increase production of various pro-angiogenic cytokines including Ang-2, PDGF-BB, VEGF along with several associated receptors.^{185,187–189} These results suggest that ECs exposed to cyclic strain prior to entrapment in fibrin may form more extensive networks and/or recruit PCs more strongly (recruitment is regulated by PDGF-BB). Cyclic pre-stretch in combination with static stretch after network formation could be a potent method for further increasing lumen density.

7.2.3. Tri-culture of ECs, PCs, and Cardiomyocytes

Although a goal has been to engineer microvascular networks with lumen densities similar to that of native myocardium, the real test of whether or not the microvessels are dense enough will be functional: they are dense enough when they can support the density of cardiomyocytes within the tissue. Indeed, this is the ultimate goal, to combine the engineered microvasculature with the engineered myocardium to create beating tissues that are sustained via perfusion of the microvascular network. This will require the tri-culture of ECs,

PCs, and cardiomyocytes, which may prove quite challenging. Although the achievement of this goal may still be far in the future, the work presented in this dissertation has made critical steps toward revolutionizing the treatment of myocardial infarction.

References

1. Park, SJ End Stage Cardiomyopathy. *Handbook of Cardiac Anatomy, Physiology, and Devices* (2005).
2. Uflacker, R *Atlas of Vascular Anatomy*. (Williams & Williams: Baltimore, MD, 1997).
3. Weinhaus, AJ & Roberts, KP Anatomy of the Human Heart. *Handbook of Cardiac Anatomy, Physiology, and Devices* (2005).
4. Fox, S. *Human Physiology*. **10**, (McGraw-Hill Science/Engineering/Math: 2007).
5. Greenbaum, R. A., Ho, S. Y., Gibson, D. G., Becker, A. E. & Anderson, R. H. Left ventricular fibre architecture in man. *Br Heart J* **45**, 248–263 (1981).
6. Davies, MJ *Atlas of Coronary Artery Disease*. (Lippincott-Raven: Philadelphia, PA, 1998).
7. Kajiya, F. & Goto, M. Integrative physiology of coronary microcirculation. *Jpn. J. Physiol.* **49**, 229–241 (1999).
8. Rakusan, K., Flanagan, M. F., Geva, T., Southern, J. & Van Praagh, R. Morphometry of human coronary capillaries during normal growth and the effect of age in left ventricular pressure-overload hypertrophy. *Circulation* **86**, 38–46 (1992).
9. Rakusan, K. Quantitative morphology of capillaries of the heart. Number of capillaries in animal and human hearts under normal and pathological conditions. *Methods Achiev Exp Pathol* **5**, 272–286 (1971).
10. Duncker, D. J. & Merkus, D. Regulation of coronary blood flow. Effect of coronary artery stenosis. *Arch Mal Coeur Vaiss* **97**, 1244–1250 (2004).
11. Stoney RJ, E. D. *Wylie's Atlas of Vascular Surgery: Basic Considerations and Techniques*. (J. B. Lippincott Company: Philadelphia, PA, 1992).
12. Coles, JA, Sigg, DC & Iaizzo, PA Reversible and Irreversible Damage of the Myocardium. *Handbook of Cardiac Anatomy, Physiology, and Devices* (2005).
13. George, I & Williams, M Myocardial Revascularization after Acute Myocardial Infarction. *Cardiac Surgery in the Adult* (2012).
14. Crawford, M. H. *Current diagnosis & treatment cardiology*. (McGraw Hill Medical: New York, 2009).
15. Vaughan, D. E. & Pfeffer, M. A. Post-myocardial infarction ventricular remodeling: animal and human studies. *Cardiovasc. Drugs Ther.* **8**, 453–460 (1994).
16. Takano, H., Hasegawa, H., Nagai, T. & Komuro, I. Implication of cardiac remodeling in heart failure: mechanisms and therapeutic strategies. *Intern. Med.* **42**, 465–469 (2003).
17. Wilson, JM & Willerson, JT Myocardial Revascularization with Percutaneous Devices. *Cardiac Surgery in the Adult* (2012).
18. Greason, KL & Sundt, TM Myocardial Revascularization with Cardiopulmonary Bypass. *Cardiac Surgery in the Adult* (2012).

19. Takayama, H, Worku, B & Naka, Y Long-Term Mechanical Circulatory Support. *Cardiac Surgery in the Adult* (2012).
20. John, R, Deng, MC & Itescu, S Immunosuppression for Cardiac Transplantation. *Cardiac Transplantation* (2004).
21. Griffith BP Immunobiology of Heart and Heart-Lung Transplantation. *Cardiac Surgery in the Adult* (2012).
22. Mancini DM & Kunavarapu, C Recipient Selection. *Cardiac Transplantation* (2004).
23. Bursac, N., Papadaki, M., Cohen, R. J., Schoen, F. J., Eisenberg, S. R., Carrier, R., Vunjak-Novakovic, G. & Freed, L. E. Cardiac muscle tissue engineering: toward an in vitro model for electrophysiological studies. *Am.J.Physiol.* **277**, H433–44 (1999).
24. Carrier, R. L., Papadaki, M., Rupnick, M., Schoen, F. J., Bursac, N., Langer, R., Freed, L. E. & Vunjak-Novakovic, G. Cardiac tissue engineering: cell seeding, cultivation parameters, and tissue construct characterization. *Biotechnol.Bioeng.* **64**, 580–589 (1999).
25. Park, H., Radisic, M., Lim, J. O., Chang, B. H. & Vunjak-Novakovic, G. A novel composite scaffold for cardiac tissue engineering. *In Vitro Cell.Dev.Biol.Anim.* **41**, 188–196 (2005).
26. Marsano, A., Maidhof, R., Wan, L. Q., Wang, Y., Gao, J., Tandon, N. & Vunjak-Novakovic, G. Scaffold stiffness affects the contractile function of three-dimensional engineered cardiac constructs. *Biotechnol. Prog.* **26**, 1382–1390 (2010).
27. Rosellini, E., Vozzi, G., Barbani, N., Giusti, P. & Cristallini, C. Three-dimensional microfabricated scaffolds with cardiac extracellular matrix-like architecture. *Int J Artif Organs* **33**, 885–894 (2010).
28. Amir, G., Miller, L., Shachar, M., Feinberg, M. S., Holbova, R., Cohen, S. & Leor, J. Evaluation of a Peritoneal-Generated Cardiac Patch in a Rat Model of Heterotopic Heart Transplantation. *Cell Transplant.* (2009).
29. Kofidis, T., Akhyari, P., Boublik, J., Theodorou, P., Martin, U., Ruhparwar, A., Fischer, S., Eschenhagen, T., Kubis, H. P., Kraft, T., Leyh, R. & Haverich, A. In vitro engineering of heart muscle: artificial myocardial tissue. *J. Thorac. Cardiovasc. Surg.* **124**, 63–69 (2002).
30. Leor, J., Aboulafia-Etzion, S., Dar, A., Shapiro, L., Barbash, I. M., Battler, A., Granot, Y. & Cohen, S. Bioengineered cardiac grafts: A new approach to repair the infarcted myocardium? *Circulation* **102**, III56–61 (2000).
31. Liao, B., Christoforou, N., Leong, K. W. & Bursac, N. Pluripotent stem cell-derived cardiac tissue patch with advanced structure and function. *Biomaterials* **32**, 9180–9187 (2011).
32. Naito, H., Melnychenko, I., Didie, M., Schneiderbanger, K., Schubert, P., Rosenkranz, S., Eschenhagen, T. & Zimmermann, W. H. Optimizing engineered heart tissue for therapeutic applications as surrogate heart muscle. *Circulation* **114**, I72–8 (2006).
33. Radisic, M., Park, H., Shing, H., Consi, T., Schoen, F. J., Langer, R., Freed, L. E. & Vunjak-Novakovic, G. Functional assembly of engineered

- myocardium by electrical stimulation of cardiac myocytes cultured on scaffolds. *Proc.Natl.Acad.Sci.U.S.A.* **101**, 18129–18134 (2004).
34. Tiburcy, M., Didié, M., Boy, O., Christalla, P., Döker, S., Naito, H., Karikkineth, B. C., El-Armouche, A., Grimm, M., Nose, M., Eschenhagen, T., Zieseniss, A., Katschinski, D. M., Hamdani, N., Linke, W. A., Yin, X., Mayr, M. & Zimmermann, W.-H. Terminal differentiation, advanced organotypic maturation, and modeling of hypertrophic growth in engineered heart tissue. *Circ. Res.* **109**, 1105–1114 (2011).
 35. Birla, R., Dhawan, V., Huang, Y.-C., Lytle, I., Tiranathanagul, K. & Brown, D. Force characteristics of in vivo tissue-engineered myocardial constructs using varying cell seeding densities. *Artif Organs* **32**, 684–691 (2008).
 36. Morritt, A. N., Bortolotto, S. K., Dilley, R. J., Han, X., Kompa, A. R., McCombe, D., Wright, C. E., Itescu, S., Angus, J. A. & Morrison, W. A. Cardiac tissue engineering in an in vivo vascularized chamber. *Circulation* **115**, 353–360 (2007).
 37. Tulloch, N. L., Muskheli, V., Razumova, M. V., Korte, F. S., Regnier, M., Hauch, K. D., Pabon, L., Reinecke, H. & Murry, C. E. Growth of engineered human myocardium with mechanical loading and vascular coculture. *Circ. Res.* **109**, 47–59 (2011).
 38. Black, L. D., Meyers, J. D., Weinbaum, J. S., Shvelidze, Y. A. & Tranquillo, R. T. Cell-induced alignment augments twitch force in fibrin gel-based engineered myocardium via gap junction modification. *Tissue Eng.Part A.* **15**, 3099–3108 (2009).
 39. Khait, L., Hodonsky, C. & Birla, R. Variable optimization for the formation of three-dimensional self-organized heart muscle. *IN VITRO CELLULAR & DEVELOPMENTAL BIOLOGY-ANIMAL* **45**, 592–601 (2009).
 40. Sekine, H., Shimizu, T., Hobo, K., Sekiya, S., Yang, J., Yamato, M., Kurosawa, H., Kobayashi, E. & Okano, T. Endothelial cell coculture within tissue-engineered cardiomyocyte sheets enhances neovascularization and improves cardiac function of ischemic hearts. *Circulation* **118**, S145–52 (2008).
 41. Shimizu, T., Yamato, M., Isoi, Y., Akutsu, T., Setomaru, T., Abe, K., Kikuchi, A., Umezumi, M. & Okano, T. Fabrication of pulsatile cardiac tissue grafts using a novel 3-dimensional cell sheet manipulation technique and temperature-responsive cell culture surfaces. *Circ.Res.* **90**, e40 (2002).
 42. Grassl, E. D., Oegema, T. R. & Tranquillo, R. T. Fibrin as an alternative biopolymer to type-I collagen for the fabrication of a media equivalent. *J. Biomed. Mater. Res* **60**, 607–612 (2002).
 43. Hasenfuss, G., Mulieri, L. A., Blanchard, E. M., Holubarsch, C., Leavitt, B. J., Littleman, F. & Alpert, N. R. Energetics of isometric force development in control and volume-overload human myocardium. Comparison with animal species. *Circ. Res.* **68**, 836–846 (1991).
 44. Godier-Furnémont, A. F. G., Martens, T. P., Koeckert, M. S., Wan, L., Parks, J., Arai, K., Zhang, G., Hudson, B., Homma, S. & Vunjak-Novakovic, G. Composite scaffold provides a cell delivery platform for cardiovascular repair. *Proc. Natl. Acad. Sci. U.S.A.* **108**, 7974–7979 (2011).

45. Li, R. K., Jia, Z. Q., Weisel, R. D., Mickle, D. A., Choi, A. & Yau, T. M. Survival and function of bioengineered cardiac grafts. *Circulation* **100**, 1163–69 (1999).
46. Bergers, G. & Song, S. The role of pericytes in blood-vessel formation and maintenance. *Neuro Oncol.* **7**, 452–464 (2005).
47. Allt, G. & Lawrenson, J. G. Pericytes: cell biology and pathology. *Cells Tissues Organs* **169**, 1–11 (2001).
48. Benjamin, L. E., Hemo, I. & Keshet, E. A plasticity window for blood vessel remodelling is defined by pericyte coverage of the preformed endothelial network and is regulated by PDGF-B and VEGF. *Development* **125**, 1591–1598 (1998).
49. Bjarnegård, M., Enge, M., Norlin, J., Gustafsdottir, S., Fredriksson, S., Abramsson, A., Takemoto, M., Gustafsson, E., Fässler, R. & Betsholtz, C. Endothelium-specific ablation of PDGFB leads to pericyte loss and glomerular, cardiac and placental abnormalities. *Development* **131**, 1847–1857 (2004).
50. Hellström, M., Gerhardt, H., Kalén, M., Li, X., Eriksson, U., Wolburg, H. & Betsholtz, C. Lack of pericytes leads to endothelial hyperplasia and abnormal vascular morphogenesis. *J. Cell Biol* **153**, 543–553 (2001).
51. Armulik, A., Abramsson, A. & Betsholtz, C. Endothelial/pericyte interactions. *Circ. Res* **97**, 512–523 (2005).
52. Mandarino, L. J., Sundarraj, N., Finlayson, J. & Hassell, H. R. Regulation of fibronectin and laminin synthesis by retinal capillary endothelial cells and pericytes in vitro. *Exp. Eye Res.* **57**, 609–621 (1993).
53. Chen, X., Aledia, A. S., Ghajar, C. M., Griffith, C. K., Putnam, A. J., Hughes, C. C. & George, S. C. Prevascularization of a fibrin-based tissue construct accelerates the formation of functional anastomosis with host vasculature. *Tissue Eng. Part A.* **15**, 1363–1371 (2009).
54. Rao, R. R., Peterson, A. W., Ceccarelli, J., Putnam, A. J. & Stegemann, J. P. Matrix composition regulates three-dimensional network formation by endothelial cells and mesenchymal stem cells in collagen/fibrin materials. *Angiogenesis* **15**, 253–264 (2012).
55. Melero-Martin, J. M., Khan, Z. A., Picard, A., Wu, X., Paruchuri, S. & Bischoff, J. In vivo vasculogenic potential of human blood-derived endothelial progenitor cells. *Blood* **109**, 4761–4768 (2007).
56. Stratman, A. N., Malotte, K. M., Mahan, R. D., Davis, M. J. & Davis, G. E. Pericyte recruitment during vasculogenic tube assembly stimulates endothelial basement membrane matrix formation. *Blood* **114**, 5091–5101 (2009).
57. Lin, Y., Weisdorf, D. J., Solovey, A. & Hebbel, R. P. Origins of circulating endothelial cells and endothelial outgrowth from blood. *J. Clin. Invest.* **105**, 71–77 (2000).
58. Leung, A. D., Wong, K. H. K. & Tien, J. Plasma expanders stabilize human microvessels in microfluidic scaffolds. *J Biomed Mater Res A* **100**, 1815–1822 (2012).

59. Zheng, Y., Chen, J., Craven, M., Choi, N. W., Totorica, S., Diaz-Santana, A., Kermani, P., Hempstead, B., Fischbach-Teschl, C., López, J. A. & Stroock, A. D. In vitro microvessels for the study of angiogenesis and thrombosis. *Proceedings of the National Academy of Sciences of the United States of America* (2012).doi:10.1073/pnas.1201240109
60. Shin, Y., Jeon, J. S., Han, S., Jung, G.-S., Shin, S., Lee, S.-H., Sudo, R., Kamm, R. D. & Chung, S. In vitro 3D collective sprouting angiogenesis under orchestrated ANG-1 and VEGF gradients. *Lab Chip* **11**, 2175–2181 (2011).
61. Stratman, A. N., Davis, M. J. & Davis, G. E. VEGF and FGF prime vascular tube morphogenesis and sprouting directed by hematopoietic stem cell cytokines. *Blood* **117**, 3709–3719 (2011).
62. Ghajar, C. M., Chen, X., Harris, J. W., Suresh, V., Hughes, C. C., Jeon, N. L., Putnam, A. J. & George, S. C. The effect of matrix density on the regulation of 3-D capillary morphogenesis. *Biophys.J.* **94**, 1930–1941 (2008).
63. Morin, K. T. & Tranquillo, R. T. Guided sprouting from endothelial spheroids in fibrin gels aligned by magnetic fields and cell-induced gel compaction. *Biomaterials* **32**, 6111–6118 (2011).
64. Grainger, S. J. & Putnam, A. J. Assessing the permeability of engineered capillary networks in a 3D culture. *PLoS ONE* **6**, e22086 (2011).
65. Caulfield, J. B. & Janicki, J. S. Structure and function of myocardial fibrillar collagen. *Technol Health Care* **5**, 95–113 (1997).
66. Dunn, G. A. & Heath, J. P. A new hypothesis of contact guidance in tissue cells. *Exp. Cell Res* **101**, 1–14 (1976).
67. Guido, S. & Tranquillo, R. T. A methodology for the systematic and quantitative study of cell contact guidance in oriented collagen gels. Correlation of fibroblast orientation and gel birefringence. *J. Cell. Sci* **105 (Pt 2)**, 317–331 (1993).
68. Robinson, P. S., Johnson, S. L., Evans, M. C., Barocas, V. H. & Tranquillo, R. T. Functional tissue-engineered valves from cell-remodeled fibrin with commissural alignment of cell-produced collagen. *Tissue Eng Part A* **14**, 83–95 (2008).
69. Lee, P., Lin, R., Moon, J. & Lee, L. P. Microfluidic alignment of collagen fibers for in vitro cell culture. *Biomed Microdevices* **8**, 35–41 (2006).
70. Heath, D. E., Lannutti, J. J. & Cooper, S. L. Electrospun scaffold topography affects endothelial cell proliferation, metabolic activity, and morphology. *J Biomed Mater Res A* **94**, 1195–1204 (2010).
71. Krishnan, L., Underwood, C. J., Maas, S., Ellis, B. J., Kode, T. C., Hoying, J. B. & Weiss, J. A. Effect of mechanical boundary conditions on orientation of angiogenic microvessels. *Cardiovasc. Res* **78**, 324–332 (2008).
72. Matsumoto, T., Sasaki, J., Alsberg, E., Egusa, H., Yatani, H. & Sohmura, T. Three-dimensional cell and tissue patterning in a strained fibrin gel system. *PLoS ONE* **2**, e1211 (2007).
73. Anderson, C. R., Ponce, A. M. & Price, R. J. Immunohistochemical identification of an extracellular matrix scaffold that microguides capillary sprouting in vivo. *J. Histochem. Cytochem* **52**, 1063–1072 (2004).

74. Korff, T. & Augustin, H. G. Integration of endothelial cells in multicellular spheroids prevents apoptosis and induces differentiation. *J. Cell Biol.* **143**, 1341–1352 (1998).
75. Sacharidou, A., Koh, W., Stratman, A. N., Mayo, A. M., Fisher, K. E. & Davis, G. E. Endothelial lumen signaling complexes control 3D matrix-specific tubulogenesis through interdependent Cdc42- and MT1-MMP-mediated events. *Blood* **115**, 5259–5269 (2010).
76. Korff, T. & Augustin, H. G. Tensional forces in fibrillar extracellular matrices control directional capillary sprouting. *J. Cell. Sci.* **112 (Pt 19)**, 3249–3258 (1999).
77. Alajati, A., Laib, A. M., Weber, H., Boos, A. M., Bartol, A., Ikenberg, K., Korff, T., Zentgraf, H., Obodozie, C., Graeser, R., Christian, S., Finkenzeller, G., Stark, G. B., Héroult, M. & Augustin, H. G. Spheroid-based engineering of a human vasculature in mice. *Nat. Methods* **5**, 439–445 (2008).
78. Laib, A. M., Bartol, A., Alajati, A., Korff, T., Weber, H. & Augustin, H. G. Spheroid-based human endothelial cell microvessel formation in vivo. *Nat. Protoc.* **4**, 1202–1215 (2009).
79. Dubey, N., Letourneau, P. C. & Tranquillo, R. T. Neuronal contact guidance in magnetically aligned fibrin gels: effect of variation in gel mechano-structural properties. *Biomaterials* **22**, 1065–1075 (2001).
80. Hudry-Clergeon, G., Freyssinet, J. M., Torbet, J. & Marx, J. Orientation of fibrin in strong magnetic fields. *Ann. N. Y. Acad. Sci* **408**, 380–387 (1983).
81. Ruggiero, M., Bottaro, D. P., Liguri, G., Gulisano, M., Peruzzi, B. & Pacini, S. 0.2 T magnetic field inhibits angiogenesis in chick embryo chorioallantoic membrane. *Bioelectromagnetics* **25**, 390–396 (2004).
82. Pacini, S., Gulisano, M., Peruzzi, B., Sgambati, E., Gheri, G., Gheri Bryk, S., Vannucchi, S., Polli, G. & Ruggiero, M. Effects of 0.2 T static magnetic field on human skin fibroblasts. *Cancer Detect. Prev* **27**, 327–332 (2003).
83. Wang, Z., Yang, P., Xu, H., Qian, A., Hu, L. & Shang, P. Inhibitory effects of a gradient static magnetic field on normal angiogenesis. *Bioelectromagnetics* **30**, 446–453 (2009).
84. Martino, C. F. Static magnetic field sensitivity of endothelial cells. *Bioelectromagnetics* (2011).doi:10.1002/bem.20665
85. Sullivan, K., Balin, A. K. & Allen, R. G. Effects of static magnetic fields on the growth of various types of human cells. *Bioelectromagnetics* **32**, 140–147 (2011).
86. Kim, Y. J., Sah, R. L., Doong, J. Y. & Grodzinsky, A. J. Fluorometric assay of DNA in cartilage explants using Hoechst 33258. *Anal. Biochem* **174**, 168–176 (1988).
87. Tower, T. T. & Tranquillo, R. T. Alignment maps of tissues: II. Fast harmonic analysis for imaging. *Biophys. J.* **81**, 2964–2971 (2001).
88. Fuller, G. Optical Rheometry. *Annual Review of Fluid Mechanics* **22**, 387–417 (1990).
89. Schmittgen, T. D. & Livak, K. J. Analyzing real-time PCR data by the comparative C(T) method. *Nat Protoc* **3**, 1101–1108 (2008).

90. Girton, T. S., Barocas, V. H. & Tranquillo, R. T. Confined compression of a tissue-equivalent: collagen fibril and cell alignment in response to anisotropic strain. *J Biomech Eng* **124**, 568–575 (2002).
91. Tranquillo, R. T. Self-organization of tissue-equivalents: the nature and role of contact guidance. *Biochem. Soc. Symp* **65**, 27–42 (1999).
92. East, E., de Oliveira, D. B., Golding, J. P. & Phillips, J. B. Alignment of astrocytes increases neuronal growth in three-dimensional collagen gels and is maintained following plastic compression to form a spinal cord repair conduit. *Tissue Eng Part A* **16**, 3173–3184 (2010).
93. Lanfer, B., Hermann, A., Kirsch, M., Freudenberg, U., Reuner, U., Werner, C. & Storch, A. Directed growth of adult human white matter stem cell-derived neurons on aligned fibrillar collagen. *Tissue Eng Part A* **16**, 1103–1113 (2010).
94. Yao, L., O'Brien, N., Windebank, A. & Pandit, A. Orienting neurite growth in electrospun fibrous neural conduits. *J. Biomed. Mater. Res. Part B Appl. Biomater* **90**, 483–491 (2009).
95. Li, J., McNally, H. & Shi, R. Enhanced neurite alignment on micro-patterned poly-L-lactic acid films. *J Biomed Mater Res A* **87**, 392–404 (2008).
96. Dickinson, R. B., Guido, S. & Tranquillo, R. T. Biased cell migration of fibroblasts exhibiting contact guidance in oriented collagen gels. *Ann Biomed Eng* **22**, 342–356 (1994).
97. Brown, W. R. & Thore, C. R. Review: cerebral microvascular pathology in ageing and neurodegeneration. *Neuropathol. Appl. Neurobiol.* **37**, 56–74 (2011).
98. Bostwick, D. G. & Iczkowski, K. A. Microvessel density in prostate cancer: prognostic and therapeutic utility. *Semin. Urol. Oncol.* **16**, 118–123 (1998).
99. Gealekman, O., Guseva, N., Gurav, K., Gusev, A., Hartigan, C., Thompson, M., Malkani, S. & Corvera, S. Effect of rosiglitazone on capillary density and angiogenesis in adipose tissue of normoglycaemic humans in a randomised controlled trial. *Diabetologia* **55**, 2794–2799 (2012).
100. Green, H. J., Burnett, M., Kollias, H., Ouyang, J., Smith, I. & Tupling, S. Association of peak aerobic power with capillary density but not oxidative potential in human vastus lateralis muscle. *Can. J. Physiol. Pharmacol.* **89**, 819–827 (2011).
101. Rufaihah, A. J., Huang, N. F., Jamé, S., Lee, J. C., Nguyen, H. N., Byers, B., De, A., Okogbaa, J., Rollins, M., Reijo-Pera, R., Gambhir, S. S. & Cooke, J. P. Endothelial cells derived from human iPSCs increase capillary density and improve perfusion in a mouse model of peripheral arterial disease. *Arterioscler. Thromb. Vasc. Biol.* **31**, e72–79 (2011).
102. Gonçalves, M. C., Bezerra, F. F., Eleutherio, E. C. de A., Bouskela, E. & Koury, J. Organic grape juice intake improves functional capillary density and postocclusive reactive hyperemia in triathletes. *Clinics (Sao Paulo)* **66**, 1537–1541 (2011).
103. Schmeling, H., Stephens, S., Goia, C., Manlhiot, C., Schneider, R., Luthra, S., Stringer, E. & Feldman, B. M. Nailfold capillary density is importantly

- associated over time with muscle and skin disease activity in juvenile dermatomyositis. *Rheumatology (Oxford)* **50**, 885–893 (2011).
104. Ranefall, P., Wester, K., Busch, C., Malmström, P. U. & Bengtsson, E. Automatic quantification of microvessels using unsupervised image analysis. *Anal Cell Pathol* **17**, 83–92 (1998).
 105. Kim, N. T., Elie, N., Plancoulaine, B., Herlin, P. & Coster, M. An original approach for quantification of blood vessels on the whole tumour section. *Anal Cell Pathol* **25**, 63–75 (2003).
 106. Cassot, F., Lauwers, F., Fouard, C., Prohaska, S. & Lauwers-Cances, V. A novel three-dimensional computer-assisted method for a quantitative study of microvascular networks of the human cerebral cortex. *Microcirculation* **13**, 1–18 (2006).
 107. Brey, E. M., King, T. W., Johnston, C., McIntire, L. V., Reece, G. P. & Patrick, C. W., Jr A technique for quantitative three-dimensional analysis of microvascular structure. *Microvasc. Res.* **63**, 279–294 (2002).
 108. Doukas, C. N., Maglogiannis, I. & Chatziioannou, A. A. Computer-supported angiogenesis quantification using image analysis and statistical averaging. *IEEE Trans Inf Technol Biomed* **12**, 650–657 (2008).
 109. Nowak-Sliwinska, P., Ballini, J.-P., Wagnières, G. & van den Bergh, H. Processing of fluorescence angiograms for the quantification of vascular effects induced by anti-angiogenic agents in the CAM model. *Microvasc. Res.* **79**, 21–28 (2010).
 110. Vickerman, M. B., Keith, P. A., McKay, T. L., Gedeon, D. J., Watanabe, M., Montano, M., Karunamuni, G., Kaiser, P. K., Sears, J. E., Ebrahim, Q., Ribita, D., Hylton, A. G. & Parsons-Wingerter, P. VESGEN 2D: automated, user-interactive software for quantification and mapping of angiogenic and lymphangiogenic trees and networks. *Anat Rec (Hoboken)* **292**, 320–332 (2009).
 111. Niemistö, A., Dunmire, V., Yli-Harja, O., Zhang, W. & Shmulevich, I. Robust quantification of in vitro angiogenesis through image analysis. *IEEE Trans Med Imaging* **24**, 549–553 (2005).
 112. Angulo, J. & Matou, S. Application of mathematical morphology to the quantification of in vitro endothelial cell organization into tubular-like structures. *Cell. Mol. Biol. (Noisy-le-grand)* **53**, 22–35 (2007).
 113. Saik, J. E., Gould, D. J., Watkins, E. M., Dickinson, M. E. & West, J. L. Covalently immobilized platelet-derived growth factor-BB promotes angiogenesis in biomimetic poly(ethylene glycol) hydrogels. *Acta Biomater* **7**, 133–143 (2011).
 114. Kaully, T., Kaufman-Francis, K., Lesman, A. & Levenberg, S. Vascularization-The Conduit to Viable Engineered Tissues. *Tissue Eng.Part B.Rev.* (2009).
 115. Price, G. M., Wong, K. H. K., Truslow, J. G., Leung, A. D., Acharya, C. & Tien, J. Effect of mechanical factors on the function of engineered human blood microvessels in microfluidic collagen gels. *Biomaterials* **31**, 6182–6189 (2010).

116. Collen, A., Hanemaaijer, R., Lupu, F., Quax, P. H., van Lent, N., Grimbergen, J., Peters, E., Koolwijk, P. & van Hinsbergh, V. W. Membrane-type matrix metalloproteinase-mediated angiogenesis in a fibrin-collagen matrix. *Blood* **101**, 1810–1817 (2003).
117. Lansink, M., Koolwijk, P., van Hinsbergh, V. & Kooistra, T. Effect of steroid hormones and retinoids on the formation of capillary-like tubular structures of human microvascular endothelial cells in fibrin matrices is related to urokinase expression. *Blood* **92**, 927–938 (1998).
118. Semino, C. E., Kamm, R. D. & Lauffenburger, D. A. Autocrine EGF receptor activation mediates endothelial cell migration and vascular morphogenesis induced by VEGF under interstitial flow. *Exp. Cell Res.* **312**, 289–298 (2006).
119. Vera, R. H., Genove, E., Alvarez, L., Borros, S., Kamm, R., Lauffenburger, D. & Semino, C. E. Interstitial Fluid Flow Intensity Modulates Endothelial Sprouting in Restricted Src-Activated Cell Clusters During Capillary Morphogenesis. *Tissue Eng. Part A*. (2008).
120. Griffith, C. K., Miller, C., Sainson, R. C., Calvert, J. W., Jeon, N. L., Hughes, C. C. & George, S. C. Diffusion limits of an in vitro thick prevascularized tissue. *Tissue Eng.* **11**, 257–266 (2005).
121. Grainger, S. & Putnam, A. J. Assessing the Permeability of Engineered Capillary Networks in a 3D Culture. *BMES Annual Meeting Abstract* (2010).
122. Sieminski, A. L., Hebbel, R. P. & Gooch, K. J. The relative magnitudes of endothelial force generation and matrix stiffness modulate capillary morphogenesis in vitro. *Exp. Cell Res.* **297**, 574–584 (2004).
123. Helm, C. L., Fleury, M. E., Zisch, A. H., Boschetti, F. & Swartz, M. A. Synergy between interstitial flow and VEGF directs capillary morphogenesis in vitro through a gradient amplification mechanism. *Proc. Natl. Acad. Sci. U.S.A.* **102**, 15779–15784 (2005).
124. Chen, X., Aledia, A. S., Popson, S. A., Him, L., Hughes, C. C. W. & George, S. C. Rapid anastomosis of endothelial progenitor cell-derived vessels with host vasculature is promoted by a high density of cotransplanted fibroblasts. *Tissue Eng Part A* **16**, 585–594 (2010).
125. Stratman, A. N., Schwindt, A. E., Malotte, K. M. & Davis, G. E. Endothelial-derived PDGF-BB and HB-EGF coordinately regulate pericyte recruitment during vasculogenic tube assembly and stabilization. *Blood* **116**, 4720–4730 (2010).
126. Levéen, P., Pekny, M., Gebre-Medhin, S., Swolin, B., Larsson, E. & Betsholtz, C. Mice deficient for PDGF B show renal, cardiovascular, and hematological abnormalities. *Genes Dev* **8**, 1875–1887 (1994).
127. Helmbold, P., Nayak, R. C., Marsch, W. C. & Herman, I. M. Isolation and in vitro characterization of human dermal microvascular pericytes. *Microvasc. Res* **61**, 160–165 (2001).
128. Clark, R. A., Nielsen, L. D., Welch, M. P. & McPherson, J. M. Collagen matrices attenuate the collagen-synthetic response of cultured fibroblasts to TGF-beta. *J. Cell. Sci.* **108 (Pt 3)**, 1251–1261 (1995).

129. Syedain, Z. H., Lahti, M., Johnson, S. L., Robinson, P. S., Ruth, G. R. & Bianco, R. W. Implantation of a Tissue-engineered Heart Valve From Human Fibroblasts Exhibiting Short Term Function in the Sheep Pulmonary Artery. *Card Vas Engr Tech* **2**, 101–112 (2011).
130. Syedain, Z. H., Meier, L. A., Lahti, M., Johnson, S. L., Hebbel, R. P. & Tranquillo, R. T. Implantation of completely biological, aligned engineered arteries pre-made from allogeneic fibroblasts in a sheep model. *Nat Med In Revision*,
131. Morin, K. T. & Tranquillo, R. T. Interstitial Flow Paper.
132. Grouf, J. L., Throm, A. M., Balestrini, J. L., Bush, K. A. & Billiar, K. L. Differential effects of EGF and TGF-beta1 on fibroblast activity in fibrin-based tissue equivalents. *Tissue Eng.* **13**, 799–807 (2007).
133. Grinnell, F. & Ho, C.-H. Transforming growth factor beta stimulates fibroblast-collagen matrix contraction by different mechanisms in mechanically loaded and unloaded matrices. *Exp. Cell Res.* **273**, 248–255 (2002).
134. Grinnell, F. Fibroblast-collagen-matrix contraction: growth-factor signalling and mechanical loading. *Trends Cell Biol.* **10**, 362–365 (2000).
135. Irving, R. J., Shore, A. C., Belton, N. R., Elton, R. A., Webb, D. J. & Walker, B. R. Low birth weight predicts higher blood pressure but not dermal capillary density in two populations. *Hypertension* **43**, 610–613 (2004).
136. Debbabi, H., Uzan, L., Mourad, J. J., Safar, M., Levy, B. I. & Tibiriça, E. Increased skin capillary density in treated essential hypertensive patients. *Am. J. Hypertens.* **19**, 477–483 (2006).
137. Fry, B. C., Lee, J., Smith, N. P. & Secomb, T. W. Estimation of blood flow rates in large microvascular networks. *Microcirculation* **19**, 530–538 (2012).
138. Secomb, T. W., Hsu, R., Park, E. Y. & Dewhirst, M. W. Green's function methods for analysis of oxygen delivery to tissue by microvascular networks. *Ann.Biomed.Eng.* **32**, 1519–1529 (2004).
139. Beard, D. A. & Bassingthwaighe, J. B. Modeling advection and diffusion of oxygen in complex vascular networks. *Ann Biomed Eng* **29**, 298–310 (2001).
140. Goldman, D. & Popel, A. S. A computational study of the effect of capillary network anastomoses and tortuosity on oxygen transport. *J. Theor. Biol.* **206**, 181–194 (2000).
141. Groebe, K. A versatile model of steady state O₂ supply to tissue. Application to skeletal muscle. *Biophys. J.* **57**, 485–498 (1990).
142. Lafleur, M. A., Handsley, M. M., Knauper, V., Murphy, G. & Edwards, D. R. Endothelial tubulogenesis within fibrin gels specifically requires the activity of membrane-type-matrix metalloproteinases (MT-MMPs). *J.Cell.Sci.* **115**, 3427–3438 (2002).
143. Chatzizisis, Y. S., Coskun, A. U., Jonas, M., Edelman, E. R., Feldman, C. L. & Stone, P. H. Role of endothelial shear stress in the natural history of coronary atherosclerosis and vascular remodeling: molecular, cellular, and vascular behavior. *J. Am. Coll. Cardiol.* **49**, 2379–2393 (2007).

144. Bogdanov, I. I., Mourzenko, V. V., Thovert, J. F. & Adler, P. M. Effective permeability of fractured porous media in steady state flow. *Water Resour.Res.* **39**, 1023 (2003).
145. Sherf, L., Ben-Shaul, Y., Lieberman, Y. & Neufeld, H. N. The human coronary microcirculation: an electron microscopic study. *Am. J. Cardiol.* **39**, 599–607 (1977).
146. Sangani, A. & Yao, C. Transport Processes in Random Arrays of Cylinders .2. Viscous-Flow. *Phys. Fluids* **31**, 2435–2444 (1988).
147. Gavin, T. P., Stallings, H. W., 3rd, Zwetsloot, K. A., Westerkamp, L. M., Ryan, N. A., Moore, R. A., Pofahl, W. E. & Hickner, R. C. Lower capillary density but no difference in VEGF expression in obese vs. lean young skeletal muscle in humans. *J. Appl. Physiol.* **98**, 315–321 (2005).
148. Duey, W. J., Bassett, D. R., Jr, Torok, D. J., Howley, E. T., Bond, V., Mancuso, P. & Trudell, R. Skeletal muscle fibre type and capillary density in college-aged blacks and whites. *Ann. Hum. Biol.* **24**, 323–331 (1997).
149. Ghanaati, S., Fuchs, S., Webber, M. J., Orth, C., Barbeck, M., Gomes, M. E., Reis, R. L. & Kirkpatrick, C. J. Rapid vascularization of starch-poly(caprolactone) in vivo by outgrowth endothelial cells in co-culture with primary osteoblasts. *J Tissue Eng Regen Med* **5**, e136–143 (2011).
150. Frerich, B., Lindemann, N., Kurtz-Hoffmann, J. & Oertel, K. In vitro model of a vascular stroma for the engineering of vascularized tissues. *Int.J.Oral Maxillofac.Surg.* **30**, 414–420 (2001).
151. Ghajar, C. M., Blevins, K. S., Hughes, C. C., George, S. C. & Putnam, A. J. Mesenchymal stem cells enhance angiogenesis in mechanically viable prevascularized tissues via early matrix metalloproteinase upregulation. *Tissue Eng.* **12**, 2875–2888 (2006).
152. Hudon, V., Berthod, F., Black, A. F., Damour, O., Germain, L. & Auger, F. A. A tissue-engineered endothelialized dermis to study the modulation of angiogenic and angiostatic molecules on capillary-like tube formation in vitro. *Br.J.Dermatol.* **148**, 1094–1104 (2003).
153. Levenberg, S., Rouwkema, J., Macdonald, M., Garfein, E., Kohane, D., Darland, D., Marini, R., van Blitterswijk, C., Mulligan, R., D'Amore, P. & Langer, R. Engineering vascularized skeletal muscle tissue. *NATURE BIOTECHNOLOGY* **23**, 879–884 (2005).
154. von Tell, D., Armulik, A. & Betsholtz, C. Pericytes and vascular stability. *Exp. Cell Res* **312**, 623–629 (2006).
155. Chang, C. C., Nunes, S. S., Sibole, S. C., Krishnan, L., Williams, S. K., Weiss, J. A. & Hoying, J. B. Angiogenesis in a microvascular construct for transplantation depends on the method of chamber circulation. *Tissue Eng Part A* **16**, 795–805 (2010).
156. Shepherd, B. R., Hoying, J. B. & Williams, S. K. Microvascular transplantation after acute myocardial infarction. *Tissue Eng* **13**, 2871–2879 (2007).
157. Shepherd, B. R., Chen, H. Y., Smith, C. M., Gruionu, G., Williams, S. K. & Hoying, J. B. Rapid perfusion and network remodeling in a microvascular

- construct after implantation. *Arterioscler. Thromb. Vasc. Biol.* **24**, 898–904 (2004).
158. Swartz, M. A. & Fleury, M. E. Interstitial flow and its effects in soft tissues. *Annu Rev Biomed Eng* **9**, 229–256 (2007).
 159. Ng, C. P., Helm, C. L. & Swartz, M. A. Interstitial flow differentially stimulates blood and lymphatic endothelial cell morphogenesis in vitro. *Microvasc. Res.* **68**, 258–264 (2004).
 160. DePaola, N., Phelps, J. E., Florez, L., Keese, C. R., Minnear, F. L., Giaever, I. & Vincent, P. Electrical impedance of cultured endothelium under fluid flow. *Ann Biomed Eng* **29**, 648–656 (2001).
 161. Seebach, J., Donnert, G., Kronstein, R., Werth, S., Wojciak-Stothard, B., Falzarano, D., Mrowietz, C., Hell, S. W. & Schnittler, H.-J. Regulation of endothelial barrier function during flow-induced conversion to an arterial phenotype. *Cardiovasc. Res.* **75**, 596–607 (2007).
 162. McIntire, L. V., Wagner, J. E., Papadaki, M., Whitson, P. A. & Eskin, S. G. Effect of Flow on Gene Regulation in Smooth Muscle Cells and Macromolecular Transport Across Endothelial Cell Monolayers. *Biol Bull* **194**, 394–399 (1998).
 163. Warboys, C. M., Eric Berson, R., Mann, G. E., Pearson, J. D. & Weinberg, P. D. Acute and chronic exposure to shear stress have opposite effects on endothelial permeability to macromolecules. *Am. J. Physiol. Heart Circ. Physiol.* **298**, H1850–1856 (2010).
 164. Tarbell, J. M. Shear stress and the endothelial transport barrier. *Cardiovasc. Res.* **87**, 320–330 (2010).
 165. Colgan, O. C., Ferguson, G., Collins, N. T., Murphy, R. P., Meade, G., Cahill, P. A. & Cummins, P. M. Regulation of bovine brain microvascular endothelial tight junction assembly and barrier function by laminar shear stress. *Am. J. Physiol. Heart Circ. Physiol.* **292**, H3190–3197 (2007).
 166. Siddharthan, V., Kim, Y. V., Liu, S. & Kim, K. S. Human astrocytes/astrocyte-conditioned medium and shear stress enhance the barrier properties of human brain microvascular endothelial cells. *Brain Res.* **1147**, 39–50 (2007).
 167. le Noble, F., Moyon, D., Pardanaud, L., Yuan, L., Djonov, V., Matthijsen, R., Bréant, C., Fleury, V. & Eichmann, A. Flow regulates arterial-venous differentiation in the chick embryo yolk sac. *Development* **131**, 361–375 (2004).
 168. Othman-Hassan, K., Patel, K., Papoutsis, M., Rodriguez-Niedenführ, M., Christ, B. & Wilting, J. Arterial identity of endothelial cells is controlled by local cues. *Dev. Biol.* **237**, 398–409 (2001).
 169. Korff, T., Dandekar, G., Pfaff, D., Füller, T., Goettsch, W., Morawietz, H., Schaffner, F. & Augustin, H. G. Endothelial ephrinB2 is controlled by microenvironmental determinants and associates context-dependently with CD31. *Arterioscler. Thromb. Vasc. Biol.* **26**, 468–474 (2006).
 170. Braun, J., Hoffmann, S. C., Feldner, A., Ludwig, T., Henning, R., Hecker, M. & Korff, T. Endothelial cell ephrinB2-dependent activation of monocytes in arteriosclerosis. *Arterioscler. Thromb. Vasc. Biol.* **31**, 297–305 (2011).

171. Gale, N. W., Baluk, P., Pan, L., Kwan, M., Holash, J., DeChiara, T. M., McDonald, D. M. & Yancopoulos, G. D. Ephrin-B2 selectively marks arterial vessels and neovascularization sites in the adult, with expression in both endothelial and smooth-muscle cells. *Dev. Biol.* **230**, 151–160 (2001).
172. Shin, D., Garcia-Cardena, G., Hayashi, S., Gerety, S., Asahara, T., Stavrakis, G., Isner, J., Folkman, J., Gimbrone, M. A., Jr & Anderson, D. J. Expression of ephrinB2 identifies a stable genetic difference between arterial and venous vascular smooth muscle as well as endothelial cells, and marks subsets of microvessels at sites of adult neovascularization. *Dev. Biol.* **230**, 139–150 (2001).
173. Kuijper, S., Turner, C. J. & Adams, R. H. Regulation of angiogenesis by Eph-ephrin interactions. *Trends Cardiovasc. Med.* **17**, 145–151 (2007).
174. Foubert, P., Silvestre, J.-S., Souttou, B., Barateau, V., Martin, C., Ebrahimian, T. G., Leré-Déan, C., Contreres, J. O., Sulpice, E., Levy, B. I., Plouët, J., Tobelem, G. & Le Ricousse-Roussanne, S. PSGL-1-mediated activation of EphB4 increases the proangiogenic potential of endothelial progenitor cells. *J. Clin. Invest.* **117**, 1527–1537 (2007).
175. Foo, S. S., Turner, C. J., Adams, S., Compagni, A., Aubyn, D., Kogata, N., Lindblom, P., Shani, M., Zicha, D. & Adams, R. H. Ephrin-B2 controls cell motility and adhesion during blood-vessel-wall assembly. *Cell* **124**, 161–173 (2006).
176. Masumura, T., Yamamoto, K., Shimizu, N., Obi, S. & Ando, J. Shear stress increases expression of the arterial endothelial marker ephrinB2 in murine ES cells via the VEGF-Notch signaling pathways. *Arterioscler. Thromb. Vasc. Biol.* **29**, 2125–2131 (2009).
177. Obi, S., Yamamoto, K., Shimizu, N., Kumagaya, S., Masumura, T., Sokabe, T., Asahara, T. & Ando, J. Fluid shear stress induces arterial differentiation of endothelial progenitor cells. *J. Appl. Physiol.* **106**, 203–211 (2009).
178. Goettsch, W., Augustin, H. G. & Morawietz, H. Down-regulation of endothelial ephrinB2 expression by laminar shear stress. *Endothelium* **11**, 259–265 (2004).
179. Wang, D. M. & Tarbell, J. M. Modeling interstitial flow in an artery wall allows estimation of wall shear stress on smooth muscle cells. *J Biomech Eng* **117**, 358–363 (1995).
180. Syedain, Z. H., Weinberg, J. S. & Tranquillo, R. T. Cyclic distension of fibrin-based tissue constructs: evidence of adaptation during growth of engineered connective tissue. *Proc. Natl. Acad. Sci. U.S.A* **105**, 6537–6542 (2008).
181. Rivilis, I., Milkiewicz, M., Boyd, P., Goldstein, J., Brown, M. D., Egginton, S., Hansen, F. M., Hudlicka, O. & Haas, T. L. Differential involvement of MMP-2 and VEGF during muscle stretch- versus shear stress-induced angiogenesis. *Am.J.Physiol.Heart Circ.Physiol.* **283**, H1430–8 (2002).
182. Milkiewicz, M., Doyle, J. L., Fudalewski, T., Ispanovic, E., Aghasi, M. & Haas, T. L. HIF-1alpha and HIF-2alpha play a central role in stretch-induced

- but not shear-stress-induced angiogenesis in rat skeletal muscle. *J.Physiol.* **583**, 753–766 (2007).
183. Hansen-Smith, F., Egginton, S., Zhou, A. L. & Hudlicka, O. Growth of arterioles precedes that of capillaries in stretch-induced angiogenesis in skeletal muscle. *Microvasc.Res.* **62**, 1–14 (2001).
 184. Wilson, C. J., Kasper, G., Schütz, M. A. & Duda, G. N. Cyclic strain disrupts endothelial network formation on Matrigel. *Microvasc. Res.* **78**, 358–363 (2009).
 185. Yung, Y. C., Chae, J., Buehler, M. J., Hunter, C. P. & Mooney, D. J. Cyclic tensile strain triggers a sequence of autocrine and paracrine signaling to regulate angiogenic sprouting in human vascular cells. *Proc. Natl. Acad. Sci. U.S.A.* **106**, 15279–15284 (2009).
 186. Kou, B., Zhang, J. & Singer, D. R. Effects of cyclic strain on endothelial cell apoptosis and tubulogenesis are dependent on ROS production via NAD(P)H subunit p22phox. *Microvasc.Res.* (2008).
 187. Morrow, D., Cullen, J. P., Cahill, P. A. & Redmond, E. M. Cyclic strain regulates the Notch/CBF-1 signaling pathway in endothelial cells: role in angiogenic activity. *Arterioscler. Thromb. Vasc.Biol.* **27**, 1289–1296 (2007).
 188. Chang, H., Wang, B. W., Kuan, P. & Shyu, K. G. Cyclical mechanical stretch enhances angiopoietin-2 and Tie2 receptor expression in cultured human umbilical vein endothelial cells. *Clin.Sci.(Lond)* **104**, 421–428 (2003).
 189. Zheng, W., Christensen, L. P. & Tomanek, R. J. Stretch induces upregulation of key tyrosine kinase receptors in microvascular endothelial cells. *Am.J.Physiol.Heart Circ.Physiol.* **287**, H2739–45 (2004).

Appendix A. Protocols

A.1 BOEC Culture

1. Collagen Coating

- a. Using the concentration listed on the collagen bottle (which varies by lot), calculate the volume of collagen solution needed to obtain 25 mg collagen. It should be around 6-7 ml.
- b. Subtract this volume from 500 and measure out this volume of ddH₂O using a 500 ml graduated cylinder.
- c. Add 0.575 ml glacial acetic acid to the ddH₂O.
- d. Sterile filter the water/acid solution using a 0.22 µm filter.
- e. Add 25 mg collagen and mix. Final concentration is 0.05 mg/ml.

2. Coating Flasks

- a. Add 5 ml (T75) or 10 ml (T175) of 0.05 mg/ml collagen to each flask and make sure the solution covers the entire bottom of the flask.
- b. Incubate at 37°C for at least 10 min (can be much longer, even up to several days).
- c. Aspirate collagen and rinse flasks with 5 ml HBSS. Aspirate HBSS.
- d. At this point the flasks can be used immediately or stored at 4°C for up to 2 weeks.

3. Thawing Cells

- a. Warm 10 ml (T75) or 23 ml (T175) of BOEC medium to 37°C.
- b. Take vial of hBOECs from liquid nitrogen. From here, move as quickly as possible.
- c. Warm the cells for 2 min. at in the 37°C waterbath.
- d. In the hood, open the vial and add warm BOEC medium to the vial. Pour contents of vial into the conical of medium.
- e. Repeat step d until the entire contents of the vial are transferred to the conical. At this point, one no longer needs to move as quickly as possible. The cells have been warmed to 37°C, and the DMSO in the freezing solution has been diluted.
- f. Transfer contents of the conical to a collagen-coated flask.
- g. Change the medium the next day to remove residual DMSO.

4. Splitting Cells

- a. Thaw 2.5-3 ml (T75) or 5 ml (T175) 0.5% trypsin per flask.
- b. Rinse flasks twice with 5 ml HBSS.
- c. Add trypsin and incubate at 37°C for 3 minutes.

- d. Quickly view flasks to make sure the cells have lifted.
- e. Add 0.5 ml (T75) or 1 ml (T175) FBS to quench the trypsin.
- f. Pipette cells into a 50 ml conical tube. Rinse each flask twice with HBSS (serial rinses are fine), pipetting the rinse solution into the conical.
- g. Centrifuge at 220xg for 5 minutes.
- h. Resuspend cells in BOEC medium. Aim for about 1 M/ml for easy counting. Expect 1-2 M (T75) or 3-4 M (T175) per flask.
- i. Add 50 µl cell solution to a trypan blue aliquot (75 µl trypan blue + 125 µl PBS). Add 10 µl of this solution to a hemocytometer and count cells.

$$\frac{\text{Cells}}{\text{ml}} = \frac{\text{Cell Count}}{4} * 5 * 10,000$$

4 represents the average of the 4 boxes counted, 5 is the dilution of the cells in trypan blue, and 10,000 is the multiplier based on the design of the hemocytometer.

- j. Plate into collagen-coated flasks at a 1:4 split. This should be about 0.4-0.5 M cells per T75 or 0.8-1 M cells per T175.

5. Freezing Cells

- a. Split cells as usual. Resuspend at twice the desired concentration in BOEC medium. (eg. for 1 M aliquots, each having 1 ml of solution, resuspend at 2 M/ml.) Place cells on ice.
- b. Make a solution of 10% DMSO in FBS. Make 0.5 ml for each aliquot. The introduction of an aqueous solution to DMSO produces heat, so put this solution on ice and do not use until it is cold.
- c. Mix cells and DMSO/FBS at a 1:1 ratio and pipette 1 ml into each pre-labeled cryovial. DMSO protects cells during freezing, but is toxic to cells at warmer temperatures, so move as quickly as possible after mixing cells and DMSO.
- d. Transfer vials to a Mr. Frosty filled with isopropyl alcohol and place at -80°C overnight. Mr. Frosty ensures a steady drop of 1°C per minute, which is optimal for most cell types.
- e. Transfer vials to liquid nitrogen.

	Supplier	Product Number	UStores Number	Storage (°C)	Description	Autoclaved?
Reagents						
Collagen	BD Biosciences	354236		4		
Glacial Acetic Acid	Fisher Scientific	BP2401-212		25		
HBSS	Gibco	14175		25		
BOEC medium	Lonza	CC-3162		EBM-2: 4, Bullet Kit: -20, BOEC Medium: 4	BOEC medium good for ~2 wk at 4C. Do not freeze.	
Trypsin	Gibco	25300		-20	0.5%	
FBS	Hyclone	"Characterized"		4 for quenching		
DMSO	Sigma	D2438		25		
Isopropyl Alcohol	Sigma	W292907		25		
Trypan Blue	Gibco	15250		25		
Equipment						
Mr. Frosty	Sigma	C1562				

A.2 HUVEC Culture

1. Gelatin Coating

- a. Mix 500 mg gelatin with 500 ml PBS. Place in 37°C water bath until gelatin is dissolved.
- b. Sterile filter using a 0.22 µm filter.
- c. Final concentration is 1 mg/ml.

2. Coating Flasks

- a. Add 7 ml (T75) or 15 ml (T175) of 1 mg/ml gelatin to each flask and make sure the solution covers the entire bottom of the flask.
- b. Incubate at RT for at least 30 min (can be much longer, but do not leave overnight).
- c. Aspirate gelatin. Do not rinse. Use immediately.

3. Thawing Cells

- a. Warm 9 ml and 20 ml supermedium to 37°C in separated tubes.
- b. Take vial of HUVECs from liquid nitrogen. From here, move as quickly as possible.
- c. Warm the cells for 2 min. at in the 37°C waterbath.
- d. In the hood, open the vial and add warm PC medium to the vial. Pour contents of vial into the conical of medium.
- e. Repeat step d until the entire contents of the vial are transferred to the conical. At this point, one no longer needs to move as quickly as possible. The cells have been warmed to 37°C, and the DMSO in the freezing solution has been diluted.
- f. Spin cells at 350xg for 5 minute.
- g. Resuspend in 5 ml.
- h. Spin cells again at 350xg for 5 minute.
- i. Resuspend in 15 ml.
- j. Transfer contents of the conical to a gelatin-coated T75 flask.
- k. Change medium every 2-3 days. Use 30 ml supermedium for a T175 flask.

4. Priming Cells

- a. Typically done in the late afternoon on the day prior to casting.
- b. Warm 9 ml antibiotic M199 for a T75 (scale everything up proportionally for a T175).
- c. Add 36 µl RSII, 9 µl FGF, and 36 µl VEGF to the M199.
- d. Replace supermedium in the flask with the priming medium.

5. Splitting Cells

- a. Thaw 2 ml (T75) or 5 ml (T175) 0.5% trypsin per flask.
- b. Rinse flasks with 10 ml (T75) or 23 ml (T175) PBS.
- c. Add trypsin and incubate at 37°C for 1 minute.
- d. Quickly view flasks to make sure the cells have lifted.
- e. Add 2 ml (T75) or 5 ml (T175) FBS to quench the trypsin.
- f. Add 6 ml (T75) or 14 ml (T175) aM199 to the flask. Pipette cells into a conical tube.
- g. Centrifuge at 350xg for 5 minutes.
- h. Resuspend cells in PC medium. Aim for about 1 M/ml for easy counting. Expect 2 M (T75) or 5 M (T175) per flask.
- i. Add 50 µl cell solution to a trypan blue aliquot (75 µl trypan blue + 125 µl PBS). Add 10 µl of this solution to a hemocytometer and count cells.

$$\frac{\text{Cells}}{\text{ml}} = \frac{\text{Cell Count}}{4} * 5 * 10,000$$

4 represents the average of the 4 boxes counted, 5 is the dilution of the cells in trypan blue, and 10,000 is the multiplier based on the design of the hemocytometer.

- j. Plate into gelatin-coated flasks at a 1:6 split.
- k. Use only fully confluent cells for experiments. HUVECs may be confluent for several days prior to casting. Use up to passage 5.

6. Freezing Cells

- a. Split cells as usual. Resuspend at twice the desired concentration in antibiotic M199. (eg. for 1 M aliquots, each having 1 ml of solution, resuspend at 2 M/ml.) Place cells on ice.
- b. Make a solution of 20% DMSO and 20% FBS in PC medium. Make 0.5 ml for each aliquot. The introduction of an aqueous solution to DMSO produces heat, so put this solution on ice and do not use until it is cold.
- c. Mix cells and DMSO/FBS/PC medium at a 1:1 ratio and pipette 1 ml into each pre-labeled cryovial. DMSO protects cells during freezing, but is toxic to cells at warmer temperatures, so move as quickly as possible after mixing cells and DMSO.
- d. Transfer vials to a Mr. Frosty filled with isopropyl alcohol and place at -80°C overnight. Mr. Frosty ensures a steady drop of 1°C per minute, which is optimal for most cell types.
- e. Transfer vials to liquid nitrogen.

	Supplier	Product Number	UStores Number	Storage (°C)	Description	Autoclaved?
Reagents						
Gelatin	Sigma	G2500		25		
PBS	Mediatech	21-031-CM		25		
Supermedium				4	See protocol	
Trypsin	Gibco	25300		-20	0.5%	
FBS	Hyclone	"Characterized"		4 for quenching		
DMSO	Sigma	D2438		25		
Isopropyl Alcohol	Sigma	W292907		25		
Trypan Blue	Gibco	15250		25		
Antibiotic M199					See protocol	
RSII					Obtained from Davis lab	
FGF	R&D Systems	233-FB/CF		-20	Stock 40 µg/ml, use at 1:1000 dilution (40 ng/ml)	
VEGF	R&D Systems	293-VE/CF		-20	Stock 10 µg/ml, use at 1:250 dilution (40 ng/ml)	
Equipment						
Mr. Frosty	Sigma	C1562				

A.3 nhDF Culture

1. Thawing Cells

- a. Warm 15 ml (T75) or 30 ml (T175) of nhDF medium to 37°C.
- b. Take vial of nhDFs from liquid nitrogen. From here, move as quickly as possible.
- c. Warm the cells for 2 min. at in the 37°C waterbath.
- d. In the hood, open the vial and add warm nhDF medium to the vial. Pour contents of vial into the conical of medium.
- e. Repeat step d until the entire contents of the vial are transferred to the conical. At this point, one no longer needs to move as quickly as possible. The cells have been warmed to 37°C, and the DMSO in the freezing solution has been diluted.
- f. Transfer contents of the conical to a gelatin-coated flask.
- g. Change the medium the next day to remove residual DMSO.

2. Splitting Cells

- a. Thaw 2.5-3 ml (T75) or 5 ml (T175) 0.5% trypsin per flask.
- b. Rinse flasks twice with 5 ml PBS.
- c. Add trypsin and incubate at 37°C for 3 minutes.
- d. Quickly view flasks to make sure the cells have lifted.
- e. Add 0.5 ml (T75) or 1 ml (T175) FBS to quench the trypsin.
- f. Pipette cells into a 50 ml conical tube. Rinse each flask twice with PBS (serial rinses are fine), pipetting the rinse solution into the conical.
- g. Centrifuge at 220xg for 5 minutes.
- h. Resuspend cells in nhDF medium. Aim for about 1 M/ml for easy counting. Expect 3-4 M (T75) or 7-8 M (T175) per flask.
- i. Add 50 µl cell solution to a trypan blue aliquot (75 µl trypan blue + 125 µl PBS). Add 10 µl of this solution to a hemocytometer and count cells.

$$\frac{\text{Cells}}{\text{ml}} = \frac{\text{Cell Count}}{4} * 5 * 10,000$$

4 represents the average of the 4 boxes counted, 5 is the dilution of the cells in trypan blue, and 10,000 is the multiplier based on the design of the hemocytometer.

- j. Plate 1.5 M/T175.

3. Freezing Cells

- a. Split cells as usual. Resuspend at twice the desired concentration in nhDF medium. (eg. for 1 M aliquots, each having 1 ml of solution, resuspend at 2 M/ml.) Place cells on ice.

- b. Make a solution of 10% DMSO in FBS. Make 0.5 ml for each aliquot. The introduction of an aqueous solution to DMSO produces heat, so put this solution on ice and do not use until it is cold.
- c. Mix cells and DMSO/FBS at a 1:1 ratio and pipette 1 ml into each pre-labeled cryovial. DMSO protects cells during freezing, but is toxic to cells at warmer temperatures, so move as quickly as possible after mixing cells and DMSO.
- d. Transfer vials to a Mr. Frosty filled with isopropyl alcohol and place at -80°C overnight. Mr. Frosty ensures a steady drop of 1°C per minute, which is optimal for most cell types.
- e. Transfer vials to liquid nitrogen.

	Supplier	Product Number	UStores Number	Storage (°C)	Description	Autoclaved?
Reagents						
PBS	Mediatech	21-031-CM		25		
nhDF medium				4	See protocol	
Trypsin	Gibco	25300		-20	0.5%	
FBS	Hyclone	"Characterized"		4 for quenching		
DMSO	Sigma	D2438		25		
Isopropyl Alcohol	Sigma	W292907		25		
Trypan Blue	Gibco	15250		25		
Equipment						
Mr. Frosty	Sigma	C1562				

A.4 Pericyte Culture

1. Gelatin Coating

- a. Mix 500 mg gelatin with 500 ml PBS. Place in 37°C water bath until gelatin is dissolved.
- b. Sterile filter using a 0.22 µm filter.
- c. Final concentration is 1 mg/ml.

2. Coating Flasks

- a. Add 7 ml (T75) or 15 ml (T175) of 1 mg/ml gelatin to each flask and make sure the solution covers the entire bottom of the flask.
- b. Incubate at RT for at least 30 min (can be much longer, but do not leave overnight).
- c. Aspirate gelatin. Do not rinse. Use immediately.

3. Thawing Cells

- a. Warm 9 ml and 18 ml PC medium to 37°C in separated tubes.
- b. Take vial of PCs from liquid nitrogen. From here, move as quickly as possible.
- c. Warm the cells for 2 min. at in the 37°C waterbath.
- d. In the hood, open the vial and add warm PC medium to the vial. Pour contents of vial into the conical of medium.
- e. Repeat step d until the entire contents of the vial are transferred to the conical. At this point, one no longer needs to move as quickly as possible. The cells have been warmed to 37°C, and the DMSO in the freezing solution has been diluted.
- f. Spin cells at 350xg for 5 minute.
- g. Resuspend in 5 ml.
- h. Spin cells again at 350xg for 5 minute.
- i. Resuspend in 13 ml.
- j. Transfer contents of the conical to a gelatin-coated T75 flask and add 2 ml freshly thawed FBS.
- k. Change medium every 2-3 days, always using freshly thawed FBS. Use 26 ml DMEM + 4 ml FBS for a T175 flask.

4. Splitting Cells

- a. Thaw 2 ml (T75) or 5 ml (T175) 0.5% trypsin per flask.
- b. Rinse flasks with 10 ml (T75) or 23 ml (T175) PBS.
- c. Add trypsin and incubate at 37°C for 1 minute.
- d. Quickly view flasks to make sure the cells have lifted.
- e. Add 2 ml (T75) or 5 ml (T175) FBS to quench the trypsin.

- f. Add 6 ml (T75) or 14 ml (T175) aM199 to the flask. Pipette cells into a conical tube.
- g. Centrifuge at 350xg for 5 minutes.
- h. Resuspend cells in PC medium. Aim for about 1 M/ml for easy counting. Expect 2 M (T75) or 5 M (T175) per flask.
- i. Add 50 μ l cell solution to a trypan blue aliquot (75 μ l trypan blue + 125 μ l PBS). Add 10 μ l of this solution to a hemocytometer and count cells.

$$\frac{\text{Cells}}{\text{ml}} = \frac{\text{Cell Count}}{4} * 5 * 10,000$$

4 represents the average of the 4 boxes counted, 5 is the dilution of the cells in trypan blue, and 10,000 is the multiplier based on the design of the hemocytometer.

- j. Plate into gelatin-coated flasks at a 1:6 split.
- k. Use only overconfluent cells for experiments (achieved by growing flasks for ~10 days between splits), as subconfluent or confluent cells will not recruit well. Use up to passage 8.

5. Freezing Cells

- a. Split cells as usual. Resuspend at twice the desired concentration in PC medium. (eg. for 1 M aliquots, each having 1 ml of solution, resuspend at 2 M/ml.) Place cells on ice.
- b. Make a solution of 20% DMSO and 20% FBS in PC medium. Make 0.5 ml for each aliquot. The introduction of an aqueous solution to DMSO produces heat, so put this solution on ice and do not use until it is cold.
- c. Mix cells and DMSO/FBS/PC medium at a 1:1 ratio and pipette 1 ml into each pre-labeled cryovial. DMSO protects cells during freezing, but is toxic to cells at warmer temperatures, so move as quickly as possible after mixing cells and DMSO.
- d. Transfer vials to a Mr. Frosty filled with isopropyl alcohol and place at -80°C overnight. Mr. Frosty ensures a steady drop of 1°C per minute, which is optimal for most cell types.
- e. Transfer vials to liquid nitrogen.

	Supplier	Product Number	UStores Number	Storage (°C)	Description	Autoclaved?
Reagents						
Gelatin	Sigma	G2500		25		
PBS	Mediatech	21-031-CM		25		
PC medium				4	See protocol	
Trypsin	Gibco	25300		-20	0.5%	
FBS	Hyclone	"Characterized"		4 for quenching		
DMSO	Sigma	D2438		25		
Isopropyl Alcohol	Sigma	W292907		25		
Trypan Blue	Gibco	15250		25		
Equipment						
Mr. Frosty	Sigma	C1562				

A.5 Culture Media

1. BOEC Medium

- a. Thaw Bullet Kit components at RT except FBS, which can be thawed in a 37°C waterbath. Thaw an additional 40 ml FBS and 5 ml penicillin/streptomycin (P/S).
- b. Centrifuge growth factors at 220xg for 5 min to ensure all liquid is at the base of the vial.
- c. Using a 1000 ml pipette, carefully pipette each growth factor into a freshly opened bottle of EBM-2.
- d. Add all FBS (total of 50 ml), and 5 ml P/S. Swirl to mix.
- e. Store at 4°C for up to 2 weeks. Do not freeze.
- f. When feeding, only warm up the amount needed for that feeding. Discard any extra that was warmed and not used.

2. PC Medium

- a. Thaw 5 ml penicillin/streptomycin (P/S).
- b. Add 5 ml P/S and 500 µl gentamicin to a freshly opened bottle of DMEM low glucose.
- c. Store at 4°C.
- d. When feeding, only warm up the amount needed for that feeding. Discard any extra that was warmed and not used. Freshly thawed FBS is added to each flask at the time of feeding.

3. nhDF Medium

- a. Thaw 50 ml FBS and 5 ml P/S.
- b. Add FBS and P/S to a freshly opened bottle of DMEM/F-12.
- c. Store at 4°C for up to 4 weeks.
- d. When feeding, only warm up the amount needed for that feeding. Discard any extra that was warmed and not used.

4. Supermedium

- a. Thaw 100 ml FBS and 5 ml antibiotic/antimycotic.
- b. Weigh 200 mg bovine brain extract and 50 mg heparin salt and add them to a freshly opened 500 ml bottle of 1x M199. Mix well.
- c. Place the M199 in a 37°C waterbath for at least 30 min.
- d. Sterile filter the M199 through a 0.22 µm filter.
- e. Add FBS and antibiotic/antimycotic.
- f. Add 600 µl Gentamicin.
- g. Store at 4°C.

- h. When feeding, only warm up the amount needed for that feeding. Discard any extra that was warmed and not used.

5. Antibiotic M199

- a. Add 5 ml antibiotic/antimycotic and 500 μ l gentamicin to a freshly opened bottle of M199.
- b. Store at 4C.
- c. When using, only warm up the amount needed. Discard any extra that was warmed and not used.

6. Defined Medium

- a. At the time of feeding, add 4 μ l RSII, 1 μ l FGF, 10 μ l ascorbic acid, and 0.25 μ l aprotinin per 1 ml of 1x antibiotic M199.
- b. FGF can be stored at 4°C for up to 4 weeks. AA can be refrozen many times.

	Supplier	Product Number	UStores Number	Storage (°C)	Description	Autoclaved?
Reagents						
BOEC medium	Lonza	CC-3162		EBM-2: 4, Bullet Kit: -20, BOEC Medium: 4		
FBS	HyClone	"Characterized"		-20		
Penicillin/Streptomycin	Gibco	15140		-20		
Gentamicin	Gibco	15710		25		
DMEM low glucose	Gibco	11885		4		
Antibiotic/antimycotic	Gibco	15240		-20		
Heparin salt	Sigma	H3393	H3393- 100KU	4		
Bovine brain extract				4	Obtained from Davis lab	
1x M199	Gibco	11150		4		
Gentamicin	Gibco	15710	15710064	25		
RSII				4	Obtained from Davis lab	
FGF	R&D Systems	233-FB/CF		-20	Stock 40 µg/ml, use at 1:1000 dilution (40 ng/ml)	
Ascorbic acid	Sigma	A5960		-20	Stock 5 mg/ml, use at 1:100 dilution (50 µg/ml)	
DMEM/F-12	Mediatech	10-090-CV		4		

A.6 BOEC Spheroid Experiments

1. Gel Formulation – Magnetically Aligned Constructs

For 1 ml Gel (3.3 mg/ml)

μl	Component
112	Fibrinogen (30 mg/ml stock)
680	EBM-2+GF
85	EC Spheroids
85	nhDF
3.2	Thrombin (50 U/ml stock)

For 3 Gels

μl	Component
1188	F solution
128	ECs
128	PCs
4.8	Thrombin
1500	Total

2. Gel Formulation – Cell-Aligned Constructs

For 1 ml Gel
(3.3 mg/ml)

μl	Component
112	Fibrinogen (30 mg/ml stock)
680	EBM-2+GF
85	EC Spheroids
85	nhDF
50	Thrombin (50 U/ml stock)

For Aspect Ratio 1

μl	Component
198	F solution
21	EC Spheroids
21	nhDF
12.	Thrombin
5	
250	Total

For Aspect Ratio 2

μl	Component
396	F solution
42	EC Spheroids
42	nhDF
25	Thrombin
500	Total

For Aspect Ratio 3

μl	Component
594	F solution
64	EC Spheroids
64	nhDF
37.	Thrombin
5	
750	Total

3. Making Methylcellulose Medium

- a. Autoclave 1.2 g methylcellulose (Sigma M0512) and a stir bar in a 100 ml glass bottle.
- b. Add 100 ml EBM-2 (Lonza).
- c. Stir at 4C for about 1 hour.
- d. Using a sterilized small spatula, break up clumps.

- e. Stir at 4C overnight.
- f. Divide evenly between 2 50 ml conical tubes.
- g. Centrifuge at 3200xg for 3 hours.
- h. Pipette all except the bottom 5 ml from each tube into a new bottle.

4. Making Spheroids

- a. Split hBOECs as usual and stain the appropriate number of cells with celltracker dye if desired.
- b. Resuspend the cells in “spheroid medium” (80% BOEC medium, 20% methylcellulose medium) at a concentration of 20,000 cell/ml.
- c. Transfer the cells to a sterile reagent reservoir for multichannel pipettes (e.g. Costar 4870).
- d. Using a multichannel pipette, transfer 25 μ l drops of cell solution onto the top of a 150 mm petri dish (e.g. Corning 430597). Using the top is critical as the drops spread out on tissue-culture treated surfaces. 12 rows of 12 drops fit well.
- e. Culture overnight at 37°C with the drops hanging down from the top of the dish.
- f. Invert the dish and view under transmitted light to verify spheroid formation.

5. Harvesting Spheroids

- a. Add 5 ml HBSS (Gibco 14175) to the top of the petri dish containing spheroid drops.
- b. Tilt the dish to spread the HBSS across the entire surface.
- c. Gently pipette the solution either into a 15 ml conical tube or onto another petri dish containing spheroid drops.
- d. Allow spheroids to settle to the bottom of the 15 ml conical tube for at least 20 minutes.
- e. Aspirate off some medium to enable a micropipette tip to reach the bottom of the tube
- f. With the micropipette tip at the bottom of the tube, collect as much volume as needed, moving the tip around the bottom as the plunger is let up. It is possible to see spheroids as tiny dots within the tip
- g. If spheroids are seen to be broken apart, try pipetting more gently in steps (c) and (f) or cutting off the tip of a micropipette tip with a sterile scissors.

6. Making Magnetically-Aligned Constructs

- a. Arrange 1 hour of time on the magnet(s) at CMRR. If multiple magnets are needed, they can be used during the same hour.
- b. Make spheroids the day before going to CMRR.
- c. Prepare the wells: Use a cotton-tipped sterile applicator to put vacuum grease on one end of 2 autoclaved Teflon rings (1.5 cm

diameter). Place an autoclaved 24x60 mm glass coverslip on top of the rings. Use another cotton-tipped sterile applicator to press the coverslip onto the rings. Make sure the seal is tight. Wrap glass coverslips in kim wipes during autoclaving to prevent them from sticking together. Place wells in plastic jars, cushioned by autoclaved kim wipes, for transport to CMRR.

- d. Take fibrinogen and thrombin out of the freezer 1.5 hours before first use at the magnet. Allow them to thaw at RT for 20 minutes, then keep on ice.
- e. Split nhDF according to standard protocol and resuspend at 3 million/ml. Keep on ice.
- f. Harvest spheroids into 2 conical tubes per magnet condition.
- g. Transfer the appropriate volume of spheroids into a sterile microcentrifuge tube and keep on ice.
- h. Transfer the appropriate volume of nhDFs into microcentrifuge tubes and keep on ice.
- i. Transfer the appropriate volume of thrombin into microcentrifuge tubes and keep on ice.
- j. Combine enough fibrinogen and EBM-2 + GF for the entire experiment. Aliquot the appropriate volume into microcentrifuge tubes and keep on ice.
- k. Pack fibrinogen solution, thrombin, spheroids, nhDF, pipettors and tips, several well plate covers, wells and a microcentrifuge tube rack for transport to CMRR.
- l. At CMRR, place the wells for a give magnet on top of a well plate cover placed on the spot that will be in the magnet's isocenter when the platform is moved in.
- m. Mix components for half of the wells (~3 gels) and pipette 500 μ l into each well. Cover wells with another well plate cover.
- n. As soon as possible, move the platform into the magnet and leave there for 15 minutes.
- o. Move the platform out of the magnet and mix the components for the rest of the wells. Pipette 500 μ l into each well and cover with the well plate cover.
- p. As soon as possible, move the platform into the magnet and leave there for 15 minutes.
- q. Back at the lab, make isotropic control gels and allow to gel for 15 min at RT.
- r. Add 1 ml BOEC medium to each well, and transfer wells to an autoclaved pyrex dish for easier incubation. Use a piece of foam in the bottom of the dish to prevent the coverslips from sticking to the bottom.

7. Making Cell-Aligned Constructs

- a. Make slab molds in the desired aspect ratios. Use the metal stamp to make score marks in the plastic of a well plate or petri dish. Draw the rectangle on the underside of the plate and use this as a guide to make score marks. Using a sterile cotton-tipped applicator, apply a dollop of sterile vacuum grease inside the left and right edges of each score mark. Attach a porous polyethylene spacer to each dollop, keeping the rougher side up. To prepare for lifting the slabs, mark the outside of a new well plate or petri dish with dots to indicate where vacuum grease will go, and lines to mark where the outer edge of the spacer should go. Apply dollops of vacuum grease to the dots.
- b. Prepare and harvest spheroids.
- c. Thaw fibrinogen and thrombin at RT. When thawed, keep on ice.
- d. Split nhDF according to standard protocol and resuspend at 3 million/ml. Keep on ice.
- e. Mix enough fibrinogen and EBM-2 + GF for the entire experiment and aliquot out enough for each slab. Keep on ice. The standard slab (gel size: 1.5 cm x 1 cm) requires 400 μ l of gel.
- f. For each slab, add the appropriate volumes of spheroids and nhDFs. Warm the vial briefly, then add thrombin. Mix gently for approximately 30 seconds.
- g. Pipette the solution into the mold. Drip some solution directly onto the inner edge of the spacer to ensure good penetration of the gel into the spacer. Ideally gellation occurs simultaneously with the end of pipetting. This timing minimizes the number of spheroids that sink to the bottom of the gel. After lifting, spheroids at the bottom of the gel form a monolayer at the bottom of the gel rather than sprouting.
- h. Cover the slabs with BOEC medium (3 ml for a standard slab in a 6 well plate). Multiple sizes of gels can also be made in a 150 mm petri dish and Teflon spacers used to minimize medium usage.
- i. The next day, aspirate the medium, and use sterile blunt-end forceps to gently loosen the top and bottom edges of the gel from the score mark. Grab both spacers simultaneously using forceps and move the spacers toward each other. The gel should easily loosen from the plate. Move the spacers left and right to ensure that the gel is completely free. Then transfer the gel to the new plate. Place the spacers on the dollops of vacuum grease and make sure the edge of the spacer is aligned with the line. Add new BOEC medium.

8. Harvesting Constructs

- a. Fix in 4% PFA for 10 min.

- i. For magnetically-aligned constructs, aspirate medium and add 1 ml PFA to each well.
 - ii. For cell-aligned constructs, lift each gel via the spacers and place into a well containing PFA. Make sure the construct is not wrinkled or folded during fixation.
- b. Rinse 3x with PBS for 5 min each.

	Supplier	Product Number	UStores Number	Storage (°C)	Description	Autoclaved?
Reagents						
Methylcellulose	Sigma	M0512		25		
HBSS	Gibco	14175		25		
EBM-2 + GF	Lonza	CC-3162		EBM-2: 4, bullet kit: -20, made up solution: -20	Same as BOEC medium, but with no FBS or P/S	
Fibrinogen	Sigma	F8630		-20	30 mg/ml stock	
Thrombin	Sigma	T7513		-80	25 U/ml stock	
4% PFA	Electron Microscopy Sciences	15710		16% stock: 4, 4% -20	Make up 4% solution from 16% by combining with 1.33x PBS	
Supplies						
Kim Wipes	UStores		CX21272			X
Glass Coverslips	Gold Seal	3322				X
Vacuum grease	Dow Corning				High vacuum grease	X
Microcentrifuge tubes	UStores		CX13136			X
Cotton-tipped applicator	UStores		MS01172			
Sterile Gloves	UStores		CX40770			
Equipment						
Teflon Rings	Custom				~12 well plate size. Inner Diameter = 1.5 cm, Height = 2.4 cm	X
Metal stamp	Custom				Makes rectangle 1x2.5 cm	X
Porous PE spacers	unknown				Cut to 0.5x1cm	X
Spatula	UStores		87731			
Blunt forceps	UStores		CX12372			

A.7 HUVEC PC Fibrin Experiments

1. Gel Formulation

For "1 ml" Gel ("10 mg/ml") Actually 1.359 ml, 7.4 mg/ml

μl	Component
1000	Fibrinogen
4	SCF
4	IL-3
4	FLT3 Ligand
2	SDF
5	FGF
100	Fibronectin
200	ECs
40	PCs
36	Thrombin

For 6 A/2 Gels

μl	Component
148	F solution
26	ECs
5.3	PCs
6.43	Thrombin
180	Total

For 1 Slab

μl	Component
41	F solution
7.2	ECs
1.47	PCs
1.78	Thrombin
50	Total

2. Gel Preparation

- Weigh enough fibrinogen for the amount of gels being made. Use at least 5 mg extra to make up for that lost in filtering.
- Add chilled PBS to the fibrinogen to make a 10 mg/ml solution and place on ice for 10 minutes.
- Filter solution through a 0.22 μm filter.
- Mix enough fibrinogen, SCF, IL-3, FLT3L, SDF, FGF, and fibronectin for all of the gels planned ("F solution"). This ensures pipetting the largest volumes of the growth factors possible, which is more accurate.
- Aliquot the F solution into sterile microcentrifuge tubes. Make one aliquot for each perfusion chamber or 6 A/2 gels. Casting in small aliquots ensures that the solution will not gel during pipetting.
- Split cells as usual, resuspending in 1x antibiotic M199 for counting. Spin cells again and resuspend at 10 M/ml in 1x antibiotic M199.

3. Casting A/2 Gels

- Add ECs, PCs and thrombin to an F solution aliquot.
- As soon as the thrombin is added, pipette 28 μl into each of 6 wells of a 96 well half area (A/2) plate. Avoid bubbles. Repeat for all aliquots. Center the gels in the plate; do not use more than 32 wells in a plate (making sure to leave rows of at least 2 wells around the edges of the plate).
- Incubate the plates at 37°C for 30 minutes.

- d. Pipette sterile ddH₂O into the unoccupied wells and spaces between wells. This helps keep humidity high near the gels and prevents evaporation of culture medium.
- e. Add 100 μ l defined medium to each gel. At subsequent feedings, remove and replace 60 μ l medium.

4. Slab Molds

- a. Prior to splitting cells, assemble molds.
- b. Draw 2 rectangles 1.75 cm x 0.5 cm on the bottom of each well of a 12 well plate. One long edge can overlap.
- c. In the hood, heat the straight edge of the large spatula and press into the bottom of each well, tracing the long edges of the rectangles. Reheat as necessary.
- d. Place dollops of sterile vacuum grease at either end of each rectangle using a cotton tipped applicator.
- e. Using sterilized forceps, place an autoclaved porous polyethylene spacer on top of each vacuum grease dollop, and press down gently, moving the spacer so it is in line with the edges of the rectangle.
- f. On the back of another 12 well plate, draw lines 1.75 cm apart, and 4 dots inside the lines by 0.25 cm. This will be the plate the slabs will be put in after detachment.
- g. Using a cotton-tipped applicator, place dollops of vacuum grease on top of the dots

5. Casting Slabs

- a. Add ECs, PCs, and thrombin to an F solution aliquot.
- b. As soon as the thrombin is added, mix and pipette 50 μ l into the slab mold. Pipette some gel solution onto the spacers to encourage attachment. Avoid bubbles. Repeat for all aliquots.
- c. Incubate at 37°C for 30 minutes.
- d. Feed with 1.5 ml defined medium

6. Detaching Slabs

- a. Typically done on day 3.
- b. Place culture medium from one well into another well of the plate (or aspirate if it is a feeding day).
- c. Sterilize 2 forceps in the hood. Grab one of the spacers of a slab with each of the forceps, and carefully slide the spacers toward each other.
- d. Eventually the gel will detach (may need to slide spacers left and right; keep the spacers close together so as not to rip the gel).

- e. When the gel is detached, lift the gel by both spacers and place spacers on top of vacuum grease in the new plate. Gently spread the gel via the spacers so the spacers are lined up with the lines on the plate.
- f. Add medium (either saved from the well or fresh)
- g. Repeat steps b-f for all slabs.

7. Harvesting Gels

- a. Remove the gels from their wells and submerge in 4% PFA for 10 min.
 - i. For A/2 gels, carefully slide jeweler's forceps in the closed position around the edge of the well, detaching the gel from the edge. Carefully draw the forceps into the center of the well at various locations around the edge to detach the gel from the bottom of the well. Grab the gel with the forceps, squeezing as small a portion of the gel as possible (the squeezed portion will be damaged), and place into PFA.
 - ii. For slabs, slide jeweler's forceps in the closed position along the interface between the tissue and the spacer, separating the two. Transfer tissue to PFA, squeezing as little as possible.
- b. Rinse 3x with PBS for 5 min each.

	Supplier	Product Number	UStores Number	Storage (°C)	Description	Autoclaved?
Reagents						
Fibrinogen	EMD Chemicals	341578		4	Make fresh for each casting (10 mg/ml in PBS)	
Thrombin	Sigma	T9549		-20	750 U/ml stock in ddH ₂ O, dilute 1:20 prior in ddH ₂ O to use	
Antibiotic M199					See protocol	
SCF	R&D Systems	255-SC/CF		-20	50 µg/ml in PBS, 20 µl aliquots	
IL-3	R&D Systems	203-IL/CF		-20	50 µg/ml in PBS, 20 µl aliquots	
SDF-1α	R&D Systems	350-NS/CF		-20	100 µg/ml in PBS, 10 µl aliquots	
FLT3 Ligand	R&D Systems	308-FK/CF		-20	50 µg/ml in PBS, 20 µl aliquots	
FGF	R&D Systems	233-FB/CF		-20	40 µg/ml, 25 µl aliquots; see protocol	
Fibronectin	Sigma	F2006		-20	1 mg/ml in PBS, 100 µl aliquots	
Sterile ddH ₂ O				25	Filter through 0.22 µm	
4% PFA	Electron Microscopy Sciences	15710		16% stock: 4, 4% -20	Make up 4% solution from 16% by combining with 1.33x PBS	
Supplies						
Microcentrifuge tubes	UStores		CX13134			X
96 well A/2 plates	Costar	3697	7200334			
Vacuum grease	Dow Corning				High vacuum grease	X
Cotton-tipped applicator	UStores		MS01172			
Equipment						
Spatula	UStores		87731			

Jeweler's Forceps	UStores		CX12376		Sharp tips	
Blunt Forceps	UStores	CX12372				
Porous Spacers	?	?	?		Porous Polyethylene	X

A.8 BOEC PC Fibrin Experiments

1. Gel Formulation

For 1 ml Gel (2.5 mg/ml)

μl	Component
85	Fibrinogen
622	1x M199
4	SCF
4	IL-3
2	SDF
200	ECs
40	PCs
50	Thrombin

For 6 A/2 Gels

μl	Component
129	F solution
36	ECs
7.3	PCs
9	Thrombin
180	Total

For 1 Perfusion Gel

μl	Component
287	F solution
80	ECs
16	PCs
20	Thrombin
400	Total

2. Gel Preparation

- Thaw fibrinogen and thrombin at RT. Put on ice immediately after thawed. Do not let the reagents get warm.
- Mix enough fibrinogen, 1x M199, SCF, IL-3 and SDF for all of the gels planned ("F solution"). This ensures pipetting the largest volumes of the growth factors possible, which is more accurate.
- Aliquot the F solution into sterile microcentrifuge tubes. Make one aliquot for each perfusion chamber or 6 A/2 gels. Casting in small aliquots ensures that the solution will not gel during pipetting.
- Split cells as usual, except resuspend in 1x M199 instead of BOEC medium for counting. Spin cells again and resuspend at 10 M/ml in 1x M199.

3. Casting A/2 Gels

- Add ECs, PCs and thrombin to an F solution aliquot.
- As soon as the thrombin is added, pipette 28 μl into each of 6 wells of a 96 well half area (A/2) plate. Avoid bubbles. Repeat for all aliquots. Center the gels in the plate; do not use more than 32 wells in a plate (making sure to leave rows of at least 2 wells around the edges of the plate).
- Incubate the plates at 37°C for about 10 minutes.
- Pipette sterile ddH₂O into the unoccupied wells and spaces between wells. This helps keep humidity high near the gels and prevents evaporation of culture medium.
- Add 100 μl BOEC medium to each gel. At subsequent feedings, remove and replace 60 μl medium.

4. Perfusion Molds

- a. Prior to splitting cells, put together perfusion molds. Wear sterile gloves.
- b. Place glass tubes into holes in piece 4, with the flare on the inside.
- c. Using a piece of scrap Teflon to hold the glass tube in place at the flared end, place a silicon o-ring over the straight end of the glass tube.
- d. Slide the o-ring down using the blunt-tipped forceps.
- e. Gently push the o-ring into the hole with one arm of a blunt-tipped forceps. Be very careful not to break the glass tube. Aim to have the o-ring flush with the ultem.
- f. Snap the bottom piece into the bottom of the middle piece. The bottom piece only fits into the side of the middle piece that has the greater distance from the glass tube to the edge. Once the bottom piece is in place, the glass tube is equidistant from the top and bottom of the well.
- g. Place molds into a sterile plastic culture jar (6 per jar).

5. Casting Perfusion Gels

- a. Fill the glass tubes of each perfusion chamber with BOEC medium using a pipette.
- b. Add ECs, PCs, and thrombin to an F solution aliquot.
- c. As soon as the thrombin is added, mix and pipette 400 μ l into a perfusion chamber. Avoid bubbles. Repeat for all aliquots.
- d. Incubate at 37°C for about 10 minutes.
- e. Wearing sterile gloves, use a sterile razor blade to pop out the bottom of the well. Add sterile plastic screws and nuts to each chamber (to keep the gel off the bottom of the jar). The top of the well during casting should be the bottom of the well during culture. On this side the gel is aligned with the top of the chamber, and so prevents bubbles from forming between the culture medium and the gel when placing the chambers into culture medium.
- f. Use a 500 ml plastic culture jar for 6 perfusion chambers. Cover with 70 ml BOEC medium. Replace all medium at feedings.

6. Detaching Perfusion Gels

- a. Typically done on day 5. Wear sterile gloves and use sterile instruments.
- b. Slide dental pick 3 down and carefully along the long edges of the chamber, detaching the gel from the ultem.
- c. Carefully run dental pick 1 around the corners of the well.
- d. Use dental pick 2 to detach the gel from the ultem near the glass tubes. Use dental pick 2 from both the top and bottom of the

chamber to get all sides near the glass tubes. Be careful not to detach the gel from the flare of the glass tube.

- e. Push in each glass tube about 1-2 mm, being careful not to break the glass.
- f. Place the chamber back in the medium.
- g. Repeat steps b-f for all chambers.
- h. Inspect each gel in the culture medium, where some contraction is likely to have already occurred. If any parts of the gel are not fully detached, use an appropriate instrument to detach it.

7. Harvesting Gels

- a. Remove the gels from their wells and submerge in 4% PFA for 10 min.
 - i. For A/2 gels, carefully slide jeweler's forceps in the closed position around the edge of the well, detaching the gel from the edge. Carefully draw the forceps into the center of the well at various locations around the edge to detach the gel from the bottom of the well. Grab the gel with the forceps, squeezing as small a portion of the gel as possible (the squeezed portion will be damaged), and place into PFA.
 - ii. For perfusion gels, mark one end of the tissue near the glass tube with Verhoeff's stain. This mark the top and inlet side of the tissue for future reference. Carefully detach the gel from the glass tubes and transfer to PFA, squeezing as little as possible to avoid damage to the gel. Preferably use a plate with wells large enough so that the gels can be fixed straight.
- b. Rinse 3x with PBS for 5 min each.

	Supplier	Product Number	UStores Number	Storage (°C)	Description	Autoclaved?
Reagents						
Fibrinogen	Sigma	F8630		-20	30 mg/ml stock	
Thrombin	Sigma	T7513		-80	25 U/ml stock	
1x M199	Gibco	11150		4		
SCF	R&D Systems	255-SC/CF		-20	50 µg/ml, 20 µl aliquots	
IL-3	R&D Systems	203-IL/CF		-20	50 µg/ml, 20 µl aliquots	
SDF-1α	R&D Systems	350-NS/CF		-20	100 µg/ml, 10 µl aliquots	
Sterile ddH2O				25	Filter through 0.22 µm	
4% PFA	Electron Microscopy Sciences	15710		16% stock: 4, 4% -20	Make up 4% solution from 16% by combining with 1.33x PBS	
Verhoeff Stain					Use waste	
Supplies						
Microcentrifuge tubes	UStores		CX13134			X
Razor Blade	UStores		CX40381			X
96 well A/2 plates	Costar	3697	7200334			
Sterile Gloves	UStores		CX40770			
Equipment						
Perfusion chambers	Custom				See Figure 6-1	X
Plastic Culture Jars	UStores		029251H			X
Polycarbonate Screws	McMaster Carr	93140A109				
Polycarbonate Nuts	McMaster Carr	94905A005				
Dental Pick 1	Fine Science Tools	10140-01			Straight tip	X
Dental Pick 2	Fine Science Tools	10140-02			Small bend	X
Dental Pick 3	Fine Science Tools	10140-03			Large bend	X
Spatula	UStores		87731			X
Jeweler's Forceps	UStores		CX12376		Sharp tips	X

Silicone O-rings	McMaster Carr	9396K101			1/32" ID	X
Scrap Teflon					Cut to ~.4x.4x2 cm	X
Glass Tubes	World Precision Instruments	1B100-4			1 mm OD, 0.58 mm ID. Cut to 1.4 cm length, flare end to 2 mm OD	X
PEEK O-ring Applicator	Custom				Cylinder with ~1.5 mm ID	X
Blunt Forceps	UStores	CX12372				X

A.9 Perfusion Experiments

1. Making Agarose Gel

- a. Pipette 20 ml PBS into a wide mouth 100 ml bottle.
- b. Weigh 1g agarose.
- c. Slowly add the agarose to the PBS, swirling the solution continuously. This prevents large clumps of agarose, which are difficult to get into solution.
- d. Immediately warm the solution in the microwave. Make sure the cap is loose. Remove from the microwave before the solution bubbles over. Swirl the solution and let cool a few moments. Return to the microwave. Repeat until the agarose is fully dissolved.
- e. Store at RT until needed.

2. Beginning Perfusion

- a. Typically done on perfusion chamber gels that are 8-14 days old. After autoclaving the tubing, attach a 2 cm segment of tubing to a luer lock fitting (need 1 per chamber).
- b. Add BOEC medium to the microcentrifuge tube caps. Sterilize dental pick 3 and let cool.
- c. Wearing sterile gloves, remove the plastic screws.
- d. Dry the chamber with sterile kim wipes.
- e. Snap in the bottom chamber piece (it only fits on the side of the chamber with the larger distance between the edge of the chamber and the hole for the glass tube).
- f. Place a microcentrifuge tube cap over the end of each glass tube, making sure the fluid in the cap covers the glass tube. This prevents evaporation of fluid from the glass tubes (any evaporation would cause a bubble when connecting the glass tube to the plastic tubing).
- g. Add fresh BOEC medium to the chamber to keep the tissue moist using the sterile transfer pipette. If any leaks out, replace as needed.
- h. Repeat steps c-f for each chamber. After this point, gloves no longer need to be sterile, as only the outside of the chambers will be touched.
- i. Prepare the needle and syringe. Place metal screws in the four corners of the chamber, heads down.
- j. Complete the following step relatively quickly, as the agarose will gel rapidly. Melt agarose in the microwave. In the hood, draw up the agarose, use the dental pick to lift the gel off the bottom of the chamber (to ensure that agarose will flow underneath the gel), and dispense agarose into the chamber. Cover the chamber with the top chamber piece, and screw the nuts on by hand. Small bubbles

are ok. Tighten with the screwdriver and wrench. The screws need to be tight to prevent leaking.

- k. Place a microcentrifuge tube cap over the end of each glass tube, making sure the fluid in the cap covers the glass tube.
- l. Repeat steps h-j for each chamber.
- m. Fill one syringe per chamber with warm BOEC medium. Use different size syringes to get different flow rates with the same pump.
- n. Connect the plastic tubing to the syringes via luer lock fittings.
- o. Bring the syringe pump, Styrofoam block, and tray into the hood and place the pump and block on the tray.
- p. Place all syringes in the syringe pump. Run the syringe pump (infuse) until medium has reached the end of all plastic tubing. Catch drips with sterile kim wipes.
- q. Remove the microcentrifuge tube caps from one chamber. Place chamber on top of the Styrofoam block, lining it up with the furthest back syringe.
- r. Squeeze the plastic tubing so a drop appears at the end. Carefully slide the glass tube into the plastic tubing, avoiding bubble formation as much as possible. If a small bubble forms, leave it rather than starting over (which usually just leads to larger bubbles). Small bubbles often are trapped in the flare of the glass tube and don't enter the tissue.
- s. Tie the plastic tube over the glass tube with dental floss. This needs to be tight to prevent leaks. Forceps can be helpful. Blot any excess medium with sterile kim wipes.
- t. Slide a 15 cm segment of plastic tubing over the outlet glass tube and tie with dental floss.
- u. Repeat steps p-t for each chamber.
- v. Direct the outlet tubing into a collection device (e.g. 50 ml conical tube). Seal with parafilm.
- w. Transfer the entire set-up into the incubator. Thread the pump power cord through the incubator port and plug in. Turn on the pump and begin perfusion.

3. Medium Changes

- a. Due to the extremely low flow rate used, fresh medium provided would not reach the tissue within 2-3 days. Therefore, no medium changes were provided throughout the 6 day culture period. However, the tissue received a continuous supply of "fresh" medium through flow.

4. Adding Gold Nanoparticles

- a. Add gold nanoparticles (GNP) to flow ~24 hours prior to harvest. Their purpose is to track the path of fluid flow at the end of interstitial flow.
- b. Stop the pump and bring the entire tray into the hood.
- c. Fill a 1 ml syringe with a 1:200 solution of GNP in BOEC medium. Attach a 30 gauge needle to the end.
- d. Mark a spot on the plastic tubing approximately 5 mm from the glass tube inlet with sharpie. Repeat for each chamber.
- e. Carefully slide the needle into the plastic tubing at the marked location. Slowly inject a small volume of GNP solution. Repeat for each chamber.
- f. Place a dollop of sterile vacuum grease on the tube to cover the opening using a cotton-tipped applicator. Repeat for each chamber.
- g. Return the tray to the incubator and resume flow.

5. Harvesting Gels

- a. Stop the pump and remove the entire setup from the incubator. Record the amount of fluid in the outlet line (length past the glass capillary tube).
- b. Remove the screws and the top chamber piece.
- c. Observe tissue through the agarose. A long bubble parallel to the tissue indicates extensive channeling. The tissue will also be very thin in this region. For some flow rates, GNP can be seen within the tissue.
- d. Slide jeweler's forceps carefully into the agarose and along the sides of the tissue. Be carefully not to damage the tissue. Separate the tissue completely from the agarose. Use a pipette tip to put a small amount of Verhoeff's dye onto the tissue near one end. This enables tracking of top/bottom and inlet/outlet sides of the tissue.
- e. Place tissues into 4% PFA for 10 min. Preferably use a plate with wells large enough to fix the gel in a straight position.
- f. Rinse 3x with PBS for 5 min each.
- g. Prepare samples for whole mount staining or sectioning.

	Supplier	Product Number	UStores Number	Storage (°C)	Description	Autoclaved?
Reagents						
Agarose	Sigma	A9539		25		
4% PFA	Electron Microscopy Sciences	15710		16% stock: 4, 4% -20	Make up 4% solution from 16% by combining with 1.33x PBS	
Gold Nanoparticles	Nanoprobes	1115		4	15 nm diameter	
Supplies						
Kim wipes	UStores		CX21274			X
Needle 15 gauge	Monoject	200029	CX41000			
Needle 30 gauge	Becton Dickinson	305106	MS57786			
6 ml syringes (and other sizes if testing different flow rates)	UStores		MS71050			
Dental floss						
Sterile Gloves	UStores		CX40770			
Vacuum grease	Dow Corning				High vacuum grease	X
Transfer Pipette	UStores		055560		Sterile	
Equipment						
Chamber Pieces 1 and 6	Custom				See drawing	X
Metal screws and nuts	McMaster Carr	91772A116			1-1/4" 4-40 Stainless Steel	X
Microcentrifuge tube caps	UStores		CX13134		Cut cap off tube	X
Silastic tubing	Dow Corning	508-005			1 2 cm segment and 1 15 cm segment per chamber	X
Female Luer lock fittings	Value Plastics	FTLL004-1			1 per chamber	X
Wrench					1/4"	
Screwdriver					Philips head	
Dental Pick 3	Fine Science Tools	10140-03			Large bend	

A.10 Immunofluorescent Staining

1. Antibodies

Antigen	Source	Host	1° Dilution	2°	Antigen Retrieval	Stock Conc	Final Conc
5B5	Abcam (ab44971)	Mouse	1:100	DAM	0.1% Triton X-100	150 µg/ml	1.5 µg/ml
VE-Cadherin	Santa Cruz sc-6458	Goat	1:200	DAG	None or 0.1% Triton X-100 for 1 min	200 µg/ml	1 µg/ml
Collagen IV	Abcam (ab6586)	Rabbit	1:200	DAR	None	1 mg/ml	5 µg/ml
Laminin	Abcam (ab11575)	Rabbit	1:100	DAR	None	500 µg/ml	5 µg/ml
Collagen I	Abcam (ab6577)	Rabbit	1:1000	DAR	None	1 mg/ml	1 µg/ml
CD31	Dako (m0823)	Mouse	1:40	DAM	None or 0.1% Triton X-100	212 µg/ml	5.3 µg/ml

2. Whole Mount Stain

- a. Complete all steps on an orbital shaker at RT. This protocol can be paused at any step by keeping at 4°C overnight. Keep slides in the dark as much as possible by covering plate with aluminum foil.
- b. If permeabilization is required, complete this step. If not, move on to step c.
- c. Incubate samples in Triton X-100 for 5 minutes.
- d. Rinse 3x 5 minutes in PBS.
- e. Incubate in 5% normal donkey serum for 2 hours.
- f. Incubate in primary antibody diluted in 5% normal donkey serum for 1 hour.
- g. Rinse 3x 5 minutes in PBS.
- h. Incubate in secondary antibody diluted in 1 µg/ml Hoechst 33342 dye for 1 hour.
- i. Rinse 3x 5 minutes in PBS.
- j. Store in PBS; image within a few days.

3. Stain of Sections

- a. This protocol can be paused at any step by keeping at 4°C overnight. Keep slides in the dark as much as possible. Do not let the sections dry out (for each section, aspirate the previous solution and immediately fill with the next solution). Fill the troughs of the staining box with water if leaving overnight.
- b. If permeabilization is required, complete this step. If not, move on to step c.
- c. Incubate samples in Triton X-100 for 5 minutes.

- d. Rinse 3x 5 minutes in PBS.
- e. Incubate in 5% normal donkey serum for 2 hours.
- f. Incubate in primary antibody diluted in 5% normal donkey serum for 1 hour.
- g. Rinse 3x 5 minutes in PBS.
- h. Incubate in secondary antibody diluted in 1 $\mu\text{g/ml}$ Hoechst 33342 dye for 1 hour.
- i. Rinse 3x 5 minutes in PBS.
- j. Coverslip using mounting medium. Image within a few days.

	Supplier	Product Number	UStores Number	Storage (°C)	Description	Autoclaved?
Reagents						
Triton X-100	Amresco	0694		25		
PBS	Mediatech	21-031-CM		25		
Normal Donkey Serum	Jackson Immuno	017-000-121		Lyophilized: 4, Reconstituted: -20 in aliquots	Reconstitute in ddH ₂ O	
Hoechst 33342 Dye	Invitrogen	H3570		Stock: -20, diluted: 4	Dilute to 1 µg/ml in PBS	
Mounting Medium	Dako	S3023		4		
Glycerol	Sigma	G7893		25		
Secondary Antibodies				-20	Dilute 1:1 in glycerol	
Donkey Anti-Mouse Green	Jackson Immuno	715-545-150			AlexaFluor 488 Use at 1:200 dilution	
Donkey Anti-Mouse Red	Jackson Immuno	715-585-150			AlexaFluor 594 Use at 1:200 dilution	
Donkey Anti-Mouse Far Red	Jackson Immuno	715-605-150			AlexaFluor 647 Use at 1:200 dilution	
Donkey Anti-Rabbit Green	Jackson Immuno	711-545-152			AlexaFluor 488 Use at 1:200 dilution	
Donkey Anti-Rabbit Red	Jackson Immuno	711-585-152			AlexaFluor 594 Use at 1:200 dilution	
Donkey Anti-Rabbit Far Red	Jackson Immuno	711-605-152			AlexaFluor 647 Use at 1:200 dilution	
Donkey Anti-Goat Green	Jackson Immuno	805-545-180			AlexaFluor 488 Use at 1:200 dilution	
Donkey Anti-Goat Red	Jackson Immuno	805-585-180			AlexaFluor 594 Use at 1:200 dilution	
Donkey Anti-Goat Far Red	Jackson Immuno	805-605-180			AlexaFluor 647 Use at 1:200 dilution	

Supplies

Pap Pen	Invitrogen	00-8877				
Equipment						
Staining Box	Evergreen Scientific	240-9020-Z10			"Immunostain Moisture Chamber"	

A.11 H&E Stain

1. Stain

- a. Begin with frozen sections on slides. Arrange them in a staining rack. For each step, transfer rack to a staining dish with the appropriate solution. Timing is critical, so prepare dishes ahead of time.
- b. Filter hematoxylin. This removes clumps that build up over time.
- c. Rinse slides briefly in distilled water.
- d. Stain in hematoxylin for 8 minutes.
- e. Wash in warm running tap water for 10 minutes. The ions present in the tap water enhance the stain.
- f. Rinse in distilled water.
- g. Rinse in 95% alcohol, 10 dips. Blot on paper towels.
- h. Counterstain in eosin for 1 minute. Blot on paper towels.
- i. Dehydrate through 95% alcohol and 2 changes of 100% alcohol, 5 minutes each. Blot on paper towels between each step.
- j. Clear in 2 changes of xylene, 5 minutes each. Blot on paper towels between each step.
- k. Mount in permount; cover with a coverslip.

	Supplier	Product Number	UStores Number	Storage (°C)	Description	Autoclaved?
Reagents						
Mayer's Hematoxylin	Sigma	MSH128		25		
Eosin-Y	Sigma	HT110332		25		
95% Alcohol	Decon Labs	2801		25		
100% Alcohol	Decon Labs	2701		25		
Xylene	Fisher Scientific	X5SK		25		
Permout	Fisher Scientific	SP15		25		
Supplies						
Filter paper	Fisher Scientific	09-795F				
Coverslips	Gold Seal	3322				
Equipment						
Staining Rack	Wheaton Science Products	900204				
Staining Dish	Wheaton Science Products	900201				

A.12 Silver Stain

1. Theory

- a. The purpose of this stain is to visualize gold nanoparticles within a section. The reagents of the silver stain (HQ Silver) are deposited on gold, physically enlarging the nanoparticle. The particles are then visible under high power (63x) as black dots.

2. Stain

- a. Begin with frozen sections on slides. Set them up in a staining box.
- b. Use a pap pen to draw hydrophobic circles around each section.
- c. Add 50 mM glycine to cover each section. Incubate 5 minutes at RT.
- d. Set up 3 staining dishes filled with ddH₂O. Transfer slides to a staining rack and dip the rack in each dish about 15 times. Do not use a metal handle, as ions could transfer from it to the water. Any ions in the solution can cause self-nucleation of the silver reagents, leading to background staining. Transfer slides back to the staining box.
- e. Mix silver reagents. First mix solutions M and I, then add solution A. As soon as the solutions are mixed, move as quickly as possible until the slides are rinsed of silver reagents, as after a certain length of time the silver reagents will start self-nucleating, causing background staining.
- f. Add silver reagents to each section and incubate 10 minutes at RT.
- g. Fill staining dishes with fresh ddH₂O. Transfer slides to the staining rack and dip the rack in each dish about 15 times. Transfer slides back to the staining box.
- h. Continue with immunostaining, H&E staining or coverslip.

	Supplier	Product Number	UStores Number	Storage (°C)	Description	Autoclaved?
Reagents						
Glycine	Fisher Scientific	BP381		25		
HQ Silver	Nanoprobes	2012		-20	3 components, store in aliquots. Mix equal amounts of each.	
Supplies						
Pap Pen	Invitrogen	00-8877				
Equipment						
Staining Box	Evergreen Scientific	240-9020-210				
Staining Rack	Wheaton Science Products	900204				
Staining Dish	Wheaton Science Products	900201				

A.13 Alignment Mapping

1. Physical Set-up

- a. This set-up is in the same area as the Instron Biaxial mechanical testing device and can be used simultaneously with that. Sign up for a time on the Yahoo! calendar. Sign in as username: umn_biaxial, password: instron
- b. Position light at the center of the table. The lamp intensity should be set between 3 and 4.
- c. Place quarterwave plate over the light.
- d. Use blocks to set a clean plastic tray over the quarterwave plate.
- e. Place a few drops of PBS in the tray over the light and place a sample in the PBS.
- f. Position the rotating polarizer over the sample and screw in place.
- g. Position the camera above the rotating polarizer so that the sample is in the viewing field. Adjust the focus.
- h. Adjust the quarterwave plate so that half of the image is covered by it and half is not. Make sure PBS is visible in both regions (these will be control areas).

2. Computer Set-up

- a. Open Phantom 5.4.7
- b. Acquisition → Setup and Recording
- c. Make sure the settings are correct: exposure time 7532, sample rate 20, post trigger 20
- d. Center the sample in the frame.
- e. Open HSMotor, a LabView program that controls the rotating polarizer. Set it to 1 Hz, 20 steps. Press run until the brightest image is on the screen (use -20 steps to go backward).
- f. Adjust the light intensity to avoid washout.

3. Calibration

- a. Set HSMotor to 1 Hz, 20000 steps.
- b. Click Capture in Phantom.
- c. Click Run in HSMotor.
- d. Click Trigger in Phantom.
- e. Save images 20 images starting at image 0 as a .cin file (use calibration in the file name)
- f. File → Convert and Process
- g. Click on the .cin file and hit ok.
- h. Save as TIF 8 with the name "filename_!5.tif" This saves each image as a TIFF file.

4. Image Capture

- a. Cover the entire image with the quarterwave plate.
- b. Repeat steps 3b-3h for each sample.

5. Troubleshooting

- a. The rotating polarizer often somehow becomes disconnected from the computer. If this occurs, perform the following steps to reconnect it.
- b. Check the control boxes (on the top shelf above the computer, on the left). The smaller box should have a green light nearest you, and the larger box should have a green light next to input 1. If the lights are correct proceed to step c. If not, unplug both boxes, wait about 30 seconds and plug them back in.
- c. Close all programs, then open Motion Architect from the start menu.
- d. Click on Terminal.
- e. Transfers → Send Motion Program.
- f. Select "sg_1.prg"
- g. Close the program, save as YOURNAME.ter
- h. Under My Computer, click on C:MA6000/EM6000.

6. Image Analysis

- a. The analysis is done in Matlab. The files needed are in the rmpscripts folder. Choose regions when specified below by clicking the upper left and lower right corners of a box.
- b. Type "kmrpmstart" (change this file to have your own initials so you can edit the location to which it changes the directory)
- c. Type "rmpcalSG_hs"
 - i. Enter the calibration filename ('filename_').
 - ii. Choose a region above the sample within the PBS. The ions in the PBS contribute to light scattering, so it is necessary that the control areas are covered in the same solution that the sample is sitting in.
 - iii. Choose a region below the sample within the PBS.
 - iv. Check to see that the image is using a large range of pixels and that the max/min of the points and line are similar
 - v. Check circular analyzer: slow axis should be $\sim 45^\circ \pm 5^\circ$, retardation should be $\sim 90^\circ \pm 10^\circ$
- d. Type "rmpcalSG_qw"
 - i. Enter the sample filename ('filename_').
 - ii. Choose a background region within the PBS.
 - iii. If the line and points are offset by 90° , type
 $pa1=pa1+90;pa2=pa2+90;$

- e. Type "rmpSG"
 - i. Choose a region containing the sample or part of the sample.
- f. The output of this program is an alignment image as well as retardation values and the average alignment angle (in an excel file). The retardation value includes all areas in the image, so if the image includes regions outside the sample, the retardation value may be artificially low. For comparison between samples, convert retardation values to birefringence using the tissue thickness (see Tower and Tranquillo⁸⁷).

A.14 Image Analysis – Sections Stained for CD31

1. Matlab Codes Required

- a. CD31.m
- b. CD31manual.m
- c. CD31frombw.m
- d. drawline.m
- e. subtractregion.m
- f. overlay.m
- g. ECMstart.m

2. Analyzing Images

- a. Note: These files can be used for either cross or longitudinal sections.
- b. Prior to beginning the analysis, edit the file ECMstart.m to recognize your file locations.
- c. Run ECMstart; this program enables Matlab to find the analysis files while in the folder containing images.
- d. Run CD31.m
 - i. Enter the appropriate information.
 - ii. The program displays the final lumen image; check each image against the original to verify accuracy.
 - iii. The quantification results are output to an Excel file that will be overwritten each time the code is run; copy the results to a new file to save them.
- e. Run CD31manual.m on any images that were not accurate.
 - i. Enter the appropriate information.
 - ii. Compare the binary image to the original image. If any rings of CD31 staining are incomplete on the binary image, click “Draw Line.” Zoom in as necessary; then press the spacebar. Click on the endpoints a line that would complete the ring. A new image appears showing the line. Repeat until all incomplete rings are completed; then click “Done.”
 - iii. Compare the lumen image to the original image. If any non-lumens are present in the lumen image, click “Subtract Region.” Zoom in as necessary; then press the spacebar. Click on the vertices of a polygon surrounding the lumen(s) to be deleted. The vertices can be modified; for more information see “roipoly” in the help menu. Double-click on the first vertex to complete the polygon. Continue removing lumens until the lumen image is accurate; then click “Done.”

- iv. The quantification results are output to an Excel file that will be overwritten each time the code is run; copy the results to a new file to save them.
- f. Both CD31.m and CD31manual.m save the final lumen image as “originalimagename_2.” If the lumen image needs to be analyzed again, run CD31frombw.m.
 - i. Enter the appropriate information.
 - ii. The quantification results are output to an Excel file that will be overwritten each time the code is run; copy the results to a new file to save them.
- g. Average the results for each construct, and analyze those data statistically.

A.15 Image Analysis – Sections Stained for Basement Membrane

1. Matlab Codes Required

- a. BasementMembrane.m
- b. ECMstart.m

2. Analyzing Images

- a. Prior to beginning the analysis, edit the file ECMstart.m to recognize your file locations.
- b. Run ECMstart; this program enables Matlab to find the analysis files while in the folder containing images.
- c. Use ImageJ to determine an appropriate threshold for the images.
 - i. In the Image menu, click Type → 8-bit.
 - ii. In the Image menu, click Adjust → Threshold. Use the interactive tool to find an appropriate threshold.
 - iii. Repeat for several images obtain a threshold that will work for all of the images.
- d. Run BasementMembrane.m.
 - i. Enter the appropriate information.
 - ii. The quantification results are output to an Excel file that will be overwritten each time the code is run; copy the results to a new file to save them.
- e. Average the results for each construct, and analyze those data statistically.

A.16 Image Analysis – Sections Stained for EphrinB2

1. Matlab Codes Required

- a. ephrin.m
- b. ECMstart.m

2. Analyzing Images

Prior to beginning the analysis, edit the file ECMstart.m to recognize your file locations.

Run ECMstart; this program enables Matlab to find the analysis files while in the folder containing images.

Use ImageJ to determine an appropriate threshold for the images.

- i. In the Image menu, click Type → 8-bit.
- ii. In the Image menu, click Adjust → Threshold. Use the interactive tool to find an appropriate threshold.
- iii. Repeat for several images obtain a threshold that will work for all of the images.

Run ephrin.m.

- i. Enter the appropriate information.
- ii. The quantification results are output to an Excel file that will be overwritten each time the code is run; copy the results to a new file to save them.
- iii. Average the results for each construct, and analyze those data statistically.

To normalize to CD31 staining levels quantified from other sections, divide the results for the total staining intensity of ECs by average value of CD31+ fraction obtained for that construct.

A.17 Image Analysis – Whole Mounts Stained for CD31

1. Matlab Codes Required

- a. QuantifyingGrowthofVessels.m
- b. CropQuantifyingGrowthofVessels.m
- c. croptopoly.m
- d. findendpoints.m
- e. findjunctions.m
- f. WMstart.m

2. Analyzing Images

- a. Note: This code can be used to analyze images of whole mount stains or stains of thick (40-60 μm) longitudinal sections that yield images similar to whole mount stains.
- b. Prior to beginning the analysis, edit the file WMstart.m to recognize your file locations.
- c. Run WMstart; this program enables Matlab to find the analysis files while in the folder containing images.
- d. Run QuantifyingGrowthofVessels.m.
 - i. Enter the appropriate information.
 - ii. The code outputs 2 images: a binary image of CD31 staining, and an image in which black lines representing the skeletonized image (from which microvessel lengths are measured) overlays the grayscale image. Compare the two images to the original image.
 - iii. The quantification results are output to an Excel file that will be overwritten each time the code is run; copy the results to a new file to save them.
- e. Strong background staining (e.g. due to a bright but out of focus microvessel) will lead to inaccurate results. If this is present in any area of the image, run CropQuantifyingGrowthofVessels.m
 - i. Enter the appropriate information.
 - ii. Click on the vertices of a polygon on the image that excludes the problem area. The vertices of the polygon can be edited; for more information go to “roipoly” in the help menu. Double click on the first vertex to complete the polygon.
 - iii. The quantification results are output to an Excel file that will be overwritten each time the code is run; copy the results to a new file to save them.
- f. Average the results for each construct, and analyze those data statistically.

A.18 Image Analysis – Optical Density

1. Matlab Codes Required

- a. opticaldensity.m
- b. kmrpmstart.m

2. Analyzing Images

- a. Note: This code is designed for use with images taken for alignment mapping.
- b. Prior to beginning the analysis, edit the file kmrpmstart.m to recognize your file locations.
- c. Run kmrpmstart; this program enables Matlab to find the analysis files while in the folder containing images.
- d. Run opticaldensity.m.
 - i. Enter the root of the image file e.g. 'Image1_'.
 - ii. Click on the vertices of a polygon in the background. This determines the image with the brightest light intensity.
 - iii. Click on the endpoints of a vertical line slightly larger than the width of the tissue. This will indicate the distance the program will translate the region(s) of interest to obtain background light information (used to correct for light intensity variation across the field of view).
 - iv. Enter the number or regions of interest to be measured.
 - v. Click on the vertices of a polygon to define your region of interest. The vertices of the polygon can be edited; for more information go to "roipoly" in the help menu. Double click on the first vertex to complete the polygon.
 - vi. The quantification results are output to an Excel file that will be overwritten each time the code is run; copy the results to a new file to save them. The outputs will be in order of the locations of the regions of interest (top left to bottom right) regardless of the order in which they are chosen.
- e. Average the results for each construct, and analyze those data statistically.

3. Outputs

- a. Normalized Optical Density – The mean pixel value of the region of interest normalized to account for variations in light intensity. The each region of interest is translated in the positive and negative y direction to obtain background values. These values are then averaged and the ratio of each to that of the first region of interest (the most top and left) is used for normalization.

Appendix B. Image Analysis Codes

B.1 CD31.m

```
%This script analyzes images of sections of gels containing ECs and
pericytes
%stained for CD31. It outputs data on endothelial structures, lumens,
and
%pericyte recruitment.

%This file is written for images taken on the LHI confocal, which
outputs
%images that contain each channel separately along with a merged image.

%Prior to running the code, run the file ECM start. This adds search
paths
%so you will be able to run this code while in the folder containing
your
%images.

clear all

n=input('How many images would you like to analyze? ');
initial=input('What is the number of the first image? ');
scale=input('What is the scale of the image? 1 pixel = __ um ');
final=n+initial-1;
result=zeros(n,23);

fname='Image%03d.tif';
fname2='Image%03d_2.tif';
for k=initial:final
if exist(sprintf(fname2,k), 'file')==1
    continue
end
    I=imread(sprintf(fname,k));
    I=rgb2gray(I);

    [m1,n1]=size(I);
    rect=[0 m1/2+1 n1/2-1 m1/2-1];
        %for images with red in lower left, green in top right
%    rect=[n1/2+1 0 n1/2-1 m1/2-1];
        %for images with red in top right, green in top left
    Icrop=imcrop(I,rect);
% %%%use the code below if you have separate image files for each
channel.
% fname='Image%04d_C003.tif';
% fname2='Image%04d_C002.tif';
% for k=initial:final
%     I=imread(sprintf(fname,k));
%     Icrop=rgb2gray(I);

    [m2,n2]=size(Icrop);
    sectionarea=m2*n2;
```



```
%To accurately identify as many lumens as possible, multiple ways of
%thresholding the image are used.
```

```
I2b=imadjust(Icrop);
level = graythresh(I2b);
bwz = im2bw(I2b,level);

level = graythresh(Icrop);
bwy = im2bw(Icrop,level);

se=strel('disk',1);
bwza=imdilate(bwx,se);
bwz=imerode(bwza,se);

se1=strel('disk',2);
bwzb=imdilate(bwx,se1);
bww=imerode(bwzb,se1);
```

```
% The following steps fill small holes in the images (large holes are
% lumens).
```

```
filledx = imfill(bwx,4,'holes');
holesx = filledx & ~bwx;
bigholesx = bwareaopen(holesx,5);
smallholesx = holesx & ~bigholesx;
bwz2 = bwz|smallholesx;
bwz3 = bwareaopen(bwz2,20,8);
ccx = bwconncomp(bwz3,8);
numberofstructures=ccx.NumObjects; %number of interconnected CD31+
structures in the image.
ccxlabel=labelmatrix(ccx);
```

```
filledy = imfill(bwy,4,'holes');
holesy = filledy & ~bwy;
bigholesy = bwareaopen(holesy,5);
```

```
filledz1 = imfill(bwza,4,'holes');
holesz1 = filledz1 & ~bwza;
bigholesz1a = bwareaopen(holesz1,5);
bigholesz1=imdilate(bigholesz1a,se);
```

```
filledz2 = imfill(bwz,4,'holes');
holesz2 = filledz2 & ~bwz;
bigholesz2 = bwareaopen(holesz2,5);
```

```
filledz3 = imfill(bwzb,4,'holes');
holesz3 = filledz3 & ~bwzb;
bigholesz3a = bwareaopen(holesz3,5);
bigholesz3=imdilate(bigholesz3a,se1);
```

```
filledz4 = imfill(bww,4,'holes');
holesz4 = filledz4 & ~bww;
bigholesz4 = bwareaopen(holesz4,5);
```

```

%This step determines the level of CD31 staining.
    totalCD31=sum(sum(bwx3))*scale^2; %units=um^2
    fractionofsectionwithCD31=sum(sum(bwx3))/sectionarea; %Fraction of
the section with positive CD31 staining

%This step merges all the lumens identified in the various thresholded
%images and removes any small lumens.

lumens1=bigholesx|bigholesy|bigholesz1|bigholesz2|bigholesz3|bigholesz4
;
    lumens=bwareaopen(lumens1,5);

% This step compares the mean intensity of the lumen to the mean
intensity
% of the area immediately surrounding the lumen. A true lumen will have
a
% high ratio of surrounding intensity to lumen intensity.
    cclumen = bwconncomp(lumens,8);
    lumenlabel=labelmatrix(cclumen);
    lumenstat=regionprops(cclumen,Icrop,'MeanIntensity');
    lumenintens=[lumenstat.MeanIntensity];
    lumens2=lumens;
    se2=strel('disk',3);
    outerintens2=zeros(1,cclumen.NumObjects);
    size1=zeros(1,cclumen.NumObjects);
    ratio=zeros(4,cclumen.NumObjects);
    for i=1:cclumen.NumObjects
        single=zeros(size(lumens1));
        single(lumenlabel==i)=1;
        size1(i)=sum(sum(single))/i;
        single2=imdilate(single,se);
        single3=imdilate(single,se2);
        outer=single3-single2;
        ccouter = bwconncomp(outer,8);
        outerstat=regionprops(ccouter,Icrop,'MeanIntensity');
        outerintens=[outerstat.MeanIntensity];
        outerintens2(i)=mean(outerintens);
        ratio(1,i)=mean(outerintens);
        ratio(2,i)=lumenintens(i);
        ratio(3,i)=mean(outerintens)/lumenintens(i);
        if mean(outerintens)/lumenintens(i)<2 %this number can be
edited to fit the image set
            lumens2(lumenlabel==i)=0;
        else
            outer2=zeros(size(outer));
            for j=1:(m1/2-1)*(n1/2-1)
                if outer(j)==1
                    outer2(j)=ccxlabel(j);
                end
            end
            uniq=unique(outer2);
            [s1,s2]=size(uniq);
            ratio(4,i)=s1;
        end
    end
    outerlabel=labelmatrix(ccouter);
end

```

```

%This step calculates properties of the true lumens (those identified
by
%the previous step).
    stats=regionprops(lumens2,'Area');
    numlumens=length([stats.Area]); %Number of lumens in the image
    numlumensper=numlumens/sectionarea/scale^2*1e6; %Number of lumens
per mm^2
    avglumenarea=mean([stats.Area])*scale^2; %units=um^2; Average area
of a lumen
    totlumenarea=sum([stats.Area])/sectionarea; %Lumen area as a
fraction of the area of the sec

    biglumens2=bwareaopen(lumens2,200,8); %only large lumens are used
here because they are the most important
    stats=regionprops(biglumens2,'Eccentricity','MajorAxisLength');
    ecc=mean([stats.Eccentricity]); %Eccentricity - a measure of how
round the lumen is (scale from 0 to 1 where 0 is a circle and 1 is a
line segment)
    mal=mean([stats.MajorAxisLength])*scale; % Major Axis Length - a
measure of the lumen length

    %This step fills in all lumens and calculates the anisotropy index for
each
%structure identified. The anisotropy index is calculated based on the
% average angle of the structures. This is meant for use with
longitudinal
% sections of aligned tissues.
    filledx2=lumens2|bwx3;
    filledx3=imfill(filledx2,'holes');
    stats2=regionprops(filledx3,'MajorAxisLength','Orientation');
    a={stats2.Orientation};
    p={stats2.MajorAxisLength};
    a2=cell2mat(a);
    p2=cell2mat(p);
    for i=1:length(a2)
        if a2(i)<0
            a2(i)=a2(i)+180;
        end
    end
    avga=ones(1,length(a2)).*mean(a2);
    AIx=p2.*abs(cos(deg2rad(a2-avga)));
    AIy=p2.*abs(sin(deg2rad(a2-avga)));
    AI=sum(AIx)/sum(AIy); %Anisotropy Index

%This step calculates how much of the structures are lumenized.
    ccfilled=bwconncomp(filledx3,8);
    filledlabel=labelmatrix(ccfilled);
    count1=0;
    count2=0;
    areacount1=0;
    filledx4=zeros(size(filledx3));
    filledx5=zeros(size(filledx3));
    filledarea=zeros(1,ccfilled.NumObjects);
    [m2,n2]=size(filledx3);

```

```

for i=1:ccfilled.NumObjects
    for j=1:m2
        for l=1:n2
            if filledlabel(j,l)==i && biglumens2(j,l)==1
                count1=count1+1;
                count2=count2+1;
            elseif filledlabel(j,l)==i && lumens2(j,l)==1
                count1=count1+1;
            end
            if filledlabel(j,l)==i
                areacount1=areacount1+1;
            end
        end
    end
    if count1>0
        filledx4(filledlabel==i)=1;
        filledarea(i)=count1/areacount1;
    end
    if count2>0
        filledx5(filledlabel==i)=1;
    end
    count1=0;
    count2=0;
    areacount1=0;
end
filledx4=logical(filledx4);
filledx5=logical(filledx5);
ccfilled2=bwconncomp(filledx4,8);
fractionnumlumen=ccfilled2.NumObjects/ccfilled.NumObjects;
%Fraction of structures that contain lumens.
    lumenareapercentavgper=mean(filledarea); %average percentage of
each structure filled with lumens
    lumenareapercent=sum(sum(lumens2))/sum(sum(filledx4)); %area
percentage of structures that are lumens (only includes structures that
are lumenized)
    stats3=regionprops(filledx5,'MajorAxisLength');

lengthlumenized=sum([stats.MajorAxisLength])/sum([stats3.MajorAxisLengt
h]); %fraction of structure length covered with lumens (only includes
lumenized structures)

%This step thresholds the pericyte image.
rectPC=[n1/2+1 0 n1/2-1 m1/2-1];
    %for images with red in lower left and green in top right
%   rectPC=[0 0 n1/2-1 m1/2-1];
    %for images with red in top right and green in top left
IcropPC=imcrop(I,rectPC);
%   rectPC=imread(sprintf(fname2,k));
%   IcropPC=rgb2gray(rectPC);
levelPC = graythresh(IcropPC);
bwPC = im2bw(IcropPC,levelPC);
bw3PC = bwareaopen(bwPC,10,8);
ccPC = bwconncomp(bw3PC,8);
[m3,n3]=size(bw3PC);

%This step determines the level of PCs.

```

```

totalPC=sum(sum(bw3PC))*scale^2; %units=um^2
fractionofsectionwithPC=sum(sum(bw3PC))/sectionarea; %Fraction of
the section with positive PC staining
numPC=ccPC.NumObjects/sectionarea/scale^2*1e6; %number PC per mm^2

%This step takes the intersection of the CD31 image and the pericyte
image.
%Those pericytes that overlap ECs are considered recruited.
%Those pericytes that have 50% of their area overlapping with ECs are
%considered fully recruited.
intersection=bwx3&bw3PC;
labelPC=labelmatrix(ccPC);
count=0;
areacount=0;
bw3PC_2=zeros(size(bw3PC));
bw3PC_3=zeros(size(bw3PC));
PCarea=zeros(1,ccPC.NumObjects);
for i=1:ccPC.NumObjects
    for j=1:m3
        for l=1:n3
            if labelPC(j,l)==i && intersection(j,l)==1
                count=count+1;
            end
            if labelPC(j,l)==i
                areacount=areacount+1;
            end
        end
    end
    if count>0
        bw3PC_2(labelPC==i)=1;
        PCarea(i)=count/areacount;
    end
    if count/areacount>0.5
        bw3PC_3(labelPC==i)=1;
    end
    count=0;
    areacount=0;
end
ccint=bwconncomp(bw3PC_2,8);
fractionrecruitedPCs=ccint.NumObjects/ccPC.NumObjects; %Fraction of
pericytes that have been recruited.
ccint2=bwconncomp(bw3PC_3,8);
fracfullyrecruitedPCs=ccint2.NumObjects/ccPC.NumObjects; %Fraction
of pericytes that have been fully recruited.

%This step thresholds the DAPI image and counts the nuclei
rect=[0 0 n1/2-1 m1/2-1];
IcropDAPI=imcrop(I,rect);
%   rectPC=imread(sprintf(fname2,k));
%   IcropPC=rgb2gray(rectPC);
levelDAPI = graythresh(IcropDAPI);
bwDAPI = im2bw(IcropDAPI,levelDAPI);
bw3DAPI = bwareaopen(bwDAPI,10,8);
ccDAPI = bwconncomp(bw3DAPI,8);
fractionofsectionwithDAPI=sum(sum(bw3DAPI))/sectionarea; %Fraction
of the section with positive DAPI staining

```

```

    numDAPI=ccDAPI.NumObjects/sectionarea/scale^2*1e6; %number nuclei
per mm^2

%The data is collected into the result matrix and output to an excel
file.
    result(k-initial+1,1)=k;
    result(k-initial+1,2)=sectionarea;
    result(k-initial+1,3)=totalCD31;
    result(k-initial+1,4)=fractionofsectionwithCD31;
    result(k-initial+1,5)=numlumens;
    result(k-initial+1,6)=numlumensper;
    result(k-initial+1,7)=avglumenarea;
    result(k-initial+1,8)=totlumenarea;
    result(k-initial+1,9)=numberofstructures;
    result(k-initial+1,10)=fractionnumlumen;
    result(k-initial+1,11)=lumenareapercentavgper;
    result(k-initial+1,12)=lumenareapercent;
    result(k-initial+1,13)=lengthlumenized;
    result(k-initial+1,14)=numPC;
    result(k-initial+1,15)=fractionofsectionwithPC;
    result(k-initial+1,16)=fractionrecruitedPCs;
    result(k-initial+1,17)=fracfullyrecruitedPCs;
    result(k-initial+1,18)=mean(PCarea(PCarea~=0)); %Area Fraction of
recruited PC overlapping with structure
    result(k-initial+1,19)=numDAPI;
    result(k-initial+1,20)=fractionofsectionwithDAPI;
    result(k-initial+1,21)=AI;
    result(k-initial+1,22)=ecc;
    result(k-initial+1,23)=mal;
    k
end

xlswrite('Result.xlsx',result);

```

B.2 CD31manual.m

```
%This script analyzes images of sections of gels containing ECs and
pericytes
%stained for CD31. It outputs data on endothelial structures, lumens,
and
%pericyte recruitment.

%This file is written for images taken on the LHI confocal, which
outputs
%images that contain each channel separately along with a merged image.

%Prior to running the code, run the file ECMstart. This adds search
paths
%so you will be able to run this code while in the folder containing
your
%images.

clear all

n=input('How many images would you like to analyze? ');
initial=input('What is the number of the first image? ');
scale=input('What is the scale of the image? 1 pixel = __ um ');
final=n+initial-1;
result=zeros(n,25);

fname='Image%02d.tif';
fname2='Image%02d_2.tif';
fname3='Image%02d_3.tif';
fname4='Image%02d_4.tif';
fname5='Image%02d_5.tif';
fname6='Image%02d_6.tif';
for k=initial:final
    I=imread(sprintf(fname,k));
    I=rgb2gray(I);

    [m1,n1]=size(I);
    rect=[0 m1/2+1 n1/2-1 m1/2-1];
        %for images with red in lower left, green in top right
%    rect=[n1/2+1 0 n1/2-1 m1/2-1];
        %for images with red in top right, green in top left
    Icrop=imcrop(I,rect);
% %%%use the code below if you have separate image files for each
channel.
% fname='Image%04d_C003.tif';
% fname2='Image%04d_C002.tif';
% for k=initial:final
%     I=imread(sprintf(fname,k));
%     Icrop=rgb2gray(I);

    [m2,n2]=size(Icrop);
    sectionarea=m2*n2;

%To accurately identify as many lumens as possible, multiple ways of
```

```

%thresholding the image are used.

I2b=imadjust(Icrop);
level = graythresh(I2b);
bwz = im2bw(I2b,level);

level = graythresh(Icrop);
bwy = im2bw(Icrop,level);

se=strel('disk',1);
bwza=imdilate(bwx,se);
bwz=imerode(bwza,se);

sel=strel('disk',2);
bwzb=imdilate(bwx,sel);
bww=imerode(bwzb,sel);

figure,imshow(bwzb)
choice=menu('Options','Subtract Region','Draw a line','Done');
while choice~=3
    switch choice
        case 1
            title('After zooming, press any key. Then draw a
polygon around the area you want to remove')
            bwzb=subtractregion(bwzb);
            imshow(bwzb)
        case 2
            title('After zooming, press any key. Then click on the
endpoints of the line you want to draw');
            bwzb=drawline(bwzb);
            imshow(bwzb)
        case 3
            break
    end
    choice=menu('Options','Subtract Region','Draw a line','Done');
end

% The following steps fill small holes in the images (large holes are
% lumens).
filledx = imfill(bwx,4,'holes');
holesx = filledx & ~bwx;
bigholesx = bwareaopen(holesx,5);
smallholesx = holesx & ~bigholesx;
bwz2 = bwz|smallholesx;
bwz3 = bwareaopen(bwz2,20,8);
ccx = bwconncomp(bwz3,8);
numberofstructures=ccx.NumObjects; %number of interconnected CD31+
structures in the image.
ccxlabel=labelmatrix(ccx);

filledy = imfill(bwy,4,'holes');
holesy = filledy & ~bwy;
bigholesy = bwareaopen(holesy,5);

filledz1 = imfill(bwza,4,'holes');

```



```

holesz1 = filledz1 & ~bwza;
bigholesz1a = bwareaopen(holesz1,5);
bigholesz1=imdilate(bigholesz1a,se);

filledz2 = imfill(bwz,4,'holes');
holesz2 = filledz2 & ~bwz;
bigholesz2 = bwareaopen(holesz2,5);

filledz3 = imfill(bwzb,4,'holes');
holesz3 = filledz3 & ~bwzb;
bigholesz3a = bwareaopen(holesz3,5);
bigholesz3=imdilate(bigholesz3a,se1);

filledz4 = imfill(bww,4,'holes');
holesz4 = filledz4 & ~bww;
bigholesz4 = bwareaopen(holesz4,5);

%This step determines the level of CD31 staining.
totalCD31=sum(sum(bwx3))*scale^2; %units=um^2
fractionofsectionwithCD31=sum(sum(bwx3))/sectionarea; %Fraction of
the section with positive CD31 staining

%This step merges all the lumens identified in the various thresholded
%images and removes any small lumens.

lumens1=bigholesx|bigholesy|bigholesz1|bigholesz2|bigholesz3|bigholesz4
;
lumens=bwareaopen(lumens1,5);

% This step compares the mean intensity of the lumen to the mean
intensity
% of the area immediately surrounding the lumen. A true lumen will have
a
% high ratio of surrounding intensity to lumen intensity.
cclumen = bwconncomp(lumens,8);
lumenlabel=labelmatrix(cclumen);
lumenstat=regionprops(cclumen,Icrop,'MeanIntensity');
lumenintens=[lumenstat.MeanIntensity];
lumens2=lumens;
se2=strel('disk',3);
outerintens2=zeros(1,cclumen.NumObjects);
sizel=zeros(1,cclumen.NumObjects);
ratio=zeros(4,cclumen.NumObjects);
for i=1:cclumen.NumObjects
single=zeros(size(lumens1));
single(lumenlabel==i)=1;
sizel(i)=sum(sum(single))/i;
single2=imdilate(single,se);
single3=imdilate(single,se2);
outer=single3-single2;
ccouter = bwconncomp(outer,8);
outerstat=regionprops(ccouter,Icrop,'MeanIntensity');
outerintens=[outerstat.MeanIntensity];
outerintens2(i)=mean(outerintens);
ratio(1,i)=mean(outerintens);
ratio(2,i)=lumenintens(i);

```

```

        ratio(3,i)=mean(outerintens)/lumenintens(i);
        if mean(outerintens)/lumenintens(i)<2 %this number can be
edited to fit the image set
            lumens2(lumenlabel==i)=0;
        else
            outer2=zeros(size(outer));
            for j=1:(m1/2-1)*(n1/2-1)
                if outer(j)==1
                    outer2(j)=ccxlabel(j);
                end
            end
            uniq=unique(outer2);
            [s1,s2]=size(uniq);
            ratio(4,i)=s1;
        %         if s1>3
        %             lumens2(lumenlabel==i)=0;
        %         end
    end
    outerlabel=labelmatrix(ccouter);
    %     figure,imshow(label2rgb(outerlabel))
end

figure,imshow(lumens2)
choice=menu('Options','Subtract Region','Done');
while choice~=3
    switch choice
        case 1
            title('After zooming, press any key. Then draw a
polygon around the area you want to remove')
            lumens2=subtractregion(lumens2);
            imshow(lumens2)
        case 2
            break
    end
    choice=menu('Options','Subtract Region','Done');
end

%This step calculates properties of the true lumens (those identified
by
%the previous step).
stats=regionprops(lumens2,'Area');
numlumens=length([stats.Area]); %Number of lumens in the image
numlumensper=numlumens/sectionarea/scale^2*1e6; %Number of lumens
per mm^2
avglumenarea=mean([stats.Area])*scale^2; %units=um^2; Average area
of a lumen
totlumenarea=sum([stats.Area])/sectionarea; %Lumen area as a
fraction of the area of the sec

biglumens2=bwareaopen(lumens2,200,8); %only large lumens are used
here because they are the most important
stats=regionprops(biglumens2,'Eccentricity','MajorAxisLength');
ecc=mean([stats.Eccentricity]); %Eccentricity - a measure of how
round the lumen is (scale from 0 to 1 where 0 is a circle and 1 is a
line segment)

```

```

    mal=mean([stats.MajorAxisLength])*scale; % Major Axis Length - a
measure of the lumen length

%This step fills in all lumens and calculates the anisotropy index for
each
%structure identified. The anisotropy index is calculated based on the
% average angle of the structures. This is meant for use with
longitudinal
% sections of aligned tissues.
    filledx2=lumens2|bwx3;
    filledx3=imfill(filledx2,'holes');
    stats2=regionprops(filledx3,'MajorAxisLength','Orientation');
    a={stats2.Orientation};
    p={stats2.MajorAxisLength};
    a2=cell2mat(a);
    p2=cell2mat(p);
    for i=1:length(a2)
        if a2(i)<0
            a2(i)=a2(i)+180;
        end
    end
    avga=ones(1,length(a2)).*mean(a2);
    AIx=p2.*abs(cos(deg2rad(a2-avga)));
    AIy=p2.*abs(sin(deg2rad(a2-avga)));
    AI=sum(AIx)/sum(AIy); %Anisotropy Index

%This step calculates how much of the structures are lumenized.
    ccfilled=bwconncomp(filledx3,8);
    filledlabel=labelmatrix(ccfilled);
    count1=0;
    count2=0;
    areacount1=0;
    filledx4=zeros(size(filledx3));
    filledx5=zeros(size(filledx3));
    filledarea=zeros(1,ccfilled.NumObjects);
    [m2,n2]=size(filledx3);
    for i=1:ccfilled.NumObjects
        for j=1:m2
            for l=1:n2
                if filledlabel(j,l)==i && biglumens2(j,l)==1
                    count1=count1+1;
                    count2=count2+1;
                elseif filledlabel(j,l)==i && lumens2(j,l)==1
                    count1=count1+1;
                end
                if filledlabel(j,l)==i
                    areacount1=areacount1+1;
                end
            end
        end
        if count1>0
            filledx4(filledlabel==i)=1;
            filledarea(i)=count1/areacount1;
        end
        if count2>0
            filledx5(filledlabel==i)=1;

```

```

        end
        count1=0;
        count2=0;
        areacount1=0;
    end
    filledx4=logical(filledx4);
    filledx5=logical(filledx5);
    ccfilled2=bwconncomp(filledx4,8);
    fractionnumlumen=ccfilled2.NumObjects/ccfilled.NumObjects;
%Fraction of structures that contain lumens.
    lumenareapercentavgper=mean(filledarea); %average percentage of
each structure filled with lumens
    lumenareapercent=sum(sum(lumens2))/sum(sum(filledx4)); %area
percentage of structures that are lumens (only includes structures that
are lumenized)
    stats3=regionprops(filledx5,'MajorAxisLength');

lengthlumenized=sum([stats.MajorAxisLength])/sum([stats3.MajorAxisLengt
h]); %fraction of structure length covered with lumens (only includes
lumenized structures)

%This step thresholds the pericyte image.
    rectPC=[n1/2+1 0 n1/2-1 m1/2-1];
        %for images with red in lower left and green in top right
%    rectPC=[0 0 n1/2-1 m1/2-1];
        %for images with red in top right and green in top left
IcropPC=imcrop(I,rectPC);
%    rectPC=imread(sprintf(fname2,k));
%    IcropPC=rgb2gray(rectPC);
levelPC = graythresh(IcropPC);
bwPC = im2bw(IcropPC,levelPC);
bw3PC = bwareaopen(bwPC,10,8);
ccPC = bwconncomp(bw3PC,8);
[m3,n3]=size(bw3PC);

%This step determines the level of PCs.
    totalPC=sum(sum(bw3PC))*scale^2; %units=um^2
    fractionofsectionwithPC=sum(sum(bw3PC))/sectionarea; %Fraction of
the section with positive PC staining
    numPC=ccPC.NumObjects/sectionarea/scale^2*1e6; %number PC per mm^2

%This step takes the intersection of the CD31 image and the pericyte
image.
%Those pericytes that overlap ECs are considered recruited.
%Those pericytes that have 50% of their area overlapping with ECs are
%considered fully recruited.
    intersection=bwx3&bw3PC;
    labelPC=labelmatrix(ccPC);
    count=0;
    areacount=0;
    bw3PC_2=zeros(size(bw3PC));
    bw3PC_3=zeros(size(bw3PC));
    PCarea=zeros(1,ccPC.NumObjects);
    for i=1:ccPC.NumObjects
        for j=1:m3
            for l=1:n3

```

```

        if labelPC(j,1)==i && intersection(j,1)==1
            count=count+1;
        end
        if labelPC(j,1)==i
            areacount=areacount+1;
        end
    end
end
if count>0
    bw3PC_2(labelPC==i)=1;
    PCarea(i)=count/areacount;
end
if count/areacount>0.5
    bw3PC_3(labelPC==i)=1;
end
count=0;
areacount=0;
end
ccint=bwconncomp(bw3PC_2,8);
fractionrecruitedPCs=ccint.NumObjects/ccPC.NumObjects; %Fraction of
pericytes that have been recruited.
ccint2=bwconncomp(bw3PC_3,8);
fracfullyrecruitedPCs=ccint2.NumObjects/ccPC.NumObjects; %Fraction
of pericytes that have been fully recruited.

%This step thresholds the DAPI image and counts the nuclei
rect=[0 0 n1/2-1 m1/2-1];
IcropDAPI=imcrop(I,rect);
%   rectPC=imread(sprintf(fname2,k));
%   IcropPC=rgb2gray(rectPC);
levelDAPI = graythresh(IcropDAPI);
bw3DAPI = im2bw(IcropDAPI,levelDAPI);
bw3DAPI = bwareaopen(bw3DAPI,10,8);
ccDAPI = bwconncomp(bw3DAPI,8);
fractionofsectionwithDAPI=sum(sum(bw3DAPI))/sectionarea; %Fraction
of the section with positive DAPI staining
numDAPI=ccDAPI.NumObjects/sectionarea/scale^2*1e6; %number nuclei
per mm^2

%The data is collected into the result matrix and output to an excel
file.
result(k-initial+1,1)=k;
result(k-initial+1,2)=sectionarea;
result(k-initial+1,3)=totalCD31;
result(k-initial+1,4)=fractionofsectionwithCD31;
result(k-initial+1,5)=numlumens;
result(k-initial+1,6)=numlumensper;
result(k-initial+1,7)=avglumenarea;
result(k-initial+1,8)=totlumenarea;
result(k-initial+1,9)=numberofstructures;
result(k-initial+1,10)=fractionnumlumen;
result(k-initial+1,11)=lumenareapercentavgper;
result(k-initial+1,12)=lumenareapercent;
result(k-initial+1,13)=lengthlumenized;
result(k-initial+1,14)=numPC;
result(k-initial+1,15)=fractionofsectionwithPC;

```

```

    result(k-initial+1,16)=fractionrecruitedPCs;
    result(k-initial+1,17)=fracfullyrecruitedPCs;
    result(k-initial+1,18)=mean(PCarea(PCarea~=0)); %Area Fraction of
recruited PC overlapping with structure
    result(k-initial+1,19)=numDAPI;
    result(k-initial+1,20)=fractionofsectionwithDAPI;
    result(k-initial+1,21)=AI;
    result(k-initial+1,22)=ecc;
    result(k-initial+1,23)=mal;
    k

    imwrite(lumens2,sprintf(fname2,k))
    close all
    end

    xlswrite('Result.xlsx',result);

```

B.3 CD31frombw.m

```
%This script analyzes images of sections of gels containing ECs and
pericytes
%stained for CD31. It outputs data on endothelial structures, lumens,
and
%pericyte recruitment.

%This file is written for images taken on the LHI confocal, which
outputs
%images that contain each channel separately along with a merged image.

%Prior to running the code, run the file ECM start. This adds search
paths
%so you will be able to run this code while in the folder containing
your
%images.

clear all

n=input('How many images would you like to analyze? ');
initial=input('What is the number of the first image? ');
scale=input('What is the scale of the image? 1 pixel = __ um ');
final=n+initial-1;
result=zeros(n,28);

fname='Image%02d.tif';
fname2='Image%02d_2.tif';
for k=initial:final
if exist(sprintf(fname2,k), 'file')==0
    continue
end
    I=imread(sprintf(fname,k));
    I=rgb2gray(I);
    [m1,n1]=size(I);
    rect=[0 m1/2+1 n1/2-1 m1/2-1];
        %for images with red in lower left, green in top right
    %    rect=[n1/2+1 0 n1/2-1 m1/2-1];
        %for images with red in top right, green in top left
    Icrop=imcrop(I,rect);

    [m2,n2]=size(Icrop);
    sectionarea=m2*n2;

    I2b=imadjust(Icrop);
    level = graythresh(I2b);
    bwx = im2bw(I2b,level);
    filledx = imfill(bwx,4, 'holes');
    holesx = filledx & ~bwx;
    bigholesx = bwareaopen(holesx,5);
    smallholesx = holesx & ~bigholesx;
    bwx2 = bwx|smallholesx;
    bwx3 = bwareaopen(bwx2,20,8);
```

```

lumens=imread(sprintf(fname2,k));
lumensclass=isa(lumens,'logical');
if lumensclass==1
    lumens2=lumens;
else
    level=graythresh(lumens);
    lumens2=im2bw(lumens,level);
end

%This step calculates properties of the true lumens (those identified
by
%the previous step).
stats=regionprops(lumens2,'Area');
numlumens=length([stats.Area]); %Number of lumens in the image
numlumensper=numlumens/sectionarea/scale^2*1e6; %Number of lumens
per mm^2
avglumenarea=mean([stats.Area])*scale^2; %units=um^2; Average area
of a lumen
totlumenarea=sum([stats.Area])/sectionarea; %Lumen area as a
fraction of the area of the sec

biglumens2=bwareaopen(lumens2,200,8); %only large lumens are used
here because they are the most important
stats=regionprops(biglumens2,'Eccentricity','MajorAxisLength');
ecc=mean([stats.Eccentricity]); %Eccentricity - a measure of how
round the lumen is (scale from 0 to 1 where 0 is a circle and 1 is a
line segment)
mal=mean([stats.MajorAxisLength])*scale; % Major Axis Length - a
measure of the lumen length

count3=0;
count4=0;
count5=0;
MAL=[stats.MajorAxisLength];
for i=1:length(MAL)
    if MAL(i)*scale>200
        count3=count3+1;
        count4=count4+1;
        count5=count5+1;
    elseif MAL(i)*scale>150
        count3=count3+1;
        count4=count4+1;
    elseif MAL(i)*scale>100
        count3=count3+1;
    end
end

%This step fills in all lumens and calculates the anisotropy index for
each
%structure identified. The anisotropy index is calculated based on the
% average angle of the structures. This is meant for use with
longitudinal
% sections of aligned tissues.
filledx2=lumens2|bw3;
filledx3=imfill(filledx2,'holes');
stats2=regionprops(filledx3,'MajorAxisLength','Orientation');

```



```

a={stats2.Orientation};
p={stats2.MajorAxisLength};
a2=cell2mat(a);
p2=cell2mat(p);
for i=1:length(a2)
    if a2(i)<0
        a2(i)=a2(i)+180;
    end
end
avga=ones(1,length(a2)).*mean(a2);
AIx=p2.*abs(cos(deg2rad(a2-avga)));
AIy=p2.*abs(sin(deg2rad(a2-avga)));
AI=sum(AIx)/sum(AIy); %Anisotropy Index

%This step calculates how much of the structures are lumenized.
ccfilled=bwconncomp(filledx3,8);
filledlabel=labelmatrix(ccfilled);
count1=0;
count2=0;
areacount1=0;
filledx4=zeros(size(filledx3));
filledx5=zeros(size(filledx3));
filledarea=zeros(1,ccfilled.NumObjects);
[m2,n2]=size(filledx3);
for i=1:ccfilled.NumObjects
    for j=1:m2
        for l=1:n2
            if filledlabel(j,l)==i && biglumens2(j,l)==1
                count1=count1+1;
                count2=count2+1;
            elseif filledlabel(j,l)==i && lumens2(j,l)==1
                count1=count1+1;
            end
            if filledlabel(j,l)==i
                areacount1=areacount1+1;
            end
        end
    end
    if count1>0
        filledx4(filledlabel==i)=1;
        filledarea(i)=count1/areacount1;
    end
    if count2>0
        filledx5(filledlabel==i)=1;
    end
    count1=0;
    count2=0;
    areacount1=0;
end
filledx4=logical(filledx4);
filledx5=logical(filledx5);
ccfilled2=bwconncomp(filledx4,8);
fractionnumlumen=ccfilled2.NumObjects/ccfilled.NumObjects;
%Fraction of structures that contain lumens.
lumenareapercentagep=mean(filledarea); %average percentage of
each structure filled with lumens

```

```

    lumenareapercent=sum(sum(lumens2))/sum(sum(filledx4)); %area
percentage of structures that are lumens (only includes structures that
are lumenized)
    stats3=regionprops(filledx5, 'MajorAxisLength');

lengthlumenized=sum([stats.MajorAxisLength])/sum([stats3.MajorAxisLengt
h]); %fraction of structure length covered with lumens (only includes
lumenized structures)

%The data is collected into the result matrix and output to an excel
file.
    result(k-initial+1,1)=k;
    result(k-initial+1,2)=sectionarea;
    result(k-initial+1,5)=numlumens;
    result(k-initial+1,6)=numlumensper;
    result(k-initial+1,7)=avglumenarea;
    result(k-initial+1,8)=totlumenarea;
    result(k-initial+1,10)=fractionnumlumen;
    result(k-initial+1,11)=lumenareapercentavgper;
    result(k-initial+1,12)=lumenareapercent;
    result(k-initial+1,13)=lengthlumenized;
    result(k-initial+1,21)=AI;
    result(k-initial+1,22)=ecc;
    result(k-initial+1,23)=mal;
    k
end

xlswrite('Result.xlsx',result);

```

B.4 BasementMembrane.m

```
%This file is written for images taken on the LHI confocal, which
outputs
%images that contain each channel separately along with a merged image.

%Prior to running the code, run the file ECM start. This adds search
paths
%so you will be able to run this code while in the folder containing
your
%images.

clear all

n=input('How many images would you like to analyze? ');
initial=input('What is the number of the first image? ');
scale=input('What is the scale of the image? 1 pixel = __ um ');
inputlevel=input('What threshold would you like to use? ');
level=inputlevel/255;
final=n+initial-1;
result=zeros(n,5);

fname='Image%02d.tif';
fname2='Image%02d_2.tif';
for i=initial:final
    I=imread(sprintf(fname,i));
    I=rgb2gray(I);

    [m1,n1]=size(I);
    rect=[0 m1/2+1 n1/2-1 m1/2-1];
        %for images with red in lower left, green in top right
%    rect=[n1/2+1 0 n1/2-1 m1/2-1];
        %for images with red in top right, green in top left
    Icrop=imcrop(I,rect);
% %%%use the code below if you have separate image files for each
channel.
% fname='Image%04d_C003.tif';
% fname2='Image%04d_C002.tif';
% for k=initial:final
%     I=imread(sprintf(fname,k));
%     Icrop=rgb2gray(I);

    [m2,n2]=size(Icrop);
    sectionarea=m2*n2; %Area of the image

    imsum=sum(sum(Icrop))/sectionarea/scale^2*1e6;
    BWim=im2bw(Icrop,level);
    cc=bwconncomp(BWim,8);
    numabove=cc.NumObjects;

    stats=regionprops(BWim,Icrop,'MeanIntensity');
    avgabove=mean([stats.MeanIntensity]);

%This step thresholds the PC image and counts the cells
```

```

rectPC=[n1/2+1 0 n1/2-1 m1/2-1];
IcropPC=imcrop(I,rectPC);
%   rectPC=imread(sprintf(fname2,k));
%   IcropPC=rgb2gray(rectPC);
levelPC = graythresh(IcropPC);
bwPC = im2bw(IcropPC,levelPC);
bw3PC = bwareaopen(bwPC,10,8);
ccPC = bwconncomp(bw3PC,8);
numPC=ccPC.NumObjects/sectionarea/scale^2*1e6; %number PC per mm^2

%This step thresholds the DAPI image and counts the nuclei
rectDAPI=[0 0 n1/2-1 m1/2-1];
IcropDAPI=imcrop(I,rectDAPI);
%   rectPC=imread(sprintf(fname2,k));
%   IcropPC=rgb2gray(rectPC);
levelDAPI = graythresh(IcropDAPI);
bwDAPI = im2bw(IcropDAPI,levelDAPI);
bw3DAPI = bwareaopen(bwDAPI,10,8);
ccDAPI = bwconncomp(bw3DAPI,8);
numDAPI=ccDAPI.NumObjects/sectionarea/scale^2*1e6; %number nuclei
per mm^2

imsumperDAPI=imsum/numDAPI;
avgaboveperDAPI=avgabove/numDAPI;

result(i-initial+1,1)=i;
result(i-initial+1,2)=sectionarea;
result(i-initial+1,3)=imsum;
result(i-initial+1,4)=numabove;
result(i-initial+1,5)=numPC;
result(i-initial+1,6)=avgabove;
result(i-initial+1,7)=numDAPI;
result(i-initial+1,8)=imsumperDAPI;
result(i-initial+1,9)=avgaboveperDAPI;
end
close

xlswrite('Result.xlsx',result);

```

B.5 ephrin.m

```
%This file is written for images taken on the LHI confocal, which
outputs
%images that contain each channel separately along with a merged image.

%Prior to running the code, run the file ECM start. This adds search
paths
%so you will be able to run this code while in the folder containing
your
%images.

clear all

n=input('How many images would you like to analyze? ');
initial=input('What is the number of the first image? ');
scale=input('What is the scale of the image? 1 pixel = __ um ');
inputlevel=input('What threshold would you like to use? ');
level=inputlevel/255;
final=n+initial-1;
result=zeros(n,20);

fname='Image%03d.tif';
fname2='Image%03d_2.tif';
for i=initial:final
    I=imread(sprintf(fname,i));
    I=rgb2gray(I);

    [m1,n1]=size(I);
    rect=[0 m1/2+1 n1/2-1 m1/2-1];
        %for images with red in lower left, green in top right
%    rect=[n1/2+1 0 n1/2-1 m1/2-1];
        %for images with red in top right, green in top left
    Icrop=imcrop(I,rect);
% %%%use the code below if you have separate image files for each
channel.
% fname='Image%04d_C003.tif';
% fname2='Image%04d_C002.tif';
% for k=initial:final
%     I=imread(sprintf(fname,k));
%     Icrop=rgb2gray(I);

    [m2,n2]=size(Icrop);
    sectionarea=m2*n2; %Area of the image

    imsum=sum(sum(Icrop))/sectionarea/scale^2*1e6;
    BWim=im2bw(Icrop,level);
    cc=bwconncomp(BWim,8);
    numabove=cc.NumObjects;

    stats=regionprops(BWim,Icrop,'MeanIntensity');
    avgabove=mean([stats.MeanIntensity]);

%This step thresholds the DAPI image and counts the nuclei
```

```

rectDAPI=[0 0 n1/2-1 m1/2-1];
IcropDAPI=imcrop(I,rectDAPI);
%   rectPC=imread(sprintf(fname2,k));
%   IcropPC=rgb2gray(rectPC);
levelDAPI = graythresh(IcropDAPI);
bwDAPI = im2bw(IcropDAPI,levelDAPI);
bw3DAPI = bwareaopen(bwDAPI,10,8);
ccDAPI = bwconncomp(bw3DAPI,8);
numDAPI=ccDAPI.NumObjects/sectionarea/scale^2*1e6; %number nuclei
per mm^2

imsumperDAPI=imsum/numDAPI;
avgaboveperDAPI=avgabove/numDAPI;

%This step thresholds the PC image and counts the cells
rectPC=[n1/2+1 0 n1/2-1 m1/2-1];
IcropPC=imcrop(I,rectPC);
%   rectPC=imread(sprintf(fname2,k));
%   IcropPC=rgb2gray(rectPC);
levelPC = graythresh(IcropPC)*4;
bwPC = im2bw(IcropPC,levelPC);
bw3PC = bwareaopen(bwPC,10,8);
intPC=bw3PC&bw3DAPI;
ccPC = bwconncomp(intPC,8);
numPC=ccPC.NumObjects/sectionarea/scale^2*1e6; %number PC per mm^2

ephPC=Icrop.*(uint8(bw3PC));
imsumPC=sum(sum(ephPC))/sectionarea/scale^2*1e6;
BWimPC=im2bw(ephPC,level);
ccPC=bwconncomp(BWimPC,8);
numabovePC=ccPC.NumObjects;

statsPC=regionprops(BWimPC,Icrop,'MeanIntensity');
avgabovePC=mean([statsPC.MeanIntensity]);
imsumPCperPC=imsumPC/numPC;
avgabovePCperPC=avgabovePC/numPC;

numEC=numDAPI-numPC;

ephEC=Icrop.*(uint8(~bw3PC));
imsumEC=sum(sum(ephEC))/sectionarea/scale^2*1e6;
BWimEC=im2bw(ephEC,level);
ccEC=bwconncomp(BWimEC,8);
numaboveEC=ccEC.NumObjects;

statsEC=regionprops(BWimEC,Icrop,'MeanIntensity');
avgaboveEC=mean([statsEC.MeanIntensity]);
imsumECperEC=imsumEC/numEC;
avgaboveECperEC=avgaboveEC/numEC;

result(i-initial+1,1)=i
result(i-initial+1,2)=sectionarea;
result(i-initial+1,3)=imsum;
result(i-initial+1,4)=numabove;
result(i-initial+1,5)=avgabove;

```

```
result(i-initial+1,6)=numDAPI;  
result(i-initial+1,7)=imsumperDAPI;  
result(i-initial+1,8)=avgaboveperDAPI;  
result(i-initial+1,9)=imsumPC;  
result(i-initial+1,10)=numabovePC;  
result(i-initial+1,11)=avgabovePC;  
result(i-initial+1,12)=numPC;  
result(i-initial+1,13)=imsumPCperPC;  
result(i-initial+1,14)=avgabovePCperPC;  
result(i-initial+1,15)=imsumEC;  
result(i-initial+1,16)=numaboveEC;  
result(i-initial+1,17)=avgaboveEC;  
result(i-initial+1,18)=numEC;  
result(i-initial+1,19)=imsumECperEC;  
result(i-initial+1,20)=avgaboveECperEC;  
end  
close  
  
xlswrite('Result.xlsx',result);
```

B.6 Quantifying Growth of Vessels.m

```
clear all

n=input('How many images would you like to analyze? ');
initial=input('What is the number of the first image? ');
scale=input('What is the scale of the image? 1 pixel = __ um ');
final=n+initial-1;
result=zeros(n,17);

fname='MD-Experiment-%04d_c3.tif';
fname2='MD-Experiment-%04d_c4.tif';
fname3='MD-Experiment-%04d_c5.tif';
for k=initial:final
%CONVERTING IMAGE TO A BLACK AND WHITE IMAGE
I=imread(sprintf(fname,k));
I=rgb2gray(I); %converts image into a grayscale image
Icrop=I;
[m1,n1]=size(Icrop);
sectionarea=m1*n1;
se=strel('disk',5); %used to dilate image
se2=strel('disk',2); %used to dilate image
I2a=imdilate(Icrop,se); %dilates the original grayscale image
I2=imerode(I2a,se2); %erodes the dilated image
I3 = imadjust(I2); %Increases the contrast of the image
level = graythresh(I3)*.9; %automatically determines threshold for
creating binary image
% % lowering the threshold level slightly ensures that all structures
are included; the automatic thresholding consistently excludes some
structures
bw = im2bw(I3,level); %converts grayscale image to binary image (using
determined threshold)
bw2 = bwareaopen(bw,50,8); %removes any continuous structure smaller
than 300 pixels in area
bw2=bwareaopen(bw2,500,8);
cc = bwconncomp(bw2,8); %function bwconncomp finds all connected
components from binary image (8=connectivity parameter)
NUMBEROFCONTINUOUSSTRUCTURES=cc.NumObjects/sectionarea/scale^2*1e6;
%gives the number of distinct objects from the previous command <--I
think this is the best determination of the total # of structures
labeled = labelmatrix(cc); %labelmatrix allows you to visualize
connected components
whos labeled; %identifies the labeled structures
RGB_label = label2rgb(labeled, @spring, 'c', 'shuffle'); %arbitrarily
assigns a color to each structure
CD31=sum(sum(bw2))/sectionarea*scale^2*1e6; %total area CD31 per mm2

%LOCATING STRUCTURES
bw3=bwmorph(bw2,'fill',Inf); %fills in any holes in the structures
resulting from the thresholding process
bw4=bwmorph(bw3,'thin',Inf);%thins objects to lines
bw5=bw4; %creates a copy of the original image bw4
juncs=findjunctions(bw4); %finds junctions from the thinned image (bw4)
```



```

juncs2=imdilate(juncs,se2); %dilates the junction points found by
'juncs'

for i=1:m1
    for j=1:n1
        if bw4(i,j)==1 && juncs2(i,j)==1
            bw4(i,j)=0;
        end
    end
end
%for each matching point in image 'bw4' (thinned image) and 'juncs2'
(dilated junction points), this deletes that point in 'bw4'-->separates
structures

bw4b=bwareaopen(bw4,20); %removes any structures from image 'bw4' that
are less than 20 pixels in length (purpose is to remove small segments
that aren't actually structures)
cc2=bwconncomp(bw4b,8);
NUMBEROFSEGMENTS=cc2.NumObjects/sectionarea/scale^2*1e6; %this is the
number of individual segments (NOT continuous structures)
bw6=bw5-bw4b; %this image is the original thinned image (bw5) minus the
structures that we want to include (bw4b)-->results in an image of the
segments we DON'T want to include
bw7a=bw5-bw6; %this is the structures we want to include in the image
(w/ junctions)
bw7b=bwmorph(bw7a,'thin',Inf); %removes any segments thicker than 1
pixel resulting from including "juncs2"
bw7=bwareaopen(bw7b,20);
% figure, imshow(bw7);
juncs3=juncs-juncs; %just a black image

endpoint=findendpoints(bw7);
endpoint2=imdilate(endpoint,se2);
for i=1:m1
    for j=1:n1
        if endpoint2(i,j)==1 && juncs2(i,j)==1
            juncs3(i,j)=1;
        end
    end
end
%this determines which of the original junctions are actually junctions
in the final image (which junction points are in the final image bw7)

%CALCULATING PARAMETERS OF INTEREST
cc3=bwconncomp(juncs3,8);
NUMBEROFJUNCTIONS=cc3.NumObjects/sectionarea/scale^2*1e6;
bw8 = bwconncomp(bw7,8); %function bwconncomp finds all connected
components from binary image (8=connectivity parameter)
stats=regionprops(bw8,'orientation','Area'); %gives stats for each
identified structure
TOTALVESSELLENGTH=sum(sum(bw7))/sectionarea/scale^2*1e6; %total vessel
length is just the area of the thinned image bw7
AVERAGEVESSELLENGTHcontinuousstructures=TOTALVESSELLENGTH/NUMBEROFCONTI
NUOUSSTRUCTURES; %this is the average length of CONTINUOUS structures

```

```

AVERAGEVESSELLENGTHsegments=TOTALVESSELLENGTH/NUMBEROFSEGMENTS; %this
is the average length of the small segments
AVERAGEDIAMETER=sum(sum(bw3))/sum(sum(bw7)); %this is the total area
divided by total vessel length
a={stats.Orientation};
p={stats.Area};
a2=cell2mat(a);
p2=cell2mat(p);
for i=1:length(a2)
    if a2(i)<0
        a2(i)=a2(i)+180;
    end
end
avga=ones(1,length(a2)).*mean(a2);
AIx=p2.*abs(cos(deg2rad(a2-avga)));
AIy=p2.*abs(sin(deg2rad(a2-avga)));
AI=sum(AIx)/sum(AIy); %Anisotropy Index

%overlay structures on original image
bw10=imdilate(bw7,se2);
Ia=imadjust(Icrop);
for i=1:m1;
    for j=1:n1;
        if bw10(i,j)==1;
            Ia(i,j)=0;
        end;
    end;
end;

%This step thresholds the pericyte image.
%   rectPC=[n1/2+1 0 n1/2-1 m1/2-1];
%           %for images with red in lower left and green in top right
% %   rectPC=[0 0 n1/2-1 m1/2-1];
%           %for images with red in top right and green in top left
%   IcropPC=imcrop(I,rectPC);
rectPC=imread(sprintf(fname2,k));
IcropPC=rgb2gray(rectPC);
levelPC = graythresh(IcropPC)*2;
bwPC = im2bw(IcropPC,levelPC);
bw3PC = bwareaopen(bwPC,10,8);
ccPC = bwconncomp(bw3PC,8);
[m3,n3]=size(bw3PC);

%This step determines the level of PCs.
totalPC=sum(sum(bw3PC))*scale^2; %units=um^2
fractionofsectionwithPC=sum(sum(bw3PC))/sectionarea; %Fraction of
the section with positive PC staining
numPC=ccPC.NumObjects/sectionarea/scale^2*1e6; %number PC per mm^2

%This step takes the intersection of the CD31 image and the pericyte
image.
%Those pericytes that overlap ECs are considered recruited.
%Those pericytes that have 50% of their area overlapping with ECs are
%considered fully recruited.
intersection=bw2&bw3PC;
labelPC=labelmatrix(ccPC);

```

```

count=0;
areacount=0;
bw3PC_2=zeros(size(bw3PC));
bw3PC_3=zeros(size(bw3PC));
PCarea=zeros(1,ccPC.NumObjects);
for i=1:ccPC.NumObjects
    for j=1:m3
        for l=1:n3
            if labelPC(j,l)==i && intersection(j,l)==1
                count=count+1;
            end
            if labelPC(j,l)==i
                areacount=areacount+1;
            end
        end
    end
    if count>0
        bw3PC_2(labelPC==i)=1;
        PCarea(i)=count/areacount;
    end
    if count/areacount>0.5
        bw3PC_3(labelPC==i)=1;
    end
    %     count
    %     areacount
    count=0;
    areacount=0;
end
ccint=bwconncomp(bw3PC_2,8);
fractionrecruitedPCs=ccint.NumObjects/ccPC.NumObjects; %Fraction of
perictyes that have been recruited.
ccint2=bwconncomp(bw3PC_3,8);
fracfullyrecruitedPCs=ccint2.NumObjects/ccPC.NumObjects; %Fraction
of perictyes that have been fully recruited.

%This step thresholds the DAPI image and counts the nuclei
%     rect=[0 0 n1/2-1 m1/2-1];
%     IcropDAPI=imcrop(I,rect);
rectDAPI=imread(sprintf(fname3,k));
IcropDAPI=rgb2gray(rectDAPI);
levelDAPI = graythresh(IcropDAPI)*2;
bwDAPI = im2bw(IcropDAPI,levelDAPI);
bw3DAPI = bwareaopen(bwDAPI,10,8);
ccDAPI = bwconncomp(bw3DAPI,8);
fractionofsectionwithDAPI=sum(sum(bw3DAPI))/sectionarea; %Fraction
of the section with positive DAPI staining
numDAPI=ccDAPI.NumObjects/sectionarea/scale^2*1e6; %number nuclei
per mm^2

figure,imshow(bwx2)
figure,imshow(Ia)

result(k-initial+1,1)=k;
result(k-initial+1,2)=sectionarea;
result(k-initial+1,3)=NUMBEROFCONTINUOUSSTRUCTURES;
result(k-initial+1,4)=NUMBEROFSEGMENTS;

```

```
result(k-initial+1,5)=NUMBEROFJUNCTIONS;
result(k-initial+1,6)=TOTALVESSELLENGTH*scale;
result(k-initial+1,7)=AVERAGEVESSELLENGTHcontinuousstructures*scale;
result(k-initial+1,8)=AVERAGEVESSELLENGTHsegments*scale;
result(k-initial+1,9)=AVERAGEDIAMETER*scale;
result(k-initial+1,10)=AI;
result(k-initial+1,11)=fractionofsectionwithPC;
result(k-initial+1,12)=numPC;
result(k-initial+1,13)=fractionrecruitedPCs;
result(k-initial+1,14)=fracfullyrecruitedPCs;
result(k-initial+1,15)=fractionofsectionwithDAPI;
result(k-initial+1,16)=numDAPI;
result(k-initial+1,17)=CD31;
k
end

xlswrite('Results.xlsx',result);
```

B.7 CropQuantifyingGrowthofVessels.m

```
clear all

n=input('How many images would you like to analyze? ');
initial=input('What is the number of the first image? ');
scale=input('What is the scale of the image? 1 pixel = __ um ');
final=n+initial-1;
result=zeros(n,17);

fname='MD-Experiment-%04d_c3.tif';
fname2='MD-Experiment-%04d_c4.tif';
fname3='MD-Experiment-%04d_c5.tif';
for k=initial:final
%CONVERTING IMAGE TO A BLACK AND WHITE IMAGE
I=imread(sprintf(fname,k));
I=rgb2gray(I); %converts image into a grayscale image
imshow(imadjust(I))
takemeout=roipoly;
takemeout=double(takemeout);
Icrop=I;
[m1,n1]=size(Icrop);
sectionarea=sum(sum(takemeout));
se=strel('disk',5); %used to dilate image
se2=strel('disk',2); %used to dilate image
I2a=imdilate(Icrop,se); %dilates the original grayscale image
I2=imerode(I2a,se2); %erodes the dilated image
I3 = imadjust(I2); %Increases the contrast of the image
level = graythresh(I3)*.9; %automatically determines threshold for
creating binary image
% % lowering the threshold level slightly ensures that all structures
are included; the automatic thresholding consistently excludes some
structures
bw = im2bw(I3,level); %converts grayscale image to binary image (using
determined threshold)
bw2 = bwareaopen(bw,50,8); %removes any continuous structure smaller
than 300 pixels in area
bw2=croptopoly(bw2,takemeout);
I4 = imadjust(Icrop); %Increases the contrast of the image
levelx = graythresh(I4)*1.4; %automatically determines threshold for
creating binary image
bwx2=bwareaopen(bw2,500,8);
cc=bwconncomp(bwx2,8); %function bwconncomp finds all connected
components from binary image (8=connectivity parameter)
NUMBEROFCONTINUOUSSTRUCTURES=cc.NumObjects/sectionarea/scale^2*1e6;
%gives the number of distinct objects from the previous command <--I
think this is the best determination of the total # of structures
labeled = labelmatrix(cc); %labelmatrix allows you to visualize
connected components
whos labeled; %identifies the labeled structures
RGB_label = label2rgb(labeled, @spring, 'c', 'shuffle'); %arbitrarily
assigns a color to each structure
CD31=sum(sum(bw2))/sectionarea*scale^2*1e6; %total area CD31 per mm2
```

```

%LOCATING STRUCTURES
bw3=bwmorph(bw2,'fill',Inf); %fills in any holes in the structures
resulting from the thresholding process
bw4=bwmorph(bw3,'thin',Inf);%thins objects to lines
bw5=bw4; %creates a copy of the original image bw4
juncs=findjunctions(bw4); %finds junctions from the thinned image (bw4)
juncs2=imdilate(juncs,se2); %dilates the junction points found by
'juncs'

for i=1:m1
    for j=1:n1
        if bw4(i,j)==1 && juncs2(i,j)==1
            bw4(i,j)=0;
        end
    end
end
%for each matching point in image 'bw4' (thinned image) and 'juncs2'
(dilated junction points), this deletes that point in 'bw4'-->separates
structures

bw4b=bwareaopen(bw4,20); %removes any structures from image 'bw4' that
are less than 20 pixels in length (purpose is to remove small segments
that aren't actually structures)
cc2=bwconncomp(bw4b,8);
NUMBEROFSEGMENTS=cc2.NumObjects/sectionarea/scale^2*1e6; %this is the
number of individual segments (NOT continuous structures)
bw6=bw5-bw4b; %this image is the original thinned image (bw5) minus the
structures that we want to include (bw4b)-->results in an image of the
segments we DON'T want to include
bw7a=bw5-bw6; %this is the structures we want to include in the image
(w/ junctions)
bw7b=bwmorph(bw7a,'thin',Inf); %removes any segments thicker than 1
pixel resulting from including "juncs2"
bw7=bwareaopen(bw7b,20);
% figure, imshow(bw7);
juncs3=juncs-juncs; %just a black image

endpoint=findendpoints(bw7);
endpoint2=imdilate(endpoint,se2);
for i=1:m1
    for j=1:n1
        if endpoint2(i,j)==1 && juncs2(i,j)==1
            juncs3(i,j)=1;
        end
    end
end
%this determines which of the original junctions are actually junctions
in the final image (which junction points are in the final image bw7)

%CALCULATING PARAMETERS OF INTEREST
cc3=bwconncomp(juncs3,8);
NUMBEROFJUNCTIONS=cc3.NumObjects/sectionarea/scale^2*1e6;
bw8 = bwconncomp(bw7,8); %function bwconncomp finds all connected
components from binary image (8=connectivity parameter)

```

```

stats=regionprops (bw8, 'orientation', 'Area'); %gives stats for each
identified structure
TOTALVESSELLENGTH=sum (sum (bw7)) /sectionarea/scale^2*1e6; %total vessel
length is just the area of the thinned image bw7
AVERAGEVESSELLENGTHcontinuousstructures=TOTALVESSELLENGTH/NUMBEROFCONTI
NUOUSSTRUCTURES; %this is the average length of CONTINUOUS structures
AVERAGEVESSELLENGTHsegments=TOTALVESSELLENGTH/NUMBEROFSEGMENTS; %this
is the average length of the small segments
AVERAGEDIAMETER=sum (sum (bw3)) /sum (sum (bw7)); %this is the total area
divided by total vessel length
a={stats.Orientation};
p={stats.Area};
a2=cell2mat (a);
p2=cell2mat (p);
for i=1:length (a2)
    if a2 (i)<0
        a2 (i)=a2 (i)+180;
    end
end
avga=ones (1, length (a2)) .*mean (a2);
AIx=p2 .*abs (cos (deg2rad (a2-avga)));
AIy=p2 .*abs (sin (deg2rad (a2-avga)));
AI=sum (AIx) /sum (AIy); %Anisotropy Index

%overlay structures on original image
bw10=imdilate (bw7, se2);
Ia=imadjust (Icrop);
for i=1:m1;
    for j=1:n1;
        if bw10 (i, j)==1;
            Ia (i, j)=0;
        end;
    end;
end;

%This step thresholds the pericyte image.
%   rectPC=[n1/2+1 0 n1/2-1 m1/2-1];
%       %for images with red in lower left and green in top right
% %   rectPC=[0 0 n1/2-1 m1/2-1];
%       %for images with red in top right and green in top left
%   IcropPC=imcrop (I, rectPC);
rectPC=imread (sprintf (fname2, k));
IPC=rgb2gray (rectPC);
IcropPC=IPC;
levelPC = graythresh (IcropPC) *2;
bwPC = im2bw (IcropPC, levelPC);
bw3PC = bwareaopen (bwPC, 10, 8);
bw3PC=croptopoly (bw3PC, takemeout);
ccPC = bwconncomp (bw3PC, 8);
[m3, n3]=size (bw3PC);

%This step determines the level of PCs.
totalPC=sum (sum (bw3PC)) *scale^2; %units=um^2
fractionofsectionwithPC=sum (sum (bw3PC)) /sectionarea; %Fraction of
the section with positive PC staining
numPC=ccPC.NumObjects /sectionarea/scale^2*1e6; %number PC per mm^2

```

```

%   intersection=bw3&bw3PC;
%   intersection2=bwareaopen(intersection,5);
%   ccint=bwconncomp(intersection2,8);
%   fractionrecruitedPCs=ccint.NumObjects/ccPC.NumObjects;

%This step takes the intersection of the CD31 image and the pericyte
image.
%Those pericytes that overlap ECs are considered recruited.
%Those pericytes that have 50% of their area overlapping with ECs are
%considered fully recruited.
    intersection=bw2&bw3PC;
    labelPC=labelmatrix(ccPC);
    count=0;
    areacount=0;
    bw3PC_2=zeros(size(bw3PC));
    bw3PC_3=zeros(size(bw3PC));
    PCarea=zeros(1,ccPC.NumObjects);
    for i=1:ccPC.NumObjects
        for j=1:m3
            for l=1:n3
                if labelPC(j,l)==i && intersection(j,l)==1
                    count=count+1;
                end
                if labelPC(j,l)==i
                    areacount=areacount+1;
                end
            end
        end
        if count>0
            bw3PC_2(labelPC==i)=1;
            PCarea(i)=count/areacount;
        end
        if count/areacount>0.5
            bw3PC_3(labelPC==i)=1;
        end
    end
%   count
%   areacount
    count=0;
    areacount=0;
end
    ccint=bwconncomp(bw3PC_2,8);
    fractionrecruitedPCs=ccint.NumObjects/ccPC.NumObjects; %Fraction of
pericytes that have been recruited.
    ccint2=bwconncomp(bw3PC_3,8);
    fracfullyrecruitedPCs=ccint2.NumObjects/ccPC.NumObjects; %Fraction
of pericytes that have been fully recruited.

%This step thresholds the DAPI image and counts the nuclei
%   rect=[0 0 n1/2-1 m1/2-1];
%   IcropDAPI=imcrop(I,rect);
    rectDAPI=imread(sprintf(fname3,k));
    IDAPI=rgb2gray(rectDAPI);
    IcropDAPI=IDAPI;
    levelDAPI = graythresh(IcropDAPI)*2;
    bwDAPI = im2bw(IcropDAPI,levelDAPI);

```



```

    bw3DAPI = bwareaopen(bwDAPI,10,8);
    bw3DAPI=croptopoly(bw3DAPI,takemeout);
    ccDAPI = bwconncomp(bw3DAPI,8);
    fractionofsectionwithDAPI=sum(sum(bw3DAPI))/sectionarea; %Fraction
of the section with positive DAPI staining
    numDAPI=ccDAPI.NumObjects/sectionarea/scale^2*1e6; %number nuclei
per mm^2

figure,imshow(bwx2)
figure,imshow(Ia)

result(k-initial+1,1)=k;
result(k-initial+1,2)=sectionarea;
result(k-initial+1,3)=NUMBEROFCONTINUOUSSTRUCTURES;
result(k-initial+1,4)=NUMBEROFSEGMENTS;
result(k-initial+1,5)=NUMBEROFJUNCTIONS;
result(k-initial+1,6)=TOTALVESSELLENGTH*scale;
result(k-initial+1,7)=AVERAGEVESSELLENGTHcontinuousstructures*scale;
result(k-initial+1,8)=AVERAGEVESSELLENGTHsegments*scale;
result(k-initial+1,9)=AVERAGEDIAMETER*scale;
result(k-initial+1,10)=AI;
result(k-initial+1,11)=fractionofsectionwithPC;
result(k-initial+1,12)=numPC;
result(k-initial+1,13)=fractionrecruitedPCs;
result(k-initial+1,14)=fracfullyrecruitedPCs;
result(k-initial+1,15)=fractionofsectionwithDAPI;
result(k-initial+1,16)=numDAPI;
result(k-initial+1,17)=CD31;
k
end

xlswrite('Results.xlsx',result);

```

B.8 opticaldensity.m

```
clear all

fname=input('Enter root for polarizer/analyzer file (ex: ''cala''): ');

sep = '';
fnp = [fname sep modind(0,5) '.tif'];
I=imread(fnp, 'TIFF');
imshow(I)

bkg=roipoly;
close

intens=zeros(1,20);
for i=1:20
    fnp2=[fname sep modind(i-1,5) '.tif'];
    I2=imread(fnp2, 'TIFF');
    stats=regionprops(bkg, I2, 'MeanIntensity');
    intens(i)=[stats.MeanIntensity];
end

for i=1:20;
    if intens(i)==max(intens)
        maxintim=i-1;
    end
end

fnp3 = [fname sep modind(maxintim,5) '.tif'];
I3=imread(fnp3);
imshow(I3)
[x1,y1]=ginput(2);
dist=abs(y1(1)-y1(2));

num=input('How many regions would you like to analyze? ');

reg=zeros(size(I3));
for i=1:num
    [ar1,x2,y2]=roipoly(I3);
    reg=reg+ar1;
    y3=y2+ones(size(y2))*dist;
    y4=y2-ones(size(y2))*dist;
    ar2=roipoly(I3,x2,y3);
    ar3=roipoly(I3,x2,y4);
    reg=reg+ar1+ar2+ar3;
end
reg=im2bw(reg);
cc=bwconncomp(reg);

stats2=regionprops(cc, I3, 'MeanIntensity');
intens2=[stats2.MeanIntensity];
intens3=zeros(2,1);
intens4=zeros(2,1);
intens5=zeros(num,1);
```

```
intens3(1)=intens2(1);
intens3(2)=intens2(3);
nor=zeros(num,1);
nor(1)=1;
intens5(1)=intens2(2);
for i=2:num
    intens4(1)=intens2(i*3-2);
    intens4(2)=intens2(i*3);
    nor(i)=mean(intens3)/mean(intens4);
    intens5(i)=intens2(i*3-1);
end

result=intens5.*nor;

xlswrite('Result.xlsx',result);
close
```

B.9 ECMstart.m

```
dirbase='C:\Krissy\UMN\Matlab\ECM Image Analysis';
imgpath='C:\Krissy\UMN\Results';

dir0=[dirbase '\BasementMembrane'];
dir1=[dirbase '\CollagenI'];
dir2=[dirbase '\CD31'];
dir3=[dirbase '\3DRecon'];

disp(['Adding search path ' dirbase]);addpath(dirbase);
disp(['Adding search path ' dir0]);addpath(dir0);
disp(['Adding search path ' dir1]);addpath(dir1);
disp(['Adding search path ' dir2]);addpath(dir2);
disp(['Adding search path ' dir3]);addpath(dir3);
disp(['Changing directory to ' imgpath]);eval(['cd ' imgpath]);
```

B.10 WMstart.m

```
dirbase='C:\Krissy\UMN\Matlab\Whole Mount Stain Analysis';  
imgpath='C:\Krissy\UMN\Results';  
  
disp(['Adding search path ' dirbase]);addpath(dirbase);  
disp(['Changing directory to ' imgpath]);eval(['cd ' imgpath]);
```

B.11 kmrpmstart.m

```
%userrpmstart.m
% This startup script sets personal
% paths and variables for the user's
% rpm settings.

% Modify the statements below to point
% to your personal matlab directory and
% to your images subdirectory.
dirbase='C:\Krissy\UMN\rpmscripts';
imgpath='C:\Krissy\UMN\Results';

%%%%%%%%%%%%%%%%%%%%%%%%%%%%%%%%%%%%%%%%%%%%%%%%%%%%%%%%%%%%%%%%%%%%%%%%
% Don't modify the statements below.
dir0=[dirbase '\RPMScripts'];
dir1=[dir0 '\rpm'];
dir2=[dir0 '\rpmsupport'];
dir2a=[dir2 '\Basic'];
dir3a=[dirbase '\High speed'];
disp(['Adding search path ' dirbase]);addpath(dirbase);
disp(['Adding search path ' dir0]);addpath(dir0);
disp(['Adding search path ' dir1]);addpath(dir1);
disp(['Adding search path ' dir2]);addpath(dir2);
disp(['Adding search path ' dir2a]);addpath(dir2a);
disp(['Adding search path ' dir3a]);addpath(dir3a);
disp(['Changing directory to ' imgpath]);eval(['cd ' imgpath]);
```

B.12 drawline.m

```
function I=drawline(I)

    zoom on
    pause;
    [x,y]=ginput(2);
    if abs(x(2)-x(1))>abs(y(2)-y(1))
        m=(y(2)-y(1))/(x(2)-x(1));
        b=y(1)-m*x(1);
        if x(1)<x(2)
            t=[x(1):1:x(2)];
            t=round(t);
            s=round(m.*t+b);
        else
            t=[x(2):1:x(1)];
            t=round(t);
            s=round(m.*t+b);
        end
    else
        m=(x(2)-x(1))/(y(2)-y(1));
        b=x(1)-m*y(1);
        if y(1)<y(2)
            s=[y(1):1:y(2)];
            s=round(s);
            t=round(m.*s+b);
        else
            s=[y(2):1:y(1)];
            s=round(s);
            t=round(m.*s+b);
        end
    end

    for i=1:length(s)
        I(s(i),t(i),1)=255;
    end
end
```

B.13 subtractregion.m

```
function I=subtractregion(I)

zoom on
pause;
takemeout=roipoly;
takemeout=double(takemeout);
indices=find(takemeout==1);
I(indices)=0;
I=double(I);
```


B.14 overlay.m

```
function y=overlay(I,red,green,blue)
```

```
R = I;  
G = I;  
B = I;  
R(red~=0) = 255;  
G(red~=0) = 0;  
B(red~=0) = 0;  
R(green~=0)=0;  
G(green~=0)=255;  
B(green~=0)=0;  
R(blue~=0)=0;  
G(blue~=0)=0;  
B(blue~=0)=255;  
  
y = cat(3,R,G,B);
```

B.15 croptopoly.m

```
function I=croptopoly(I,takemeout)

indices=find(takemeout==0);
I(indices)=0;
I=double(I);
```

B.16 findendpoints.m

```
function y=findendpoints(x)
```

```
lut=
```

```
[0 0 0 0 0 0 0 0 0 0 0 0 0 0 0 0 0 1 1 1 1 1 0 1 1 1 1 0 0 0 0 0 0 0 ...  
 0 0 0 0 0 0 0 0 0 0 0 0 0 0 0 0 0 1 0 0 0 1 0 0 0 0 0 0 0 0 0 0 0 0 ...  
 0 0 0 0 0 0 0 0 0 0 0 0 0 0 0 0 0 1 0 0 0 0 0 0 0 0 1 1 0 0 0 0 0 0 ...  
 0 0 0 0 0 0 0 0 0 0 0 0 0 0 0 0 0 0 0 0 0 0 0 0 0 0 0 0 0 0 0 0 0 0 ...  
 0 0 0 0 0 0 0 0 0 0 0 0 0 0 0 0 0 1 0 0 0 0 0 0 0 0 0 0 0 0 0 0 0 0 ...  
 0 0 0 0 0 0 0 0 0 0 0 0 0 0 0 0 0 1 0 0 0 0 0 0 0 0 0 0 0 0 0 0 0 0 ...  
 0 0 0 0 0 0 0 0 0 0 0 0 0 0 0 0 0 0 0 0 0 0 0 0 0 0 0 0 0 0 0 0 0 0 ...  
 0 0 0 0 0 0 0 0 0 0 0 0 0 0 0 0 0 1 0 0 0 0 0 0 0 0 0 0 0 0 0 0 0 0 ...  
 0 0 0 0 0 0 0 0 0 0 0 0 0 0 0 0 0 1 0 0 0 1 0 0 0 0 0 0 0 0 0 0 0 0 ...  
 0 0 0 0 0 0 0 0 0 0 0 0 0 0 0 0 0 0 0 0 0 0 0 0 0 0 0 0 0 0 0 0 0 0 ...  
 0 0 0 0 0 0 0 0 0 0 0 0 0 0 0 0 0 0 0 0 0 0 0 0 0 0 0 0 0 0 0 0 0 0 ...  
 0 0 0 0 0 0 0 0 0 0 0 0 0 0 0 0 0 1 0 0 0 0 0 0 0 0 0 0 0 0 0 0 0 0 ...  
 0 0 0 0 0 0 0 0 0 0 0 0 0 0 0 0 0 0 0 0 0 0 0 0 0 0 0 0 0 0 0 0 0 0 ...  
 0 0 0 0 0 0 0 0 0 0 0 0 0 0 0 0 0 1 0 0 0 0 0 0 0 0 0 0 0 0 0 0 0 0 ...  
 0 0 0 0 0 0 0 0 0 0 0 0 0 0 0 0 0 0 0 0 0 0 0 0 0 0 0 0 0 0 0 0 0 0];
```

```
y=applylut(x,lut);
```


Appendix C. Model Code

```
clear all

delx=.0005; %cm = 5 um distance between nodes
perm=9.92e-11; %cm^2 tissue permeability
mu=.0089; %P viscosity
u=1333.22; %(g/s^2/cm)/mmHg = unit multiplier
kx=perm/mu*u; %2.67e-6; %10^-5/60; %cm^2/(s*mmHg) x direction
ky=perm/mu*u; %2.67e-6; %10^-5/60; %cm^2/(s*mmHg) y direction
Dx=1/delx; %Darcy's Law component x direction
Dy=1/delx; %Darcy's Law component y direction
Dx2=kx/delx; %Darcy's Law component x direction
Dy2=ky/delx; %Darcy's Law component y direction
P=pi/8/mu/delx^3*u; %Poiseuille Flow component(mass balance) - mult by
r^4, divide by tubule length
P2=1/8/mu*u; %Poiseuille Flow component(mom. balance) - mult by r^2,
divide by tubule length
gelwidth=41; %number of node points per construct width
gellength=51; %number of node points per construct length
gelsize=gelwidth*gellength;
vxinlet=1.33e-4; %cm/s average x velocity at inlet
poutlet=0; %mmHg pressure at outlet
pinlet=vxinlet*delx*gellength/kx+poutlet; %pressure at inlet
vxcomp=gelsize;
vycomp=2*gelsize;
result=zeros(6,21);

%Tubule Characteristics
rmean=.0003; %cm = 3 um radius
rstdev=.0000125; %cm = 0.125 um
lmean=.01; %cm = 100 um length
lstdev=.001; %cm = 10 um
amean=0; %angle
astdev=pi/9*2;
n=100; %number of tubules
bi=22; %number of bifurcations (must be <= n/3)

for aa=1:1
%Matrix T: endpoints matrix notation(4),endpoints vector notation(2),
%radius(1),ideal length(1),angle(1),actual length(1)
T=zeros(n,10);
T(:,7)=rmean+rstdev.*randn(n,1);
T(1:(bi*3),8)=lmean/2+(lstdev/2).*randn(bi*3,1);
T((bi*3+1):n,8)=lmean+lstdev.*randn(n-(bi*3),1);
T(:,9)=amean+astdev.*randn(n,1);
for i=1:bi*3
while T(i,7)<0
T(i,7)=rmean+rstdev.*randn(1,1);
end
while T(i,9)>pi/2||T(i,9)<-pi/2
T(i,9)=amean+astdev.*randn(1,1);
end
while T(i,8)<sqrt(2)*delx
T(i,8)=lmean/2+(lstdev/2).*randn(1,1);
```

```

    end
end
for i=bi*3+1:n
    while T(i,7)<0
        T(i,7)=rmean+rstdev.*randn(1,1);
    end
    while T(i,9)>pi/2||T(i,9)<-pi/2
        T(i,9)=amean+astdev.*randn(1,1);
    end
    while T(i,8)<sqrt(2)*delx
        T(i,8)=lmean+lstdev.*randn(1,1);
    end
end
end

B=zeros(bi,2); %Bifurcation nodes
B(:,1)=ceil(rand*(gelwidth-3))+1;
B(:,2)=ceil(rand*(gellength-2))+1;
for i=1:bi
    for j=i:bi
        if B(i,1)==B(j,1)&&B(i,2)==B(j,2)
            B(j,1)=ceil(rand*(gelwidth-2))+1;
            B(j,2)=ceil(rand*(gellength-2))+1;
        end
    end
end
end
for i=1:bi
    %First bi rows are tubules leading up to bifurcations
    T(i,1)=B(i,1)-round(sin(T(i,9))*T(i,8)/delx);
    T(i,2)=B(i,2)-round(cos(T(i,9))*T(i,8)/delx);
    T(i,3)=B(i,1);
    T(i,4)=B(i,2);
    %Second bi rows are tubules leading away from bifurcations
    T(i+bi,1)=B(i,1);
    T(i+bi,2)=B(i,2);
    T(i+bi,3)=T(i+bi,1)+round(sin(T(i+bi,9))*T(i+bi,8)/delx);
    T(i+bi,4)=T(i+bi,2)+round(cos(T(i+bi,9))*T(i+bi,8)/delx);
    %Third bi rows are other tubules leading away from bifurcations
    T(i+2*bi,1)=B(i,1);
    T(i+2*bi,2)=B(i,2);
    T(i+2*bi,3)=T(i+2*bi,1)+round(sin(T(i+2*bi,9))*T(i+2*bi,8)/delx);
    T(i+2*bi,4)=T(i+2*bi,2)+round(cos(T(i+2*bi,9))*T(i+2*bi,8)/delx);
end

%Rest of T = single tubules
for i=3*bi+1:n
    % for i=1:n
        T(i,1)=ceil(rand*(gelwidth-3))+1;
        T(i,2)=ceil(rand*(gellength-2))+1;
        T(i,3)=T(i,1)+round(sin(T(i,9))*T(i,8)/delx);
        T(i,4)=T(i,2)+round(cos(T(i,9))*T(i,8)/delx);
    end
    for i=1:n
        T(i,5)=gellength*(T(i,1)-1)+T(i,2);
        T(i,6)=gellength*(T(i,3)-1)+T(i,4);
        T(i,10)=sqrt((T(i,1)-T(i,3))^2+(T(i,2)-T(i,4))^2)*delx;
    end
end

```

```

% Make sure all tubules are within the gel
for i=1:bi
    while T(i,1)>gelwidth-2||T(i,1)<2||T(i,2)>gellength-
1||T(i,2)<2||...
        T(i,3)>gelwidth-2||T(i,3)<2||T(i,4)>gellength-
1||T(i,4)<1||...
            T(i+bi,1)>gelwidth-2||T(i+bi,1)<2||T(i+bi,2)>gellength-
1||T(i+bi,2)<2||...
                T(i+bi,3)>gelwidth-2||T(i+bi,3)<2||T(i+bi,4)>gellength-
1||T(i+bi,4)<2||...
                    T(i+2*bi,1)>gelwidth-
2||T(i+2*bi,1)<2||T(i+2*bi,2)>gellength-1||...
                        T(i+2*bi,2)<2||T(i+2*bi,3)>gelwidth-2||T(i+2*bi,3)<2||...
                            T(i+2*bi,4)>gellength-1||T(i+2*bi,4)<2
B(i,1)=ceil(rand*(gelwidth-3))+1;
B(i,2)=ceil(rand*(gellength-2))+1;
    T(i,1)=B(i,1)-round(sin(T(i,9))*T(i,8)/delx);
    T(i,2)=B(i,2)-round(cos(T(i,9))*T(i,8)/delx);
    T(i,3)=B(i,1);
    T(i,4)=B(i,2);
    T(i+bi,1)=B(i,1);
    T(i+bi,2)=B(i,2);
    T(i+bi,3)=T(i+bi,1)+round(sin(T(i+bi,9))*T(i+bi,8)/delx);
    T(i+bi,4)=T(i+bi,2)+round(cos(T(i+bi,9))*T(i+bi,8)/delx);
    T(i+2*bi,1)=B(i,1);
    T(i+2*bi,2)=B(i,2);

T(i+2*bi,3)=T(i+2*bi,1)+round(sin(T(i+2*bi,9))*T(i+2*bi,8)/delx);

T(i+2*bi,4)=T(i+2*bi,2)+round(cos(T(i+2*bi,9))*T(i+2*bi,8)/delx);
    T(i,5)=gellength*(T(i,1)-1)+T(i,2);
    T(i,6)=gellength*(T(i,3)-1)+T(i,4);
    T(i,10)=sqrt((T(i,1)-T(i,3))^2+(T(i,2)-T(i,4))^2)*delx;
    T(i+bi,5)=gellength*(T(i+bi,1)-1)+T(i+bi,2);
    T(i+bi,6)=gellength*(T(i+bi,3)-1)+T(i+bi,4);
    T(i+bi,10)=sqrt((T(i+bi,1)-T(i+bi,3))^2+(T(i+bi,2)-
T(i+bi,4))^2)*delx;
    T(i+2*bi,5)=gellength*(T(i+2*bi,1)-1)+T(i+2*bi,2);
    T(i+2*bi,6)=gellength*(T(i+2*bi,3)-1)+T(i+2*bi,4);
    T(i+2*bi,10)=sqrt((T(i+2*bi,1)-T(i+2*bi,3))^2+...
        (T(i+2*bi,2)-T(i+2*bi,4))^2)*delx;

    end
    if T(i+bi,3)==T(i+2*bi,3)&&T(i+bi,4)==T(i+2*bi,4)
        r=round(rand*2);
        if r==1
            T(i+2*bi,3)=T(i+2*bi,3)+1;
        else
            T(i+2*bi,3)=T(i+2*bi,3)-1;
        end
    end
end
end
for i=3*bi+1:n
% for i=1:n
    while T(i,1)>gelwidth-2||T(i,1)<2||T(i,2)>gellength-
1||T(i,2)<2||...

```

```

        T(i,3)>gelwidth-2||T(i,3)<2||T(i,4)>gellength-
1||T(i,4)<2||T(i,10)==0
        T(i,1)=ceil(rand*(gelwidth-3))+1;
        T(i,2)=ceil(rand*(gellength-2))+1;
        T(i,3)=T(i,1)+round(sin(T(i,9))*T(i,8)/delx);
        T(i,4)=T(i,2)+round(cos(T(i,9))*T(i,8)/delx);
        T(i,5)=gellength*(T(i,1)-1)+T(i,2);
        T(i,6)=gellength*(T(i,3)-1)+T(i,4);
        T(i,10)=sqrt((T(i,1)-T(i,3))^2+(T(i,2)-T(i,4))^2)*delx;
    end
end

%Darcy's Law Base
A=sparse(zeros(3*gelsize));
%middle
for i=1+gellength:(gelwidth-1)*gellength
    if rem(i,gellength)==2
        for k=i:i+gellength-3
            %mass balance
            A(k,k+1+vxcomp)=Dx;
            A(k,k+vxcomp)=-Dx;
            A(k,k+gellength+vycomp)=Dy;
            A(k,k+vycomp)=-Dy;
            %x-momentum balance
            A(k+vxcomp,k+vxcomp)=1;
            A(k+vxcomp,k-1)=-Dx2;
            A(k+vxcomp,k)=Dx2;
            %y-momentum balance
            A(k+vycomp,k+vycomp)=1;
            A(k+vycomp,k-gellength)=-Dy2;
            A(k+vycomp,k)=Dy2;
        end
    end
end

%top
for i=2:gellength-1
    %mass balance
    A(i,i+1+vxcomp)=Dx;
    A(i,i+vxcomp)=-Dx;
    A(i,i+vycomp)=-Dy;
    A(i,i+gellength+vycomp)=Dy;
    %x-momentum balance
    A(i+vxcomp,i+vxcomp)=1;
    A(i+vxcomp,i-1)=-Dx2;
    A(i+vxcomp,i)=Dx2;
    %y-momentum balance
    A(i+vycomp,i+vycomp)=1;
end

%bottom
for i=(gelwidth-1)*gellength+2:gelsize-1
    %mass balance
    A(i,i+1+vxcomp)=Dx;
    A(i,i+vxcomp)=-Dx;
    A(i,i-gellength+vycomp)=-Dy;
    A(i,i+vycomp)=Dy;
end

```



```

    %x-momentum balance
    A(i+vxcomp,i+vxcomp)=1;
    A(i+vxcomp,i-1)=-Dx2;
    A(i+vxcomp,i)=Dx2;
    %y-momentum balance
    A(i+vycomp,i+vycomp)=1;
end

%inlet&outlet
for i=gellength+1:gelsize-gellength
    if rem(i,gellength)==0
        %mass balance
        A(i,i)=1;
        %x-momentum balance
        A(i+vxcomp,i+vxcomp)=1;
        A(i+vxcomp,i-1)=-Dx2;
        A(i+vxcomp,i)=Dx2;
        %y-momentum balance
        A(i+vycomp,i+vycomp)=1;
        A(i+vycomp,i-gellength)=-Dy2;
        A(i+vycomp,i)=Dy2;
    elseif rem(i,gellength)==1
        %mass balance
        A(i,i+vxcomp)=-Dx;
        A(i,i+1+vxcomp)=Dx;
        A(i,i+gellength+vycomp)=Dy;
        A(i,i+vycomp)=-Dy;
        %x-momentum balance
        A(i+vxcomp,i+vxcomp)=1;
        %y-momentum balance
        A(i+vycomp,i+vycomp)=1;
    end
end

%corners
    %mass balance
    A(1,1+vxcomp)=-Dx;
    A(1,2+vxcomp)=Dx;
    A(1,1+vycomp)=-Dy;
    A(1,1+gellength+vycomp)=Dy;

    A(gellength,gellength)=1;

    A(gelsize-gellength+1,gelsize-gellength+1+vxcomp)=-Dx;
    A(gelsize-gellength+1,gelsize-gellength+2+vxcomp)=Dx;
    A(gelsize-gellength+1,gelsize-gellength+1+vycomp)=Dy;
    A(gelsize-gellength+1,gelsize-gellength*2+1+vycomp)=-Dy;

    A(gelsize,gelsize)=1;

    %x-momentum
    A(1+vxcomp,1+vxcomp)=1;

    A(gellength+vxcomp,gellength+vxcomp)=1;
    A(gellength+vxcomp,gellength)=Dx2;

```

```

A(gellength+vxcomp,gellength-1)=-Dx2;

A(gelsize-gellength+1+vxcomp,gelsize-gellength+1+vxcomp)=1;

A(gelsize+vxcomp,gelsize+vxcomp)=1;
A(gelsize+vxcomp,gelsize)=Dx2;
A(gelsize+vxcomp,gelsize-1)=-Dx2;

    %y-momentum
A(1+vycomp,1+vycomp)=1;

A(gellength+vycomp,gellength+vycomp)=1;

A(gelsize-gellength+1+vycomp,gelsize-gellength+1+vycomp)=1;

A(gelsize+vycomp,gelsize+vycomp)=1;

%Add Tubule Flow
for i=1:bi
%inlet of bifurcation
    %mass balance
    A(T(i,5),T(i,5))=A(T(i,5),T(i,5))+...
        P*T(i,7)^4/T(i,10)*(1-T(i,7)^4/T(i,10)/...
            (T(i,7)^4/T(i,10)+T(i+bi,7)^4/T(i+bi,10)+T(i+2*bi,7)^4/T(i+2*bi,10)));
    A(T(i,5),T(i+bi,6))=A(T(i,5),T(i+bi,6))-...
        P*T(i,7)^4/T(i,10)*T(i+bi,7)^4/T(i+bi,10)/...
            (T(i,7)^4/T(i,10)+T(i+bi,7)^4/T(i+bi,10)+T(i+2*bi,7)^4/T(i+2*bi,10)));
    A(T(i,5),T(i+2*bi,6))=A(T(i,5),T(i+2*bi,6))-...
        P*T(i,7)^4/T(i,10)*T(i+2*bi,7)^4/T(i+2*bi,10)/...
            (T(i,7)^4/T(i,10)+T(i+bi,7)^4/T(i+bi,10)+T(i+2*bi,7)^4/T(i+2*bi,10)));

    %x-momentum balance
    A(T(i,5)+vxcomp,T(i,5))=A(T(i,5)+vxcomp,T(i,5))-...
        P2*T(i,7)^2/T(i,10)*cos(T(i,9))*(1-T(i,7)^4/T(i,10)/...
            (T(i,7)^4/T(i,10)+T(i+bi,7)^4/T(i+bi,10)+T(i+2*bi,7)^4/T(i+2*bi,10)));
    A(T(i,5)+vxcomp,T(i+bi,6))=A(T(i,5)+vxcomp,T(i+bi,6))+...
        P2*T(i,7)^2/T(i,10)*cos(T(i,9))*T(i+bi,7)^4/T(i+bi,10)/...
            (T(i,7)^4/T(i,10)+T(i+bi,7)^4/T(i+bi,10)+T(i+2*bi,7)^4/T(i+2*bi,10)));
    A(T(i,5)+vxcomp,T(i+2*bi,6))=A(T(i,5)+vxcomp,T(i+2*bi,6))+...
        P2*T(i,7)^2/T(i,10)*cos(T(i,9))*T(i+2*bi,7)^4/T(i+2*bi,10)/...
            (T(i,7)^4/T(i,10)+T(i+bi,7)^4/T(i+bi,10)+T(i+2*bi,7)^4/T(i+2*bi,10)));

    %y-momentum balance
    A(T(i,5)+vycomp,T(i,5))=A(T(i,5)+vycomp,T(i,5))-...
        P2*T(i,7)^2/T(i,10)*sin(T(i,9))*(1-T(i,7)^4/T(i,10)/...
            (T(i,7)^4/T(i,10)+T(i+bi,7)^4/T(i+bi,10)+T(i+2*bi,7)^4/T(i+2*bi,10)));
    A(T(i,5)+vycomp,T(i+bi,6))=A(T(i,5)+vycomp,T(i+bi,6))+...
        P2*T(i,7)^2/T(i,10)*sin(T(i,9))*T(i+bi,7)^4/T(i+bi,10)/...
            (T(i,7)^4/T(i,10)+T(i+bi,7)^4/T(i+bi,10)+T(i+2*bi,7)^4/T(i+2*bi,10)));

```

```

(T(i,7)^4/T(i,10)+T(i+bi,7)^4/T(i+bi,10)+T(i+2*bi,7)^4/T(i+2*bi,10));
  A(T(i,5)+vycomp,T(i+2*bi,6))=A(T(i,5)+vycomp,T(i+2*bi,6))+...
  P2*T(i,7)^2/T(i,10)*sin(T(i,9))*T(i+2*bi,7)^4/T(i+2*bi,10)/...

(T(i,7)^4/T(i,10)+T(i+bi,7)^4/T(i+bi,10)+T(i+2*bi,7)^4/T(i+2*bi,10));

%%outlet 1 of bifurcation
  %mass balance
  A(T(i+bi,6),T(i+bi,6))=A(T(i+bi,6),T(i+bi,6))+...
  P*T(i+bi,7)^4/T(i+bi,10)*(1-T(i+bi,7)^4/T(i+bi,10)/...

(T(i,7)^4/T(i,10)+T(i+bi,7)^4/T(i+bi,10)+T(i+2*bi,7)^4/T(i+2*bi,10));
  A(T(i+bi,6),T(i,5))=A(T(i+bi,6),T(i,5))-...
  P*T(i+bi,7)^4/T(i+bi,10)*T(i,7)^4/T(i,10)/...

(T(i,7)^4/T(i,10)+T(i+bi,7)^4/T(i+bi,10)+T(i+2*bi,7)^4/T(i+2*bi,10));
  A(T(i+bi,6),T(i+2*bi,6))=A(T(i+bi,6),T(i+2*bi,6))-...
  P*T(i+bi,7)^4/T(i+bi,10)*T(i+2*bi,7)^4/T(i+2*bi,10)/...

(T(i,7)^4/T(i,10)+T(i+bi,7)^4/T(i+bi,10)+T(i+2*bi,7)^4/T(i+2*bi,10));

  %x-momentum balance
  A(T(i+bi,6)+vxcomp,T(i+bi,6))=A(T(i+bi,6)+vxcomp,T(i+bi,6))-...
  P2*T(i+bi,7)^2/T(i+bi,10)*cos(T(i+bi,9))*(1-
T(i+bi,7)^4/T(i+bi,10)/...

(T(i,7)^4/T(i,10)+T(i+bi,7)^4/T(i+bi,10)+T(i+2*bi,7)^4/T(i+2*bi,10));
  A(T(i+bi,6)+vxcomp,T(i,5))=A(T(i+bi,6)+vxcomp,T(i,5))+...
  P2*T(i+bi,7)^2/T(i+bi,10)*cos(T(i+bi,9))*T(i,7)^4/T(i,10)/...

(T(i,7)^4/T(i,10)+T(i+bi,7)^4/T(i+bi,10)+T(i+2*bi,7)^4/T(i+2*bi,10));
  A(T(i+bi,6)+vxcomp,T(i+2*bi,6))=A(T(i+bi,6)+vxcomp,T(i+2*bi,6))+...
P2*T(i+bi,7)^2/T(i+bi,10)*cos(T(i+bi,9))*T(i+2*bi,7)^4/T(i+2*bi,10)/...

(T(i,7)^4/T(i,10)+T(i+bi,7)^4/T(i+bi,10)+T(i+2*bi,7)^4/T(i+2*bi,10));

  %y-momentum balance
  A(T(i+bi,6)+vycomp,T(i+bi,6))=A(T(i+bi,6)+vycomp,T(i+bi,6))-...
  P2*T(i+bi,7)^2/T(i+bi,10)*sin(T(i+bi,9))*(1-
T(i+bi,7)^4/T(i+bi,10)/...

(T(i,7)^4/T(i,10)+T(i+bi,7)^4/T(i+bi,10)+T(i+2*bi,7)^4/T(i+2*bi,10));
  A(T(i+bi,6)+vycomp,T(i,5))=A(T(i+bi,6)+vycomp,T(i,5))+...
  P2*T(i+bi,7)^2/T(i+bi,10)*sin(T(i+bi,9))*T(i,7)^4/T(i,10)/...

(T(i,7)^4/T(i,10)+T(i+bi,7)^4/T(i+bi,10)+T(i+2*bi,7)^4/T(i+2*bi,10));
  A(T(i+bi,6)+vycomp,T(i+2*bi,6))=A(T(i+bi,6)+vycomp,T(i+2*bi,6))+...
P2*T(i+bi,7)^2/T(i+bi,10)*sin(T(i+bi,9))*T(i+2*bi,7)^4/T(i+2*bi,10)/...

(T(i,7)^4/T(i,10)+T(i+bi,7)^4/T(i+bi,10)+T(i+2*bi,7)^4/T(i+2*bi,10));

%%outlet 2 of bifurcation
  %mass balance

```

```

A(T(i+2*bi,6),T(i+2*bi,6))=A(T(i+2*bi,6),T(i+2*bi,6))+...
P*T(i+2*bi,7)^4/T(i+2*bi,10)*(1-T(i+2*bi,7)^4/T(i+2*bi,10)/...
(T(i,7)^4/T(i,10)+T(i+bi,7)^4/T(i+bi,10)+T(i+2*bi,7)^4/T(i+2*bi,10));
A(T(i+2*bi,6),T(i,5))=A(T(i+2*bi,6),T(i,5))-...
P*T(i+2*bi,7)^4/T(i+2*bi,10)*T(i,7)^4/T(i,10)/...
(T(i,7)^4/T(i,10)+T(i+bi,7)^4/T(i+bi,10)+T(i+2*bi,7)^4/T(i+2*bi,10));
A(T(i+2*bi,6),T(i+bi,6))=A(T(i+2*bi,6),T(i+bi,6))-...
P*T(i+2*bi,7)^4/T(i+2*bi,10)*T(i+bi,7)^4/T(i+bi,10)/...
(T(i,7)^4/T(i,10)+T(i+bi,7)^4/T(i+bi,10)+T(i+2*bi,7)^4/T(i+2*bi,10));

%x-momentum balance
A(T(i+2*bi,6)+vxcomp,T(i+2*bi,6))=A(T(i+2*bi,6)+vxcomp,T(i+2*bi,6))-...
P2*T(i+2*bi,7)^2/T(i+2*bi,10)*cos(T(i+2*bi,9))*(1-
T(i+2*bi,7)^4/T(i+2*bi,10)/...
(T(i,7)^4/T(i,10)+T(i+bi,7)^4/T(i+bi,10)+T(i+2*bi,7)^4/T(i+2*bi,10));
A(T(i+2*bi,6)+vxcomp,T(i,5))=A(T(i+2*bi,6)+vxcomp,T(i,5))+...
P2*T(i+2*bi,7)^2/T(i+2*bi,10)*cos(T(i+2*bi,9))*T(i,7)^4/T(i,10)/...
(T(i,7)^4/T(i,10)+T(i+bi,7)^4/T(i+bi,10)+T(i+2*bi,7)^4/T(i+2*bi,10));
A(T(i+2*bi,6)+vxcomp,T(i+bi,6))=A(T(i+2*bi,6)+vxcomp,T(i+bi,6))+...
P2*T(i+2*bi,7)^2/T(i+2*bi,10)*cos(T(i+2*bi,9))*T(i+bi,7)^4/T(i+bi,10)/
..
(T(i,7)^4/T(i,10)+T(i+bi,7)^4/T(i+bi,10)+T(i+2*bi,7)^4/T(i+2*bi,10));

%y-momentum balance
A(T(i+2*bi,6)+vycomp,T(i+2*bi,6))=A(T(i+2*bi,6)+vycomp,T(i+2*bi,6))-...
P2*T(i+2*bi,7)^2/T(i+2*bi,10)*sin(T(i+2*bi,9))*(1-
T(i+2*bi,7)^4/T(i+2*bi,10)/...
(T(i,7)^4/T(i,10)+T(i+bi,7)^4/T(i+bi,10)+T(i+2*bi,7)^4/T(i+2*bi,10));
A(T(i+2*bi,6)+vycomp,T(i,5))=A(T(i+2*bi,6)+vycomp,T(i,5))+...
P2*T(i+2*bi,7)^2/T(i+2*bi,10)*sin(T(i+2*bi,9))*T(i,7)^4/T(i,10)/...
(T(i,7)^4/T(i,10)+T(i+bi,7)^4/T(i+bi,10)+T(i+2*bi,7)^4/T(i+2*bi,10));
A(T(i+2*bi,6)+vycomp,T(i+bi,6))=A(T(i+2*bi,6)+vycomp,T(i+bi,6))+...
P2*T(i+2*bi,7)^2/T(i+2*bi,10)*sin(T(i+2*bi,9))*T(i+bi,7)^4/T(i+bi,10)/
..
(T(i,7)^4/T(i,10)+T(i+bi,7)^4/T(i+bi,10)+T(i+2*bi,7)^4/T(i+2*bi,10));
end

for i=3*bi+1:n
% for i=1:n
%mass balance
A(T(i,5),T(i,5))=A(T(i,5),T(i,5))+P*T(i,7)^4/T(i,10);

```

```

A(T(i,5),T(i,6))=A(T(i,5),T(i,6))-P*T(i,7)^4/T(i,10);
A(T(i,6),T(i,5))=A(T(i,6),T(i,5))-P*T(i,7)^4/T(i,10);
A(T(i,6),T(i,6))=A(T(i,6),T(i,6))+P*T(i,7)^4/T(i,10);

%x-momentum balance
A(T(i,5)+vxcomp,T(i,5))=A(T(i,5)+vxcomp,T(i,5))-
P2*T(i,7)^2/T(i,10)*cos(T(i,9));

A(T(i,5)+vxcomp,T(i,6))=A(T(i,5)+vxcomp,T(i,6))+P2*T(i,7)^2/T(i,10)*cos
(T(i,9));

A(T(i,6)+vxcomp,T(i,5))=A(T(i,6)+vxcomp,T(i,5))+P2*T(i,7)^2/T(i,10)*cos
(T(i,9));
A(T(i,6)+vxcomp,T(i,6))=A(T(i,6)+vxcomp,T(i,6))-
P2*T(i,7)^2/T(i,10)*cos(T(i,9));

%y-momentum balance
A(T(i,5)+vycomp,T(i,5))=A(T(i,5)+vycomp,T(i,5))-
P2*T(i,7)^2/T(i,10)*sin(T(i,9));

A(T(i,5)+vycomp,T(i,6))=A(T(i,5)+vycomp,T(i,6))+P2*T(i,7)^2/T(i,10)*sin
(T(i,9));

A(T(i,6)+vycomp,T(i,5))=A(T(i,6)+vycomp,T(i,5))+P2*T(i,7)^2/T(i,10)*sin
(T(i,9));
A(T(i,6)+vycomp,T(i,6))=A(T(i,6)+vycomp,T(i,6))-
P2*T(i,7)^2/T(i,10)*sin(T(i,9));
end

%set BC (inlet vx, inlet vy(=0); outlet P)
C=zeros(3*gelsize,1);
for i=1:gelwidth
    C((i-1)*gellength+1+vxcomp,1)=vxinlet;
    C(i*gellength,1)=poutlet;
end
p=A\C;

pmap=zeros(gelwidth,gellength);
vxmap=zeros(gelwidth,gellength);
vymap=zeros(gelwidth,gellength);
for i=1:gelsize
    q=floor((i-1)/gellength)+1;
    r=rem((i-1),gellength)+1;
    pmap(q,r)=p(i);
    vxmap(q,r)=p(i+vxcomp);
    vymap(q,r)=p(i+vycomp);
end
[mpmap,npmap]=size(pmap);

pmap2=zeros(5*size(pmap));
vxmap2=zeros(5*size(vxmap));
vymap2=zeros(5*size(vymap));
for i=1:mpmap
    for j=1:npmap
        for k=1:5
            for l=1:5

```

```

        pmap2(i*5-k+1,j*5-l+1)=pmap(i,j);
        vxmap2(i*5-k+1,j*5-l+1)=vxmap(i,j);
        vymap2(i*5-k+1,j*5-l+1)=vymap(i,j);
    end
end
end
end

vt=zeros(n,1);
Qt=zeros(n,1);
for i=1:bi

pbifur=(T(i,7)^4/T(i,10)+T(i+bi,7)^4/T(i+bi,10)+T(i+2*bi,7)^4/T(i+2*bi,
10));
    vt(i)=P2*T(i,7)^2/T(i,10)*...
        ((1-T(i,7)^4/T(i,10)/pbifur)*p(T(i,5))-...
        T(i+bi,7)^4/T(i+bi,10)/pbifur*p(T(i+bi,6))-...
        T(i+2*bi,7)^4/T(i+2*bi,10)/pbifur*p(T(i+2*bi,6)));
    Qt(i)=P*T(i,7)^4/T(i,10)*...
        ((1-T(i,7)^4/T(i,10)/pbifur)*p(T(i,5))-...
        T(i+bi,7)^4/T(i+bi,10)/pbifur*p(T(i+bi,6))-...
        T(i+2*bi,7)^4/T(i+2*bi,10)/pbifur*p(T(i+2*bi,6)))*delx^3;

    vt(i+bi)=P2*T(i+bi,7)^2/T(i+bi,10)*...
        ((-1+T(i+bi,7)^4/T(i+bi,10)/pbifur)*p(T(i+bi,6))+...
        T(i,7)^4/T(i,10)/pbifur*p(T(i,5))+...
        T(i+2*bi,7)^4/T(i+2*bi,10)/pbifur*p(T(i+2*bi,6)));
    Qt(i+bi)=P*T(i+bi,7)^4/T(i+bi,10)*...
        ((-1+T(i+bi,7)^4/T(i+bi,10)/pbifur)*p(T(i+bi,6))+...
        T(i,7)^4/T(i,10)/pbifur*p(T(i,5))+...
        T(i+2*bi,7)^4/T(i+2*bi,10)/pbifur*p(T(i+2*bi,6)))*delx^3;

    vt(i+2*bi)=P2*T(i+2*bi,7)^2/T(i+2*bi,10)*...
        ((-1+T(i+2*bi,7)^4/T(i+2*bi,10)/pbifur)*p(T(i+2*bi,6))+...
        T(i,7)^4/T(i,10)/pbifur*p(T(i,5))+...
        T(i+bi,7)^4/T(i+bi,10)/pbifur*p(T(i+bi,6)));
    Qt(i+2*bi)=P*T(i+2*bi,7)^4/T(i+2*bi,10)*...
        ((-1+T(i+2*bi,7)^4/T(i+2*bi,10)/pbifur)*p(T(i+2*bi,6))+...
        T(i,7)^4/T(i,10)/pbifur*p(T(i,5))+...
        T(i+bi,7)^4/T(i+bi,10)/pbifur*p(T(i+bi,6)))*delx^3;

end
for i=3*bi+1:n
% for i=1:n
    vt(i)=P2*T(i,7)^2/T(i,10)*(p(T(i,5))-p(T(i,6)));
    Qt(i)=P*T(i,7)^4/T(i,10)*(p(T(i,5))-p(T(i,6)))*delx^3;
end
binaryt=ones(n,1)*255;

x1=T(:,1)*5-ones(n,1)*2;
y1=T(:,2)*5-ones(n,1)*2;
x2=T(:,3)*5-ones(n,1)*2;
y2=T(:,4)*5-ones(n,1)*2;
tmap=drawlines(x1,y1,x2,y2,pmap2,vt);
tmap2=drawlines(x1,y1,x2,y2,pmap2,Qt);
tmap3=drawlines(x1,y1,x2,y2,pmap2,binaryt);

```

```

maxvx=max (max (vxmap2) ) +max (max (vxmap2) ) /10;
for i=1:5*mpmap
    for j=1:5*npmap
        if tmap(i,j)~=0
            pmap2(i,j)=max (max (pmap) ) +max (max (pmap) ) /10;
            vxmap2(i,j)=maxvx+maxvx/10;
            vmap2(i,j)=maxvx+maxvx/10;
        end
    end
end

aix=0;aiy=0;
for i=1:n
    aix=aix+abs (T(i,4)-T(i,2));
    aiy=aiy+abs (T(i,3)-T(i,1));
    ai=aix/aiy;
end

flowgel=zeros (gelwidth-2,1);
sumflowgel1=zeros (gellength-2,1);
sumflowgel2=zeros (gellength-2,1);
sumflowtubes=zeros (gellength-2,1);
percentflowthrutubes1=zeros (gellength-2,1);
percentflowthrutubes2=zeros (gellength-2,1);
for i=gellength/3+1:gellength/3*2
    for j=2:gelwidth-2
        flowgel(j)=sqrt (vxmap2 (j*5,i*5)^2+vmap2 (j*5,i*5)^2);
    end
    flowtubes=zeros (n,1);
    lumenarea=zeros (n,1);
    for l=1:n
        if T(l,2)<=i && T(l,4)>=i
            flowtubes(l)=vt(l)*T(l,7)^2*pi;
            lumenarea(l)=T(l,7)^2*pi;
        end
    end
    sumflowgel1(i)=sum (flowgel) *(((gelwidth-3)*delx)^2-sum (lumenarea));
    sumflowgel2(i)=sum (flowgel) *(((gelwidth-3)*delx)^2);
    sumflowtubes(i)=sum (flowtubes);

percentflowthrutubes1(i)=sumflowtubes(i) / (sumflowgel1(i)+sumflowtubes(i));

percentflowthrutubes2(i)=sumflowtubes(i) / (sumflowgel2(i)+sumflowtubes(i));
end
avgpercent1=mean (percentflowthrutubes1);
avgpercent2=mean (percentflowthrutubes2);

figure, image (pmap2, 'CDataMapping', 'scaled')
caxis ([0,max (max (pmap2) ) *1.1])
colormap (jet)
colorbar
min (min (pmap2) )
max (max (pmap2) )

```

```

figure, image(vxmap2, 'CDataMapping', 'scaled')
caxis([min(min(vxmap)),max(max(vxmap))+max(max(vxmap))/10])
colormap(jet)
colorbar

figure, image(vymap2, 'CDataMapping', 'scaled')
caxis([min(min(vxmap)),max(max(vxmap))+max(max(vxmap))/10])
caxis([-1e-3,1e-3])
colormap(jet)
colorbar

figure, image(tmap, 'CDataMapping', 'scaled')
caxis([0,max(max(tmap))])
colormap(jet)
colorbar

Qmap=zeros(size(vxmap2));
for i=1:5*mpmap
    for j=1:5*npmap
        if tmap2(i,j)~=0
            Qmap(i,j)=tmap2(i,j);
        else

Qmap(i,j)=sqrt((vxmap2(i,j)*delx^2)^2+(vymap2(i,j)*delx^2)^2);
        end
    end
end

figure, image(Qmap, 'CDataMapping', 'scaled')
caxis([0,1e-8])%1e-10]
colormap(jet)
colorbar

figure, imshow(~tmap3)
hold on
x5=zeros(gellength,1);
y5=zeros(gelwidth,1);
for i=1:gellength
    x5(i)=i*5-2;
end
for i=1:gelwidth
    y5(i)=i*5-2;
end
vtx=zeros(gelwidth,gellength);
vty=zeros(gelwidth,gellength);
for i=1:bi
    vtx(T(i,1),T(i,2))=vt(i)*cos(T(i,9));
    vty(T(i,1),T(i,2))=vt(i)*sin(T(i,9));
end
for i=bi+1:bi*3
    vtx(T(i,3),T(i,4))=vt(i)*cos(T(i,9));
    vty(T(i,3),T(i,4))=vt(i)*sin(T(i,9));
end
for i=bi*3+1:n
% for i=1:n
    vtx(T(i,1),T(i,2))=vt(i)*cos(T(i,9));

```



```

        vty(T(i,1),T(i,2))=vt(i)*sin(T(i,9));
        vtx(T(i,3),T(i,4))=vt(i)*cos(T(i,9));
        vty(T(i,3),T(i,4))=vt(i)*sin(T(i,9));
    end
    quiver(x5,y5,vtx*15000,vty*15000,0);
    quiver(x5,y5,vxmap*15000,vymap*15000,0);
    % hold off

    result(aa,1)=delx;
    result(aa,2)=perm;
    result(aa,3)=mu;
    result(aa,4)=gelwidth;
    result(aa,5)=gellength;
    result(aa,6)=vxinlet;
    result(aa,7)=poutlet;
    result(aa,8)=rmean; %avg tube radius
    result(aa,9)=rstdev;
    result(aa,10)=lmean; %avg tube length
    result(aa,11)=lstdev;
    result(aa,12)=amean; %avg tube angle
    result(aa,13)=astdev;
    result(aa,14)=vxinlet*((gelwidth-1)*delx)^2; %Q tissue inlet defined
    result(aa,15)=mean(Qt); %Q tube
    result(aa,16)=mean(vt); %v tube
    result(aa,17)=mean(pmap(:,1)); %P tissue inlet
    result(aa,18)=vxinlet*(gellength-1)*delx/result(aa,17)*mu/u; %effective
    k
    result(aa,19)=ai; %anisotropy index
    result(aa,20)=mean(vxmap(:,gellength))*((gelwidth-1)*delx)^2; %Q tissue
    outlet
    result(aa,21)=mean(sum(tmap3)/255)/((gelwidth-1)*delx*10)^2;
    %numberlumens/mm^2
end

xlswrite('result.xls',result);

```